Performance Studies of a Time Projection Chamber at the ILC

and

Search for Lepton Flavour Violation at HERA II

Dissertation

zur Erlangung des Doktorgrades

des Department Physik
der Universität Hamburg

vorgelegt von

Matthias Enno Janssen
aus Oberhausen

Hamburg
April 2008

Gutachter der Dissertation:	Prof. Dr. Rolf-Dieter Heuer JProf. Dr. Johannes Haller
Gutachter der Disputation:	Prof. Dr. Rolf-Dieter Heuer Prof. Dr. Peter Schleper
Datum der Disputation:	07. Mai 2008
Vorsitzende des Prüfungsausschusses:	Prof. Dr. Caren Hagner
Vorsitzender des Promotionsausschusses:	Prof. Dr. Joachim Bartels
Dekan der MIN-Fakultät:	Prof. Dr. Arno Frühwald
Leiter des Department Physik:	Prof. Dr. Robert Klanner

Die Physik erklärt die Geheimnisse der Natur nicht, sie führt sie nur auf tieferliegende Geheimnisse zurück.
Physics does not explain the secrets of nature, it only leads them back to even more subjacent secrets.

Carl Friedrich von Weizsäcker

Abstract

It is expected, that new physics beyond the Standard Model can be discovered in the energy range of 1 TeV. One of the next projects in high energy physics will be a linear collider. A proposal for such a machine is the International Linear Collider (ILC), where electrons and positrons are brought to collision with a centre of mass energy up to 500 GeV with the possibility to upgrade it to 1 TeV.

The precision measurement of this new physics sets high requirements on the performance of the detector at the ILC. As the main tracking device for a detector at the ILC, a Time Projection Chamber (TPC) has been proposed. To reach these requirements a new amplification techniques based on Micro Pattern Gas Detectors (MPGD) is under investigation.

In this thesis, data are analysed, that were taken using the prototype MediTPC, whose amplification system is based on Gas Electron Multipliers (GEM). Different magnetic fields of up to 4 T, two gas mixtures and differed arrangement of the pads have also been investigated.

The main part of this thesis deals with the study of the performance of two different approaches to determine track parameters. A new method based on a likelihood fit of the expected charge to the measured one is compared to a traditional approach using reconstructed space points and a χ^2 minimisation technique. Different aspects such as the performance in the presence of non working channels and the angular dependency are investigated.

Finally the determined spatial resolution (in the $r\phi$-plane) is presented. At zero drift length a resolution of the order of 100 µm can be achieved.

In the second part of this thesis the results of a search for lepton flavour violation mediated by leptoquarks is presented. Data of electron-proton collisions with a centre-of-mass energy of 320 GeV taken with the H1 experiment are investigated.

The analysis concentrates of the $e^- p$ data of the HERA II phase, which were taken in the years 2004-2006. They correspond to an integrated luminosity of $158.9\,\mathrm{pb}^{-1}$. Only final states with muon are considered.

No evidence for a deviation from the Standard Model via lepton flavour violation has been observed. Therefore, limits on Yukawa coupling of LQ to a muon and a light quark using an extension of Buchmüller-Rückl-Wyler model are derived. Assuming a coupling of 0.3, leptoquark masses between 290 GeV and 406 GeV can be excluded with a 95% confidence level depending on leptoquark type.

Kurzfassung

Es wird erwartet, dass neue Physik, die über das Standard Modell hinausgeht, in Bereich bis zu einer Energie von 1 TeV beobachtet werden kann. Als eines der nächten Projekte in der Hochenergiephysik ist ein Linearbeschleuniger vorgesehen. Ein Vorschlag für eine solche Maschine ist der International Linear Collider (ILC). In diesem sollen Elektronen und Positronen zur mit einer Schwerpunktsenergie von 500 GeV zur Kollision gebracht werden. Es ist möglich die Schwerpunktsenergie auf 1 TeV zu erhöhen.

Um zu ermöglichen, dass neue Physik mit einer hohen Präzision vermessen werden kann, muss ein Detektor am ILC sehr hohen Ansprüchen genügen. einige Konzepte für einen solchen Detektor sehen eine Zeit-Projektions-Kammer (eng: Time Projection Chamber [TPC]) als zentrale Spurkammer vor. Um die hohen Anforderungen zu erfüllen zu können, werden neue Technologien zur Gasverstärkung untersucht, die auf Mikro-Struktur-Gasdetektoren basieren.

In dieser Arbeit werden Daten analysiert,die mit den TPC Prototyp MediTPC aufgenommen wurden. Dieser Prototyp nutzt eine auf Gas-Elektronen-Vervielfachern basierende Verstärkungsstruktur. Der Einfluss eines Magnetfeldes (bis zu 4 T) sowie unterschiedliche Auslesestrukturen wurden untersucht.

Der Hauptteil der Analyse konzentriert sich auf die Untersuchung zweier verschiedener Anzätze zur Rekonstruktion der Spurparameter. Ein Ansatz basiert auf einer Maximum-Likelihood-Anpassung der erwarteten Ladung an die gemessene. Diese neue Ansatz wird mit dem traditionellen vergleichen, der rekonstruierte Raum-punkte und eine χ^2-Minimierung benutzt. Verschiedene Aspekte wie z. B. die Winkelabhängigkeit oder das Leistungsvermögen bei nicht arbeitenden Auslesekanälen wurden untersucht.

Zum Schluss dieses Abschnitts wird die Einzelpunktauflösung (in der $r\phi$ Ebene) präsentiert. Direkt vor dem Verstärkungssystem kann eine Auflösung von 100 µm erreicht werden.

Der zweite Teil der Arbeit beschäftigt sich mit der Suche nach Lepton-Familienzahl-Verletzung, die durch Leptoquarks vermittelt wird. Daten von Elektron-Proton-Kollisionen mit einer Schwerpunktsenergie von 320 GeV werden untersucht. Diese Daten wurden von dem H1 Experiment aufgezeichnet. Die Analyse konzentriert sich auf die e^-pDaten, die wärend der HERA II Phase in den Jahren 2004-2006 genommen wurden. Diese Daten entsprechen einer integrierten Luminosität von $158.9\,\mathrm{pb}^{-1}$. Nur Ereignisse mit einem Myon im Endzustand wurden berücksichtigt.

Die Suche ergab keinen Hinweise für eine Abweichung von der Erwartung des Standardmodells. Daher wurden Grenzen für die Yukawa-Kopplung für Leptoquarks, die in ein Myon und ein leichtes Quark zerfallen, bestimmt. Hierzu wurde eine Erweiterung des Buchmüller-Rückl-Wyler-Modells verwendet. Mit der Annahme einer Kopplungsgröße von 0,3, können obere Grenzen für die Leptoquarkmassen bestimmt werden. Diese variieren je nach Typ des Leptoquarks zweichen 290 und 406 GeV.

Contents

Chapter 1

Introduction

1.1 The Standard Model of Particle Physics

The current knowledge about particle physics is described in the Standard Model [1]. It is based on the concept of local gauge invariance and classifies the elementary particles and predicts the interactions between them. According to the Standard Model, the fundamental particles are divided into fermions with a spin of one half and the bosons which have an integer spin. The fermions appear in three generations, which are also known as flavours. Each generation contains two leptons – an electron-type particle and the according neutrino – and two quarks – an up-type and a down-type quark. It should be mentioned, that the SM as a gauge theory would be not renormalisible, if only leptons or only quarks would exsit as well as if the number of generation of both groups would differ. The exact number of generation is not predicted by the theory. Furthermore, there is no fundamental explanation why leptons and quarks are related in such a way as discribed above.

All twelve particles are summarised in Table 1.1. Additionally, anti-particles exist for each particle, which have the opposite charge.

	1.Generation	**2.Generation**	**3.Generation**	**Charge**
Quarks	**u**p (1.5-3 MeV)	**c**harm (1.1-1.4 GeV)	**t**op (174 GeV)	$+\frac{2}{3}$
	down (3-7 MeV)	**s**trange (70-120 MeV)	**b**ottom (4.1-4.8 GeV)	$-\frac{1}{3}$
Leptons	Electron (e) (511 keV)	Muon (μ) (106 MeV)	Tau (τ) (1.78 GeV)	-1
	e-Neutrino ν_e (<3 eV)	μ-Neutrino ν_μ (<0.19 MeV)	τ-Neutrino ν_τ (<18.2 MeV)	0

Table 1.1: *Particles of the Standard Model: leptons and quarks, anti-particles not included (numbers in parentheses are mass values [2]).*

The interaction between the fermions is mediated by the exchange of vector bosons. The photon (γ) is the particle connected with the electromagnetic force. The weak interaction is mediated by three particles: W^+, W^- and Z^0. The strong interaction acts only between quarks and is mediated by eight gluons (g). The leptons interact by via all three forces.

Table 1.2 gives an overview of all gauge bosons of the Standard Model. The graviton is added

Force	**Mediator(s)**	**Range**	**Mass**
strong	8 Gluons (g)	10^{-15} m	0
electromagnetic	Photon (γ)	∞	0
weak	$Z^0/W^{\pm}$	10^{-18} m	91,17 GeV / 80,22 GeV
Higgs field	Higgs (H^0)		> 114.4 GeV
gravitation	Graviton	∞	0

Table 1.2: *Particles of the Standard Model: force mediators. For completeness, the table includes the Graviton, which is not described in the Standard Model. The Higgs is the last particle predicted by the SM, which has not been discovered*

to the table for completeness, even though it is not described by the Standard Model.

All particles of the Standard Model, which have been discovered until now, are presented in Figure 1.1.

From the theoretical point of view, one additional particle is expected to be part of the SM. The principle of local gauge invariance requires the gauge bosons to be massless. But in contrast to the photon or the gluons, the mediators of the weak interaction ($W^{\pm}$ and Z^0) are massive.

In the SM, this *spontaneous electroweak symmetry breaking* is introduced by the *Higgs Mechanism* [4]. An additional term is added to the Lagrangian which describes the fusion of the electromagnetic and the weak interaction. This leads to a non zero vacuum expectation value. The additional free parameters are chosen in such a way, that a new particle is introduced: the Higgs Boson (H^0) which is massive and spinless. It couples to the bosons and the fermions according to their mass. The photon is still massless.

The Higgs particle is the only particle of the Standard model which has not been discovered yet, and its mass still remains a free parameter.

The experiments at the Large Electron Positron collider (LEP) at CERN made a direct search for the Higgs boson. From this search a lower limit for the mass can be set at 114.4 GeV (95% CL) [6]. In Figure 1.2, this excluded area is highlighted in yellow. Also indirect experimental bounds can be derived. This is done by a fit to the precision measurements of the electroweak observable, and masses of the $W^{\pm}$ and the top-quark. The fit favours a Higgs boson with a mass of 89^{+38}_{-28} GeV [5]. The $\Delta\chi^2$ of the fit including the theocratical uncertainties is depicted in Figure 1.2 as a blue band. From this band an upper limit for the Higgs mass of < 189 GeV(95% CL) can be derived.

If the Higgs Mechanism of the Standard Model is realised in nature, the Higgs will be discovered

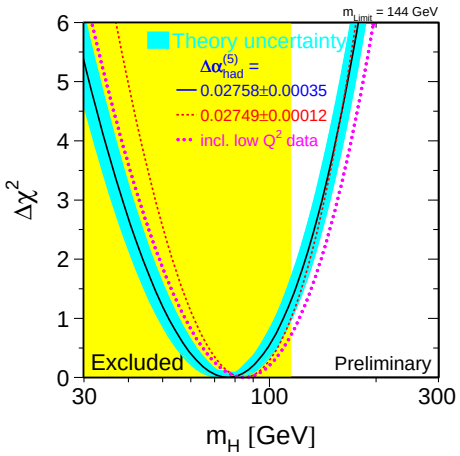

Figure 1.2: *Limits on the Higgs mass determined by a global SM fit. [5]*

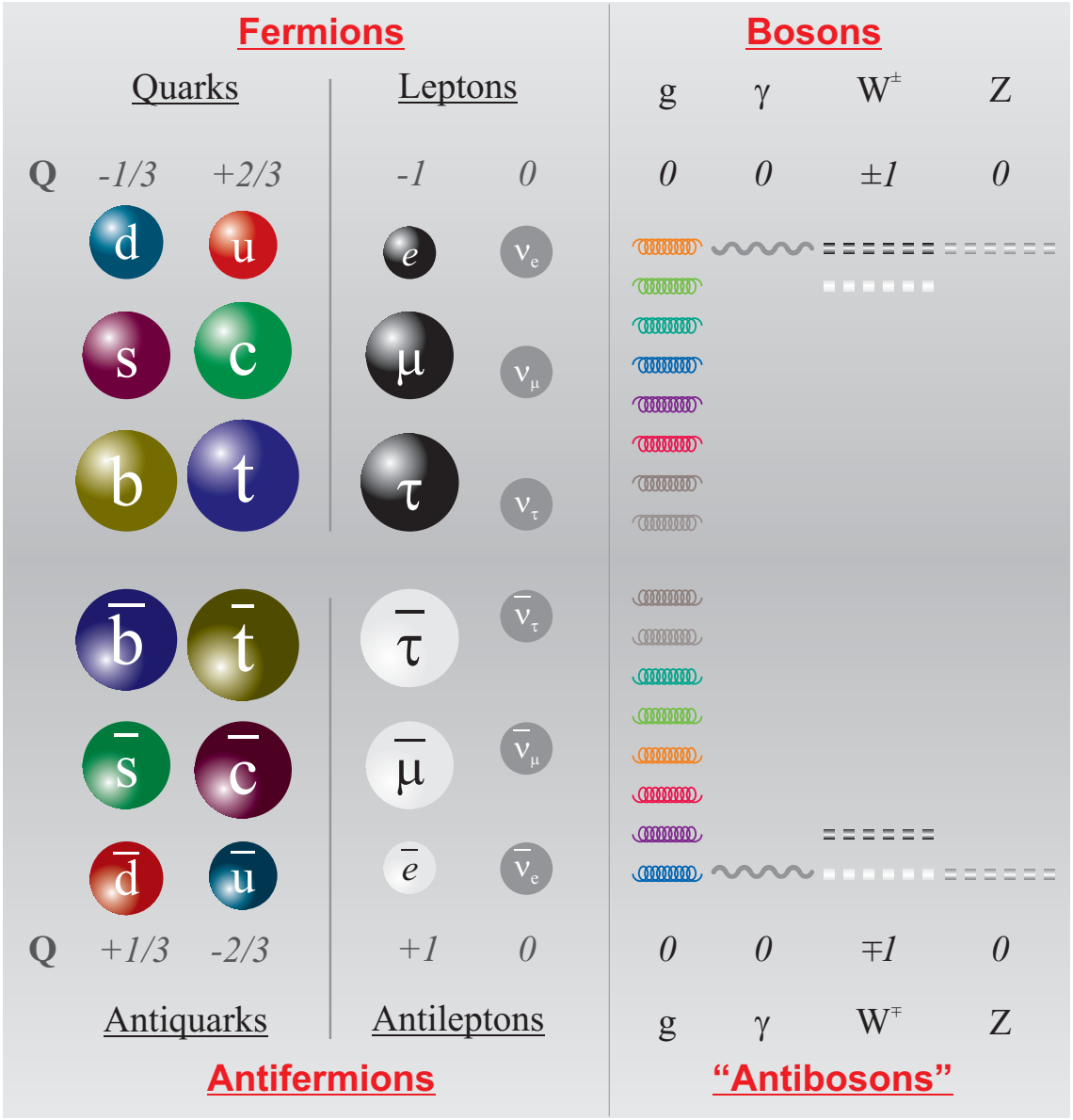

Figure 1.1: *The Standard Model of particle physics: [3].*

by the experiments at the Large Hadron Collider (LHC), which is scheduled to start at CERN late in 2008. A high precision measurement of the properties of the Higgs boson will be possible at the International Linear Collider (ILC), which is presented in Section 2.

1.2 Lepton Flavour

In all interactions, which have been observed, lepton number is conserved. This number is given by the number of leptons minus the number of antileptons participating in an interaction.

$$L = n_l - n_{\bar{l}} \tag{1.1}$$

Additionally, the lepton flavour[1] numbers are defined:

$$\begin{aligned} L_e &= n_e + n_{\nu_e} - n_{\bar{e}} - n_{\bar{\nu}_e} \\ L_\mu &= n_\mu + n_{\nu_\mu} - n_{\bar{\mu}} - n_{\bar{\nu}_\mu} \\ L_\tau &= n_\tau + n_{\nu_\tau} - n_{\bar{\tau}} - n_{\bar{\nu}_\tau} \end{aligned} \tag{1.2}$$

In contrast to the quark sector, where the weak interaction changes the quark type also over generation borders, the lepton flavour numbers are assumed to be individually conserved in the SM. Although this is not based on an underlying gauge symmetry.

Lepton Flavour Violation via Neutrino Oscillation

In the Standard Model the neutrinos are assumed to be massless. This is needed to conserve the lepton flavour. Since 1998, there is a strong evidence for oscillation in the neutrino sector [7]. The upper bounds for the neutrino masses (see Table 1.1) lead to only small effects in the decay of charged leptons or neutral current deep inelastic scattering (NC DIS see Section 12.1). The lepton flavour violation (LFV) due to the neutrino mixing is consistent with the experimental upper bounds and can be integrated in the Standard Model by a non-unity matrix V_{NMS}[2]. Therefore, a direct observation of LFV would be a clear evidence for new physics beyond SM.

1.3 Limitations and Extentions of the SM

Even though the Standard Model describes the observations of particle physics very well, it has its limitations. The limits of the Standard Model and possible solution are presented in this section.

The Hierarchy Problem Such example of the limitations is the *Hierarchy Problem*: The interaction with the Higgs field gives the particles of the Standard Model their mass. The mass is proportional to their coupling strength to the Higgs. The self-coupling of the Higgs boson results in the mass of the Higgs. The scalar Higgs field contains divergent one loop corrections which are depicted in Figure 1.3. These corrections can be as large as the largest mass scale in the theory. This can lead to an enormous Higgs mass, if a cut-off scale in the range of the Planck scale is implied. However, as mentioned before, the electroweak precision measurements suggest a light Higgs mass.

[1] also: lepton family

[2] named after M. **N**akagawa, Z. **M**aki and S. **S**akata [8]

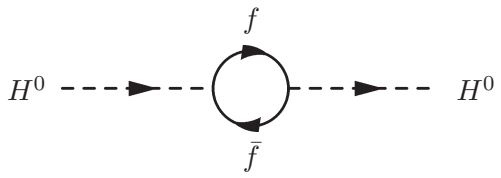

Figure 1.3: *Feynman diagram for the divergent one-loop correction to the Higgs field. After renormalisation, the Higgs boson mass m_{H^0} depends quadratically on a cut-off scale Λ. The largest contribution comes from top-quark loops.*

Dark Matter Also other measurements raise questions which can not be answered by the SM. New results from astrophysical analysis prove, that only 5% of the matter in the universe consists of particles described by the SM. The remaining 95% consists of dark matter and dark energy. As the name implies, this new kind of matter is not visible. Therefore a candidate for dark matter must be neutral. Its cross section with the visible matter, which is described by the SM, is very small. The SM neutrinos can not be considered as candidates, because their masses are to small.

Extentions of the Standard Model

The given examples of the limitations of the Standard Model shows, that new fundamental theories are needed. They must extend the SM in such a way that they still fit the experimental results. A set of new measurements are needed to distinguish between several theories. The experiments at the ILC will contribute to these measurements (see Section 2).

One preferred candidate for such an extention of the Standard Model is the theory of *Supersymmetry* (SUSY). It introduces for each fermion a new boson and vice versa. These new particles can solve the hierarchy problem. They lead to new terms in the loop-corrections, which cancel out the divergent parts. Naturally, one would expect the same mass for the supersymmetric partners as for the SM particles. But this is in contradiction with observation. Therefore, a breaking mechanism of SUSY must lead to different masses. It should be added, that all supersymmetric models predict at least one light Higgs with a mass below 200 GeV. Further, many new particles with masses up to 1 TeV are introduced. These particles would be observable at the ILC.

There are other candidates for a theory beyond the SM:

- Pati-Salam's $SU(4)_C$ model [9], where the lepton number is treated as a fourth colour;
- a grand unified theory (GUT) [10], where the SM gauge group is embedded in a larger symmetry group.
- Technicolour [11], solving the hierarchy problem by introducing new electroweak doublets and singlets (technifermions) as multiplets of a non-abelian gauge interaction (technicolour)

As mentioned above, it is still an open question why the same number of lepton and quark generations exist. All these models introduce a new relation between the lepton and the quark sector. This will be discussed in more detail in the second part of this thesis, especially in Section 12.3.

1.4 Scope of This Thesis

Part I

One of the next projects proposed in high energy physics is the International Linear Collider (ILC). This e^+e^- accelerator with a centre-of-mass energy up to 500 GeV will provide an unique environment to discover and measure new particles with a very high precision. It is possible to increase the energy to 1 TeV, if other measurements imply this. If no new particles will be observed, measurement of SM parameters with an unrivalled precision, may give hints for extentions beyond the SM.

These precision measurements of SM process or of new physics phenomena put many requirements on the detector, such as momentum and energy resolution as well as tracking efficiency, etc. Several Detector-Concepts at the ILC have been proposed. Some of them suggest to use a Time Projection Chamber (TPC) the main tracker. A new amplification device based on Micro Pattern Gas Detectors (MPGD) will be used.

Part II

As mentioned above, many theories which extend the SM, introduce a new particle that mediates between the lepton and the quark sector. The Buchmüller-Rückl-Wyler model (BRW) [12] describes new particles called *Leptoquarks*. Additionally, it can be introduced, that these particles mediate lepton flavour violation.

As the only electron-proton collider in the world, the HERA collider at DESY provided a unique environment to study the relation between leptons and quarks. The data of the H1 experiment have been searched for lepton flavour violating leptoquarks.

Part I

Resolution Studies for a GEM based TPC at the ILC

Chapter 2

The International Linear Collider

As one of the next projects in high energy physics, it is planned to build a linear collider. One of the proposals is the *International Linear Collider* (ILC). It would provide a tunable centre of mass energy between 200 GeV and 500 GeV. The particles would be accelerated in two 11 km long linacs, which are shown in Figure 2.1. They would use superconducting cavities which provide a field above 31.5 MV/m. It is planned to polarise the beams up to 80% (50%) for electrons (positrons). The positrons would be produced by an undulator based source. Besides this positron source and the main accelerator, Figure 2.1 shows two damping rings. In these rings the electrons and positrons are stored and pre-accelerated before they are further accelerated in the linear accelerator. During this process the particles lose some of their energy via synchrotron radiation. This 'cools down' the particles, which reduces their emmitance. This procedure is needed to reach the design luminosity of $2 \times 10^{34}\,\mathrm{cm^{-1}s^{-1}}$. The two beams would collide under a crossing angle of 14 mrad. The total length of the accelerator including the beam delivery system is 31 km. If the physics results of the Large Hadron Collider (LHC) implies that is will be necessary, the centre of mass energy of the ILC can be upgraded up to 1 TeV by adding 11 km to the linacs on each side.

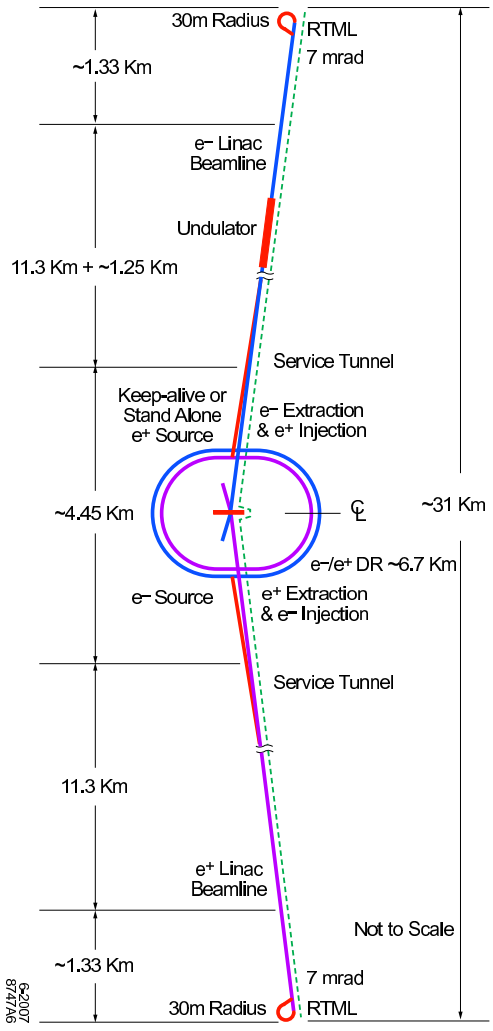

Figure 2.1: *Sketch of the ILC [13]*

2.1 Physics Motivation

As mentioned in the previous chapter, the Standard Model of particle physics is not yet completed. In addition, many theories are proposed,

which extend the SM. Some of them are mentioned in Section 1.3.

If the Higgs Mechanism is realised in nature, the corresponding particle(s) will be discovered at LHC. This includes the cases, where the Higgs is a particle described by a theory beyond the Standard Model. Complementary to the results of the LHC, the ILC will provide an environment for a very precise measurement of the spin and the parity of the Higgs. Also, the determination of the branching ratio can be improved by the ILC in comparison with these measured at the LHC. Further, many of the particles which are predicted by supersymmetric models are in the energy range of the ILC.

There are many good examples for the complementarity of the measurements at the ILC and the LHC: if SUSY is realised, the LHC will provide a precise measurement of squarks, while at the ILC the sleptons can be measured very accurate. If the results of both accelerators are combined, the determination of many SUSY parameters will be more precise than it would be the case of one machine alone.

Even if no new particles will be found, the very precise measurement of SM parameters such as top-mass and the properties of Z and $W^{\pm}$ at the ILC may give hints for alternative theory.

2.2 A Detector for the ILC

Many of the interesting physical processes have topologies which are challenging for the detector. To distinguish between the particles $W^{\pm}$, Z^0, the Higgs H^0 and the top quark, a good reconstruction of invariant masses of the jets is required. To reach these requirements an jet energy resolution of $\sigma_E/E < 3-4\%$ (a jet resolution of $30\%/\sqrt{E}$ for jet energies below 100 GeV) is needed. This is two times better than the resolution achieved using the detectors at LEP. Ongoing studies show that this can be reached, if the *particle flow* concept is used: The energy of the charged particles is measured in the tracker. The corresponding track is matched with the energy cluster in the calorimeter. The amount of energy which is isolated by this procedure is subtracted from the total energy measured by the calorimeter. The remaining energy is therefore from neutral hadrons and photons. The particle flow concept requires a highly efficient and hermetic tracking system. The calorimeter must provide a very fine transverse and longitudinal segmentation, to allow reconstruction of individual showers.

Some decays of SUSY particles are only detectable by the energy taken by these particles which is then missing in the reconstructed event. To ensure a reliable measurement of the total energy of the physical process, a hermetic detector down to low angles (θ) is needed.

The possibility of identifying the type of the particle (ID) leads to an improvement of the flavour tagging and the reconstruction of charm-particles and Bs.

2.2.1 A Time Projection Chamber at the ILC

The above mentioned reconstruction techniques put high requirements on the tracking in respect to hermeticity, efficiency and accuracy. To reach these aims a Time Projection Chamber (TPC) is a good choice. It provides conditions for very good pattern recognition and the possibility for particle identification by the measurement of the specific energy loss dE/dx. Details are explained in the next chapter. Additionally, the low material budget of a TPC, which is concentrated at the walls of the detector component, enables a very good energy resolution in calorimeter.

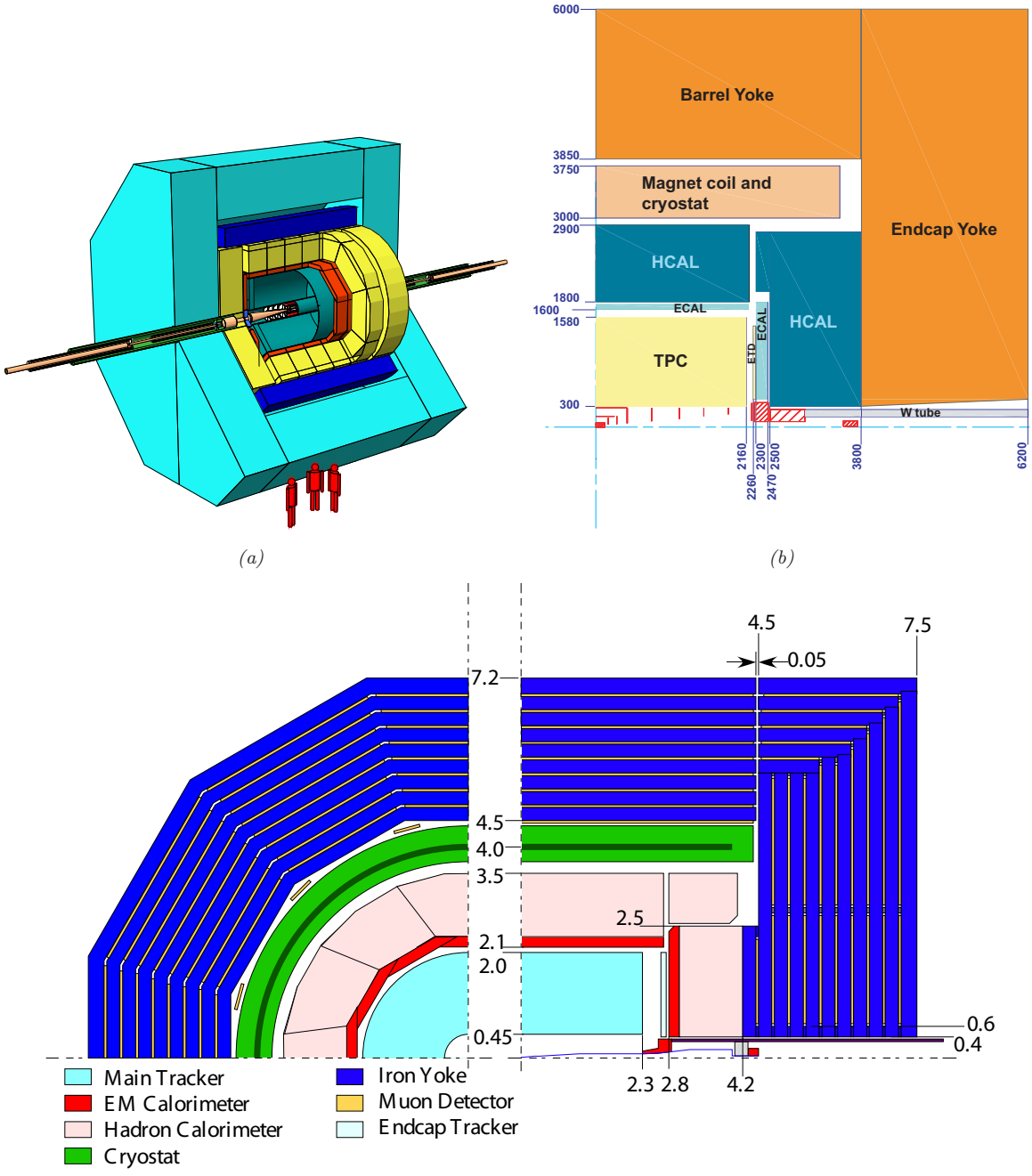

(a) *(b)* *(c)*

Figure 2.2: *Detector concepts at the ILC: The detector proposals of the LDC (Figure (a) and (b)) and the GLD (Figure (c)) use a TPC as the main tracking device [14].*

Two of the proposals for a detector at the ILC plan to use a TPC as the main tracking device. The main structure of these two concepts is similar, as is depicted in Figure 2.2. Therefore, the groups working on the LDC and GLD concepts, joined their efforts in a new detector proposal: the ILD.

2.2.2 Requirements

To identify a charged particle, its momentum is needed. This information can be reconstructed from the curvature C of the projection of the trajectory of the particle perpendicular to the magnetic field B and the inclination angle (θ) in the rz-plane:

$$p = p_T \cdot \sin\theta \tag{2.1a}$$

$$\frac{p_T}{\mathrm{GeV}} \approx 0.3 \cdot \frac{\rho}{\mathrm{m}} \cdot \frac{B}{\mathrm{T}} \qquad \text{with} \qquad \rho = \kappa^{-1}\,, \tag{2.1b}$$

where ρ denotes the radius of the circle, which describes the projection. Further details about track parameters can be found in [15].

One of the interesting measurements at ILC is the precise determination of the properties of the Higgs. To measure the mass, the Higgs-strahlung process can be used, which is depicted in Figure 2.3. The mass of the Higgs boson is determined by subtracting the reconstructed

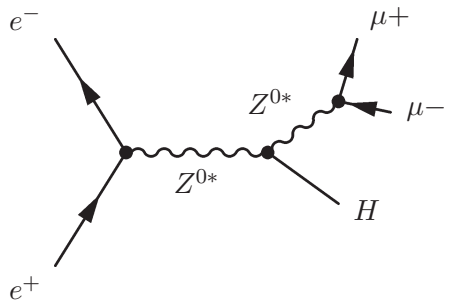

Figure 2.3: *Feynman graph of the Higgs-strahlungs process: One of the possible decay modes of the Z^0 is depicted. The process can be identified without an exact knowledge of the decay mode of the Higgs. Therefore, it is model independent.*

mass of the Z^{0*} from the known centre of mass energy known as the recoil mass method. The direct reconstruction of the mass of the Higgs, using the particles in which the Higgs decays, is not needed. This makes this method independent of the underlying theory, which describes the Higgs: e. g. SM or SUSY. Figure 2.3 depicts the case, where the Z^{0*} boson decays into a muon anti-muon pair. This decay mode provides the best detectable topology of the Higgs-strahlung process, because the identification of the muons and the precise measurements of their properties is quite simple.

Nevertheless, the precision of the measurements of the Higgs mass is closely related to the momentum resolution of the tracking device. Figure 2.4 shows the spectra of the Higgs recoil mass for different momentum resolutions. It is assumed, that the Higgs mass is 120 GeV and the centre of mass energy is $\sqrt{s} = 350\,\mathrm{GeV}$. The number of events which are taken into account comply with an integrated luminosity of $500\,\mathrm{fb}^{-1}$. The tracker momentum resolution is parametrised by ${}^{\delta p_T}/_{p_T^2} = a \oplus b(p_T \sin\theta)^{-1}$. To ensure a precision of 150 MeV, the parameters must be at less than: $a = 4 \times 10^{-5}$ and $b = 1 \times 10^{-3}$: Significantly better precision can be reached, if the tracker resolution is improved further.

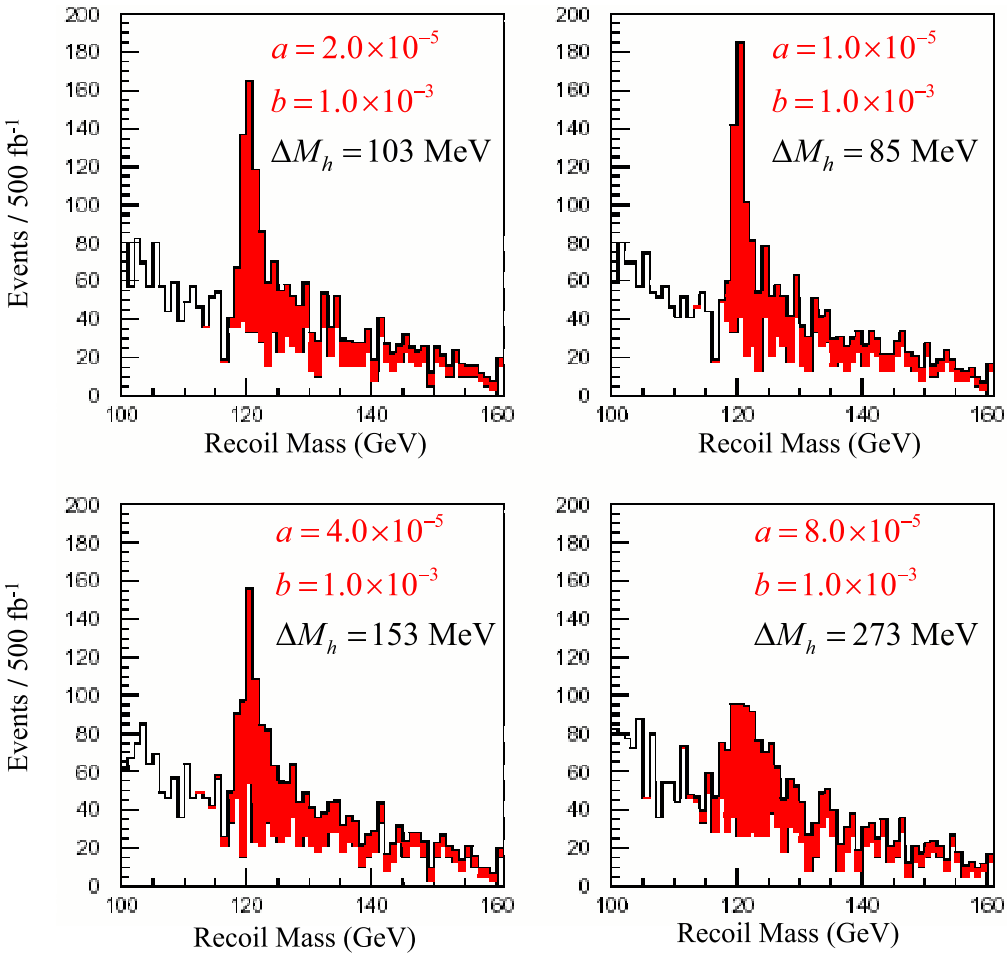

Figure 2.4: *The Higgs recoil mass spectra for several momentum resolutions of the tracking system, which is parametrised as* $\delta p_T/p_T^2 = a \oplus b(p_T \sin\theta)^{-1}$. *[14]*

A close relation between the momentum resolution of the detectors $\delta(1/p_T)$ and the spatial resolution $\sigma_{r\phi}$ of the tracking part in the $r\phi$-plane is given by the Glückstern equation [16]. If a number of measured space points (N) are used to determine the particle trajectory of length L (given by the radius of the tracker):

$$\delta\left(\frac{1}{p_T}\right) = \frac{\delta p_T}{p_T^2} = \frac{\sigma r\phi}{0.3L^3B}\sqrt{\frac{720}{N+4}} \cdot \left(\frac{\mathrm{T\,m}}{\frac{\mathrm{GeV}}{c}}\right), \tag{2.2}$$

where B denotes the magnetic field.

For a detector at the ILC with a TPC as the main tracking device, it is proposed to divide the readout into 200 pad rows. This will provide a highly efficient and robust pattern recognition hence at least 150 space point will be reconstructed with a sufficient quality. Assuming a magnetic field B of 4 T, a spatial resolution of the order of 100 µm is needed to reach the requirements. Motivated by the outcome of this and other studies, the pad width was reduced to 1 mm. Before, a pad width of 2 mm was proposed in [17]. Therefore, this is the value used for the pad design of the prototype used in this study (Section 4.1.4). All important design parameters for a TPC at the ILC are summarised in Table 2.1 [18]. The table shows that the momentum resolution improves if the space points provided by the vertex

Parameter	**Requirement**
Size (LDC-GLD average)	$\phi = 3.6\,\mathrm{m}, L = 4.3\,\mathrm{m}$ outside dimensions
Momentum resolution ($B = 4\,\mathrm{T}$)	$\delta(1/p_T) \sim 10 \times 10^5$ c/GeV TPC only; $\times 0.4$ incl. IP $\delta(1/p_T) \sim 3 \times 10^5$ c/GeV (TPC+IT+VTX+IP)
Solid angle coverage	Up to at least $\cos\theta \sim 0.98$
TPC material budget	$< 0.03\,X_0$ to outer field cage in r $< 0.30\,X_0$ for read out end cap in z
Number of pads	1×10^6 per end cap
Pad size / number of pad rows	$1\,\mathrm{mm} \times 4 - 6\,\mathrm{mm}$ / ~ 200 (standard read out)
$\sigma_{\mathrm{singlepoint}}$ in $r\phi$	100 µm (for radial tracks, average over drift length)
$\sigma_{\mathrm{singlepoint}}$ in rz	0.5 mm
2-hit resolution in $r\phi$	$< 2\,\mathrm{mm}$
2-hit resolution in rz	$< 5\,\mathrm{mm}$
dE/dx resolution	$< 5\%$
Performance robustness (for comparison)	$> 95\%$ tracking efficiency for all tracks – TPC only ($> 95\%$ tracking efficiency for all tracks – VTX only) $> 99\%$ all tracking
Background robustness	Full precision efficiency in background of 1% occupancy (simulation estimate $< 0.5\%$ for nominal background
Background safety factor	Chamber will be prepared for $10\times$ worse background at the ILC start up

Table 2.1: *Performance goals and design parameters for a TPC with standard electronics at the ILC detector [18].*

detector (small number of space points with a significantly better resolution) are taken into account.

Chapter 3

Time Projection Chamber

In the following section, the basic principles of gaseous detectors are presented. Afterwards, the working principles and the main components of a Time Projection Chamber (TPC) such as the field cage and the amplification region are described. Gas Electron Multipliers as an alternative amplification device are introduced. A short discussion of the advantages and disadvantages of a TPC as the main tracker of a detector at the ILC follows.

3.1 Gaseous Detectors

The basic detection principle of all gaseous detectors is that charged particles with sufficient energy or high energy photons ionise the gas while traversing the detector. The electrons produced are called *primary electrons*. They drift to an anode, due to the presence of an electric field and are detected there. Because in general the number of primary electrons is low, an amplification stage is needed to multiply them before being read out. In most types of gaseous detectors this is done using an avalanche process which takes place in high electric fields.

For many applications, it is necessary to preserve the information of the number of primary electrons. This allows for the measurement of the energy loss of the traversing particle, which than can be used to identify the type of particles (see Section 3.1.2). In this case, the amplification device must operate in the proportional mode.

The Time Projection Chamber (TPC), which is studied in this thesis, was introduced by David R. Nygren in 1975 for a high energy experiment at the PEP facility at SLAC [19]. Its structure and working principle will be explained in Section 3.2. First, more general aspects of gaseous detectors are presented.

3.1.1 Detector Gas

In principle all gases are usable which possess a low attachment coefficient for electrons. The choice of the gas mixture is mainly influenced by the technical requirements, e. g. amplification, drift velocity and diffusion. Nobel gases are often used, as they are chemically inert and have a low ionising potential. In the amplification process photons with an energy above the ionising potential of the gas molecules can be produced. To catch these photons, which would produce primary electrons themselves, a so called quencher gas is added. These gas components have a

high cross section for the photons in the appropriate energy range. The energy of the photons is transfered into rotation and oscillation states of the gas molecules.

One must be aware of gas impurities such as water or oxygen. Even a small amount of the order of 100 ppm can change the gas properties dramatically, such as the drift velocity in the case of water. Only a few 10 ppm oxygen in the gas can lead to the loss of the signal due to attachment of the electrons. The source of impurities may be due to out-gassing materials, imperfect tightness of the gas system or the manufacturing process of the gas mixture. The gas properties can by calculated using Monte Carlo simulations such as MAGBOLTZ , GARFIELD and HEED [20–22]. Here, gas impurities can be taken into account.

3.1.2 Energy Loss and Particle Identification

The mean energy loss of a particle traversing material can be calculated using the Bethe Bloch equation [23]. It is deduced using the following assumptions:

- The transfer of energy and momentum does not change the direction of the ionising particle.
- The impacted shell electron is free and at rest.
- the mass of the ionising particle is much larger than the mass of the electron ($m \gg m_e$).

For highly relativistic particles ($v \approx c \Leftrightarrow \gamma \gg 1$) the Fermi Density Correction must be taken into account. It describes the weakening of the electric field due to polarisation caused by relativistic effects.

The following equation gives the mean energy loss of a traversing particle per distance x:

$$-\frac{dE}{dx} = \frac{e^2 N_A z^2}{\epsilon_0^2 \beta^2}\frac{Z}{A}\left[\ln\left(\frac{2m_e c^2\gamma^2\beta^2}{I}\right) - \beta^2 - \frac{\delta}{2} - \frac{C}{Z}\right] \text{ with} \tag{3.1}$$

dE/dx : energy loss per distance x

e : electron charge $= (1.602189 \pm 5) \cdot 10^{-19}\,\mathrm{C}$

N_A : Avogadro's Number $= (6.02205 \pm 3) \cdot 10^{23}\,\mathrm{mol}^{-1}$

z : charge of the traversing particle in units of e

Z, A : atomic and mass number of the absorber

m_e : electron mass $= (9.10953 \pm 5) \cdot 10^{-31}\,\mathrm{kg}$

ϵ_0 : dielectrical constant of vacuum $= 8.8542 \cdot 10^{-12}\,\mathrm{As/Vm}$

c : speed of light $= 299792458\,\mathrm{m/s}$

$\beta = v/c = p/(mc)$

v : velocity, p : momentum and m : mass of the particle

$\gamma = (1-\beta^2)^{-1/2}$

I : average ionization energy of the absorber

δ, C : parameters of the Fermi Density and Shell Correction

Figure 3.1 displays the measurements taken with the ALEPH TPC. The energy loss is shown versus the momentum of the particle. The solid lines mark the prediction for different types of particles. The measurements, which are shown as dots, follow these lines. At low momentum (p) the data for different types of particles are well separated. This provides the possibility to identify the type of particle using the measurement of the energy loss.

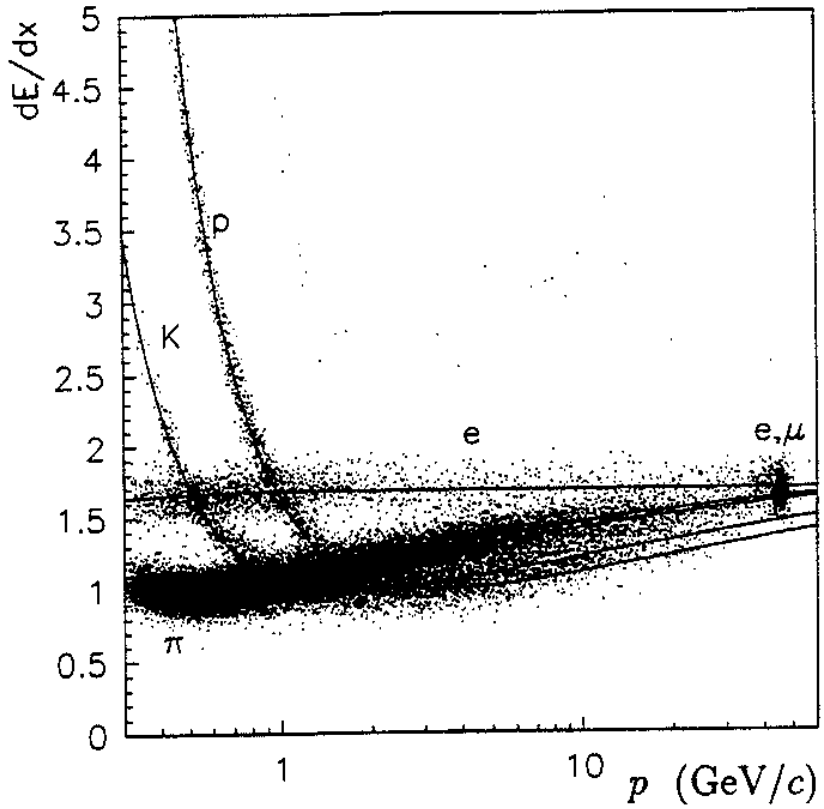

Figure 3.1: *Energy loss of pions, kaons, protons and electrons measured by the* ALEPH TPC *[24]. Solid lines: mean energy loss (Bethe-Bloch); dots: measured energy losses*

.

Energy Straggling The Bethe Block equation predicts only the mean value of $^{dE}/_{dx}$. The loss of energy while traversing the medium is a statistical process. The shape of the distribution depends on the thickness of the absorber. For thick absorbers the distribution can be described by a Gaussian distribution. Gases can normally be treated as a thin absorber. Here the energy loss is described by a Landau distribution [25]. It shows a long tail to higher energy transfers, which are caused by so called delta electrons (see Figure 3.2). These electrons receive a high momentum during the ionising process and can travel several millimetres. They are able to ionise the gas themselves and produce further primary electrons, which are not located on the particle trajectory. In between these two cases of thin and thick absorbers, the Vavilov model is valid [26, 27]. The Vavilov distribution for various model parameter κ, which is related to the thickness of the absorber, are shown in Figure 3.2.

Number of Primary Electrons Since the deposited energy cannot be measured directly, the relation between the energy stored in the gas and the number of produced primary electrons n_e is important:

$$n_e = \frac{dE}{dx} \cdot W^{-1} \tag{3.2}$$

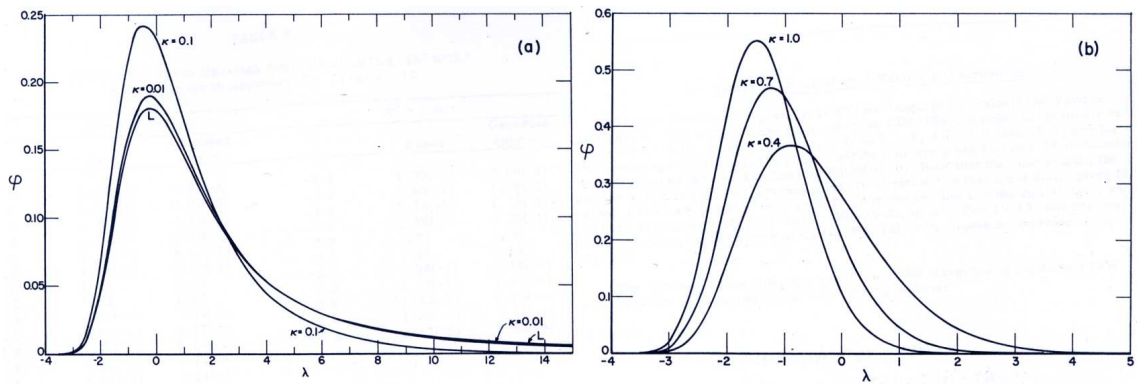

Figure 3.2: *Vavilow energy straggling distribution for various distinguishing parameters $\kappa = {}^{\Delta(\bar{x}')}/_{W_{\max}}$, where $\Delta(\bar{x}')$ denotes the mean energy loss in the hole absorber thickness x' and $W_{\max}$ the maximum energy transfer in one collition. The specific energy loss is espressed in the paramter $\lambda \sim \Delta - \Delta_0$, where Δ_0 denotes the mean enegry loss. On the left side (a) the case of a thin absorber is depicted. For small values of κ,the distribution equalizes to a Landau distribution,which is denoted with L. The right figure (b) shows the cases of thick absorber. The distribution adapts to a Gaussian function ($\kappa \geq 1$). [27]*

As before, ${}^{dE}/_{dx}$ denotes the energy loss on the path dx of the traversing particle (see Equation (3.1)). The average energy needed to produce an electron is given by W. It is larger than the ionising potential of the gas, because a part of the energy is also transformed into excitation energy (X) and kinetic energy of the primary electron and the remaining ion.

Gas	$\boldsymbol{W}$ **(eV)**	$\boldsymbol{I}$ **(eV)**	$\boldsymbol{X}$ **(eV)**
Ar	26.3	15.8	11.6
Ne	36.4	21.6	16.6
He	42.3	24.6	19.8
Xe	21.9	12.1	8.4
CO_2	32.8	13.7	10.0
CH_4	27.1	13.1	–

Table 3.1: *Average energy (W) for electron-ion pair production and mean excitation (X) and ionisation potentials (I) for different gases (values from [23, 28]).*

Some values for W, the mean ionising potential (I) and the mean excitation potential (X) are summarised in Table 3.1. For the error on the number of electrons, one has to take energy conservation into account. Therefore the error is given by

$$\sigma_{n_e} = \sqrt{n_e \cdot F}\,, \tag{3.3}$$

where F denotes the Fano factor [29].

3.1.3 Gas Amplification

In the presence of a high electric field electrons are accelerated. If the field is above $10\,^{\mathrm{kV}}/_{\mathrm{cm}}$, they can gain enough energy between two collisions with gas molecules to ionise the gas. The produced electrons are called *secondary electrons*. They are accelerated and can produce new electrons, too. This cascading process builds up an avalanche of electron ion pairs. It will continue while the conditions comply.

The Townsend coefficient α is used to quantify the avalanche. It denotes the probability for one ionisation per unit length and depends on the gas mixture. If the amplification is operated in the proportional mode, which is set by the strength of the electric field, the gain is given by:

$$G = \frac{N(x_f)}{N(x_0)} = \exp\left(\int_{x_0}^{x_f} \alpha(x)dx\right) , \tag{3.4}$$

where x_0 denotes the starting point of avalanche and x_f the end point. The gain is the quotient of the number of primary electrons before the avalanche process $N(x_0)$ and the electrons after amplification $N(x_f)$.

3.1.4 Drift Velocity

For the reconstruction of the particle trajectory in a TPC, the drift velocity v_D is essential. In the presence of an electric field $\vec{E}$ and a magnetic field $\vec{B}$, it can be deduced from the *Langevin equation* [30]:

$$m\frac{dv}{dt} = e\vec{E} + e\vec{v} \times \vec{B} - K\vec{v}\,, \tag{3.5}$$

where e is the charge of an electron. Furthermore, a noise term $\vec{Q}(t) = -K\vec{v}$ is assumed, where K denotes the viscosity.

The time between two collisions can be expressed by $\tau = {}^{m}/_{K}$. Averaged over a time $t \gg \tau$ Equation (3.5) has a steady solution ${}^{dv}/_{dt} = 0$:

$$\vec{v}_D = \langle v \rangle = \frac{\mu E}{1+\omega^2\tau^2} \cdot \left[\hat{E} + \omega\tau\hat{E} \times \hat{B} + \omega^2\tau^2\left(\hat{E}\cdot\hat{B}\right)\hat{B}\right] , \tag{3.6}$$

with the following definitions: $E = |\vec{E}|$, $B = |\vec{B}|$, $\hat{E} = {}^{\vec{E}}/_{E}$ and $\hat{B} = {}^{\vec{B}}/_{B}$. The mobility of the electron is given by $\mu = \tau \cdot {}^{e}/_{m}$ and $\omega = B \cdot {}^{e}/_{m}$ denotes the cyclotron frequency. The parameters μ and τ depend on the properties of the gas.

Inside the drift region of the TPC the electric and the magnetic field are parallel. In this case, the second term in Equation (3.6) vanishes:

$$\omega\tau \cdot \hat{E} \times \hat{B} = 0$$

and the last term can be written as

$$\underbrace{\left(\hat{E}\cdot\hat{B}\right)}_{=1}\hat{B} = \hat{B} = \hat{E}\,.$$

This leads to the follow equation, which equals the case without a magnetic field:

$$\begin{aligned} \vec{v}_D &= \frac{\mu E}{1+\omega^2\tau^2} \cdot \hat{E}\left(1+\omega^2\tau^2\right) \\ &= \mu\vec{E} = \vec{v_D}(\vec{B}=0)\,. \end{aligned} \tag{3.7}$$

3.1.5 Diffusion

A cloud of charged particles diffuses from their place of production. This has an major impact on spatial resolution, because it smears the position of the ionising process on the trajectory of the traversing particle.

In the field free case, the diffusion is isotopical and caused by the thermic energy. The velocity v of the electrons in any direction is given by

$$v = \sqrt{\frac{8kT}{\pi m_e}}, \text{ with} \tag{3.8}$$

$$k : \text{Boltzmann constant} \tag{3.9}$$

$$T : \text{gas temperature}$$

$$M_e : \text{electron mass}.$$

Influence of the Electric Field As mentioned, τ denotes the mean time between two collisions. Therefore, the probability that an electron did not undergo an interaction with a gas molecule is $\frac{1}{\tau}\exp(-\frac{-t}{\tau})$. The distance that the electron can fly between collisions is given by the fraction $\frac{t}{\tau}\lambda$, where λ is the free path length. For the electron, the deviation from its expected position is

$$\delta_0^2 = \frac{1}{3}\int_0^\infty \frac{dt}{\tau}\exp\left(-\frac{t}{\tau}\right)\cdot\left(\lambda\frac{t}{\tau}\right)^2 = \frac{2}{3}\lambda^2\,. \tag{3.10}$$

Assuming that all electrons have the same drift velocity, the spread of the charge cloud after a large number of collisions ($t \gg \tau$) is given by

$$\sigma_0^2(t) = \frac{2}{3}\lambda^2\frac{t}{\tau}\,.$$

from this equation, a diffusion coefficient can be defined as

$$\tilde{D}_0 = \frac{\sigma_0^2(t)}{2t} = \frac{1}{3}\frac{\lambda^2}{\tau} = \frac{1}{3}v\lambda\,, \tag{3.11}$$

where the subscript '0' denotes the case without a magnetic field. In this thesis a different definition is used, which is more common:

$$D_0 = \sqrt{\frac{2\tilde{D}_0}{v_D}} \tag{3.12}$$

Figure 3.4 shows the dependency of D_0 on the electric field for two gas mixtures.

Influence of the Magnetic Field While the longitudinal diffusion is not affected by the presence of a magnetic field, the transverse diffusion is reduced by the magnetic force. This force acts perpendicular to the motion of the particle and the magnetic field. Hence, it bends the path of the particle transversally to the field. As shown in Figure 3.3, the particle travels on a circle with a radius of $\rho = v_T/\omega$, where $v_T = \frac{2}{3}\frac{\lambda^2}{\tau^2}$ denotes the mean transverse velocity.

Analogous to the field-free case in Equation (3.10), it is valid:

$$\begin{aligned}\delta^2(B) &= \frac{1}{2}\int_0^\infty \frac{dt}{\tau}\exp\left(-\frac{t}{\tau}\right)\cdot\left[2\rho\sin\frac{tv_T}{2\rho}\right]^2 \\ &= \frac{1}{2}\frac{\tau^2 v_T^2}{1+\omega^2\tau^2}\,. \end{aligned} \tag{3.13}$$

Calculating the spread after a time $t \gg \tau$ leads to:

$$\sigma^2(B,t) = \frac{t}{2}\frac{\tau v_T^2}{1+\omega^2\tau^2} = t\frac{\tilde{D}_0}{1+\omega^2\tau^2} \tag{3.14}$$

Hence, the transverse diffusion coefficient D_T for the presence of a magnetic field B can be defined:

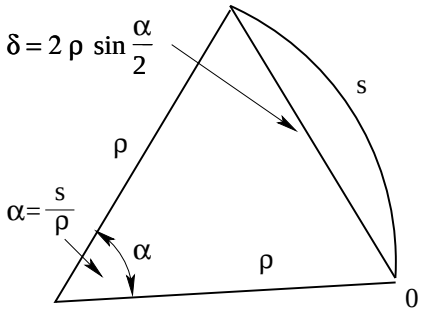

Figure 3.3: *Sketch of the transverse distance of electrons in presents of a magnetic field*

$$\tilde{D}_T(B) = \frac{\tilde{D}(0)}{1+\omega^2\tau^2} \longleftrightarrow D_T(B) = \frac{D(0)}{\sqrt{1+\omega^2\tau^2}} \tag{3.15}$$

Table 3.2 on page 26 summarises some values for the diffusion coefficient D_T for different magnetic fields and gas mixtures.

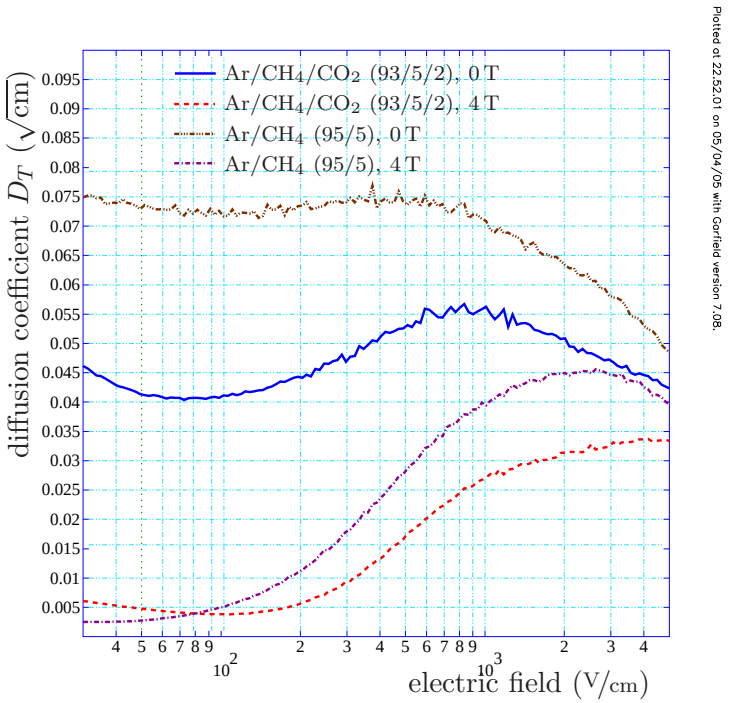

Figure 3.4: *Dependence of the transverse diffusion coefficient D_T in dependence on the electric field for a magnetic field of 4 T and no magnetic field. The values are simulated with GARFIELD (version 7) for the gas mixtures $Ar/CH_4/CO_2$ (93/5/2) and Ar/CH_4 (95/5). [31]*

In addition to the case with no magnetic field, the dependence of the diffusion coefficient on the electric field is shown in Figure 3.4 for a magnetic field of 4 T. It is clearly visible, that for both gas mixtures and all electric fields the values for a magnetic field of 4 T are lower than for the field free case. The difference decreases with the increase of the electric field.

3.2 Working Principle of a Time Projection Chamber

The main component of a Time Projection Chamber is the sensitive volume filled with gas. The cathode provides a negative potential of several 10 kV resulting in field of the order of 100 V/cm in the sensitive area. The electrons produced are read out on the side of the anode which is at ground potential. Figure 3.5 shows a sketch of a TPC.

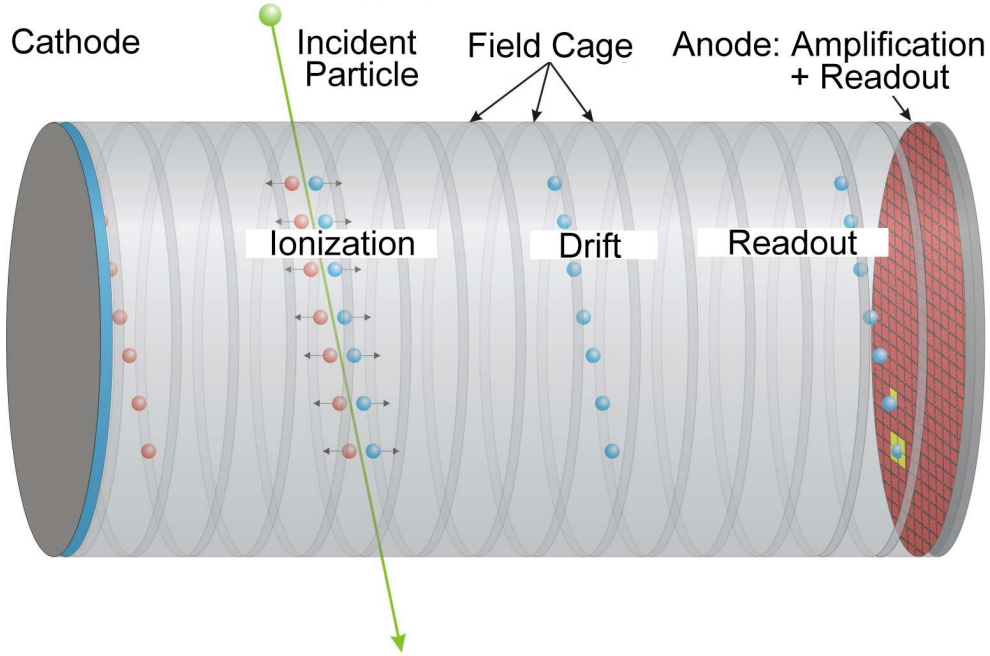

Figure 3.5: *Sketch of a Time Projection Chamber and its working principle. [3]*

If used as a 4π-detector in high energy physics, the sensitive volume is usually cylindrical. The rotation axis is the beam pipe. The cathode is located at the interaction point of the initial particles and splits the detector in two separate TPCs which are readout at both ends.

Figure 3.5 demonstrates also the detection mechanism for charged particles. The particles ionise the gas molecules in the sensitive volume along their trajectory. Due to the electric field, the primary electrons and the ions are separated and drift to the opposite ends. The electron signal is read out at the anode which is segmented to provide a spatial information. The ions are not used in the detection. The traversing particle effectively produces $\mathcal{O}(100)$ electron ion pairs per centimetre. Therefore an amplification is needed to create a measurable signal. The amplification device must operate in the proportional mode, which allows for an identification of the particle using the $^{dE}/_{dx}$ information (see Section 3.1.2). Here, more than one technique is possible, as presented in Section 3.2.2.

In a TPC used as a central tracking device in high energy physics, typically the following coordinate system is used: The z-axis is defined along the rotation axis (beam pipe) of the TPC. The xy-plane is perpendicular to z-axis. Because of the radial symmetry, normally $r\phi$-coordinates are used.

The r- and the ϕ- or the x- and the y-coordinate are reconstructed by the projection of the particle trajectory on the segmented anode. Using the drift velocity v_D, the z-coordinate

is reconstructed using the drift time of the primary electrons:

$$z = v_D \cdot (t_1 - t_0) \ , \tag{3.16}$$

where t_1 is the arrival time of the signal at read-out. The time t_0 is set when the particle traverses the chamber. This information is provided by a trigger or a similar timing information (e. g. the vertex detector). At the ILC, the TPC will be read out during one bunch train without triggering. The particle trajectories will be matched offline with the time stamped information of the calorimeter and the vertex detector.

To use this technique of reconstruction of the z-coordinate, a constant drift velocity v_D is necessary (see Section 3.1.4). Therefore, a gas mixture should be chosen, which provides a region where a change of the electric field E leads to very small variations of v_D. The function $v_D(E)$ must have a maximum with a small derivative. Also distortions of the electric field must be avoided.

3.2.1 Field Cage

To provide a very homogeneous electric field, the walls of the chamber are covered with field strips, which build the field cage. They are made out of conductive material such as copper, have the same width and are equidistant. Their potential decreases uniformly from the cathode to the anode. This is realised by a resistor chain connecting the field strips.

To allow a more homogeneous field near the wall, mirror strips can be used. These strips are located at the gaps between two field strips on the other side of an isolating layer. They should have an intermediate potential.

3.2.2 Amplification Region

As mentioned before, the electron signal must be amplified before the read out. Afterwards, the signal should be proportional to the number of primary electrons. In the past Multi Wire Proportional Chambers (MWPC) were used, which were introduced by Georges Charpak [32]. Figure 3.6 shows a sketch of a MWPC in a configuration often used in TPCs. The electrons are amplified in the wire plane, which consist of field wires and sense wires with alternating potential. The amplification takes place near the sense wires due to the high electric field which increases with decreasing distance to a wire. The fast signal produced by the electrons on these wires is used as a timing signal to determine the z-coordinate. The produced ions lead to an induction signal on the segmented pad plane, where it is read out. This signal is less accurate in its time development than the signal on the wires. It is used for the reconstruction of the $r\phi$-projection of the particle trajectory.

To ensure a homogeneous field in the drift volume, an additional grid of wires shield this volume from the field in the amplification region. The ions which are produced in a large number during the amplification process drift back into the sensitive volume and can lead to field distortions. To avoid this, a gating grid is installed, which catches the ions in its closed configuration. Figure 3.6 shows the two configurations, with an open and a closed gate. For a proper operation of the gating, a trigger is needed to open the gate for the read out of the chamber. As mentioned, at the ILC no trigger is provided between two bunches. During one bunch train, the chamber will be read out continously. Therefore, gating is impossible at the bases of bunches and unfavoured between two bunch trains.

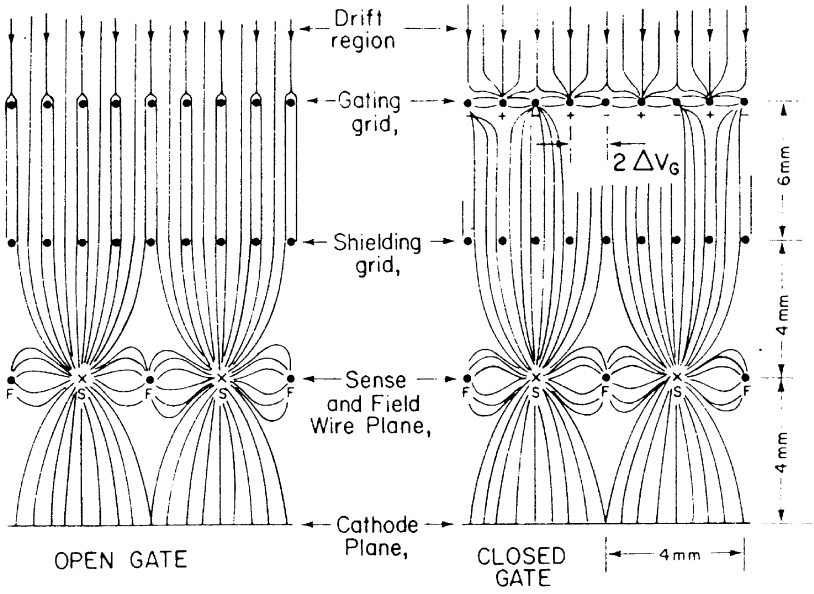

Figure 3.6: *Multi Wire Proportional Chamber: The chamber consists of several planes. In the wire plane, alternating sense and field wires provide an electric field in which the amplification takes place. The shielding grid reduces the influence of this field to the field in the drift region. The gating grid in its closed configuration (right) catches the ions produced during the amplification. The open gate is configured to have a negligible influence to the drift field and the incoming electrons. [33]*

Additionally, the spatial resolution of a MWPC based read out is limited due to the minimal distance between two wires of the order of 1 mm. The wires must be installed under high tension to ensure a precise distance between them, which is needed for a reliable field configuration. This leads to a large amount of material needed for the support structure.

Gas Electron Multiplier

Therefore, other amplification techniques are studied for the ILC. They are based on Micro Pattern Gas Detectors (MPGDs). Two types of MPGDs are studied: Gas Electron Multipliers (GEMs) which have been introduced by Fabio Sauli [34] and MicoMEGAS which have been proposed by Yannis Giomataris [35]. This thesis concentrates on GEMs, which provide a broad operational field. As well as in high energy physics [36], they are used in medical physics [37].

As shown in Figure 3.7(a), a Standard CERN GEM consists of a thin kapton foil (50 µm) coated with copper on both sides (5 µm). Holes with a diameter of 70 µm are etched into the foil. They build a hexagonal structure with a distance of 140 µm between the centres of the holes. Hence, GEMs provide a very small amplification structure which is of the order of the expected spatial resolution ($\approx$ 100 µm). Furthermore, they need only a light support structure.

During operation, a voltage is applied between both sides, which leads to a high electric field inside the holes. This is shown in Figure 3.7(b). The field is high enough, that an avalanche process can start (see Section 3.1.3). Depending on the voltage, a single GEM can provide a gain of 10^4. If higher gains are needed, a multi GEM structure can be used (see

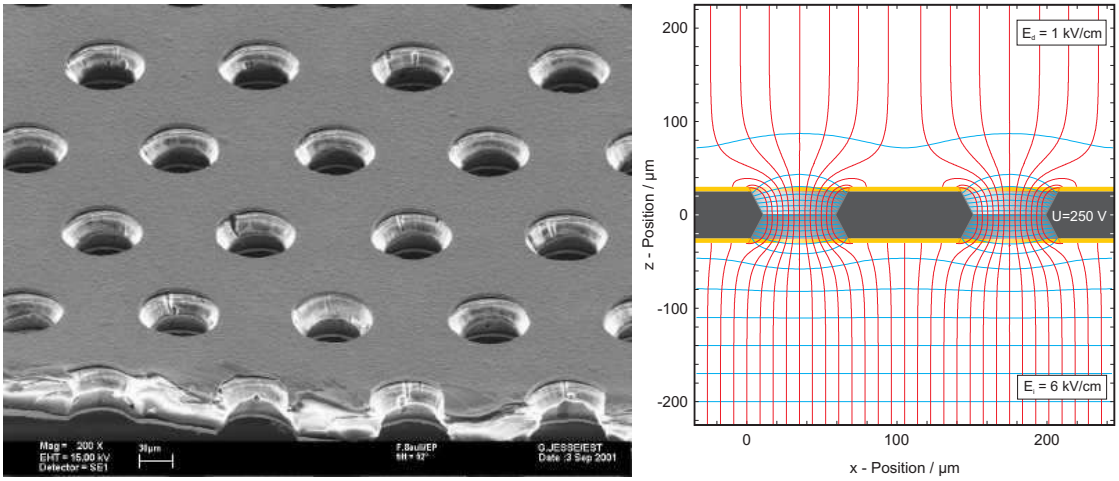

(a) *(b)*

Figure 3.7: *Gas Electron Multiplier: (a) photo of the structure taken with an electron microscope [38] and (b) sketch of the working principle [3].*

Section 4.1.3). If more than one GEMs is used, the gain per GEM can be reduced, which leads to a lower discharge probability. This is desirable for stable operation.

If the electric field before the GEM (seen from the travel direction of an electron) is lower than after the GEM, most of the field lines which go through the hole start on the upper surface. On the other side, only a few of the field lines end on the surface. This is depicted in Figure 3.7(b). This field configuration is valid for the first GEM in a TPC amplification structure. The ions produced during the amplification process, follow the field lines and are neutralised at the GEM surface. The electrons follow the field lines in the other direction and leave the hole. This leads to an intrinsic ion back drift suppression, one of the advantages of GEMs.

In the amplification structure the electric field and the magnetic field are no longer parallel. It is considered, that the resulting $\vec{E} \times \vec{B}$ effects are small and do no effect the resolution. But this fact supports the ion back drift suppression. The mass of electrons and ions differs by a factor of $\mathcal{O}(10^3)$, which leads to much smaller values of $\omega\tau$ for ions. From Equation (3.6) it can be easily seen, that ions follow the electric field lines while electrons follow the magnetic field lines. This means in case of the field in a GEM hole, that the number of ions which leave the GEM hole is not increased much by the influence of the magnetic field. The electrons are guided out of the hole, even if some of the electric field lines end on the lower surface. Hence, their number is increased by the magnetic field. Though, a lower gain per GEM is needed and the number of ions is reduced.

The suppression of back drifting ions can be further improved in a multi GEM structure, where most of the ions produced at the following GEMs are absorbed by the GEMs above. With a sufficient ion back drift suppression, which means that the number of ions is of the same order as the one of the primary ions, no gating between two bunches is needed. Using a multi GEM structure, it is possible to gate between two bunch trains. This procedure is under discussion. An additional specially designed GEM would be used for that purpose.

Defocussing

Similar to the diffusion of the charge cloud on its way to the amplification structure, the spread of the cloud increases further between two GEMs and between a GEM and the read out plane. Due to the different strength of the electric field between two GEMs or the pad plane in comparison with the field in the sensitive volume, the diffusion coefficient D_T is different. As mentioned before, usually the field between GEMs is much higher that in the sensitive volume. As all electrons travel the same distance through the amplification structure until they reach the pad plane, the additional broadening of the signal is the same for all drift distances of the primary electrons in the chamber. Therefore, it can be described by a single value: the defocussing constant σ_0. At the pad plane, the total width of the charge cloud is given by

$$\sigma_{\text{charge}}(z) = \sqrt{D_T^2 \cdot z + \sigma_0^2}\,. \tag{3.17}$$

Some values for the diffusion coefficient D_T and the defocussing constant σ_0, which are valid for the setup described in the following chapter, are summarised in Table 3.2.

B	**Ar/CH$_4$ (95/5)**		**Ar/CH$_4$/CO$_2$ (93/5/2)**	
	D_T ($\sqrt{\text{mm}}$)	σ_0 (mm)	D_T ($\sqrt{\text{mm}}$)	σ_0 (mm)
1 T	0.0495	0.477	0.0584	0.377
2 T	0.0269	0.436	0.0339	0.332
4 T	0.0139	0.375	0.0176	0.266

Table 3.2: *The diffusion coefficient D_T and the defocussing constant σ_0 for Ar/CH_4 (95/5) and $Ar/CH_4/CO_2$ (93/5/2) and magnetic fields between 1 and 4 T. During the calculation of the diffusion coefficient D_T the electric field was set to 203 V/cm for Ar/CH_4 (95/5) and 92 V/cm for $Ar/CH_4/CO_2$ (93/5/2) . The used GEM setup is presented in Section 4.1.3. The presented values are calculated with the program package GARFIELD [21] version 9.*

In comparison with the diffusion in the sensitive volume, the defocussing of the signal has a much lower influence on the resolution. Due to the amplification in the first GEM, the statistics is increased and the smearing of the mean position of a charge cloud due to the diffusion after the GEMs is smaller that before the amplification. This can be expressed as a theoretical limit for the resolution.

The precision of the mean of a Gaussian distribution is given by its width σ divided by $\sqrt{n}$, where n is the amount of the distribution. In the sensitive part of the chamber the number of primary electrons is n_{prim}. In the amplification region the number is increased after each GEM due to the gain. For the theoretical limit the number of electrons reaching the pad plane is used. This is a clear overestimation. These assumptions lead to a limit of

$$\sigma_{\text{theo}}(z) = \sqrt{\frac{D_T^2 \cdot z}{n_{\text{prim}}} + \frac{\sigma_0^2}{n_{\text{amp}}}}\,. \tag{3.18}$$

Due to the statistics of the primary electrons, the resolution can not be better than this limit.

Additionally it should be mentioned, that the defocussing of the signal in the amplification structure can improve the resolution by minimising a systematic effect which is caused by the Pad Response Function. Details 0f this can be found in Section 6.1.1.

3.2.3 Advantages and Disadvantages

In this section the advantages and disadvantages of a TPC as a central tracker for a detector at the ILC are discussed.

The TPC consists mainly of gas, which leads to a low material budget. A radiation length of below $3\%X_0$ can be achieved. The material is concentrated at the walls of the detector. The low probability of scattering and shower initiation ensures a precise measurement of the energy in the following calorimeter. With a large number of three dimensional space points the pattern recognition is highly efficient and leads to a reliable track reconstruction. Furthermore a TPC provides a good $^{dE}/_{dx}$ measurement, which can be used to identify the particles. Here, the large number of points improve the resolution, too.

One of the main disadvantages is the long read out time of the detector. During this time, other bunch crossings will produce further events, which overlay the events in the read out process. This drawback can be compensated by the highly efficient and reliable pattern recognition. In comparison with other tracking detectors, the TPC provides a worse single point resolution. But due to the high number of space points, the resulting momentum resolution fulfils the requirements. The slow ions drifting back to the cathode can distort the electric field, which can lead to a false space point reconstruction. This effect is considered to be small and can be corrected during the reconstruction, if the number of ions leaving the amplification structure is of the same order as the number of primary ions, produced by the traversing particles, which are to be detected.

Chapter 4

Measurements and Simulation

In this chapter the measurement setup is presented. This includes the descriptions of the TPC prototype called MediTPC and the magnet test stand at DESY. Furthermore, a simulation program is described, which generates data for comparison with that measured using the protopye. Within the program it is possible to supply values which were used in the measurement setup such as trigger configuration, gas mixture and pad layout as input parameters.

4.1 The Measurement Setup

To study a TPC using a GEM based amplification device, several prototypes have been build. One of them is dedicated for tests in a high magnetic field. It is designed to fit into the magnet test stand at DESY which provides a magnetic field of up to 5 T. The MediTPC is described in detail in [31, 39]. Figure 4.1 shows a picture of the MediTPC and the magnet test stand.

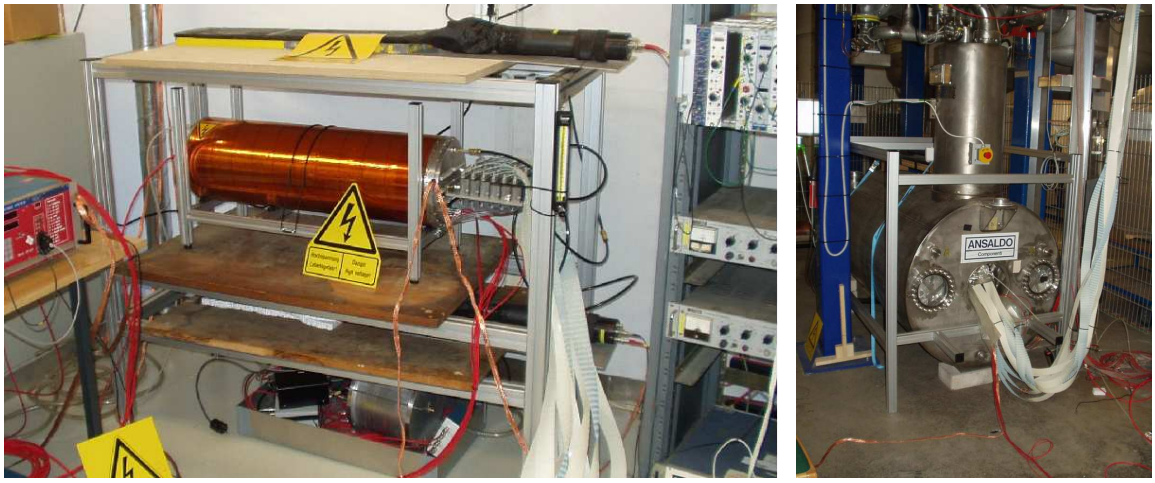

(a) Laboratory test stand *(b)* Magnet test stand

Figure 4.1: *Picture of the MediTPC prototype: (a) in the laboratory [31] (b) inside the magnet test stand.*

4.1.1 MediTPC

The prototype has a length of 800 mm and a diameter of 270 mm. The inner diameter is 250 mm. The inner dimensions of the sensitive volume are $666.0 \times 49.6 \times 52.8\,\mathrm{mm}^3$. The last two numbers denote the height and the width which are determined by the size of the pad plane (see Section 4.1.4).

4.1.2 Field Cage

The field cage is constructed using a sandwich structure to demonstrate the possibility of a light weight design. It consists of a honeycomb structure covered by carbon fibres, which ensures the stiffness of the field cage. To shield the chamber from noise, the outer surface of the barrel is covered with a copper foil. Inside, three layers of a kapton foil isolate the field strips from the ground potential at the outside. The field strips are coated on the inner kapton layer. Four chains of SMD resistors inside the chamber provides the decreasing potential of the 245 field strips. The field cage is completed on one side by a cathode which provides the high potential of up to 16 kV. It is a circular piece of G10 with copper cladding.

On the opposite side, the last field strip is connected to a shielding which is located on the same position as the first GEM of the amplification structure which is described in the next section. This shield is connected to the ground via an adjustable resistor. The adjustment is set that the shield is at the same potential as the upper surface of the first GEM. The GEM tower is powered by a separate high voltage supply.

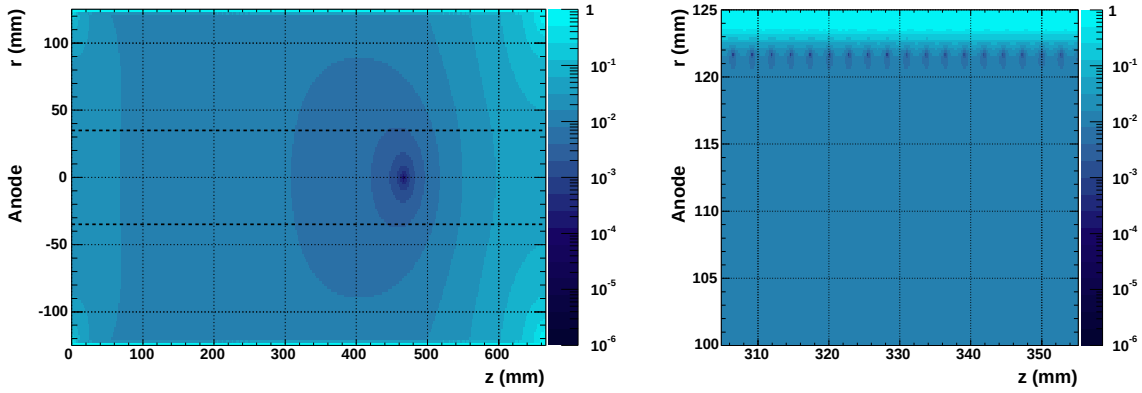

(a) *(b)*

Figure 4.2: *The homogeneity of the electric field in the MediTPC: The deviation from the nominal field is shown [40]:* $E_{\mathrm{nom}}^{-1} \cdot \sqrt{(E_z - E_{\mathrm{nom}})^2 + E_r^2}$*, where* $E_{z,r}$ *denotes the field components along the* z *and the* r *axis. The nominal field* E_{nom} *should point in the direction of the* z *axis. Figure (a) shows the full detector volume of the MediTPC. Additionally the sensitive volume is depicted by the two dashed lines. Figure (b) presents an area near the wall.*

The MediTPC has no mirror strips, which leads to distortions of the electric field near the walls of the chamber. This is shown in Figure 4.2. The centred sensitive volume is with a maximal radial expanse of $\approx 50\,\mathrm{mm} \times \sqrt{2} \approx 70\,\mathrm{mm}$ (diagonal of the pad plane) small and far away from the walls. Inside this volume, the deviations from the nominal field are $\mathcal{O}(2\%)$. These maybe considered negligible for the resolution studies.

4.1.3 GEM Tower

As an amplification device a tower of three GEMs is used. Is is shown in Figure 4.3. The distance between two GEMs is 2 mm. The electric field between two GEMs is called Transfer field. The distance between the third GEM and the pad plane, which is described in the next section, is 3 mm. The electric field in this region is named induction field.

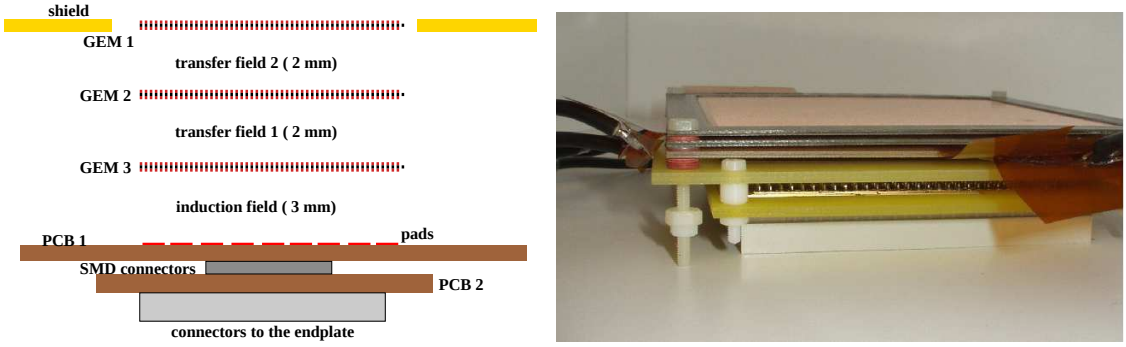

(a) Sketch *(b)* Photo

Figure 4.3: *The GEM tower: (a) Sketch and (b) Photo*

The setup is operated with a transfer field of $1.5\,\mathrm{kV/cm}$ and an induction field of $3\,\mathrm{kV/cm}$. The voltages between the two GEM sides is set to values between 320-340 V. It is adjusted to ensure a gain that leads to a good signal to noise ratio and only a few signals outside the range of the electronics.

4.1.4 The Pad Layout

The pad plane is made out of a copper and gold coated PC board with the pad structure etched on to it. The pads have a size of $6 \times 2\,\mathrm{mm}^2$. The space between the pads is 0.2 mm on all sides, which leads to a pitch of the pads of $6.2 \times 2.2\,\mathrm{mm}^2$. Because all field lines are forced to end on the copper surface, the pitch gives the size of the effective pad area. This number is important for comparison of the resolution measured with different prototypes.

As Figure 4.4(a) shows, the 28×12 pads are surrounded by a metal plane. To ground the outer two columns and rows, they are connected to this plane via resistors of $100\,\mathrm{k}\Omega$. A resistor instead of a direct connection was chosen to avoid crosstalk between the metal plane and the outer rows. Unfortunately, this procedure does not work properly. This will be discussed in the next section. The active area contains $24 \times 8 = 192$ pads that are read out.

Two different pad layouts have been investigated which differ in the arrangement of the pads. In one layout, the pads are aligned in columns (see Figure 4.4(b)). In the other layout, every second row is shifted by half a pad pitch (1.1 mm) which leads to a staggered arrangement of the pads (see Figure 4.4(c)).

In a circular read out plane of a large TPC detector, these layouts will be realised as the two extreme pad row alignments. Even though the staggered layout provides more hits per event with the charge signal shared by more than one pad, this does not lead to an improvement of the resolution as it was naively expected. This is due to the systematic shifts which are described in Section 6.1.1.

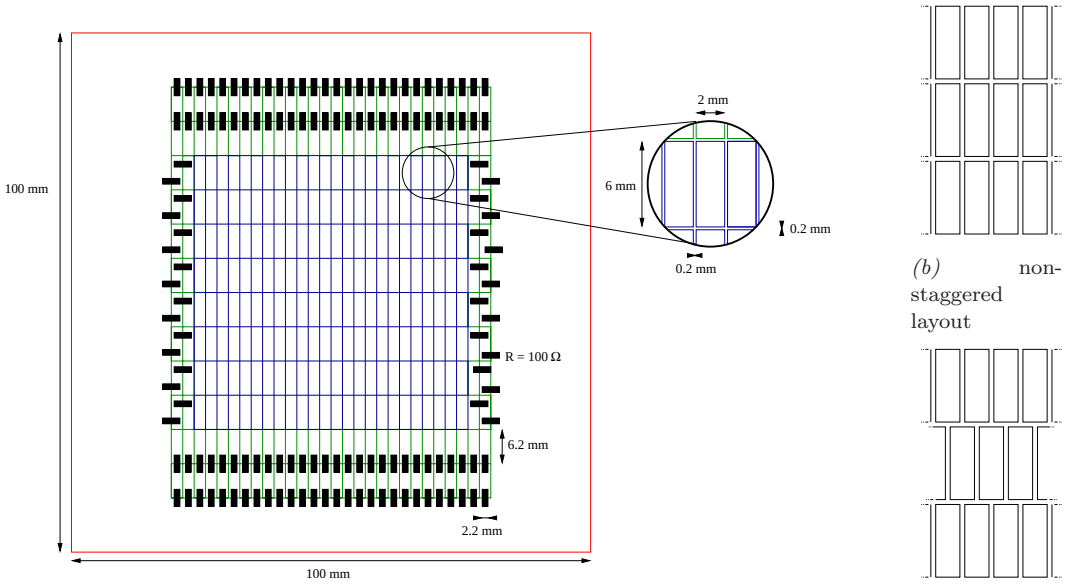

(a) Pad plane

(b) non-staggered layout

(c) staggered layout

Figure 4.4: *Sketch of the pad plane: Figure (a) shows the total pad plane including the outer pad which are connected via resistors to the surrounding metal plane. Figures (b) and (c) depict the two investigated layouts.*

Cross Talk

The arriving cloud of electrons on its way from the last GEM to the pad plane induces a signal on the pad plane. This signal is much broader than the signal directly produced by the electrons on the pads. Therefore, the maximum per pad of the induction signal is much smaller than this direct signal and does not influence the actual signal.

This is depicted in Figure 4.5(a). It is clearly visible, that the induction signal is integrated on the surrounding metal plane. There it is much stronger than on the pads and can lead to cross talk with the outer pads. The resistors between the outer pads that are not read out and the metal plane should prevent the measurements from being effected by the cross talk. This procedure did not work effectively, as visible in Figure 4.5(b). The number of pulses measured on each pad during one run is shown. The excess on the outer pads of the read-out ones in comparison with the central region demonstrates the presence of cross talk. Even though the pulses caused by the cross talk are usually measured earlier than the electron signal, they can still disturb the reconstruction. To ensure an accurate and reliable reconstruction, only the inner six rows are used. Furthermore, the pads in the outer two columns are disabled. They are marked as non working pads. Figure 4.5(b) shows also some pads with no reconstructed pulse in the central region. They are also labelled as damaged, which is taken into account in the reconstruction program MultiFit (see Section 5.1.1).

4.1.5 The DESY Magnet Test Stand

The magnet used for the data taking is based on superconducting technology and can sustain a current of 1000 A. This corresponds to a magnetic field of 5.25 T. The magnet design ensures a

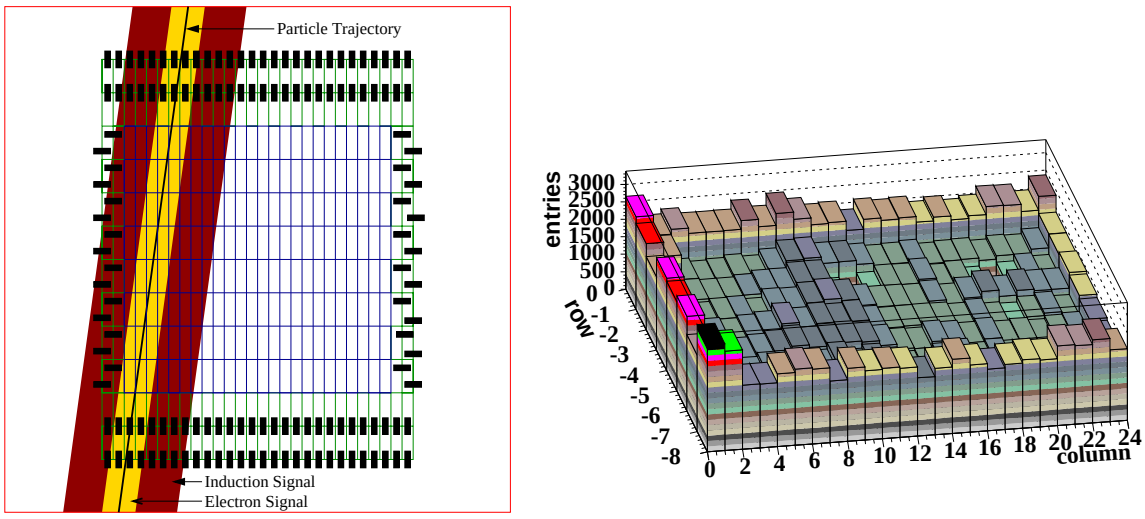

(a) *(b)*

Figure 4.5: *Cross-talk between outer pads and the surrounding plane: (a) electron (yellow) and induction signal (red) on the pad plane and the surrounding plane (b) number of pulses per pad integrated over a measurement run [31].*

high homogeneity of the magnetic field in a large area inside the bore. As shown in Figure 4.6, the MediTPC is located inside this area. The inhomogeneity of the magnetic field in the sensitive volume, which is marked with a different colour (yellow), is below 3% [39]. The trigger system that provides the t_0 time information consists of two plastic scintillators on the top and the bottom of the magnet. They are read out by photo multiplier tubes. A passing particle, which goes through the sensitive volume produces a light flash in both scintillators. The trigger gives a signal if both tubes give a coincident signal. Here, runtime differences and the time resolution are taken into account. To allow for the superconducting operation of the coil, it must be cooled with liquid helium. As shown in Figure 4.6, the helium support lines go into on top of the magnet. This prevents a symmetric alignment of the trigger system in reference to the centre of the magnetic field.

4.1.6 Read-Out Electronics

The signal on the pads is read out using modified ALEPH electronics [41]. The pads are connected via short cables to the charge sensitive preamplifiers-shapers. These are connected to FADCs, called Time-Projection-Digitiser (TPD). When a trigger is received, the signals are sampled with a frequency of 12.5 MHz and stored into a 512 time bin array. The 80 ns time bins are read out by a Fast-Intelligent-Controller (FIC) and send to a Linux computer, where they are stored using the LCIO-format [42]. A detailed description can be found in [43].

4.1.7 Datasets

Several measurement runs have been taken with the setup using the magnet test stand (see Figure 4.6).

Two gas mixtures have been investigated. One of them, $Ar/CH_4/CO_2$ (93/5/2) is proposed in the design report of TESLA [17], the predecessor project of the ILC. The other Ar/CH_4

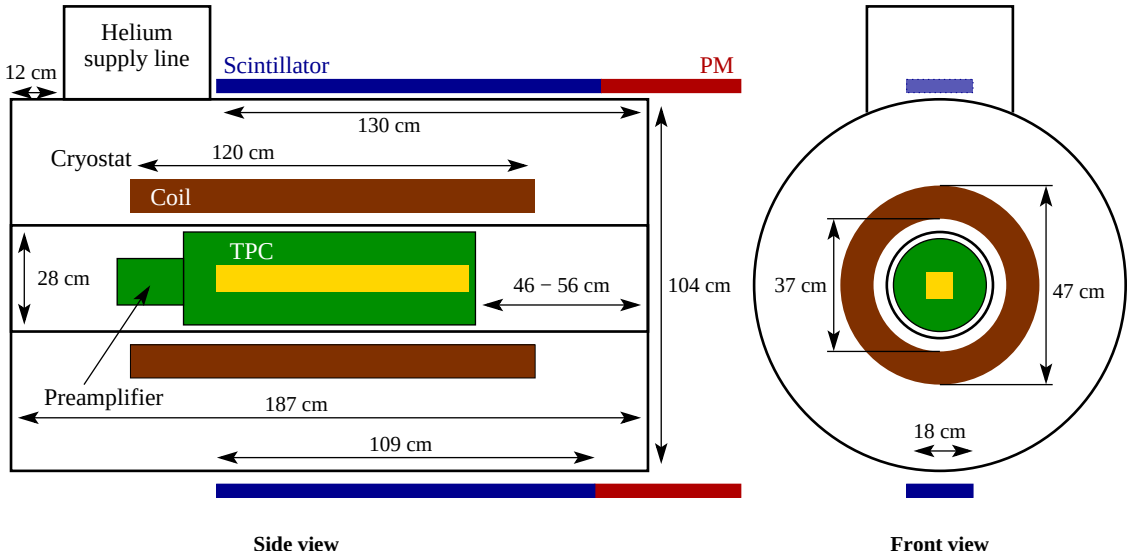

Figure 4.6: *Sketch of the magnet test stand with the TPC prototype MediTPC including dimensions.*

(95/5), is used as a reference in an agreement between the groups doing research for a TPC at the ILC.

Magnetic fields from 0 to 4 T have been investigated. This analysis will concentrate on the data sets with non zero field. Data sets have been taken for all combination of the two gas mixtures, three magnetic fields (1 T, 2 T and 4 T) and the two pad layouts which were presented in Section 4.1.4. The ones used in this analysis are summarised in Table 4.1. Some data sets with the same setting are separated in time by several weeks. The environmental conditions can change significantly during this time. Therefore, they are treated as separate data sets and important properties for the reconstruction such as the drift velocity v_D are calculated for each subset.

4.2 Monte Carlo Simulation

One of the main advantages of simulated data is that the true track trajectory is known. This allows several studies, which can lead to a deeper understanding of effects during the reconstruction process: e. g. the deviation of reconstructed and true hit position as shown in Figure 7.2 on page 64. Furthermore, modifications of the measurment setup can be studied: e. g. the influence of damaged pads or the use of more pad rows (see Chapter 7).

The Monte Carlo simulation which was used for this analysis is still under development. It works in several steps. In the first step the incident particle is generated. A muon generator is used to simulate cosmic muons with a realistic angular and energy spectra.

The position of the scintillators which provide the trigger signal (see Section 4.1.5) is implemented as well as the geometry of the chamber. This information is used to filter the relevant events for geometric acceptance. During this filtering process as in all other steps of the simulation the tracks are assumed to be straight, even if a magnetic field is applied.

In the next step the gas properties are taken into account. Besides the composition of the gas mixture, impurities such as water can be considered. This is not taken into account

gas mixture	layout	B	v_D	n_{event}
$Ar/CH_4/CO_2$ (93/5/2)	non-staggered	1 T	4.204 $^{cm}/_{\mu s}$	15817
		2 T	4.090 $^{cm}/_{\mu s}$	4437
		4 T	4.296 $^{cm}/_{\mu s}$	6641
			4.291 $^{cm}/_{\mu s}$	15250
	staggered	1 T	4.283 $^{cm}/_{\mu s}$	6295
			4.315 $^{cm}/_{\mu s}$	33520
		2 T	4.345 $^{cm}/_{\mu s}$	15541
		4 T	4.280 $^{cm}/_{\mu s}$	20349
Ar/CH_4 (95/5)	non-staggered	1 T	4.104 $^{cm}/_{\mu s}$	7028
		2 T	4.050 $^{cm}/_{\mu s}$	3789
			4.023 $^{cm}/_{\mu s}$	12760
		4 T	4.089 $^{cm}/_{\mu s}$	10163
			4.040 $^{cm}/_{\mu s}$	3682
			4.043 $^{cm}/_{\mu s}$	5962
			4.047 $^{cm}/_{\mu s}$	3296
			4.090 $^{cm}/_{\mu s}$	23109
			4.075 $^{cm}/_{\mu s}$	2253
			4.033 $^{cm}/_{\mu s}$	2836
	staggered	1 T	4.107 $^{cm}/_{\mu s}$	14827
			4.106 $^{cm}/_{\mu s}$	6852
			4.063 $^{cm}/_{\mu s}$	17631
		2 T	4.099 $^{cm}/_{\mu s}$	29672
		4 T	4.105 $^{cm}/_{\mu s}$	467
			4.121 $^{cm}/_{\mu s}$	3940
			4.126 $^{cm}/_{\mu s}$	13924

Table 4.1: *Measured data sets: Various data sets have been taken under different configurations such as gas mixture, pad layout and magnetic field B. For some configurations, more than one data set is itemised. These data sets are not taken adjacent in time, which can lead to a slight difference in the conditions such as the drift velocity v_D or the gain. The value n_{event} denotes the number of events after the track finding process.*

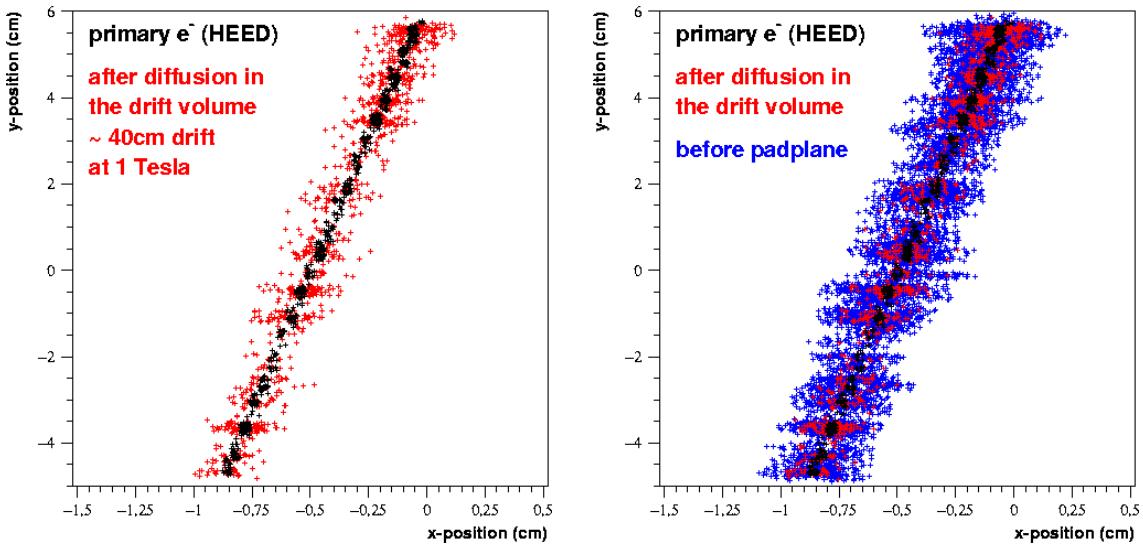

(a) after 40 cm drift, before GEMs

(b) after amplification, before pad plane

Figure 4.7: *Diffusion evolution of the electron cloud during the drift in a Monte Carlo simulation for a magnetic field of 1 T [44]:*
black crosses: primary electrons from HEED; red crosses: electrons after drift; blue crosses: electrons after amplification (only shown in (b)).

for the simulation used in this analysis. The primary ionisation along the track is simulated with HEED [22]. In this step the influence of the magnetic and electric field is not considered. Hence, the generated three dimensional electron cloud follows a straight trajectory and is field independent. The drift velocity v_D of electrons and the diffusion coefficient D_T are simulated with GARFIELD [21]. In this simulation the magnetic field and the electric field are taken into account. The values used for the diffusion coefficient D_T are summarised in Table 3.2 on page 26.

Using this information the evolution of the position of the each electron is calculated. Therefore, a Gaussian smearing in three dimensions is used. After this procedure, the electron has following coordinates:

$$x_i = x_{0,i} + R_{\text{Gauss}} \cdot \sqrt{l_{\text{drift}}} \cdot D_T \tag{4.1a}$$

$$y_i = y_{0,i} + R_{\text{Gauss}} \cdot \sqrt{l_{\text{drift}}} \cdot D_T \tag{4.1b}$$

$$z_i = z_{0,i} + R_{\text{Gauss}} \cdot \sqrt{l_{\text{drift}}} \cdot D_L \,, \tag{4.1c}$$

where x_0, y_0 and z_0 specifies the coordinates of the electrons before the smearing. The shape of the smearing comes in by R_{Gauss} which denotes a Gaussian distributed random number. The drift length l_{drift} determines the width of the distribution. Here, the transversal and longitudinal diffusion coefficient $D_{T,L}$ are taken into account. The procedure is illustrated in Figure 4.7(a).

In the following step the amplification structure is simulated. If an electron reaches the GEMs, it is forced into the nearest GEM hole. An effective gain is applied and smeared with a Polya distributed random number. The effective gain is set in several iterations to provide the best comparability of measured and simulated data.

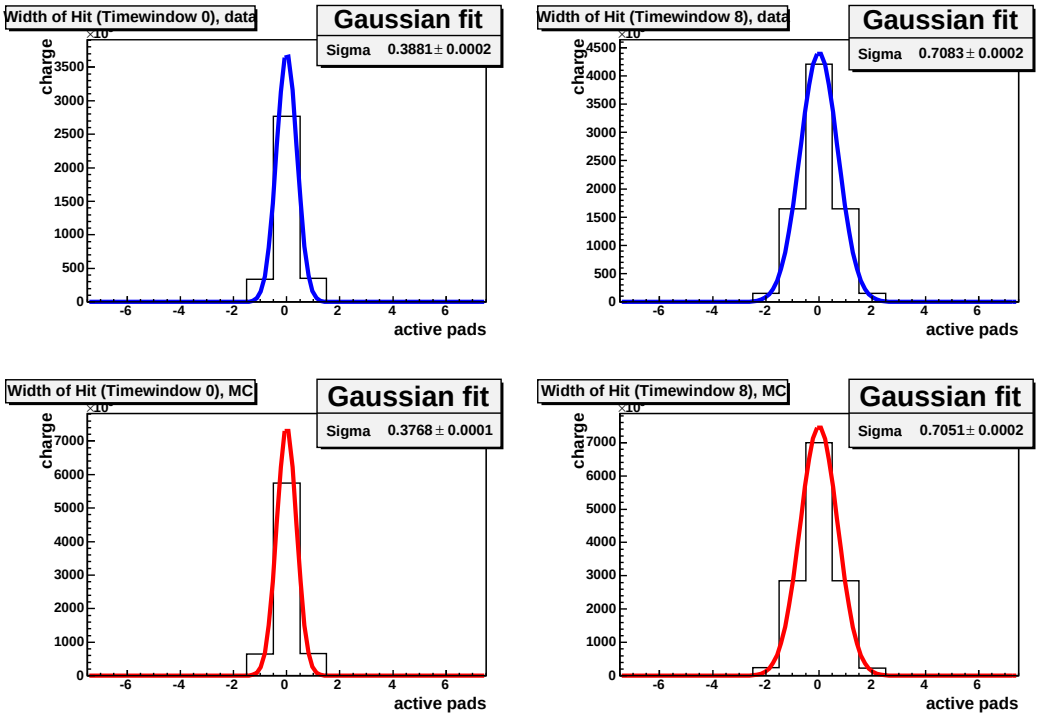

Figure 4.8: *Comparison of the signal width between measured (top, blue) and simulated (bottom, red) data for two different drift distance ranges: left side 0-75 mm, right side 525-600 mm. These values are for $Ar/CH_4/CO_2$ (93/5/2) and 1 T magnetic field (figure from [44]).*

The new electrons produced in the amplification process are distributed uniformly inside the GEM hole. The position of the primary and the secondary electrons is smeared to simulate the drift after the GEM. This is done similar to the drift before the GEMs. Here also the Equations (4.1) are used, but the diffusion coefficient ${D_T}^{T,L}$ differs due to the different strength of the electric field. For the next GEMs, the procedure is repeated until the electrons reach the pad plane. The broadening of the charge cloud in the amplification structure is depicted in Figure 4.7(b). The effect can be expressed by a defocussing constant σ_0 as described in Section 3.2.2. Values for the defocussing constant σ_0 are summarised in Table 3.2.

The electrons arriving at the pad plane are collected on the pads. Different layouts and sizes of the pads can be simulated. To produce FADC spectra out of the number of electrons per pad a simplified simulation of the electronics is done.

For many studies, the ratio between the signal width and the pad width is essential, because this specifies the number of active pads per row. Figure 4.8 shows the width of the signal for measured and simulated data. It demonstrates a good agreement between the measurements and the Monte Carlo simulation.

Table 4.2 summarises the simulated data sets used in this analysis. Only data using a staggered pad layout has been generated. This choice is motivated by the systematic effects caused by the Pad Response Function (see Section 6.1.1) which is best visible here. The data is generated assuming uniform conditions which means: no gas impurities such as water or oxygen, a constant temperature of 23 °C and a constant pressure of 1013 hPa. The data set

gas mixture	layout	B	v_D	n_{event}
Ar/CH_4 (95/5)	staggered	2 T	4.062 $^{\text{cm}}/_{\mu\text{s}}$	151196
		4 T	4.066 $^{\text{cm}}/_{\mu\text{s}}$	151185

Table 4.2: *Simulated data sets: The two data sets contain data for 19 rows. They are simulated with no gas impurities such as water or oxygen. Therefore the drift velocity shows only a slight difference. In comparison with the measured data set (see Table 4.1) the simulated ones provide at least five times more events (n_{event}).*

contains data for 19 pads rows. In this data all channels are working. For some studies only the data of the six centre rows is used. More about the further handling of the generated data is described in Section 7.1.1.

Chapter 5

Reconstruction Algorithms

In this chapter the reconstruction software MultiFit and a method to determine the point resolution in a TPC are described.

5.1 The Reconstruction Program MultiFit

The software program MultiFit [39] is designed to reconstruct tracks from the measured charge information. It is applicable to different small TPC prototypes. As it provides values needed for the analysis of the detector performance, such as track parameters, residuals and detailed information for studies of reconstruction algorithms.

MultiFit is written in C++ and makes use of several frameworks: ROOT [45], LCIO [42] and DotConf [46]. It is a program in development, the methods described here can differ from descriptions mentioned in other publication. The methods and numbers given here, refer to those used during the analysis presented in this thesis.

The program consists of three modules, which can work independently:

ClusterFinder The first module reconstructs hits (3 dimensional points) in a three step process using the charge information stored in the raw data.

TrackFinder The next module combines these hits to tracks using a track following algorithm.

TrackFitter In the last step, the track parameters and additional values needed for the further analysis are calculated. This module provides different methods to determine these parameters.

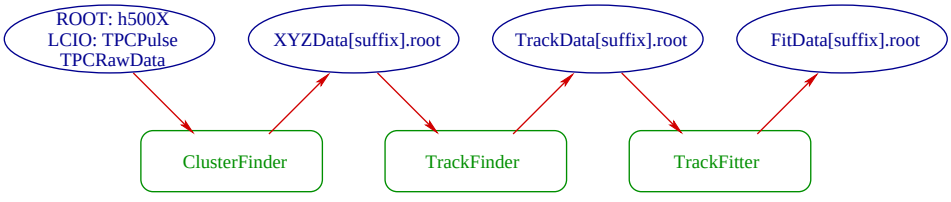

Figure 5.1: *The modules of the reconstruction software* MultiFit *and the corresponding input and output files.*

Figure 5.1 shows these modules and the corresponding input and output files, which are stored in the ROOT format. Additionally the ClusterFinder can read the raw data in the LCIO format. During the reconstruction process it is assumed that the tracks are transversing the chamber only from the top to the bottom.

MultiFit uses a right handed coordinate system which is shown in Figure 5.2. The z axis runs parallel to the drift direction starting from the pad plane. The x axis runs along the pad rows, while the y axis is pointing downwards perpendicular to the pad rows. The origin of the system is located at the upper left corner of the sensitive volume of the TPC, viewed from the outside towards the pad plane.

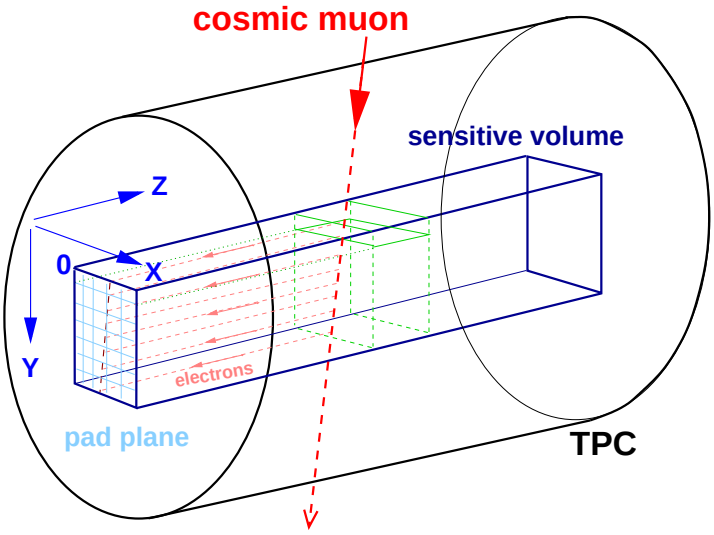

Figure 5.2: *The coordinate system used in the calculations of* MultiFit *together with a sketch of the TPC prototype. [47]*

5.1.1 ClusterFinder

After the raw data is assigned to a pad via the channel ID, the pedestals are subtracted. The required information for the channel pad assignment and the pedestal correction are stored in a steering file. Furthermore, this file contains the length of the time bins and the drift velocity, which are required to determine the z-coordinate.

For each pad the corrected raw data is scanned for signals by applying a threshold of six ADC-counts[1] which is above five times the width of the noise. To include the full charge of the pulse, two time bins before the first bin over threshold are saved. A second threshold of three ADC-counts is applied to detect the end of the pulse. Additionally, four time bins after the last bin over threshold are saved.

The program provides algorithms to split pulses which are merged in time. Details can be found in [48], which presents a study of the double track capability of GEM based TPCs. For the analysis presented here, only events with one track are taken into account and no separation is needed. Nevertheless, separation algorithms will be used in future reconstruction, which may influence the resolution. To take these effects into account a simple algorithm is used,

[1] Most of the mentioned values can be set via the steering file, the numbers mentioned here refer to the values used in the presented analysis.

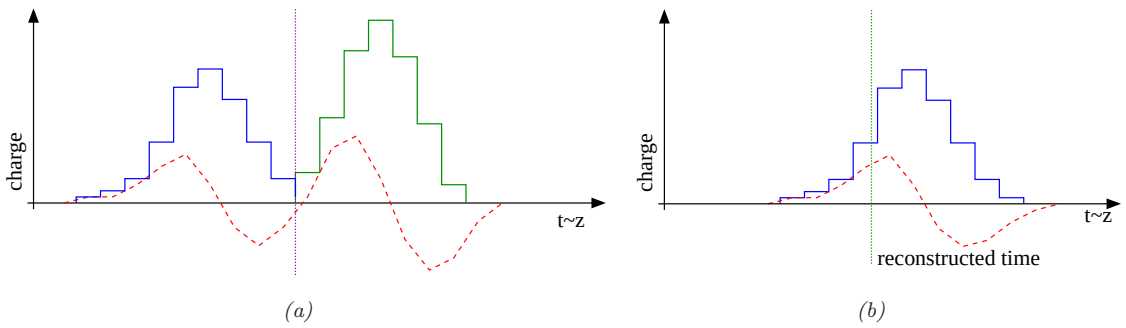

Figure 5.3: *Pulse reconstruction: The figures show the charge versus time. The dashed red line denotes the derivative of the distribution. Figure (a) explains the separation of double pulses: The pulses are separated at the bin where the derivative turns from negative to positive values. This is indicated by the vertical line. Figure (b) shows the time reconstruction of the pulse: The mean value of the positive part of the derivative is used as the arrival time of the pulse. This is indicated by the vertical line.*

which scans the pulse for changes in the slope of the charge curve from negative (decreasing values) to positive (increasing values). The pulse is separated at the dedicated time bin, as it is shown in Figure 5.3(a).

In the second step, the integrated charge and time related information for each pulse is calculated. The charge is stored in units of 'primary electrons' applying a factor given by the gain of the GEMs and the sampling electronics. Using as arrival time the inflexion point of the rising slope, instead of the mean of the pulse, makes the time information mostly independent of the height of the pulse. To minimise the uncertainty caused by the sampling structure, the mean of the positive part of the derivative is calculated, as it is depicted in Figure 5.3(b). This technique is deduced from the methods described in [49]. The sampling frequency of 12.5 MHz results in a width of the bins of 80 ns (see Section 4.1.6). This information is used to calculate the time information from the bin number.

After the detection of the pulses on each pad separately, these pulses are combined row wise to hits. In the first step, the pulses are merged together, using only the time information of the pulses. The procedure starts with the pulse with the highest charge in a row. A time window is defined, which is centred around the time information of this starting hit. It will not be changed during the search for associated pulses. Its width can be set in the steering file. Other pulses of the neighbouring pads are added to the hit, if their time value is inside the defined window. The search procedure will stop if a gap (a pad with no charge information) is detected or no pulse on this pad lies inside the defined time window. Pads which are marked as dead are skipped and the search continues with the next neighbouring pad. This ensures that dead channels do not lead to an artifical separation of pulses belonging to one hit. Pulses which are already assigned to a hit are ignored during the search.

After the pulses are merged together, different algorithms can be used to detect and split double hits in the xy-plane (see [48]). As for the pulses, a simple algorithm is used for this analysis. The algorithm searches for changes in the sign of the slope from negative to positive while scanning the charge information of the pulses, starting from low x-coordinates. During the comparison of the charge information, fluctuations below a certain value, which is set via the steering file, are ignored.

The time information of the pulse with the highest integrated charge is used for the z-coordinate of the hit. The time information is transfered to a length using the drift velocity v_D. The y-coordinate is given by the the centre of the row. The x-coordinate is determined by a simple algorithm calculating the centre-of-gravity of the hit charge. This algorithm leads to systematic shifts, if only a few pads contribute to the hit. This systematic is described in detail in Section 6.1.1.

5.1.2 Track Finder

Independently of the methods used for the determination of the track parameter, in this module the hits are combined to a track by a simple three-dimensional track following algorithm. Due to the short length of the track in comparison to the radius of the track, which is mainly limited by the geometry of the measurement setup, a straight trajectory for the track in the xy- and the yz-plane is assumed. This is in contrast to the final track fit, which is performed in the last module, where straight as well as curved hypotheses are used.

The search is initialised with a track hypothesis calculated from two hits. A suitable minimal distance between these hits, which is set to the height of two rows, stabilises the track finding algorithm during the initialisation. No further selection criteria are applied to the initial hits. The search for hits which belong to the track is continued row wise. A three dimensional search window is defined around the most probable position of the next hit. It is calculated out of the actual track hypothesis. If the search windows contains:

one hit The hit is added to the track and the hypothesis is recalculated for the search in the next row.

more than one hit A hypothesis for each hit is calculated and only that one yielding the smallest χ^2 is added to the track.

no hit The search is continued in the next row, if a hit was added during the search in the previous row. The allowed number of adjacent rows without a hit can be set in the steering file. It is set to one for the presented studies.

The algorithm is illustrated in Figure 5.4.

The search for hits is performed from the bottom to the top. After that a second search is done in the opposite direction to fill gaps in the track and to verify the hits used for initialisation. After the search, the track is checked, if it passes the cut for the minimal number of hits. For the studies presented a track must contain at least six hits. Additionally a cut on the minimal probability of the track can be applied. It is set to 0, which ensure that all tracks pass this cut at this level of reconstruction. If a track passes the cuts, it is stored in the file and all hits of the track are marked as used. These hits will not be assigned to other tracks during the continuing search for further track.

5.1.3 Track Fitter

The last module uses the information of the hits combined into a track to perform the final fit to determine the track parameters. For this purpose, several methods to determine the track parameters are provided. In conrtrast to the track finding alogrithm, they can use straight and curved hypothesis for the xy-plane. In this analysis, only the curved track hypothesis is used. The two methods investigated in this thesis are discussed in detail in Section 6. Both method results in the same set of track parameters:

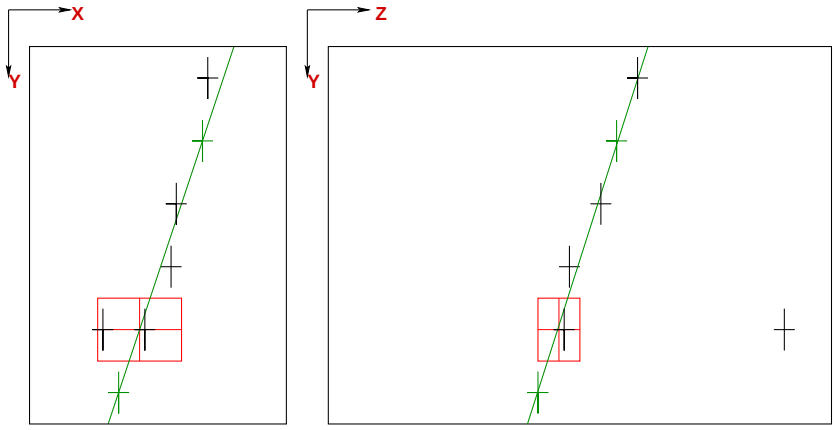

(a) Initialisation hits and first track hypothesis (in green) and first search window (red rectangle)

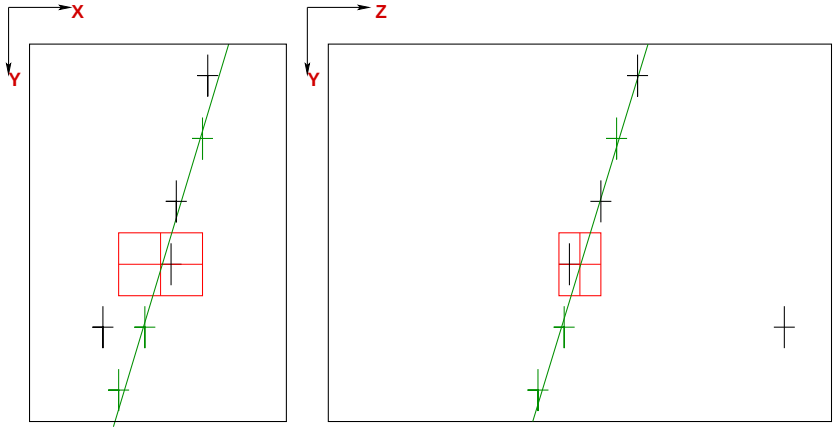

(b) Track hypothesis resulting from newly added hit (green) and next search window (red rectangle)

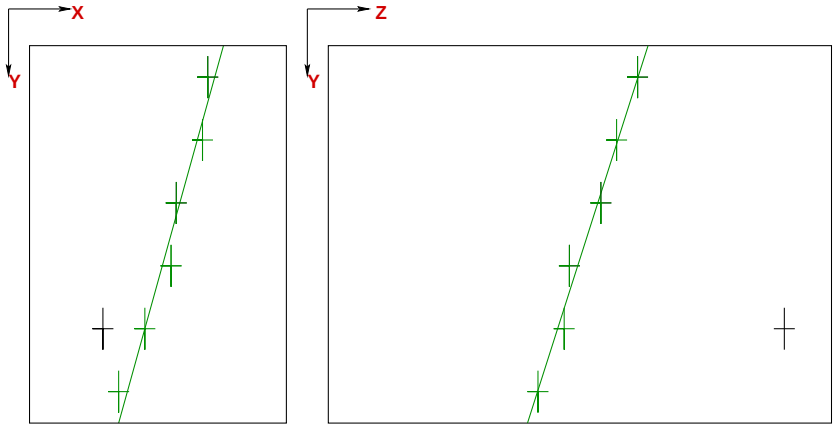

(c) Completed track collection (green)

Figure 5.4: *Illustration of the track following algorithm.*

x_0, y_0 centre coordinates of a circle

κ curvature of the circle arc: $\kappa = \rho^{-1}$, where ρ denoted the radius.

Additionally, the following parameters as an alternative set replacing the two centre coordinates of the circle are stored:

I_x intercept of the track at $y = 0$

ϕ_0 the inclination angle at $y = 0$

In the yz-projection the approximation of a straight track is used. The projection is described by the following two parameters:

I_z intercept of the track at $y = 0$

θ_0 the inclination angle at $y = 0$

5.2 Determination of the resolution: Geometric Mean Method

In the ideal case without systematic shifts, the reconstructed hit coordinates are spread around the true track following a Gaussian distribution. This is mainly caused by the diffusion (see Section 3). The single point resolution can be estimated from the width of this distribution. In real experiments the problem arises, that the true track trajectory is unknown. The prototype setup used (see Section 4.1) does not include any external reference, such as a hodoscope, to measure the trajectory with high precision. Therefore, the resolution must be estimated from the fitted track parameters. Especially for small prototypes with a low number of rows, the fitted and the true track can differ significantly, due to the correlation between the parameters and the measured points. The presented Geometric Mean Method can solve this problem by balancing the uncertainties in a two fit approach [50]. The first fit is done using the information of all hits belonging to the track. The difference of this track and the x-coordinate of the hits at the same y-coordinate is denoted as '*distance*'. In the second step all track parameters are re-fitted without the use of the information of one hit. The difference between this hit and the re-fitted track is denoted as '*residual*'. This re-fitting procedure is done for each hit of the track. These definitions are illustrated for one hit in Figure 5.5.

To get the minimal 'distance' and 'residual' between track and hits, which is perpendicular to the track, the calculated values are multiplied with $\cos(\phi_{\text{hit}})$. Here, ϕ_{hit} denotes the angle of the track at the y-coordinate of the hit:

$$\phi_{\text{hit}} = \sin^{-1}(\sin(\phi_0) - y_{\text{hit}} \cdot \kappa)\,. \tag{5.1}$$

In the case of the 'distance', the considered hit 'pulls' the reconstructed track in the direction of its deviation, which means that the 'distance' is usually smaller that the deviation of the hit from the true track. In contrast, in the determination of the 'residual' the remaining hits 'pull' the track away from the hit which is left out. This results in systematical larger values. For a large number of hits on the track, the fit uncertainties are reduced and the 'distance' and the 'residual' converge. The width of the distribution of the deviation of the hits to the true track estimates the resolution σ. In comparison to this width the distributions are smaller in case of the 'distance' (σ_{distance}) and larger for the 'residuals' (σ_{residual}). For straight tracks, it can be shown analytically, that the geometric mean of both widths reproduces the width of the true deviations [50]. Hence, the single point resolution can be determined for each row separately by:

$$\sigma_{\text{row}} = \sqrt{\sigma_{\text{distance}} \cdot \sigma_{\text{residual}}} \tag{5.2}$$

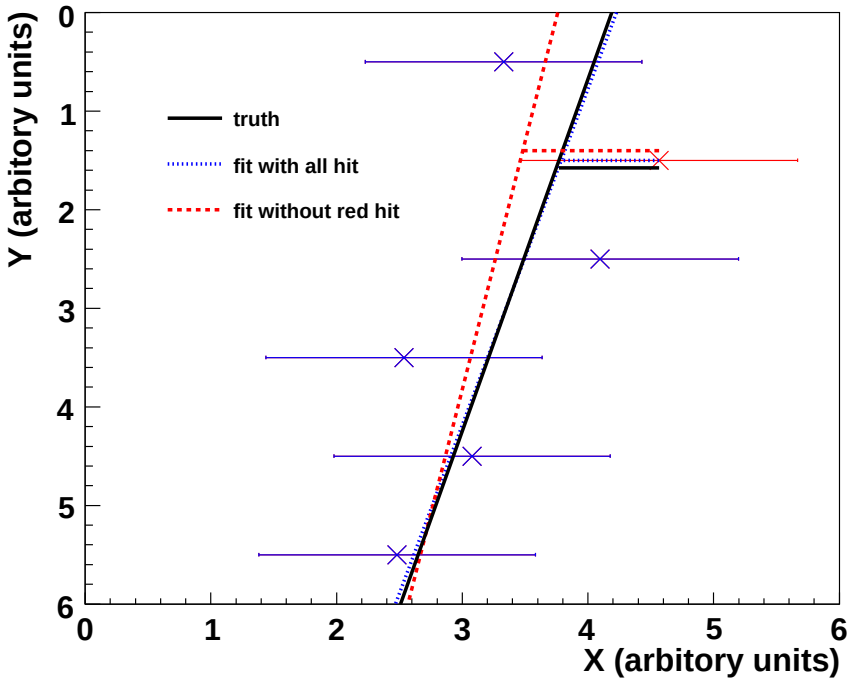

Figure 5.5: *Determination of 'residual' and 'distance' of a hit: The hits are Gaussian distributed around the true track (black, solid). Two fits are performed. the first makes use of all hits (blue, dashed) and defines the 'distance' of the hit. The second (red, dotted) is done without the hit in question (second from above). It defines the 'residual' for this hit.*

For curved tracks this technique was verified with a Monte Carlo simulation. This simulation generates two dimensional space points that are randomly distributed around a track, following a Gaussian distribution with a width of 200 µm. The generated tracks are going through the centre of the volume. The radius varies between 500 mm and 2000 mm. Left and right bent tracks (positive and negative curvature) were produced. Figure 5.6 shows the resulting widths of the mentioned distributions. As expected, the width of 'distances' distribution is too small for all rows. In contrast the 'residuals' show broad distributions. The Monte Carlo truth of 200 µm is correctly reproduced in every row by the geometric mean of both. This shows that the method described above can also be used for curved tracks.

During the analysis the two required widths are determined by a Gaussian fit to the distributions. Each row is analysed separately. The final resolution is given by the error weighted mean of all rows:

$$\sigma = \frac{\sum \frac{\sigma_{\text{row}}}{\Delta_{\sigma_{\text{row}}}}}{\sum \frac{1}{\Delta_{\sigma_{\text{row}}}}}, \tag{5.3}$$

while the error for each row is determined by taking into account the errors of the fits $\Delta_{\sigma_{\text{distance}}}$ and $\Delta_{\sigma_{\text{residual}}}$:

$$\Delta_{\sigma_{\text{row}}} = \frac{\Delta_{\sigma_{\text{distance}}}\sigma_{\text{residual}} + \sigma_{\text{distance}}\Delta_{\sigma_{\text{residual}}}}{2\sqrt{\sigma_{\text{distance}} \cdot \sigma_{\text{residual}}}} \tag{5.4}$$

Nevertheless, Figure 5.6 shows a huge divergence of the both values 'distance' and 'residual' from the truth in the most outer rows. This is caused by the limited number of points used

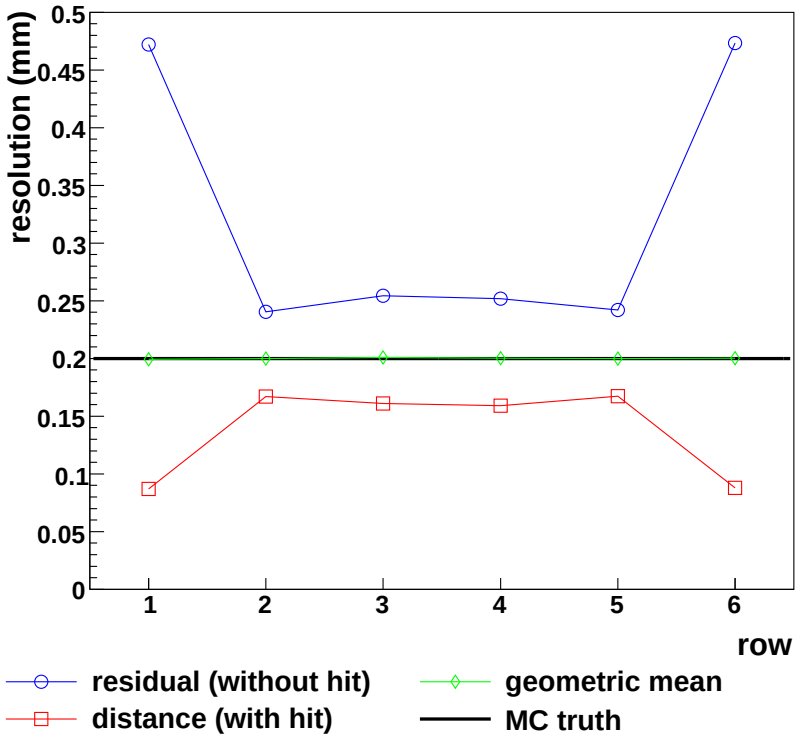

Figure 5.6: *Monte Carlo test of the Geometric Mean Method for curved tracks. The reconstructed width of the distributions of the 'distances' and the 'residuals' are shown for each row. The calculated geometric mean of 'distance' and 'residual' reproduce the Monte Carlo truth.*

for the track fit and the large lever arm of the outer rows. The behaviour in the outer rows can lead to false reconstruction of the geometric mean due to numerical problem. Therefore the outer rows are not taken into account, during the averaging over the rows.

Chapter 6

Reconstruction Methods

In this section, two methods to determine the track parameters in the xy-projection (see Section 5.1.3) are described. The first method follows the traditional approach by using a χ^2-minimisation technique to fit a circle to the reconstructed hits. The hit positions are corrected to take systematic effects caused by the Pad Response Function (PRF) into account. The second method uses a maximum likelihood technique to fit a charge expectation, determined by the track parameters, to the measured charge. Afterwards, the implementation of both methods is described.

Both methods use the same technique, based on a χ^2-minimisation-method, to determine the track parameter (I_z and θ_0) in the yz-projection. Therefore, this comparative study concentrates on results for the xy-projection.

It should be noted, that some of the results presented in this and the following chapter have been worked out in close cooperation with Ralf Diener. Part of the presented studies were part of his graduate work, which can be found in his thesis [47].

6.1 Traditional Approach: Chi Square Method

The method presented first follows a traditional approach of track reconstruction, which was used in previous experiments [51]. It is based on the reconstruction chain presented in Section 5. This chain contains the reconstruction of three-dimensional hits, a pattern recognition step to detect tracks and a fit to determine the track parameter. The fit is done using a least square minimisation of the χ^2 of the track, which gives the method its name. During this fit, the parameter $\vec{a}$ of a track hypothesis $f(\vec{x}_i, \vec{a})$, where $\vec{x}_i$ contains the coordinates of the reconstructed hit i, are varied to minimise the distances between these hits and the track:

$$\chi^2 = \sum_i \frac{(\vec{x}_i - f(\vec{x}_i, \vec{a}))^2}{\sigma_{x_i}^2} \stackrel{!}{=} \min\,, \tag{6.1}$$

where $\sigma_{x_i}^2$ denotes the error of $\vec{x}_i$ in the direction orthogonal to the track.

For the fit it is assumed that the track can be described in the yz-plane by a straight line. In this anaysis only tracks of a charged particle are investigated. They are bent by the magnetic field and can be described by a part of a circle in the xy-plane. In case of tracks produced by a laser, the trajectory of the particle is a straight line. This case is not studied in this thesis, but could be found in [48].

6.1.1 Pad Response Function

As mentioned in Section 5.1.1, the x-coordinate of a hit is given by the centre-of-gravity of the charge information taken from the localised pulses on the pads, which build the hit:

$$x_{\text{hit}} = \frac{\sum_{\text{pulses}} x_{\text{pad}} \cdot Q}{\sum_{\text{pulses}} Q}\,, \tag{6.2}$$

where x_{pad} denotes the centre of the pad.

As previous studies [31] showed, a systematic effect can influence the accuracy of the centre-of-gravity information. This effect is clearly visible in Figure 6.1 and is caused by a

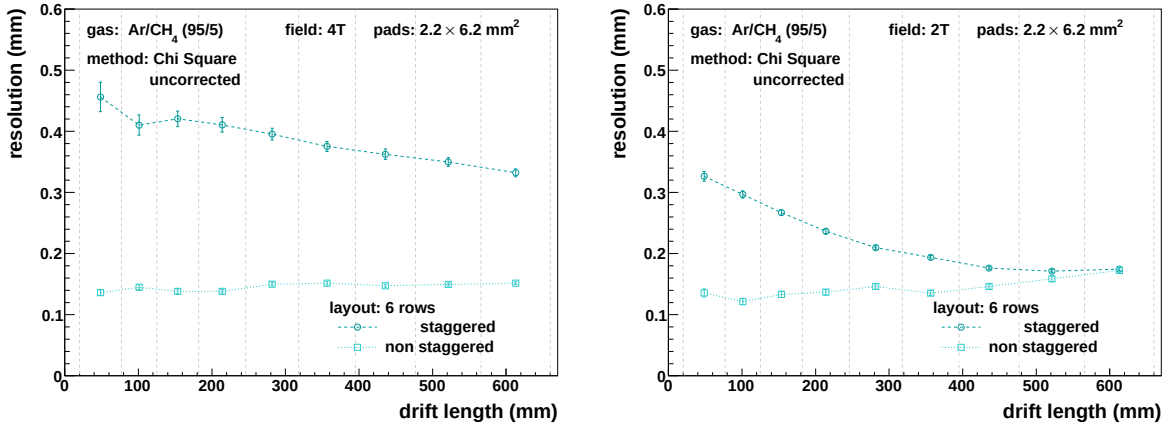

(a) 4T *(b)* 2T

Figure 6.1: *Results showing the effect of the Pad Response Function for differed pad layouts: The results for the two layouts (staggered and non-staggered) show huge differences, due to effects caused by systematic shifts in the Pad Response Function.*

non optimal ratio between the signal width and the pad width. Scince the signal width is reduced by the magnetic field (see Section 3.1.5), the ratio is worse for the data measured in high magnetic fields. In this case, the resolution determined differs significantly using different pad layouts, but the same gas.

Figure 6.2 illustrates the systematic effect. The reconstructed centre of the charge distribution differs from the true one, which is defined by the mean of the Gaussian distribution shown in the same figure. For tracks with an inclination angle $\phi = 0$, the signal can be described by a Gaussian. It is assumed that this is true also for small angles, which are investigated in this thesis. As mentioned before, the shift of the reconstructed position due to this systematic effect influences the resolution. Figure 6.3 illustrates the effect on the determination of the resolution using the Geometric-Mean-Method, which is described in Section 5.2. In the case of a staggered pad arrangement, the systematic shift is in the opposite direction for adjacent rows. Therefore the determined 'residuals' and 'distances' are larger than in the case with no shift of the hit position. This leads to a systematically larger resolution. Also using a non-staggered layout, the hit positions are shifted. But the direction is the same for all rows and the reconstructed track is shifted, too. While the particle trajectory is unknown, this leads to systematically smaller 'residuals' and 'distances'. Hence the determined resolution is artificially better than veritable. In the case without any shift of the hit positions, the

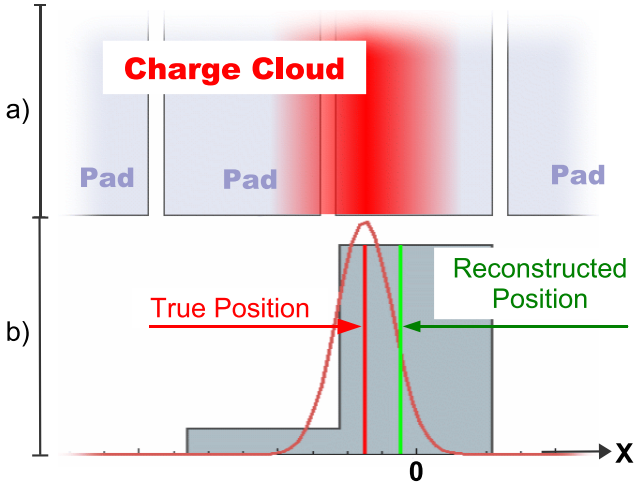

Figure 6.2: *Effect of the Pad Response Function for the reconstruction using the centre-of-gravity: The upper part a) shows the charge distribution on the pads, which follows a Gaussian distribution (shown in the lower part b)). The lower part shows additionally a binned histogram of the measured charge of each pad and the reconstructed centre-of-gravity. It can clearly be seen, that the true position given by the mean of the Gaussian and the reconstructed position differ significantly. This effect is caused by the non linear behaviour of the Pad Response Function. [47]*

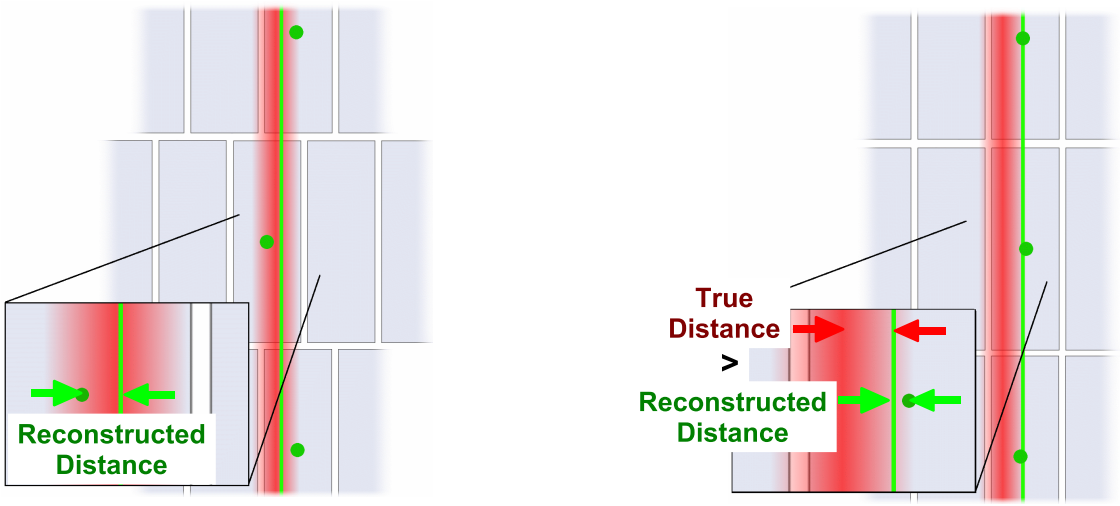

(a) staggered *(b)* non-staggered

Figure 6.3: *Sketch showing the effect of the Pad Response Function for differed pad layouts: Figure (a) shows, that in case of a staggered pad layout, the PRF causes a shift of the reconstructed hit positions in the opposite direction for adjacent rows. This leads to systematically larger residuals. In case of the non-staggered layout (Figure (b)), the shift direction is the same for all rows. Here the residuals are systematically smaller. [47]*

resolution determined for the two layouts should agree with each other. Further details can be found in Section 5.4 of [31] and Section 5.1.2 of [47].

The effect is described by the *Pad Response Function* (PRF). The PRF parametrises the signal from the pad as a function of the position of the hit on this pad. The ratio of the signal to the pad width and the lower limit of the charge which can be measured have to be taken in to account. The limit on the measured charge is defined by the thresholds applied during the pulse finding.

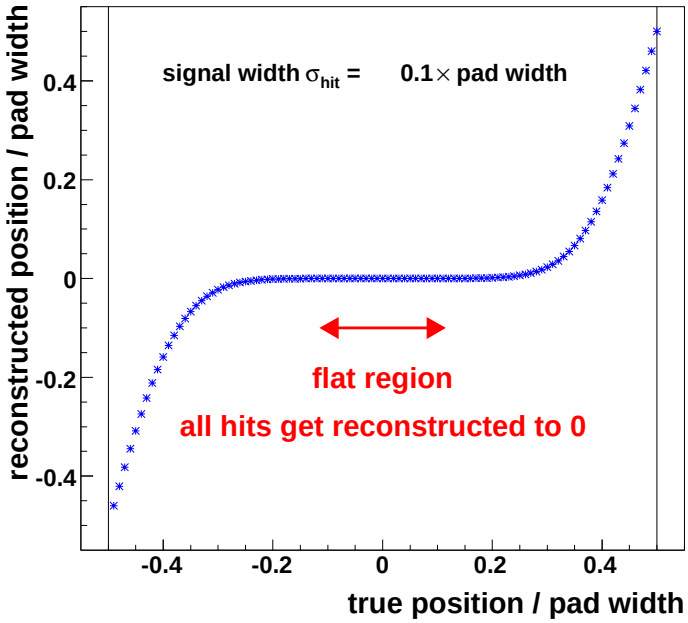

Figure 6.4: *The Pad Response Function for a Gaussian signal with a width* $\sigma_{\text{hit}} = 0.1\times$*pad width. The* x *axis shows the true position of the hit, which is given by the mean of the Gaussian distribution. The* y *axis shows the reconstructed position of the signal using the centre-of-gravity of all signals, which are above 0.1‰ of the total signal height. For universality both axis are normalised to the width of a pad. The zero denotes the middle of the pad. It can be clearly seen that for the presented signal width, the PRF shows a flat region, which is denoted by the red arrow. In this region the signal is located on only one pad and all hits will be reconstructed at* $x = 0$.

Figure 6.4 shows an example of the PRF for a signal width of 0.1×pad width. As mention before, this example assumes a track with an inclination angle $\phi = 0$. If the signal is located only on one pad, there is no indication for the centre of the signal. Therefore, the hit position is reconstructed to the centre of the pad. This can be seen as a flat region. The figure shows also that the PRF differs for this kind of signal a lot from the ideal case. In the ideal case, the reconstruction of the true position, the PRF would be a straight diagonal line.

Outside the flat region, a unique assignment of the reconstructed position and the true position seems to be possible. This means that in the case of a signal on at least two pads the systematic shift of the centre-of-gravity can be corrected. For the correction, the signal width must be known.

How this is done within the reconstruction for thsi analysis will be described in Section 6.3.1. The procedure is based on a parametrisation of the inverse PRF depending on the

signal width. This width σ_{hit} is calculated using theoretical values of the diffusion coefficient D_T and the defocussing constant σ_0 (cf. Equation (3.17)):

$$\sigma_{\text{hit}}(z) = \sqrt{D_T^2 \cdot z + \sigma_0^2}\,, \tag{6.3}$$

where z denotes the reconstructed z-coordinate of the signal. The effect of this correction is demonstrated in Section 7.2.

6.2 The Global Fit Method

The second method, which was investigated, is the so called Global Fit Method and has been proposed by Dean Karlen et al. [52]. In contrast to the traditional approach, this method does not use the pre-calculated hit positions to determine the track parameters. A maximum likelihood fit is used to fit a charge expectation to the actual charge measured on the pads.

The method does not use a row based approach, but takes the charge information of all pads into account at once. This gives the method its name. The advantage of this method is that missing or low-grade information in one row can be better compensated by the other rows. No quantitative information from outside the fit are needed to correct for PRF effects. Furthermore, it is possible with this method to determine diffusion information such as the diffusion coefficient D_T and the defocussing constant σ_0. This will be discussed in Section 7.5.

6.2.1 Principle

This method makes use of a track based model of the charge distribution of the primary ionisation. It is assumed that the radius of the circle describing the track is much larger than the pad height. Therefore, in each row the track can be described as a straight line. The density of the primary ionisation is assumed to be uniform along the row. The fluctuations of the ionisation are disregarded in this range. Due to the diffusion in the drift volume and the defocusing during the amplification (see Section 3.2.2), the distribution of the charge measured on the pad plane is assumed to be described by a two-dimensional, isotropic, Gaussian function. The width σ_{row} of the function is assumed to be constant over the height of the row. The charge expected on each pad is given by

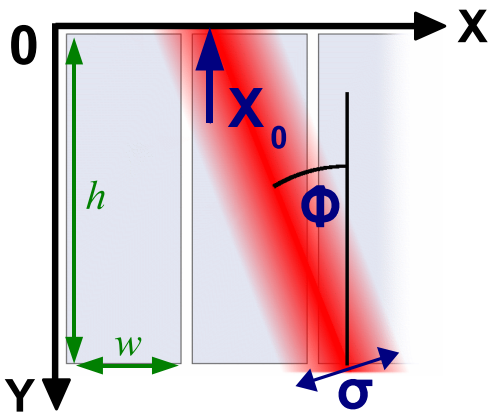

Figure 6.5: *Sketch of parameters of the likelihood function used in the Global Fit Method. [47]*

$$Q_{\text{exp}} = \int_{-h/2}^{h/2} dy \int_{-w/2}^{w/2} dx \; \frac{1}{2\pi\sigma} \times \exp\left(\frac{[(x - X_d)\cos\phi_{\text{row}} + y \sin\phi_{\text{row}}]^2}{2{\sigma_{\text{row}}}^2}\right), \tag{6.4}$$

where the integration variables x and y follow the axis of the coordinate system. The height of the pad is denoted by h and the width by w as depicted in Figure 6.5. The angle ϕ_{row} is the azimuthal angle for this row. It is given by (cf. Equation (5.1)):

$$\phi_{\text{row}} = \sin^{-1}(\sin(\phi_0) - y_{\text{row}} \cdot \kappa)\,, \tag{6.5}$$

where ϕ_0 is the angle at $y = 0$ and as usual κ denotes the curvature. The vertical centre of the pad is given by y_{row}. The horizontal distance between the centre of the pad, for which the expectation is calculated, and the track defines

$$X_d = x_{\text{pad}} - x_{\text{row}}\,, \tag{6.6}$$

where $\mathrm{x_{row}}$ denoted the track position at the vertical centre $\mathrm{y_{row}}$ of the row.

The likelihood which is to be maximised is:

$$\mathcal{L} = \prod^{i} p_i\,, \tag{6.7}$$

where p_i denotes the probability for each pad. The probability to measure the charge Q_{measured} on a pad, where the charge Q_{exp} is expected, can be described by a Poisson distribution:

$$p_i = \frac{\lambda_i^{n_i}}{n_i!} e^{-\lambda_i}\,, \tag{6.8}$$

where n_i is the measured charge Q_{measured} in units of primary electrons. The expectation value λ_i is given by Q_{exp}.

Since sums are numerically nore stable as products, instead of the likelihood itself its logarithm

$$\log \mathcal{L} = \log\left(\prod_i \frac{\lambda_i^{n_i}}{n_i!} e^{-\lambda_i}\right) = \sum_i \left(n_i \log \lambda_i - \lambda_i - \log(n_i!)\right) = \sum_i \left(n_i \log \lambda_i\right) + \text{const.} \tag{6.9}$$

is maximised. This leads to the same result, since the logarithm is a strictly monotonically increasing function. Note that $\sum n_i!$ is determined by the measured charge on the pad plane and therefore independent of the track parameters, which are varied to maximise the logarithm of the likelihood. The term $\sum \lambda_i$ is constant if we normalise the expected charge for each row. With $\lambda_i = Q_{\text{exp}}^{n,m} / \sum_{n=1}^{n_{\text{row}}} Q_{\text{exp}}^{n,m}$ the term to be maximised is:

$$\log \mathcal{L} = \sum_{m=1}^{\text{rows}} \sum_{n=1}^{n_{\text{row}}} Q_{\text{measured}}^{n,m} \cdot \log\left[\frac{Q_{\text{exp}}^{n,m}}{\sum_{n=1}^{n_{\text{row}}} Q_{\text{exp}}^{n,m}}\right]\,. \tag{6.10}$$

6.2.2 Noise Value

Events can contain noise pulses, which is illustrated in Figure 6.6. Some of these pulses would most likely not be used in the fit, if a clustering algorithm in the form of a hit and track finding method is used as in this analysis. Using Equation (6.10), the probability to measure charge far from the track trajectory is small. Noise pulses can lead to charge values that do not coincide with the likelihood for these pads.

The distribution of the noise pulses is assumed to be flat relative to the signal position. To make the fit more robust, the probability for each pad is modified by adding a constant offset N:

$$p_i \rightarrow \frac{p_i + N}{1 + N \cdot n_{\text{row}}} \tag{6.11}$$

This modification includes a renormalisation, given by the denominator. Here, n_{row} denotes the number of pads per row. The addition of the noise factor N provides a small probability for each pad to measure charge caused by noise, also far from the track trajectory.

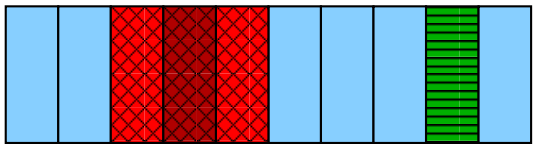

Figure 6.6: *Sketch of pad signals from a hit (three red dashed pads) and a noise pulse (one green corded pad). [47]*

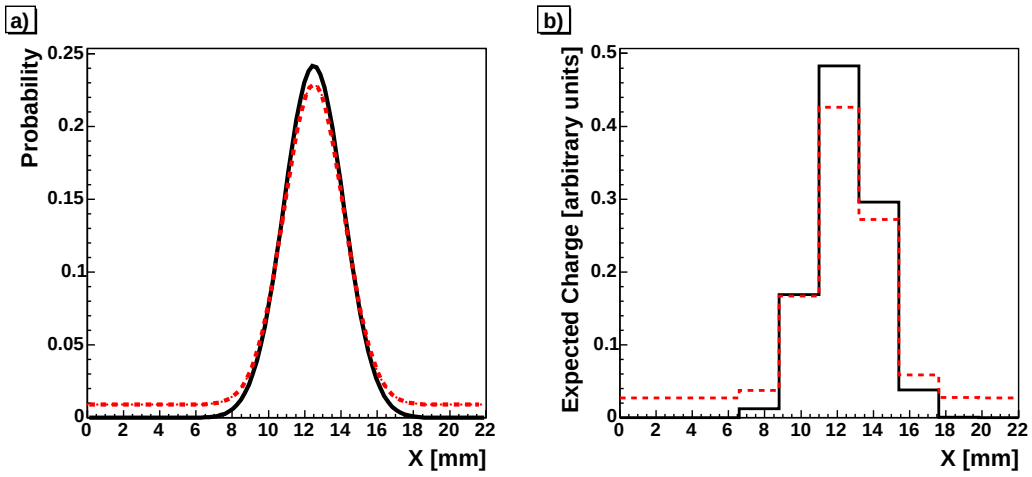

Figure 6.7: *Example for a charge distribution with (dashed line) and without noise (solid line): The distributions are shown as a function (a) and a binned histogram (b), which is similar to the case of a measurement using pads. For the noise effected distribution the noise was set to be 1%. [47]*

Figure 6.7 demonstrates the effect of adding the constant noise term. The probability function for a Gaussian signal and the same signal with a constant term of 1% are shown. To demonstrate the effect on the probability of each pad, the same functions are shown as a binned histogram, where each bin contains the probability integrated between the borders of the bin.

The change of the probability for each pad leads to the following likelihood function:

$$\log \mathcal{L} = \sum_{m=1}^{\text{rows}} \sum_{n=1}^{n_{\text{row}}} Q^{n,m}_{\text{measured}} \log \left[\left(\frac{Q^{n,m}_{\text{exp}}}{\sum_{n=1}^{n_{\text{row}}} Q^{n,m}_{\text{exp}}} + N \right) \Big/ \left(1 + \sum_{n=1}^{n_{\text{row}}} N \right) \right] . \tag{6.12}$$

6.2.3 Calculation of the Hit Position, Residual and Distance

As mentioned in Section 5.2, the two values 'residual' and 'distance' are needed to calculate the resolution. Because the Global Fit Method does not operate with pre-calculated hit positions, the x-coordinates of the hits are recalculated by a modified fitting procedure. Afterwards, the

two values are determined using this coordinates. In the case of the calulation of the 'residual' a refit is done. The procedure is decribed in the following.

The x-coordinates of the hits are determined by redoing the fit using only the pulses that are assigned to the hit which position is to be recalculated. During this fit, only the intercept I_x is varied. The other parameters ϕ_0, κ and σ_0 are fixed to the values, which have been determined by the fit to all pulses of the track. The new hit coordinate is given by the track trajectory of the refit at the vertical centre of the row of the hit (cf. Equation (6.16)). In the case of a single pulse hit, no refit is done. The coordinate remains at the value calculated during the cluster finding, which is given by the centre of the pad.

Using this new hit coordinate, the 'distance' is calculated as described in Section 5.2 on page 44. The track trajectory determined by the fit to all pulses.

To ascertain the 'residual', a second track fit is needed. This fit does not use the information of the hit, for which the 'residual' is calculated. This means that the likelihood fit is redone with all pulses except the pulses belonging to the mentioned hit. For the refit, the width σ_0, which sets σ_{row}, is fixed to the value determined by the fit to all pulses. In the case that σ_0 is given by the steering file, this value is used. All other track parameters are free and redefined by the new fit. However, the hit coordinate is not recalculated once more using the this new track parameter. Instead, the hit coordinate is used which was determined for the 'distance' calculation.

This procedure is very similar to the one described in [52].

6.3 The MultiFit-Implementation

In this section, the MultiFit-implementation of both methods will be presented.

6.3.1 Implementation of the Chi Square Method

For the tracks, the χ^2 is defined and minimised separately for the two projections:

$$\chi^2_x = \sum \frac{\left(x_i - \left(\sqrt{(\kappa^{-2} - (y_i - y_0)^2)} + x_0\right)\right)^2}{\sigma_{x_i}} \tag{6.13a}$$

$$\chi^2_z = \sum \frac{(z_i - (I_z + y_i \cdot \tan(\theta_0)))^2}{\sigma_{z_i}} \tag{6.13b}$$

It can be seen that the y coordinates of the hits, which are given by the centre of the row of the hit, are assumed to be errorless. Only the errors σ_{x_i} and σ_{z_i} are taken into account. In the case of the straight track hypothesis the minimisation is done analytically. The parameters are calculated from of the given values for z_i and σ_{z_i}. For the curved trajectories, the parameters $\vec{a} = (x_0, y_0, \kappa)$ are determined numerically using the 'Minimise' command of the Minuit framework [53] which is embedded into the framework ROOT [45]. The used procedure is a combination of the Mirgad and the Simplex algorithm.

The Pad Response Function Correction

In this implementation the parametrisation of the inverse PRF neglects the angular dependency of the PRF. The consequences and limitations of this assumption are discussed in Section 7.4.3.

First, the PRF is calculated for various signal widths using a toy simulation. It is assumed, that the signal in one row can be described by a Gaussian distribution. This is true only for tracks with an inclination angle of the track is $\phi = 0$. For each signal width, the signal on the pads in one row is simulated for various signal positions on the pad. The hit position is reconstructed using Equation (6.2). Here, a threshold of 0.1‰ of the total signal height is applied. This means that all pads with a charge below this threshold are not used for the reconstruction. The choice of the threshold value is justified by the result of the correction procedure which is presented later (see Figure 7.2 on page 64). The influence of changing this value should be studied.

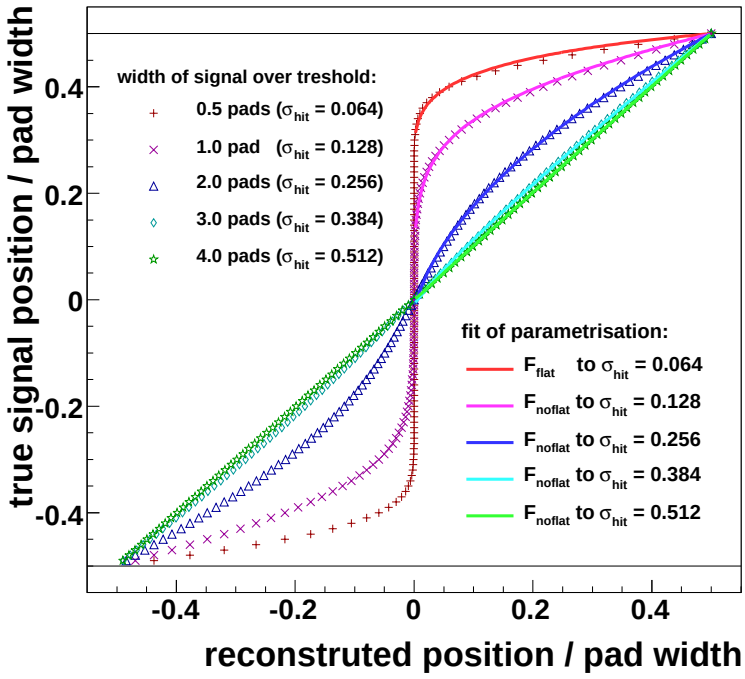

Figure 6.8: *The Pad Response Function Correction for relevant signal widths: The signal width of $\sigma_{\text{hit}} = 0.128\times$pad width corresponding to a width of the signal over the 0.1‰ threshold. This means that for every hit position two pads are active. For lower signal widths the PRF contains a flat region. If more than 5 pads are active (width of signal over threshold of at least 4 pads) the PRF and the PRF correction become a straight line.*

In a second step, the calculated PRFs are inverted. Figure 6.8 shows some examples of the inverse PRFs for different signal widths. One of the extreme cases is a width of the signal distribution σ_{hit} of 0.128×pad width. This width of the Gaussian leads to a width over threshold (0.1‰) which is equal to the width of one pad. This means that for every hit position on the pad, at least two pads are active. Therefore, the PRF for a signal width $\sigma_{\text{hit}} > 0.128\times$pad width shows no flat region. A second value for σ_{hit} which is of interest is 0.512×pad width. In this case, the signal is located on at least 5 pads and no correction is needed, because the PRF describes a straight diagonal line.

Two different functions are fitted to the inverted PRFs. One is modelled to describe the

flat region of the PRF, which leads to an offset in the inverse PRF. The other function is forced to go through the origin and is able to describe the ideal PRF, which is defined as a straight line:

$$F_{\text{noflat}}(x) = P_1 x + P_2 \cdot \sqrt{x} + \left(\frac{1 - P_1}{2} - \frac{P_2}{\sqrt{2}} \right) \cdot \sqrt[3]{2x} \tag{6.14a}$$

$$F_{\text{flat}}(x) = P_0 + P_2 \cdot \sqrt{x} + \left(\frac{1 - 2P_0}{2} - \frac{P_2}{\sqrt{2}} \right) \cdot \sqrt[3]{2x}\,, \tag{6.14b}$$

where P_0, P_1 and P_2 are fitting parameters and x denotes the x-coordinate in reference to the pad centre. Because the functions are odd, they are only fitted in the positive domain (see Figure 6.8). It should be pointed out, that these functions are not motivated by any physical meaning, but by describing the inverse PRF with a minimal set of parameters.

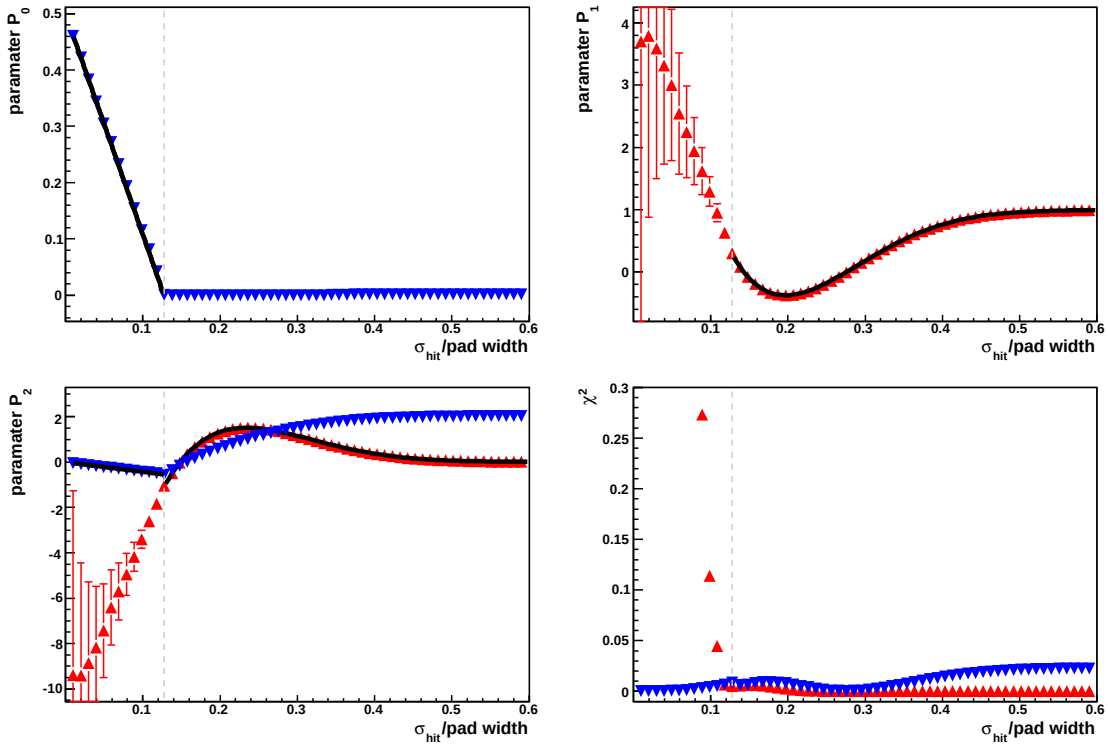

Figure 6.9: *Parameter P_0, P_1, P_2 and χ^2 value of the functions F_{noflat} (red triangles pointing up) and F_{flat} (blue triangles pointing down): The functions are defined in Equations (6.14). The displayed values are derived from fits to PRFs with different signal widths (normalised to pad width). The figures also show the functions (Equations (6.15)) fitted to the parameter values. The grey dashed horizontal line represents the border between PRFs with and without a flat region.*

The resulting parameters P_0, P_1 and P_2 for various signal widths σ_{hit} are shown in Figure 6.9. The change of PRFs with and without a flat region at $\sigma_{\text{hit}} = 0.128\times$pad width is shown as a horizontal line. As expected, the parameter P_0, which describes the length of the flat region, is zero for larger values of σ_{hit}. Also, the other parameters show a change of the behaviour (slope or size of the error) at this point. As mentioned before, a second important point is given by $\sigma_{\text{hit}} = 0.512\times$pad width. Above this value, the following is valid for the

parameter of F_{flat}: $P_1 = 1$ and $P_2 = 0$. In this case the function F_{flat} describes a straight line, which indicates that no correction is needed.

To implement the PRF correction, it is necessary to describe the parameters P_0, P_1 and P_2 in dependence on σ_{hit}. Therefore the following functions are used:

$$P_{0,\text{flat}}\ (\sigma_{\text{hit}}) = a_{01} \cdot \big((1 - \sigma_{\text{hit}})/a_{00}\big) \tag{6.15a}$$

$$P_{1,\text{noflat}}(\sigma_{\text{hit}}) = a_{15}\sigma_{\text{hit}}^5 + a_{14}\sigma_{\text{hit}}^4 + a_{13}\sigma_{\text{hit}}^3 + a_{12}\sigma_{\text{hit}}^2 + a_{11}\sigma_{\text{hit}} + a_{10} \tag{6.15b}$$

$$P_{2,\text{flat}}\ (\sigma_{\text{hit}}) = a_{26}\sigma_{\text{hit}} \tag{6.15c}$$

$$P_{2,\text{noflat}}(\sigma_{\text{hit}}) = a_{25}\sigma_{\text{hit}}^5 + a_{24}\sigma_{\text{hit}}^4 + a_{23}\sigma_{\text{hit}}^3 + a_{22}\sigma_{\text{hit}}^2 + a_{21}\sigma_{\text{hit}} + a_{20} \tag{6.15d}$$

To determine the values of a_i, the functions are fitted to the parameters depicted in Figure 6.9. The functions labelled with 'flat' are only fitted in the region $\sigma_{\text{hit}} =]0, 0.128] \times$pad width. The other, labelled with 'no flat' are fitted to the values above $0.128 \times$pad width. The resulting curves are shown in Figure 6.9. The parameters a_i are summarised in Table 6.1.

Func.	**Parameters**					
$P_{0,\text{flat}}$	a_{01}	a_{00}				
	0.49900	0.12800				
$P_{1,\text{noflat}}$	a_{15}	a_{14}	a_{13}	a_{12}	a_{11}	a_{10}
	−832.538	1936.17	−1739.82	739.665	−141.994	9.52257
$P_{2,\text{flat}}$	a_{26}					
	−4.21678					
$P_{2,\text{noflat}}$	a_{25}	a_{24}	a_{23}	a_{22}	a_{21}	a_{20}
	1398.15	−3350.91	3126.27	−1399.78	292.479	−21.2726

Table 6.1: *Values of the function parameters for the Pad Response Function Correction $P_{k,(\text{no})\text{flat}}$ implemented in* MultiFit.

During the correction, the above procedure is reversed. First, the width of the hit σ_{hit} is calculated using the reconstructed z-coordinate of the hit and Equation (6.3). The theoretical values of diffusion coefficient D_T and defocussing constant σ_0, which are used in this calculation, are summarised in Table 6.2. Knowing the signal width, the correction function (F_{flat} or F_{noflat}) is chosen. The parameters P_i are calculated using Equations (6.15) and Table 6.1.

B	**Ar/CH$_4$ (95/5)**		**Ar/CH$_4$/CO$_2$ (93/5/2)**	
	D_T^2 (mm)	σ_0^2 (mm^2)	D_T^2 (mm)	σ_0^2 (mm^2)
1 T	0.002457	0.2277	0.003411	0.1422
2 T	0.000724	0.1899	0.001150	0.1102
4 T	0.000192	0.1404	0.000309	0.0708

Table 6.2: *Diffusion parameters for different gases used in* MultiFit*: The diffusion coefficient ${D_T}^2$ and defocussing constant ${\sigma_0}^2$ for Ar/CH_4 (95/5) and $Ar/CH_4/CO_2$ (93/5/2) and for magnetic fields between 1 and 4 T are presented. These values are calculated with the program GARFIELD [21] version 9. (see Table 3.2)*

With the coordinate x_{COG} reconstructed using the centre-of-gravity of the hit which is defined by Equation (6.2), the corrected coordinate $x = F_{(\mathrm{no})\mathrm{flat}}(x_{\mathrm{COG}})$ is determined. The error of the hit is recalculated from the slope of the correction function at the position x_{COG} and its error using Gaussian error propagation. Hits with only a single pulse are not corrected. Their position is set to the middle of the pad and the error is given by $\sigma_{x_i} = \frac{w}{\sqrt{12}}$, where w denotes the width of the pad.

6.3.2 Implementation of the Global Fit Method

The Global Fit Method was first implemented in a simulation and analysis package called JTPC [54], developed by the Dean Karlen et al who proposed this method. It has been adapted and implemented in the program MultiFit, which is used for the presented studies.

In the original implementation no pattern recognition, e.g. hit and track finding, is done. The fit works directly on the charge information of all pulses found in one event. Hence it should be pointed out that the implementation in MultiFit works on the pulses assigned to one track via the found hits. Although, the reconstructed hit coordinates are not used in the fit, they are used to determine the start parameter for the fit. Due to the pattern recognition before the fit, the MultiFit-implementation provides a better handling of multi track events and pulses caused by noise. The effect of hits caused by noise will be discussed later in Section 7.3. If events contain more that one track they can be fitted separately, if the distance in z- or x-direction between them is big enough. If this is not the case, MultiFit provides also the possibility to fit the tracks together, as presented in [48]. In this analysis, only one track events are taken into account.

To determine the expected charge for each pad using Equation (6.6), the track position x_{row} at the vertical centre of the row y_{row} is needed. This position is calculated using the following approximation:

$$x_{\mathrm{row}} = I_x + y_{\mathrm{row}} \cdot \tan(\phi_0) + \frac{y_{\mathrm{row}}^2 \cdot \kappa}{2\cos(\phi_0)^3} + \frac{y_{\mathrm{row}}^3 \cdot \kappa^2 \tan(\phi_0)}{2\cos(\phi_0)^4} \tag{6.16}$$

Additionally the signal width for σ_{row} for each row is needed. Three possibilities to determine this parameter are implemented in MultiFit:

- If no information describing the expected diffusion is given, σ_{row} is assumed to be constant over the hole track length: $\sigma_{\mathrm{row}} = \sigma_0$. In this case, σ_0 is a free parameter which is fitted together with the other track parameters.

- If the diffusion coefficient D_T is given[1], the width assumed for each row varies. It is calculated from the z position of the hit in that row (see also Equation (6.3)):

  $$\sigma_{\mathrm{row}} = \sigma_{\mathrm{hit}}(z) = \sqrt{D_T^2 \cdot z + \sigma_0^2}$$

  Here σ_0 is still a free parameter, which is determined during the fit.

- In the third case, the diffusion information is completely determined by setting the defocussing constant σ_0. Here, the width σ_{row} is fixed and the fit has one free parameter less. This case is comparable to the Chi Spare Method, where the width of the hit is needed to correct for the PRF effects.

[1] by the steering file

To take the statistics of the primary electrons into account, the measured charge Q_{measured} must be given in units of primary electrons. The factor for conversion of ADC-counts into primary electrons is given by the steering file. It is composed by the gain of the amplification structure and the electronics which record the signal.

If the initial fit or one of the other fits, which are performed to calculate hit coordinates and residuals, fails the whole track will not be stored.

Chapter 7

Performance of the Reconstruction Methods

The two methods presented in the last chapter were tested with simulated events and data measured using cosmic muon. The measuring setup and the simulation are described in Chapter 4. Studies of systematic effects are presented for both methods. These include the effect of not working channels and angular dependencies.

7.1 Introduction

The testing of the methods using Monte Carlo generated data provides the advantages of a controllable environment and the information of the true track position. To determine the resolutions the Geometric Mean Method is used, which is described in Section 5.2.

7.1.1 Handling of Simulated Data

The sets of simulated data are presented on page 38 in Table 4.2. Only data using a staggered pad layout was simulated. As it is shown in Figure 6.1 this choice provides a prominent and clearly visible effect caused by systematic shifts. This allows to test the methods in the most extreme case. To make the simulated data more realistic, noise is generated. It is described by integers following a Gaussian distribution with a width of one ADC count and a mean of zero.

As mentioned in Section 4.2 the simulated data sets are generated for a pad layout with 19 rows. It provides a better ratio between the parameters which are varied during the fitting procedure and the number of the hits of the track. This leads to a more stable environment for the fits.

In addition, to investigate a setup as close as possible to the one used during the data taking, which provides six usable rows only, the middle rows of the 19 row sets are used. The middle rows are chosen, because the position of the scintillator trigger, which are also simulated, must be taken into account. To ensure the same staggering, the first seven rows and last six rows are ignored. This is done by excluding the corresponding channels from the mapping in the MultiFit steering file.

In contrast to the measured data, all channels are working in the simulated data. Hence, the methods can be tested with this ideal scenario. Additionally, the effect of damaged pads

was investigated by deactivating designated pads via the MultiFit steering file. The outcome is presented in Section 7.4.2.

7.1.2 Cuts

If not explicitly mentioned, the following cuts are applied during the analysis of measured and simulated data: To ensure a high quality of the track, it must contain a hit in every row. Depending on the set used, this means six or 19 hits for each track: $n_{\text{hit}} = n_{\text{row}}$. This cut is applied during reconstruction. As mentioned before, this analysis concentrates on events with exactly one reconstructed track: $n_{\text{track}} = 1$. Furthermore, all the hits of a track must be located in the central region of the readout: $6.6\,\text{mm} < x_{\text{hit}} < 47.3\,\text{mm}$. This condition excludes tracks with hits reconstructed in the outer three columns on each side. Some part of these hits could be missing or the hit is influenced by crosstalk from the surrounding shielding (see Section 4.1.4).

In addition, two cuts are applied to the inclination angle in the yz-plane $|\theta_0| < 450\,\text{mrad}$ and the curvature $|\kappa| < 0.02\,\text{mm}^{-1}$ of the track. The last cut rejects outliers, where the reconstruction may fail. The cut on the inclination angle in the xy-plane is discussed in more detail in Section 7.4.4. It is applied to the angle of each hit given by Equation (5.1): $|\phi_{\text{hit}}| < 100\,\text{mrad}$.

cut	**number of events**		
no cut	14000	100.0%	
$n_{\text{track}} == 1$	13982	99.8%	99.8%
$6.6\,\text{mm} < x_{\text{hit}} < 47.3\,\text{mm}$	11729	83.8%	83.8%
$\lvert\theta_0\rvert < 450\,\text{mrad}$	10141	72.4%	86.5%
$\lvert\kappa\rvert < 0.02\,\text{mm}^{-1}$	10127	72.3%	99.9%
	$\boldsymbol{n}_{\text{hit}} = \boldsymbol{n}_{\text{track}} \cdot \boldsymbol{n}_{\text{row}}$		
	60762	72.3%	
$\lvert\phi_{\text{hit}}\rvert < 100\,\text{mrad}$	50321	59.9%	82.8%

Table 7.1: *Cut flow for the analysis of the resolution: The table displays the cut flow for the data set measured at the following settings: 4 T, Ar/CH_4 (95/5) , staggered pad layout. The first percentages denote the total amount of events left from the number without cuts. The second denote the reduction from the cut before.*

Table 7.1 shows a typical cut flow for the data measured using a staggered pad layout, a magnetic field of 4 T and Ar/CH_4 (95/5). Figure 7.1 presents the distribution of the cut variables for the same data set. The selected events are indicated. During the measurement of the presented data set, three pads were not working. In combination with the requirement of the maximum possible number of hits per track, this explains the dips in the distribution of x_{hit} (Figure 7.1(b)). If the signal width is small, it is possible that only one pad is hit in a row. If in addition this pad is not working, no hit is reconstructed in this row and no track using the full number of rows can be found. Additionally, the table and the Figure 7.1(d) show that, as mentioned before, the cut on the curvature κ rejects only a few events which are mainly far from typical values.

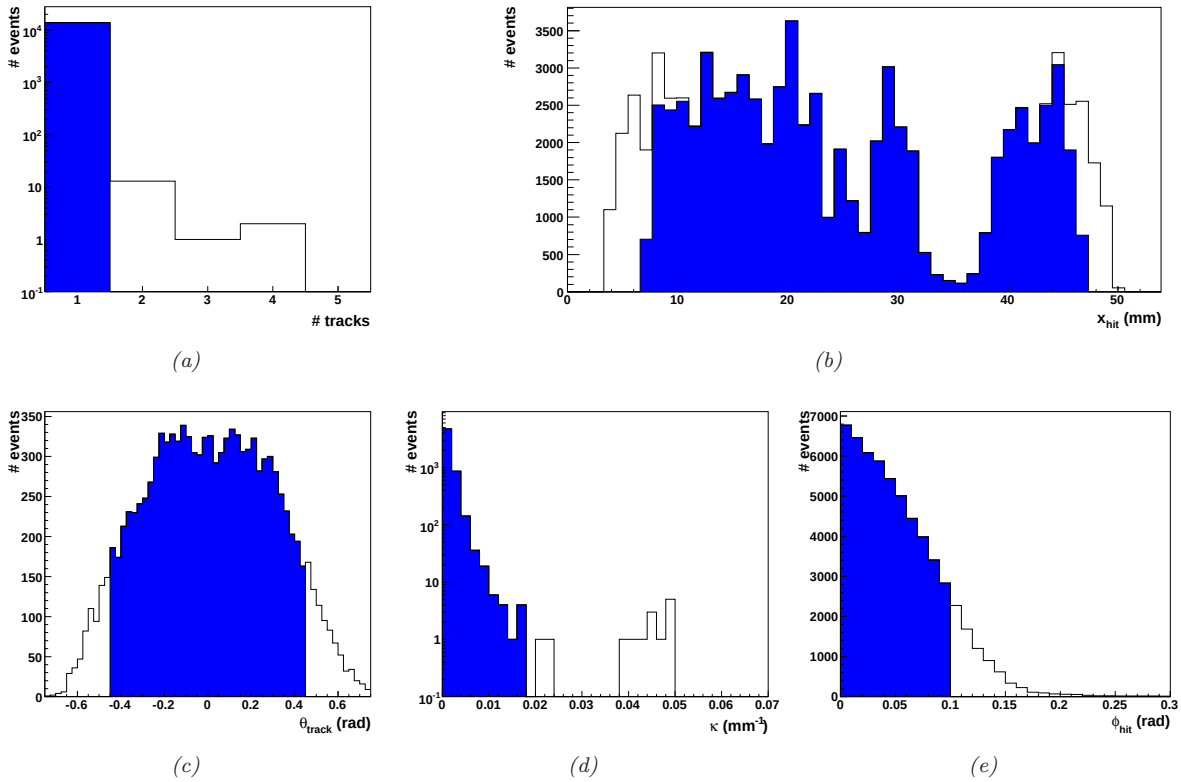

Figure 7.1: *Cut flow for the analysis of the resolution for the data set measured at the following settings: 4 T, Ar/CH_4 (95/5) , staggered pad layout. The figures display the distribution before the cut on the variable which is shown. The selected region is indicated by the blue solid filling.*

7.2 Effect of the PRF Correction used in the Chi Square Method

Figure 7.2 shows the effectivity of the correction algorithm which is described in Section 6.3.1. The mean deviation of the reconstructed and the corrected hit positions from the Monte Carlo truth, known from the MC generation, are plotted. It is clearly visible that the deviation of the corrected hit position is much smaller. The accuracy and the limitation of this correction method for the determination of the spatial resolution, will be discussed in Section 7.4.1.

7.3 The Choice of the Noise Value for the Global Fit Method

As MultiFit performs clustering before the track fitting, it is obvious to assume, that no noise correction is needed and the noise factor can be set to $N = 0$. A detailed study of the influence of the noise value N showed that this is not the case. Details can be found in Section 5.2.3 of [47]. There, among others, the fit efficiency for five different noise values is studied. Only the following cases are investigated:

- The diffusion coefficient D_T is set to 0 and the defocussing constant σ_0 is free
- The diffusion coefficient D_T is set by the steering-file and the defocussing constant σ_0 is

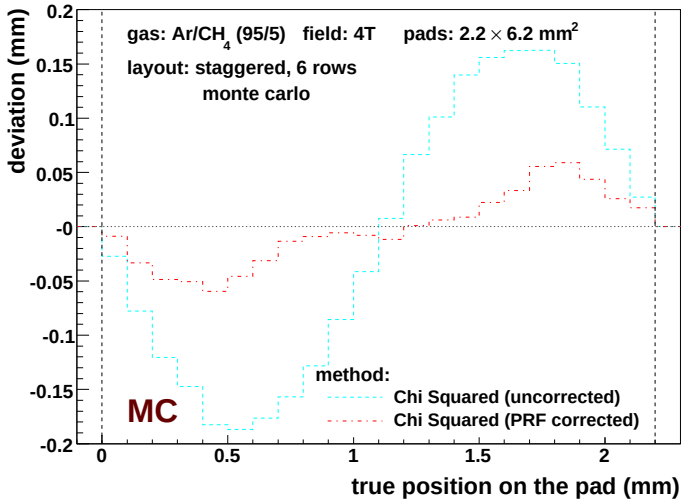

Figure 7.2: *Effect of PRF correction for the deviation of the reconstructed hit position from the MC truth: The mean deviation is shown in dependency of the true hit position given by the MC information. The two vertical dashed lines mark the borders of the pad. It has a width of 2.2 mm. The deviation for the corrected hit positions are much smaller then the uncorrected one. This shows the effectivity of the PRF correction.*

fixed

Noise Factor N	D_T given, σ fixed	D_T= 0, σ free
0.0500	80.9	43.6
0.0100	81.3	68.1
0.0010	82.5	84.0
0.0001	83.2	91.7
0.0000	82.3	100.0

Table 7.2: *Global Fit Method: Percentage of fitted tracks relative to the biggest number (18496) as a function of the noise factor. [47]*

The results are shown in Table 7.2. For the case where the diffusion coefficient D_T and the defocussing constant σ_0 are given, the efficiency varies only little and is above 80%. In the case where a defocussing constant σ_0 is a free parameter and the diffusion coefficient D_T set to zero, the efficiency is decreasing with an increase of the noise value.

Additionally, the studies mentioned above showed the resolution determined using different noise factors. In this study the results for the two cases match best for a noise factor of $N = 1\%$.

Concluding, it turned out that the noise value of 0.0 is not the best value, as it was naively expected. This can be explained with a little noise still present in the data after the pedestal subtraction and the clustering. In the following a noise factor of $N = 1\%$ will be used. Further advantages of this choice are the comparability of the results with Dean Karlen et all, who use the same value in the JTPC implementation.

7.4 Comparison of the Different Reconstruction Methods

In the following, four different methods and variation of settings are investigated:

- Chi Squared Method with PRF correction.
- Global Fit Method with the diffusion coefficient D_T set to 0 and the defocussing constant σ_0 as a free parameter.
- Global Fit Method with the expected diffusion coefficient D_T given and the defocussing constant σ_0 as a free parameter.
- Global Fit Method with the expected diffusion coefficient D_T given and the defocussing constant σ_0 fixed to the predicted value.

The values for the diffusion coefficient D_T and the defocussing constant σ_0 used for the Global Fit Method are the same as used for the PRF correction during the Chi Square Method. They are summarised in Table 6.2 on page 57.

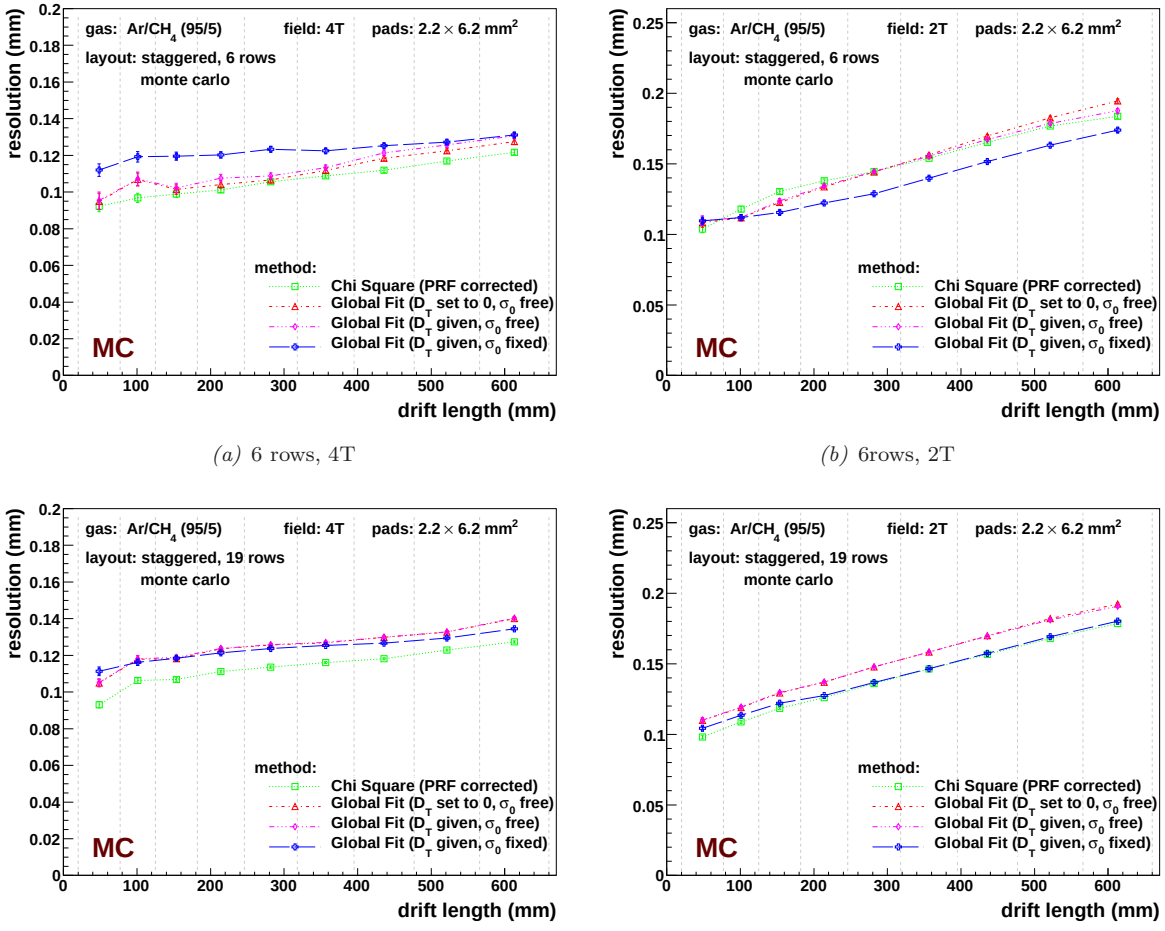

(a) 6 rows, 4T

(b) 6rows, 2T

(c) 19 rows, 4T

(d) 19 rows, 2T

Figure 7.3: *Comparison of different reconstruction methods using MC generated data: Two different layout were used, both using a staggered arrangement of pads, one with six rows (similar to the layout used during the measurement) and the other with 19 rows. The results for two magnetic fields (2 T and 4 T) are presented.*

The results using simulated data are shown in Figure 7.3. In general, the resolution measured with a magnetic field of 2 T shows a stronger dependency on the drift length. This can be easily understood, by comparing the defocussing inside the amplification structure and the diffusion in the chamber of the two cases. Table 7.3 shows the broadening of the signal due

B	σ_0 (cm)	$D_T \times \sqrt{z}$ (mm)	
		$z = 100\,\text{mm}$	$z = 500\,\text{mm}$
2 T	0.436	0.269	0.601
4 T	0.375	0.139	0.311

Table 7.3: *Comparison of the effect of diffusion and defocussing for two different drift lengths and magnetic fields. The numbers shown refer to Ar/CH$_4$ (95/5) .*

to diffusion in Ar/CH$_4$ (95/5) for two drift lengths (100 mm and 500 mm) in comparison to the broadening due to the defocussing of the signal. In the case of a magnetic field of 4 T, the effect of the defocussing dominats for both drift distances, which leads to a smaller dependence of the resolution on the drift length. But for a magnetic field of 2 T, the diffusion for large drift distances is larger than the defocussing. For shorter drift distances, the defocussing dominates. This explains the stronger dependency. Furthermore, the broader signal at 2 T leads to more active pads per row. This ensures a more reliable reconstruction.

For all tested sets the two variations of the Global Fit Method, with σ_0 as a free parameter show similar results. The two variations differ in the information of the diffusion coefficient D_T: One makes use of the theoretical prediction for D_T, while for the other it is assumed that $D_T = 0$. This leads to the conclusion, that the signal width σ_{row} varies only slightly from row to row. Due to the θ_0 cut, the difference Δz between the part of the track with the shortest drift length to the one with the longest is limited:

$$\Delta z = y_{\max} \cdot \cos(\max(\theta_0)) = 6 \times 6.2\,\text{mm} \cdot \cos(0.45) = 33.5\,\text{mm}$$

Taking this maximal difference into account, it can be easily deduced from Table 6.2 that the defocussing is at least one order of magnitude larger than the difference in diffusion for one track. Also for the other presented studies, the two mentioned variations produce very similar results. Therefore, from these two variations, only the one with $D_T = 0$ is discussed further. This choice make use of as few predictions as possible.

Comparing the remaining methods, the outcomes for the two investigated magnetic fields differ. For a magnetic field of 2 T, the Global Fit Methods with σ_0 as a free parameter shows larger values for the resolution than the Global Fit Method with a fixed σ_{row} (by given the diffusion coefficient D_T and the defocussing constant σ_0). This behaviour is visible for the two investigated layouts with six and 19 rows. The Chi Squared Method agrees with the Global Fit Method with a fixed σ_{row} for 19 rows. In the case of the six row layout, the results of the Chi Squared Method are simular to those of the Global Fit Methods with σ_0 as a free parameter.

In the case of the higher magnetic field of 4 T, the results for 19 and six rows are not compatible for the two variations of the Global Fit Method using σ_0 as a free parameter. For the tests with the 19 row layout, Figure 7.3(c) shows an agreement with the Global Fit Method using a fixed σ_{row}. In contrast, the results which are determined using a layout with six rows (Figure 7.3(a)) show, for short drift distances, an agreement with the Chi Square

Method and for large drift distances with the other variation of the Global Fit Method. The conclusion can be drawn, that the limited number of rows and the additional free parameter σ_0 makes the fit less stable.

The results for the Global Fit Method with fixed σ_{row} shows an agreement between the six and 19 rows layouts for the two magnetic fields. In the case of a magnetic filed of 4 T, it provides the most conservative estimation in comparison with the other methods. Therefore, this method will give an upper limit on the resolution. On the other hand, the Chi Squared method shows the best results for the same magnetic field. In the next section, it will be shown that the Chi Squared Method shows less deviations between staggered and non-staggered layouts than the Global Fit Methods using a fixed σ_{row}. Both methods agree only in the case of a magnetic field of 2 T and 19 rows, which provides the best fit condition via a better ratio between signal width and pad width and a larger number of points.

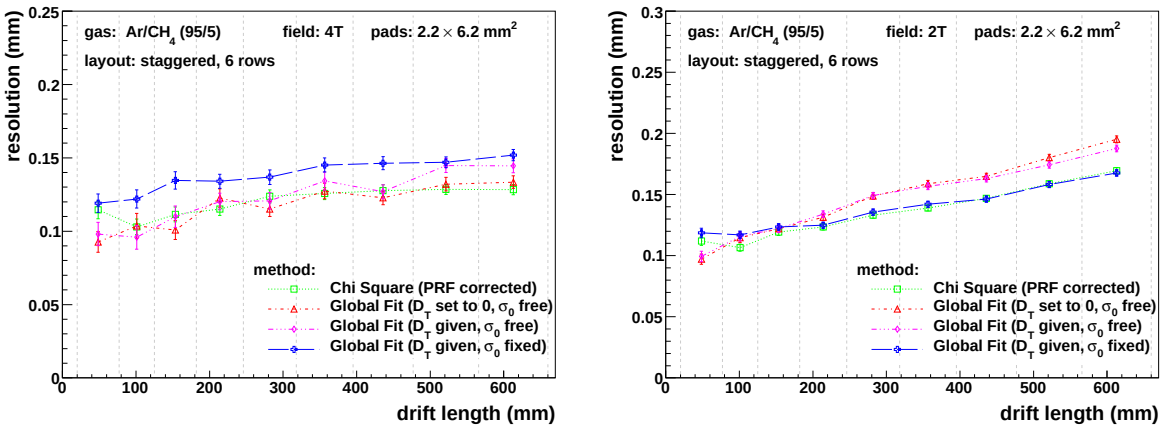

(a) 4T *(b)* 2T

Figure 7.4: *Comparison of different reconstruction methods using measured data: The results for magnetic fields of 2 T and 4 T are shown for comparison with the results presented for simulated data (Figure 7.3). Both are determined out of data measured with a staggered pad layout using six rows.*

The results of the study of the measured data are summarised in Figure 7.4. For comparability with the simulated data, the results for the same gas mixture and pad layout are shown. As mentioned before, only six rows are usable in the measured data. All methods show stable results for a magnetic field of 2 T. But in contrast to the case of simulated data, the same Chi Spare Method agrees with the Global Fit Method with a fixed σ_{row}. The case of 4 T is more important with reference to the proposed detector parameter (see Section 2.2.1). The results for this case are very similar to the one determined with simulated data. Due to the smaller number of events, the instability of the both variation of the Global Fit Method using σ_0 as a free parameter is more clearly visible. The instability leads also to larger errors than for the two other methods.

The values determined by the methods differ between measured data and simulated data. The difference is of the order of 5% for 2 T and 10% for 4 T. It can be explained by the absence of crosstalk, the simple simulation of the electronic noise, and that the simulated data contains only straight tracks (see Section 4.2), which are fitted using a curved hypothesis. This leads

to smaller deviations between hits and tracks which results in a too optimistic estimation of the resolution. As presented in Section 7.4.2, the influence of non working pads is small for the both methods which use the diffusion coefficient D_T and the defocussing constant σ_0 . For the presented studies, the reproduction of the more general behaviour of the method and their differences is most important. In that sense, the agreement between simulated and measured data is sufficient.

All investigated methods show the expected dependency on the drift length. This dependency is much stronger in the case of a magnetic field of 2 T, which is due to the larger diffusion. Nevertheless, the methods do not agree with each other. Some of the discrepancies can be explained by the fit conditions. It tured out, that the number of free parameter has an influence. Further, the width of the signal affects the results which can be seen by comparing the results for the different magnetic fields. This impact is closely related to the possibility to correct PRF effects. This is presented in the next section.

7.4.1 Limitation of the PRF Correction due to the Pad Size

The possibility to correct the systematic shifts caused by the PRF (see Section 6.1.1) is limited. In the case of a very small signal width in comparison to the pad width, only one pad contains the signal and no correction is possible. This is most often the case for a magnetic field of 4 T, which limits the broadening due to diffusion. Therefore, here the limitation of the correction can be studied best. The important limits on the signal width are discussed quantitatively in Section 6.3.1.

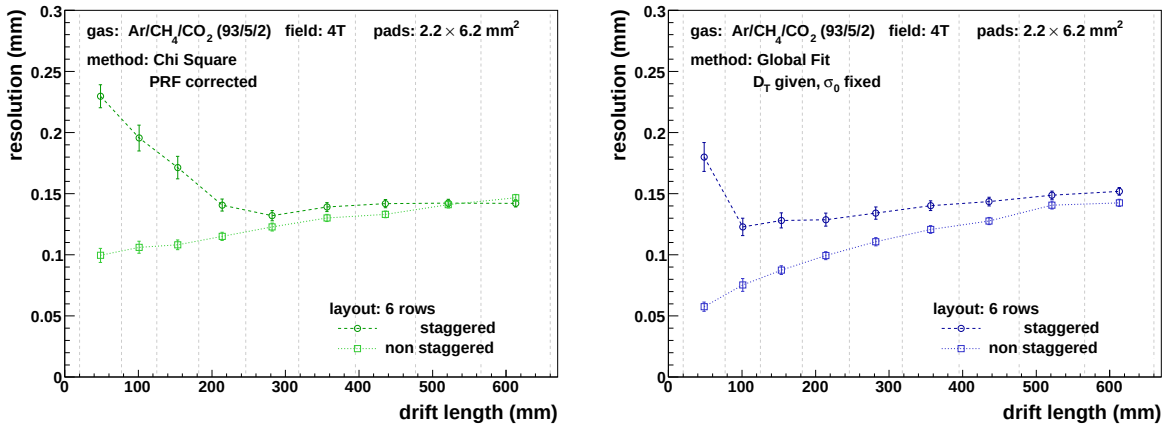

(a) *(b)*

Figure 7.5: *Comparison of different layouts for measured data using $Ar/CH_4/CO_2$ (93/5/2) and with a magnetic field of 4 T: It is clearly visible, that both methods (Chi Square with PRF correction and Global Fit with σ_{row} fixed by given values for D_T and σ_0) produce different results for the two layouts (staggered and non-staggered). This is caused by the large amount of hits with a small width of the signal, where no correction is possible.*

Figure 7.5 and 7.6 compare the results determined with the two different layouts types: staggered and non-staggered. The figures show that the choice of $Ar/CH_4/CO_2$ (93/5/2) leads to huge deviations between the layouts especially at small drift lengths. As explained

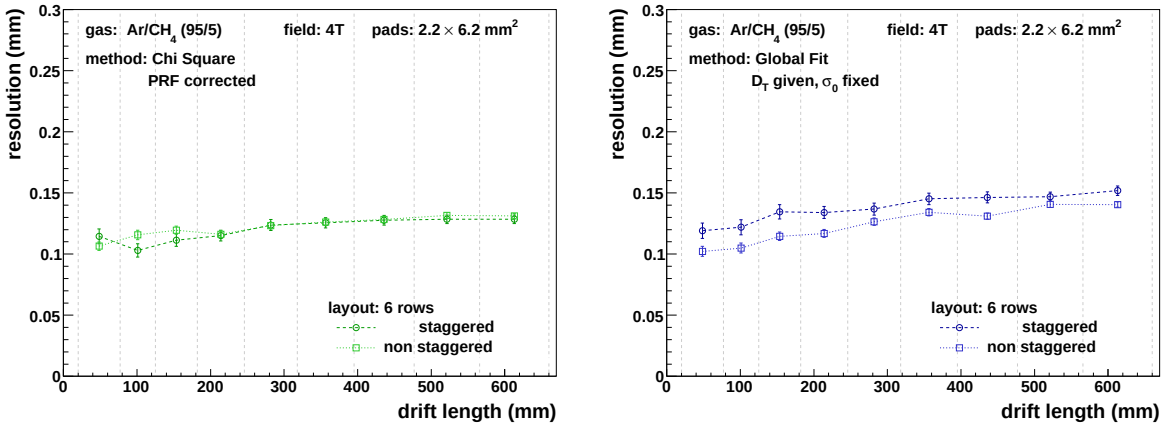

(a) *(b)*

Figure 7.6: *Comparison of different layouts for measured data using Ar/CH_4 (95/5) and with a magnetic field of 4 T: In comparison with the results for $Ar/CH_4/CO_2$ (93/5/2) (Figure 7.5), the presented results show a better agreement between the two layouts.*

in Section 6.1.1, in the case of a staggered pad layout the systematic shift leads to more pessimistic values for the resolution. The same shift gives over optimistic values in the case of a non-staggered layout. This underlines, that the results are not reliable for neither of the two layouts.

The analysis of the measured data using the gas mixture Ar/CH_4 (95/5) shows only small deviations. This can be easily understood by taking the different diffusion parameter of the two gas mixtures into account. As shown in Table 7.4, the signal width using $Ar/CH_4/CO_2$

gas mixture	**signal width**		
	$z = 100\,\text{mm}$	$z = 300\,\text{mm}$	$z = 500\,\text{mm}$
$Ar/CH_4/CO_2$ (93/5/2)	0.319	0.404	0.475
Ar/CH_4 (95/5)	0.399	0.445	0.486

Table 7.4: *Signal width at different drift distances for the two investigated gas mixtures. The With is calculated using Equation (6.3) and values from Table 6.2.*

(93/5/2) is smaller than for Ar/CH_4 (95/5) for all drift distances. For drift distances of $z > 300\,\text{mm}$ the results for $Ar/CH_4/CO_2$ (93/5/2) show a stability that is comparable with the results for Ar/CH_4 (95/5) at small drift distances. At a drift distances of 300 mm the signal width of $Ar/CH_4/CO_2$ (93/5/2) is at the same magnitude as the signal for Ar/CH_4 (95/5) at 100 mm. This leads to the conclusion, that a signal width of more than 400 µm is needed for a reliable hit reconstruction.

Additionally, the Chi Square Method is compared to the Global Fit Method with a fixed σ_{row}. As described in Section 6.2, the Global Fit Method takes the PRF automatically into account. Nevertheless, it shows larger deviations between the two layouts for both investigated gas mixtures. In the case of the Chi Square Method, the results for both layouts are compatible for a larger drift length of $z > 300\,\text{mm}$. In contrast, the Global Fit Method shows deviations

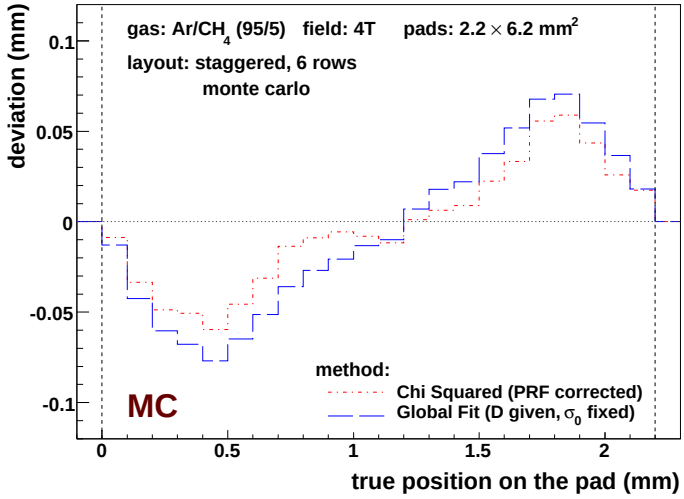

Figure 7.7: *Limitation from the effects of the Pad Response Function: The figure shows the deviation of the reconstructed hit position from the MC truth in dependency of the true hit position given by the MC information. The two vertical dashed line mark the borders of the pad. It has a width of 2.2 mm. Systematic shifts of the hit positions are clearly visible for both presented methods: Chi Square with PRF correction and Global Fit with σ_{row} fixed by given values for D_T and σ_0*

also in this region.

As mentioned above, the deviation between the studied layouts shows that the results are not reliable, because they are highly influenced by systematic effects that acts different in the two cases. The agreement between both layouts indicates, that the systematic shift is under control. In this case, the results are more reliable. The Chi Square Method shows smaller deviations between the layout This leads to the conclusion, that it can correct better the systematic shift caused by the PRF than the Global Fit Method. Further, it has been shown, that the results for the data measured with $Ar/CH_4/CO_2$ (93/5/2) at a magnetic field of 4 T disagree between the two investigated layout. This shows that these results are clearly influenced by systematic effects. Therefore, they can not be used as a reference for the resolution.

The limitation caused by the PRF is also visible in the simulated data. This data has the advantage that the true track position is known from the MC information. Figure 7.7 shows the deviation between the reconstructed hit position and the true hit position in as a function of this true position. The true hit position is determined from the track position at the vertical centre of the row. Please note the different scale of this figure in comparison to Figure 7.2. The shown deviations are averaged over all drift length. This is valid, as Figure 7.3(a) shows, the resolution depends only slightly on the drift length z. As in all studies in this chapter, the hit positions used by the Chi Square Method are PRF corrected.

The systematic shifts caused by the PRF are clearly visible. The deviation vanishes, if the track goes through the horizontal centre of the pad or through the border between two pads. In these cases, the hit reconstruction gives the true position as shown in Figure 6.8 on page 55.

It is clearly visible that the Global Fit method shows larger deviations, maximally 80 µm.

The PRF corrected Chi Square Method shows deviations up to 60 µm. The resolution, if presented as a function of the drift length, shows the average over these systematic deviations. Therefore, the total influence of the limitations caused by the PRF is much smaller than the maximal values shown in Figure 7.7. But it must be taken into account, that there are still deviations in the reconstructed hit positions for the important case of a magnetic field of 4 T. This is true for both methods tested.

7.4.2 Performance of Different Reconstruction Methods in the Presence of Damaged Pads

While the other studies of simulated data use all channels, this section will present the influence of non working pads. In a final detector, it may occur that some channels do not work properly. During the data taking for these studies some pads provided no signals. The total number of these dead pads varied between one and three. To compare measured data and simulation, the same conditions are chosen: Ar/CH_4 (95/5) and a staggered layout. The number of damaged pads for the data measured using these conditions is three. The following pads were not working (row/column): (2/12), (4/16) and (5/17).

The simulated data provides a set, in which all channels are working. This provides the possibility to choose the pads which are not working via the MultiFit steering file. For the studies using only the middle six rows of the simulated data, the same three pads are deactivated as in the measured data. In the case where all 19 rows are used, two scenarios are investigated. In one scenario, six pads of the $19 \times 24 = 456$ pads in the layout are marked as damaged. In the second case, twelve pads are not working. These pads are chosen randomly in all rows (row/column): (1/13), (2/17), (8/12), (12/17),(13/8), (14/4) and additionally in the case of 12 non working pads (4/17), (6/4), (11/16), (13/17), (18/13), (19/17).

	# rows:	6	19	
	# damaged pads:	3	6	12
2 T	hits	17,2%	11,4%	18,5%
	tracks	38,3%	65,7%	66,4%
4 T	hits	17,2%	13,1%	16,3%
	tracks	49,9%	53,4%	54,4%

Table 7.5: *Quota of hits and track influenced by non working pads. Results for two magnetic fields (2 and 4 T) and three different layout (6 rows with 3 non working pads and 19 rows with 6 and 12 non working pads) are shown.*

Table 7.5 shows the quota of hits and tracks which are influenced by the non working pads. Between 10% to 20% of the all reconstructed hits are marked, that information may be missing due to a non working pad. This pad can be in the middle of the hit as well as on the side. Naively one would expect a larger difference in the number of effected hits between the two magnetic fields of 2 T and 4 T. But one has to take into account, that the probability of one-pulse hits increase with the magnetic field due to the decrease of the signal width. If the small signal lies on a damaged pad, no hit is reconstructed. If the signal is large enough to be measured on two pads, a hit will be reconstructed even though, one of the pads is not working. The probability that a track is influenced by non working pads is much higher than

for hits, because only one hit of the 6 or 19 hits of the track is sufficient to mark the track. The quota for the tracks varies between 38% and 67%.

Figure 7.8 compares the resolution determined with several methods using a fully working layout and one using the setting with three damaged pads. In contrast to the other two methods, the results determined with the Global Fit Method with σ_0 as a free parameter show large differences between the investigated layouts. Also here, the additional free parameter gives a larger degree of freedom. This results in less stable conditions for the fit. Also for the data simulated with a magnetic field of 2 T, which showed more stable conditions in the other studies presented, discrepancies are visible.

Due to the construction of the likelihood (Equation (6.12)), pads with no signal and non working pads are treated in the same way. Therefore, the missing charge information could be interpreted as a smaller width of the signal. This would lead to a smaller estimation of the values of σ_0. In Section 7.5, it is shown that the values determined for σ_0 do not depend on the presence of damaged pads. Therefore, this is not explanationn for the observed effect.

The layout with 19 rows provides more stable conditions for the methods. This investigation is most important for the understanding of the Global Fit Method where σ_0 is a free parameter. The results are shown in Figure 7.9.

In the case of the Global Fit Method with σ_0 as a free parameter, the discrepancies between the layouts with different numbers of non working pads are still present. It can be concluded, that these discrepancies are most likely not caused by unstable conditions for the fit. The source of this high dependency on the number of damaged pads is not finally understood. Therefore, none of the two variations of the Global Fit Methods in which σ_0 is a free parameter will be further discussed.

The other two methods do not seem to suffer much from the damaging of several pad. Especially for the Global Fit Method, the use of the theoretical predictions of the defocussing constant σ_0 decreases the dependence on the number of non working pads. Only at small drift distances, discrepancies between the investigated layouts can be seen. In contrast to the expectation, the resolution becomes better for a larger number of non working pads. This effect is visible in the results of both methods in the same magnitude. It is not yet understood. In the case of six rows it is not visible. This may be caused by a lower fit stability.

7.4.3 Angular Dependency for different reconstruction methods

As mentioned in Section 6.3.1, no angular dependency is implemented in the PRF correction of the Chi Square Method. Therefore, it is necessary to study the performance for different inclination angles. Additionally, the method is compared with the Global Fit Method which takes the angular dependency of the PRF into account.

The data sets which are generated by the simulation are divided into seven subsets for different ranges of the inclination angle ϕ. This angle is defined for each row by Equation (5.1). The subsets cover the ranges between 0, 10, 20, 40, 60, 80, 100 and 150 mrad. The results for the tested methods are summarised in Figure 7.10. Both methods show similar behaviour for magnetic fields of 2 T and 4 T.

The theoretical limit for the resolution is given by Equation (3.18). Following this ansatz, the function

$$\sigma = \sqrt{D_r^2 \cdot z + \sigma_{\text{zero}}^2} \tag{7.1}$$

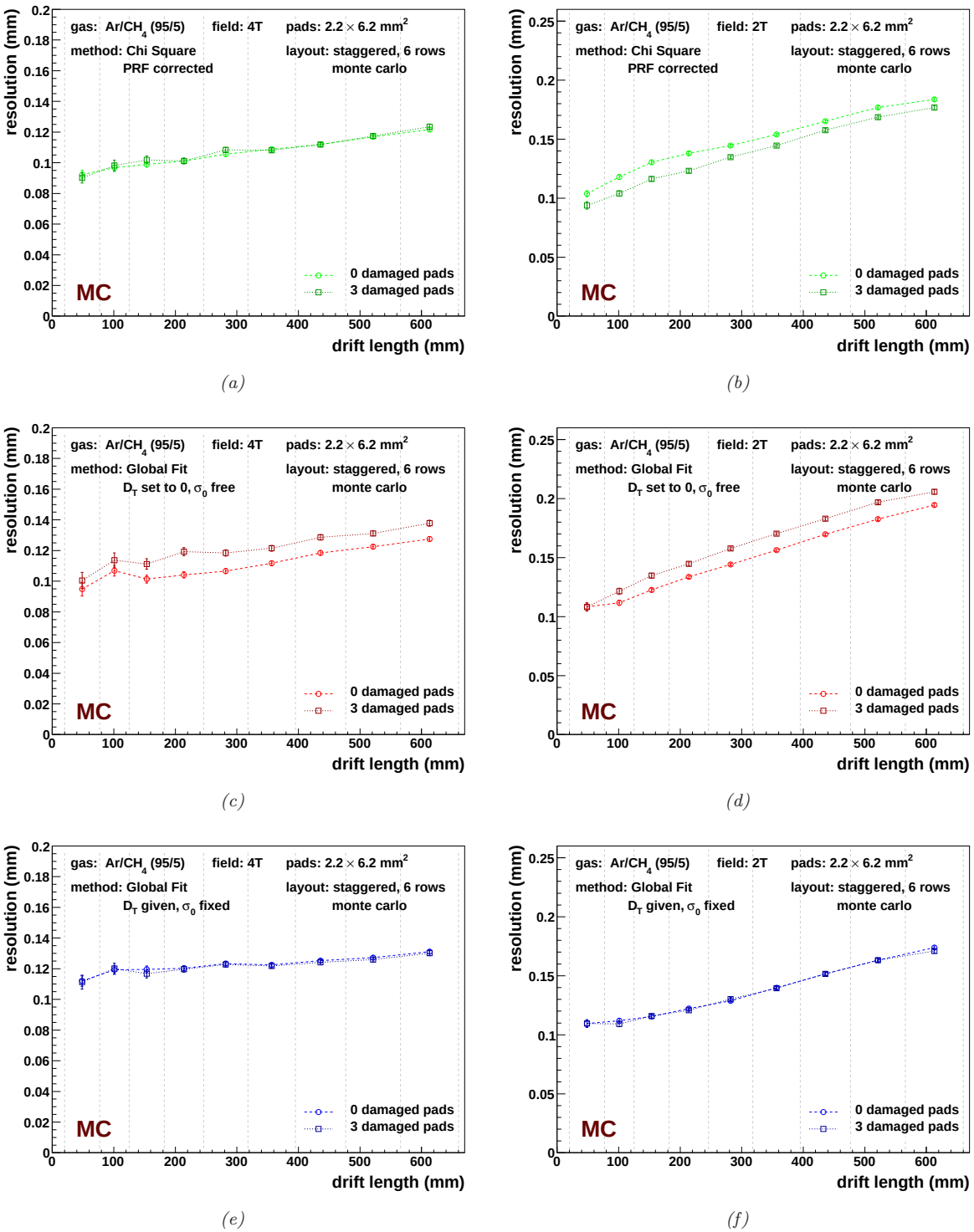

Figure 7.8: *Influence of damaged pads for different reconstruction methods using MC generated data with six rows: In one set all pads were working. In contrast to the other where 3 pads are disabled. Thiscase iss compatible to the measuring setup. Three reconstruction methods (Chi Square with PRF correction, Global Fit with σ_{row} free ($D_T = 0$) and fixed by given values for D_T and σ_0) are investigated for magnetic fields of 2 T and 4 T.*

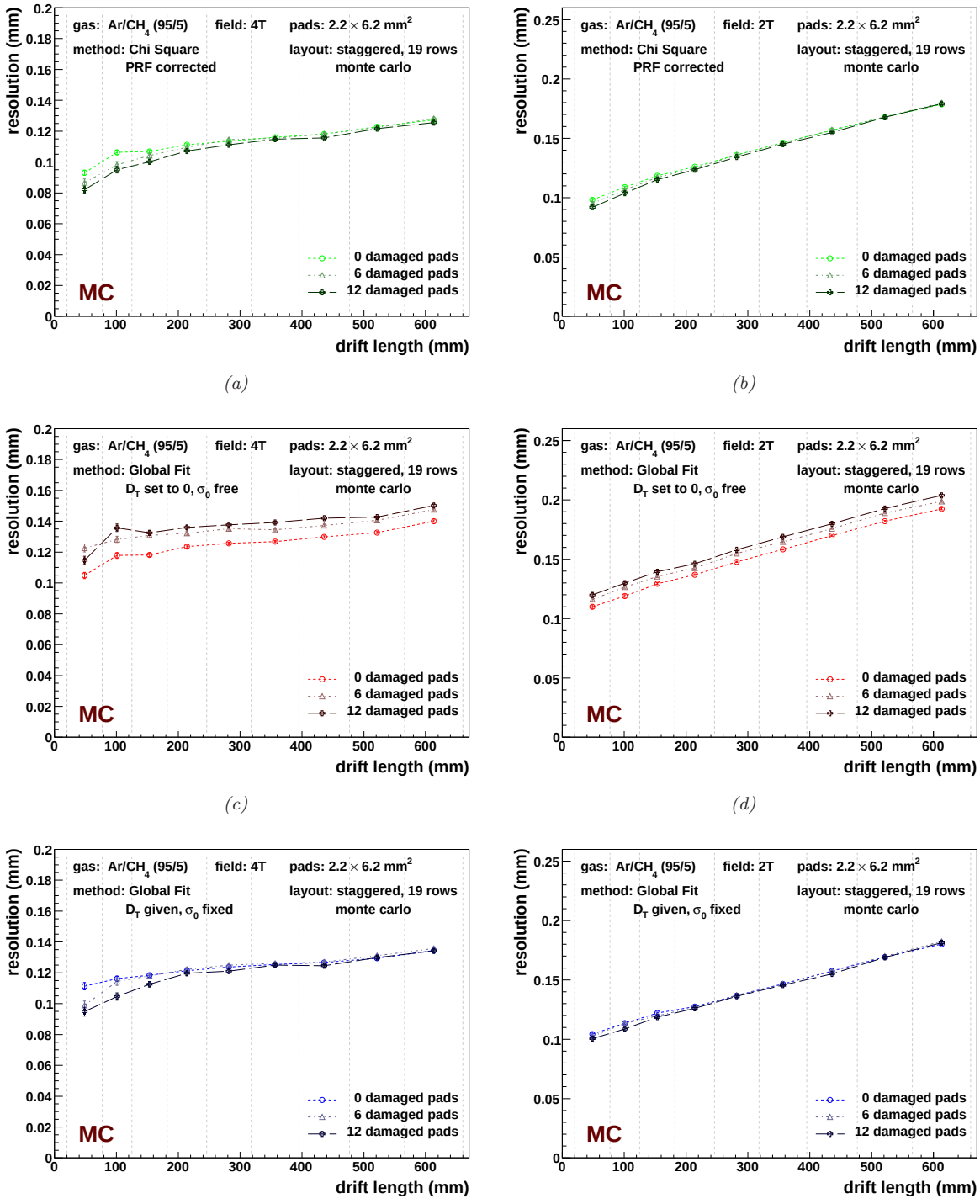

Figure 7.9: *Influence of damaged pads for different reconstruction methods using MC generated data with 19 rows: The performance of the three reconstruction methods (Chi Square with PRF correction, Global Fit with σ_{row} free ($D_T = 0$) and fixed by given values for D_T and σ_0) are shown for two layouts containing six and 12 damaged pads and a layout, where all pads working. All layouts use a staggered pad arrangement. Results are shown for two magnetic fields of 2 T and 4 T*

is fitted to the results. It must be mentioned, that the two free parameters D_r and σ_{zero} are not to be confused wit the diffusion coefficient D_T and the defocussing constant σ_0.

The parameter σ_{zero} can be interpreted as the resolution at zero drift length. The determined values are shown in Figure 7.10(e) and 7.10(f). Again, both methods behave very similarly. Only small differences can be observed. It should be remarked, that the largest angular cut of $|\phi_{\text{hit}}| < 150\,\text{mrad}$ is still small. The distribution of the inclination angle is limited by the position of the trigger in the experimental setup. The positions of the triggering scintillators are also implemented in the simulation. As shown in Figure 7.13 only a few events provide angles above 150 mrad.

To compare a simulated data set to a measured one, the setting with six rows is also studied. The data sets are divided in the same seven subsets, chosen for the analysis of the 19 row layout. Again, the Equation (7.1) is fitted to the results which are shown in Figure 7.11.

In the case of six rows, clear differences between both methods are visible. The Chi Square Method shows very similar results as in the case of the 19 row pad layout. Only for low angle and small drift distances the method reveals an unphysical behaviour. The results determined with the Global Fit Method do not match with the ones using all 19 rows. In contrast, the results for the different angles differ less. This means, that in this case the Global Fit Method shows a smaller angular dependency. This is also visible in Figure 7.11(e). If this behaviour would be an effect of the implemented angle depended PRF, the results using 19 rows, should show the same behaviour. Since this is not the case, it is more likely that the smaller differences between the subsets are caused by a instability of the fit due to the limited number of rows.

The measured data sets contain much fewer events than the simulated sets. Hence, these data sets are divided in only four subsets. They cover the ranges between, 0, 30, 60, 100 and 150 mrad. Figure 7.12 displays the results. They show a similar behaviour as those determined with the simulated data using six rows. Again, the Global Fit Method shows a smaller angular dependency, which may be artificial as explained before. The results of the subsets $100\,\text{mrad} < |\phi_{\text{hit}}| < 150\,\text{mrad}$ are not convincing due to the large errors. As shown in Figure 7.13, the measured data provides insufficient statistic above 100 mrad.

As discussed before, the conclusion that can be drawn from the measured and simulated data is not clear. For angles $|\phi_{\text{hit}}| < 100\,\text{mrad}$, which are used for the other studies presented, both methods behave similarly. In this angular range, the Chi Square Method is not discriminated by neglecting the angular dependency in PRF correction.

7.4.4 Influence of Angular Cuts for the Determination of the Resolution

As the previous study pointed out, the resolution shows a strong angular dependency. Therefore, it is very important to emphasise that the determination of the resolution is very sensitive to the choice of the applied angular cut. To make the results of different analysis comparable, the same angular cut must be used. The different groups working on the development of a TPC for an ILC detector agreed on an angular cut of $\phi < 100\,\text{mrad}$ in the xy-plane.

To evaluate the results, it is also important to take the ϕ distribution into account. Because this distribution is mainly influenced by the measurement setup, it is more difficult to equalise it in different analysis. Figure 7.13 shows the distribution of ϕ_{hit} for the data sets measured and simulated with the settings: Ar/CH_4 (95/5) , 4 T, staggered pad layout. These settings are similar to the values proposed for an ILC detector, and can therefore be used as a reference point.

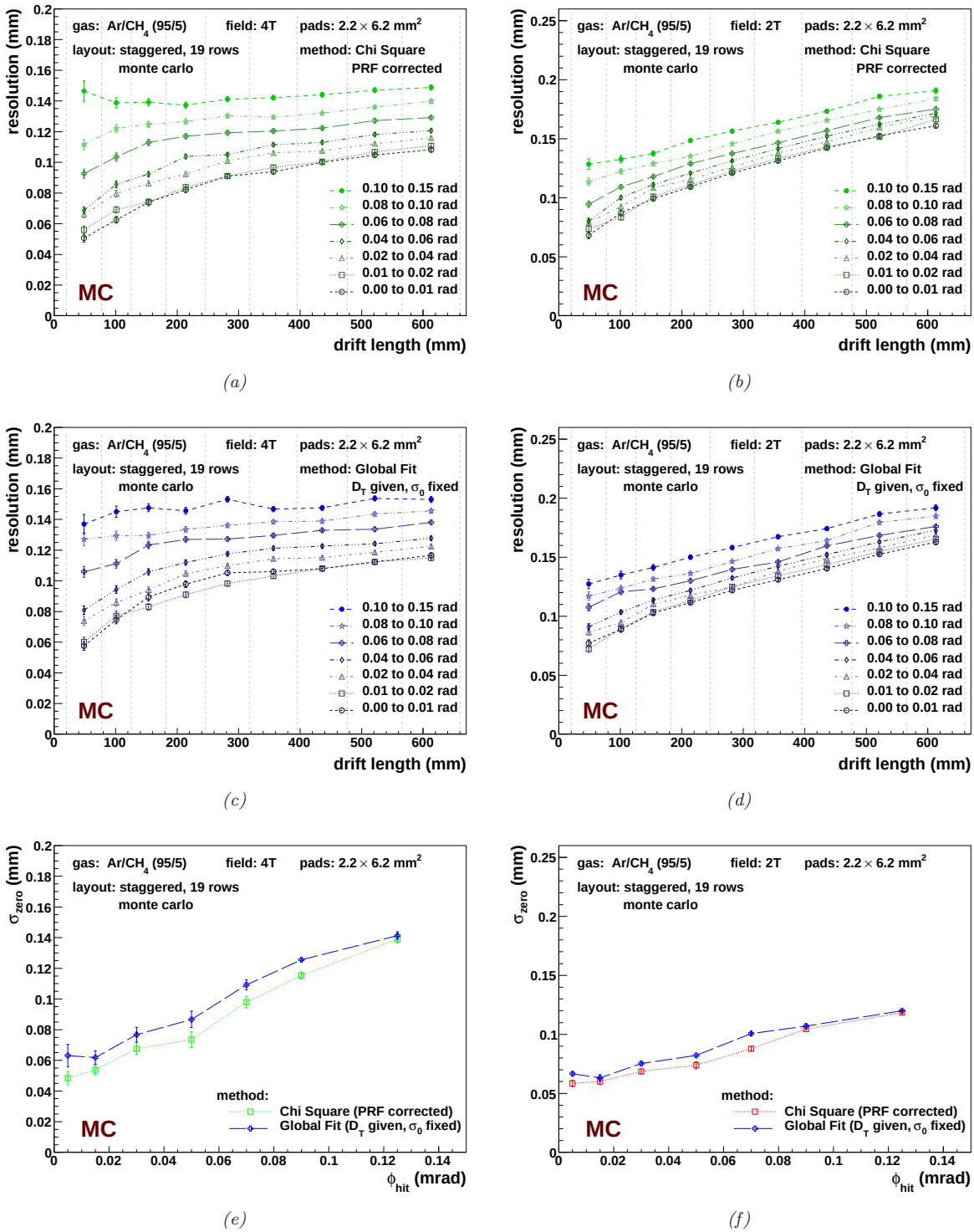

Figure 7.10: *Angular dependency for different reconstruction methods using MC generated data with 19 rows: Results for two magnetic fields (2 T and 4 T) and the reconstruction methods Chi Square with PRF correction and Global Fit with σ_{row} given by D_T and σ_0 are shown. The data is separated in seven subsets using different angle intervals between 0 and 150 mrad.*

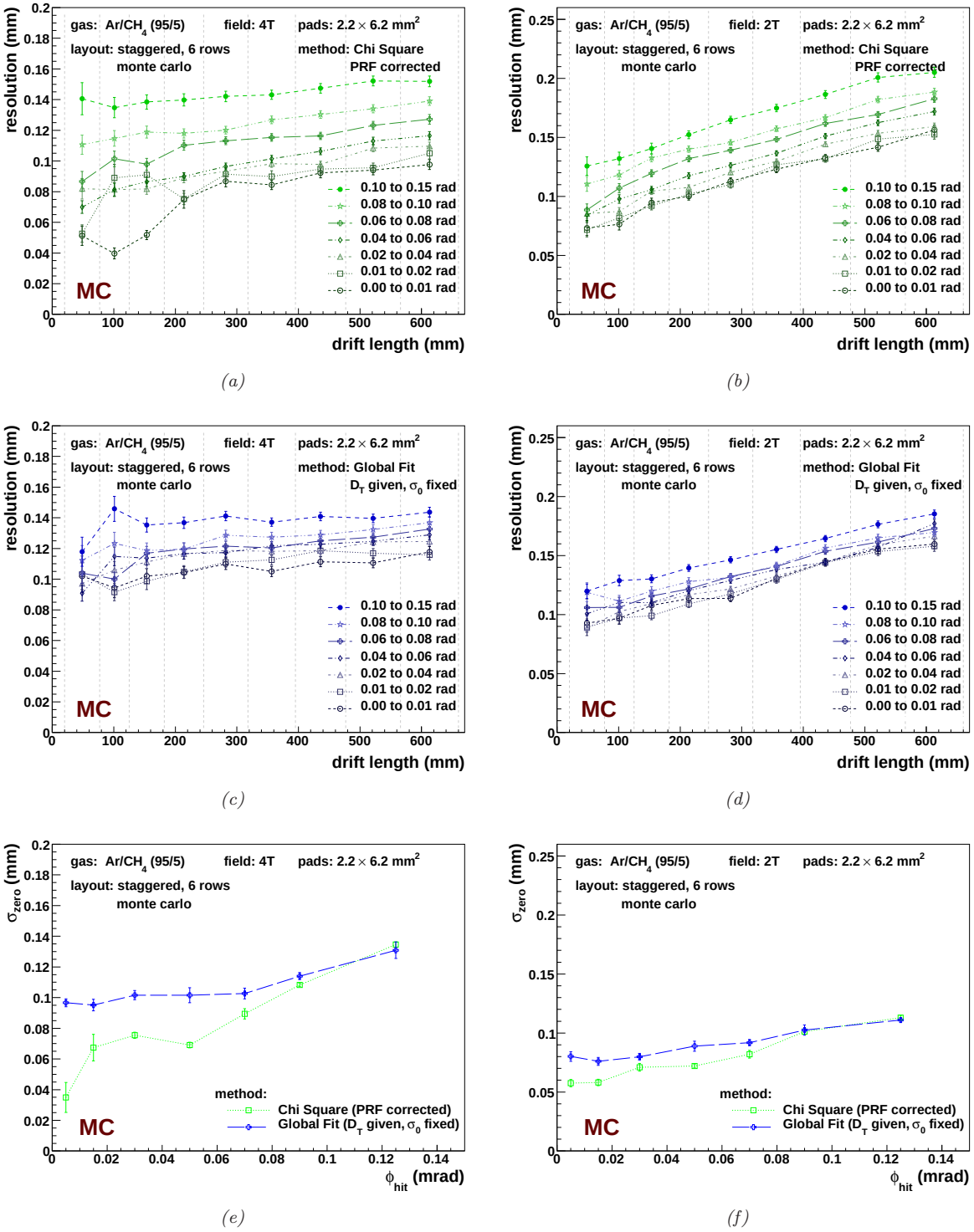

Figure 7.11: *Angular dependency for different reconstruction methods using MC generated data with six rows: As in Figure 7.10 the data is separated in seven subsets using different angle intervals between 0 and 150 mrad. Results for two magnetic fields (2 T and 4 T) and for the reconstruction methods Chi Square with PRF correction and Global Fit with fixed σ_{row} determined by given values for D_T and σ_0 are shown.*

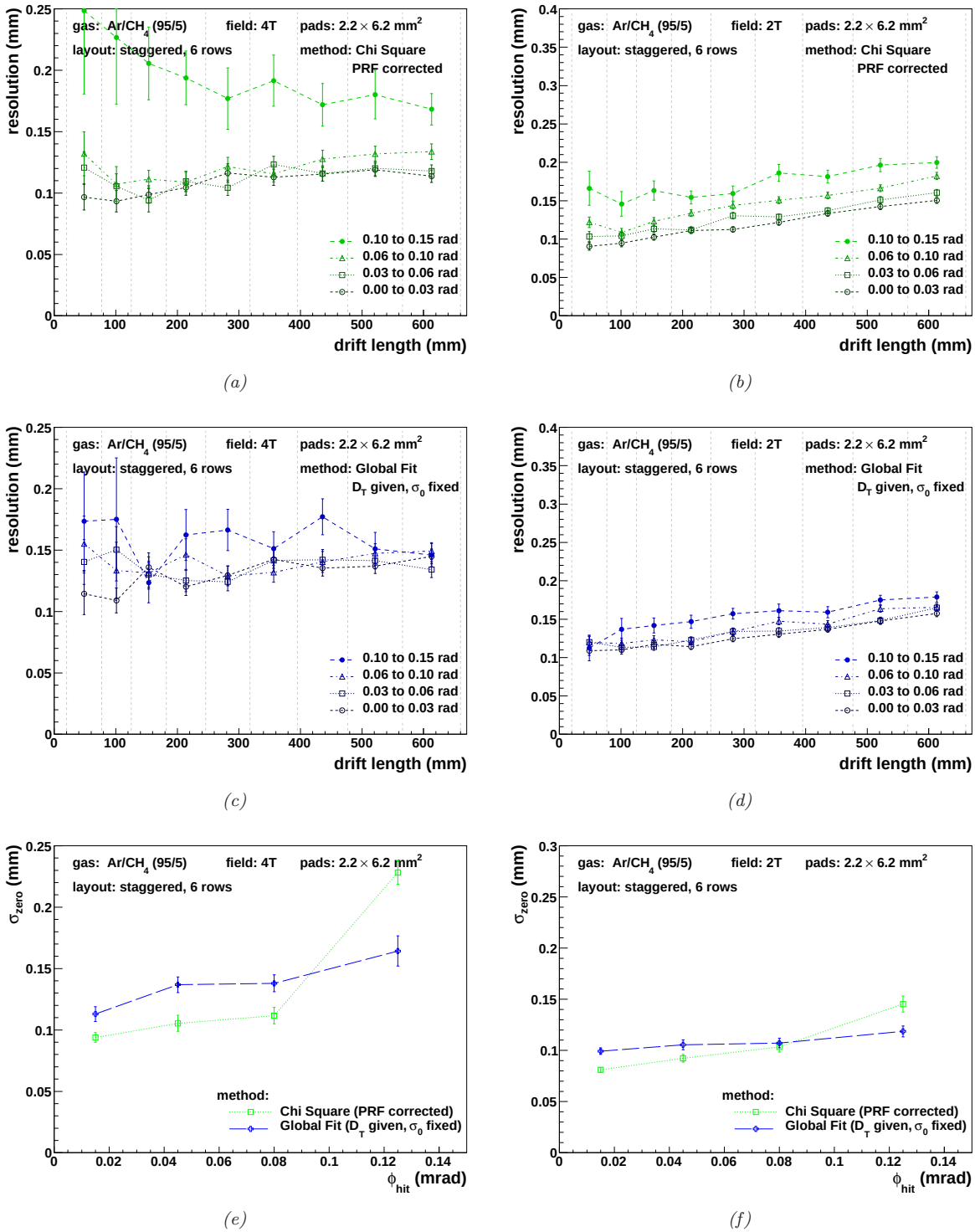

Figure 7.12: *Angular dependency for different reconstruction methods using measured data: Due to less statistics the data is separated in only 4 subsets using different angle intervals between 0 and 150 mrad. As for the simulated data (Figure 7.10 and 7.11) results are shown for the reconstruction methods Chi Square with PRF correction and Global Fit with σ_{row} fixed by given values for D_T and σ_0. Two magnetic fields (2 T and 4 T) have been investigated.*

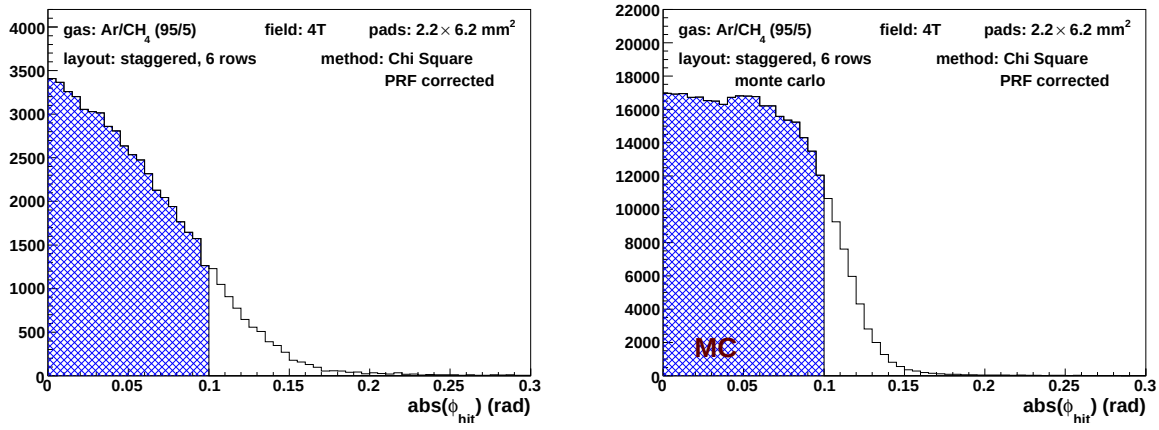

(a) measured data set

(b) simulated data set

Figure 7.13: *Distribution on the level of hits: One set of measured data and one set of simulated data are presented. Both use the same conditions, as gas mixture, magnetic field and pad layout. The Chi Squared Method is used for reconstruction. The range used for this analysis is hatched in blue.*

7.5 Determination of Diffusion Using the Global Fit Method

Apart from the resolution measurement, the Global Fit Method provides the possibility to determine the diffusion parameters: the diffusion coefficient D_T and the defocussing constant σ_0. The variation of this method with $\sigma_{\text{row}} = \sigma_0$ is used for this determination. To make sure that the signal width does not vary too much for the different rows, only the most vertical tracks are used. A cut on the inclination angle in the yz-plane of $|\theta| < 10°$ is applied. While no hit information is used, the cut on ϕ_{hit} is replaced by $|\phi_0| < 100\,\text{mrad}$, where ϕ_0 is the inclination angle of the track at $y = 0$.

First, the fit parameter σ_0 of each track is filled in a histogram as a function of the reconstructed intercept I_z. The histogram is divided into several bins for different drift length intervals given by I_z. A Gaussian distribution is fitted to the projection of each of these bins. The mean value is interpreted as σ_{charge} where z is given by the centre of the bin. Equation (3.17) is fitted to these pairs (z, σ_{charge}). The diffusion coefficient D_T and the defocussing constant σ_0 are the free parameters during the fit.

A few examples for data at a magnetic field of 2 T illustrate this procedure. Figure 7.14 shows the examples for data measured with the staggered and the non-staggered pad layout. The use of simulated data is displayed in Figure 7.15. Here layouts with six and 19 rows have been investigated. In all examples, the left figures show the histogram filled with the result of the fit parameter σ_0. The vertical lines mark the borders of the bins. The averaged value σ_{charge}, determined for each bin by a the Gaussian fit, is shown in the right figures. The fit to these values is also displayed.

The procedure described yields values for the diffusion coefficient D_T and the defocussing constant σ_0 . The results for measured data are displayed in Figure 7.16. In addition, the values predicted by a GARFIELD simulation are shown (see Table 3.2). The following equation

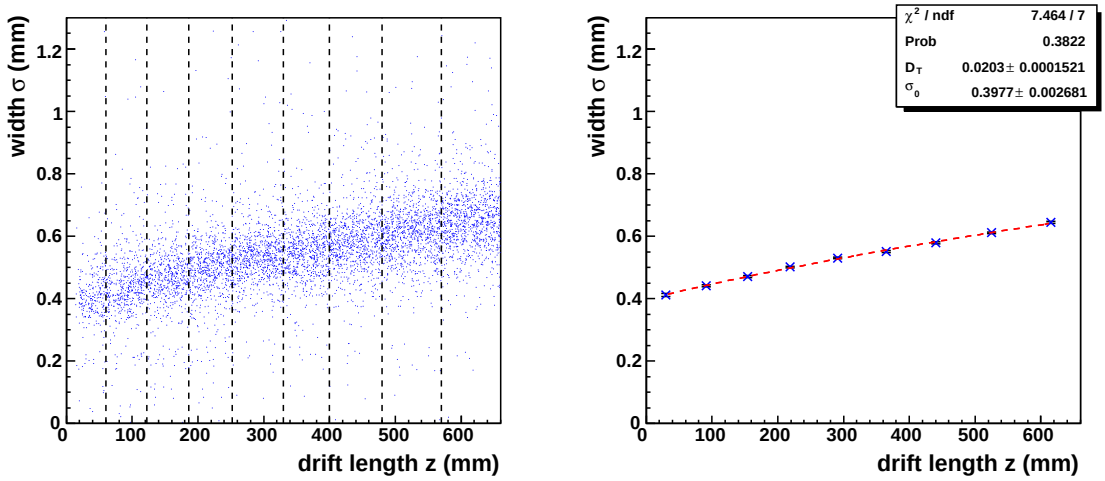

(a) 2T, staggered layout

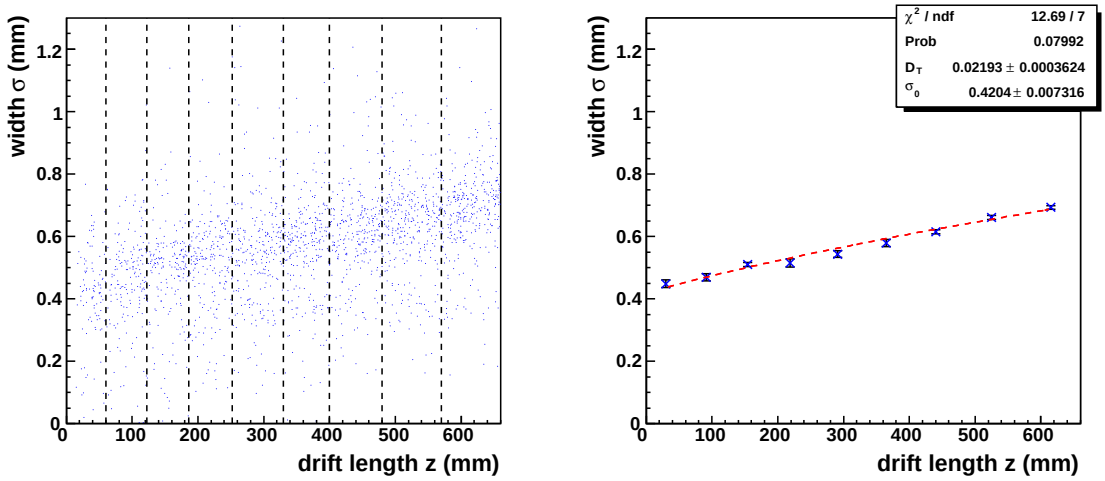

(b) 2T, non-staggered layout

Figure 7.14: *Diffusion determined using the Global Fit Method for data measured using Ar/CH_4 (95/5) with 2T and (non) staggered layout: Using the fit parameter σ_{track} of the global fit method with $D_T = 0$, it is possible to determine the diffusion parameter D_T and σ_0. The figure on the left side shows the distribution of the fit parameter σ_{track} for tracks with low inclination angle ($\theta < 10\,^\circ$) versus the drift length z. Indicated with vertical lines, this distribution is separated in several drift length intervals. To each interval a Gaussian is fitted and the mean value is shown in the right figure. To these values a function $\sigma_D = \sqrt{D_T^2 \cdot z + \sigma_0}$ is fitted with D_T and σ_0 as free parameter. The results of the fit are shown in Figure 7.16 together with results for other settings (gas, field and layout).*

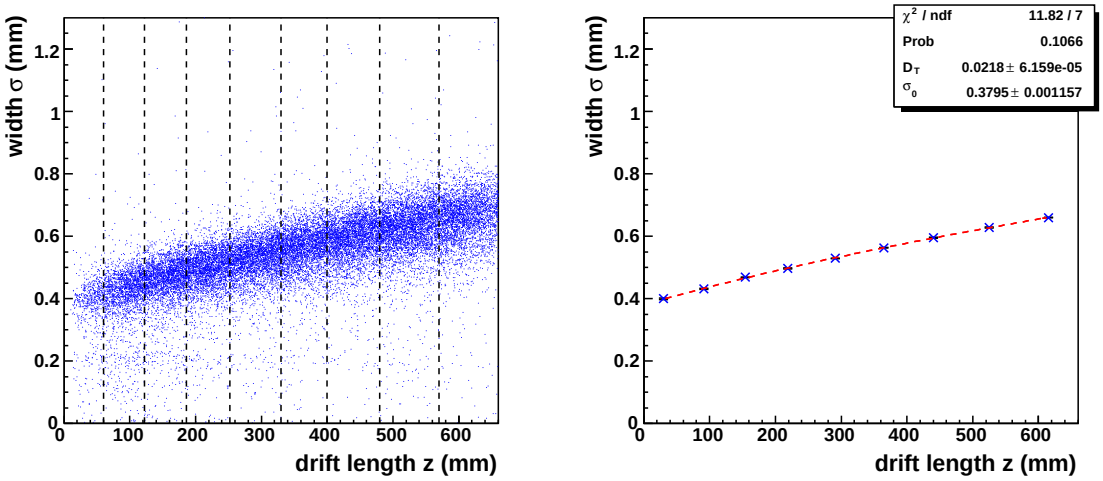

(a) 2T, staggered layout with six rows

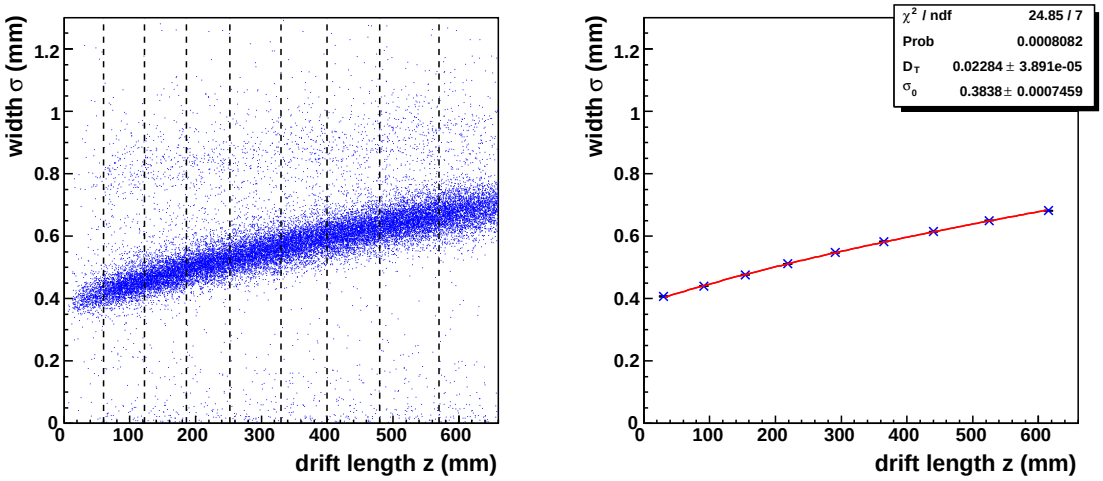

(b) 2T, staggered layout with 19 rows

Figure 7.15: *Diffusion determined using the Global Fit Method for data simulated with 2T and staggered layouts with 6 and 19 rows: As in Figure 7.14 distributions of the parameter σ_{row} versus drift length z are shown on the left side. The resulting values for different drift length intervals and a fit of the function $\sigma_D = \sqrt{D_T^2 \cdot z + \sigma_0}$ are shown on the right side. Different to Figure 7.14 the results for simulated data are shown and the two presented samples both use staggered layout and differ in the number of rows. The results of the fit are shown in Figure 7.17 together with results for 4 T and layouts containing damaged pads.*

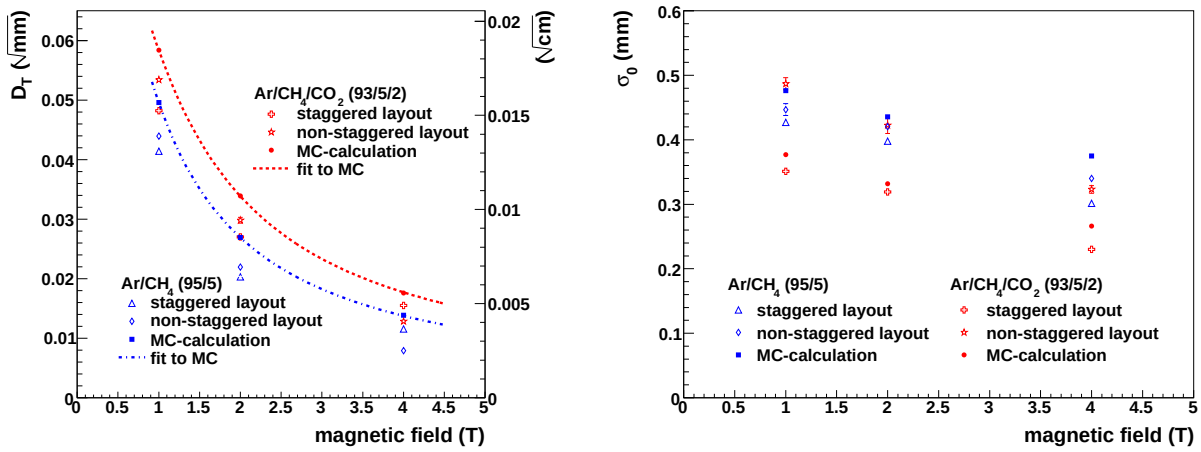

(a) *(b)*

Figure 7.16: *Diffusion coefficient D_T and defocussing constant σ_0 for measured data: Results of a method, which is described in Figure 7.14, to determine the diffusion parameter diffusion coefficient D_T (Figure (a)) and defocussing constant σ_0 (Figure (b)) using the Global Fit method are presented for different gases ($Ar/CH_4/CO_2$ (93/5/2) and Ar/CH_4 (95/5)), pad layouts ((non-)staggered) and magnetic fields. Additionally the values predicted by a GARFIELD simulation [21] are shown (see Table 3.2). For the diffusion coefficient D_T the function $D_T = \frac{D(0)}{\sqrt{1+\alpha^2 \cdot B^2}}$ is fitted to the predicted values.*

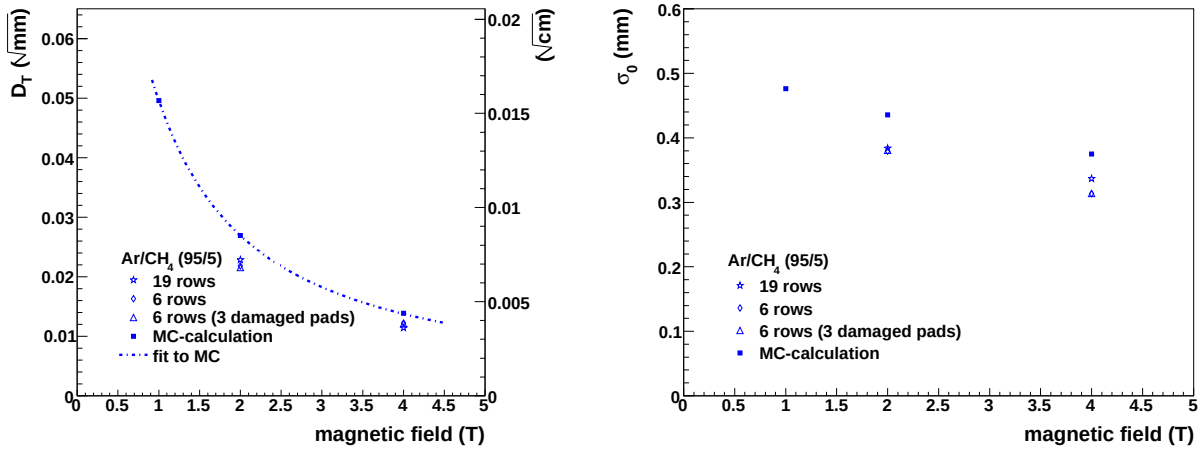

(a) *(b)*

Figure 7.17: *Diffusion coefficient D_T and defocussing constant σ_0 for simulated data: As in Figure 7.16 values of the fit shown in Figure 7.15 (2 T) are presented together with results for 4 T. As reference to Figure 7.16 the values predicted by a GARFIELD simulation [21] are included.*

is fitted to the values for the diffusion coefficient D_T (cf. Equation (3.15)):

$$D_T(B) = \frac{D_0}{\sqrt{1 + \alpha^2 \cdot B^2}} \tag{7.2}$$

The free parameter D_0 can be interpreted as the diffusion coefficient for no magnetic field. The parameter $\omega\tau$ in Equation (3.15) can be written as $\omega\tau = \alpha B$. During the fit, B is given and the parameter α is varied.

The determined values for the diffusion coefficient D_T lie below the GARFIELD predictions. The difference is between 0.03 to 0.08 $\sqrt{\text{mm}}$ and does not depend on the magnitude of the predicted value. It is more likely a constant offset. The comparison between staggered and non-staggered layout gives no clear picture. Comparing the values for a certain magnetic field, none of the layout provide the lowest value for all cases.

Also the values for the defocussing constant σ_0 do not match the predictions. Most values are below the expectation. The only exception are the values for $Ar/CH_4/CO_2$ (93/5/2) using a non-staggered layout. In contrast to the diffusion coefficient D_T all determined values for σ_0 using a staggered layout are below those for a non-staggered layout.

To get a better understanding, if the underestimation of the diffusion parameter is due to the data quality or due to the method, the analysis is repeated using simulated data. Unfortunately, no data sets using a non-staggered layout were available. During the MC simulation the GARFIELD predictions were used as input parameters for the modelling of the diffusion. Therefore, they should be reproduced, if the deviation which is seen in the analysis of the measured data, is caused by a difference between the prediction of GARFIELD and the real diffusion during the data taking.

As Figure 7.17 shows, the determined values for the diffusion coefficient D_T are for the case of the simulated data below the GARFIELD prediction. The discrepancies are visible even at the most stable conditions for the Global Fit Method provided by the layout with 19 rows and no damaged pads. These values are slightly better that one determined using a full working layout with six rows. For a better comparison with the measured data sets, a layout with six rows and three non working pads was studied, too. It turned out, that the presence of damaged pads has no influence on the outcome.

The conclusion can be drawn that the MultiFit implementation of the Global Fit Method determines the diffusion parameters in the right order of magnitude. But it underestimates the diffusion coefficient D_T and the defocussing constant σ_0. Perhaps, this effect is due to the noise value of 1% or the clustering procedure before the actual determination of the track parameters. Both features can lead to a smaller estimation of the width of the charge distribution. Here also the non optimal ratio between the signal width and the width of the pad limits the accuracy. Therefore this method should be tested again under better conditions.

Chapter 8

Spatial Resolution

In this chapter the final results for the spatial resolution which can be achieved in the $R\phi$-plane with the prototype described in Section 4.1 are presented. The results are discussed in the context of further studies and the design of a TPC for the ILC.

The results of the analysis of the spatial resolution is very sensitive to the cuts which are applied. The following cuts are used:

- Only events with exactly one reconstructed track are taken into account.
- The track must contain the maximal possible number of hits, which is given by the numbers of rows.
- All hits from the track must not lie in the outer three pad columns.
- The curvature κ of the track should be smaller than $0.02\,\mathrm{mm}^{-1}$.
- Only tracks with an absolute inclination angle in the yz-plane below 450 mrad are taken into account.
- Only the residuals of hits with a related track angle ϕ_{hit} (Equation (5.1)) of less than 100 mrad are used.

The main reason for these cuts is to ensure a high quality of the data. They are explained in more detail in Section 7.1.2.

It is essential to point out again, that the applied angular cut of $|\phi_{\mathrm{hit}}| < 100\,\mathrm{mrad}$ and the and phi distribution (see Figure 7.13) have a large influence on the final result. The reasons are presented in the previous chapter in Section 7.4.4. The value of the angular cut is an agreement between the groups working on research and development projects for a TPC at the ILC.

For the results which are presented in this chapter the following two methods are used:

- Chi Square Method with PRF correction
- Global Fit Method with σ_{row} fixed.

As the detailed study of the different methods which is presented in previous chapter shows, these two methods are the most stable ones. The layout of the pads and the presence of non working pads have only a small impact on the results which are determined using these two methods. Both use information about the diffusion. The values for the diffusion coefficient ${D_T}^2$ and the defocussing constant ${\sigma_0}^2$ are summarised in Table 6.2 on page 57.

The data sets which are analysed are summarised in Table 4.1 on page 35. Various magnetic fields between 1 T and 4 T are investigated. Figure 8.1 shows the results for the data measured

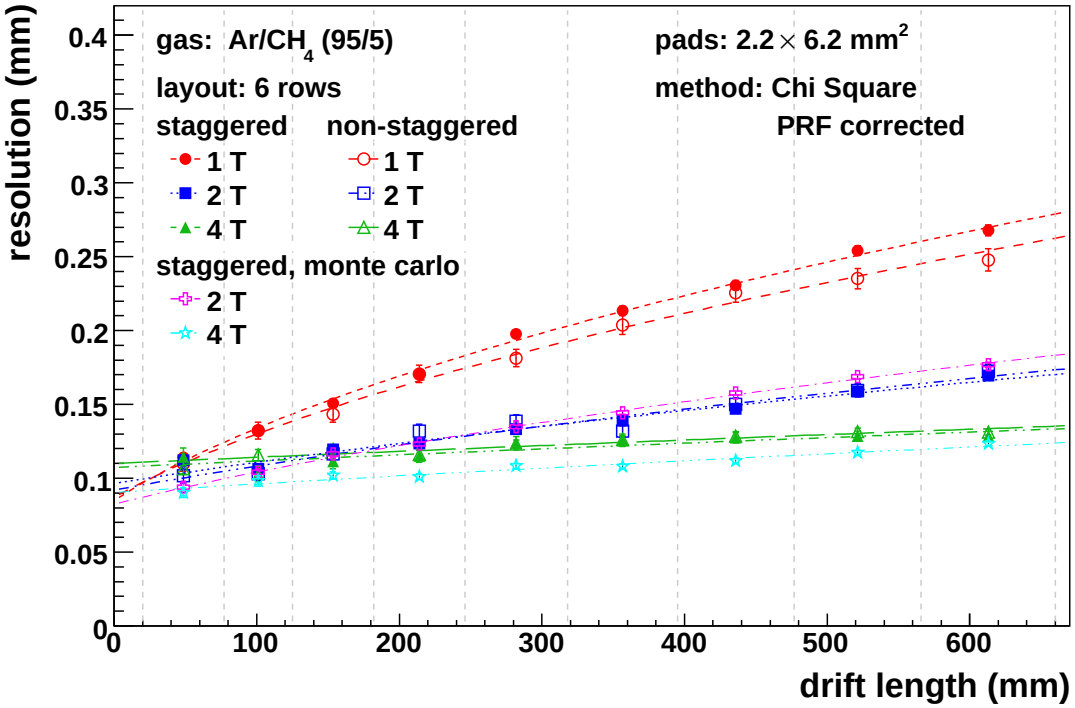

(a)

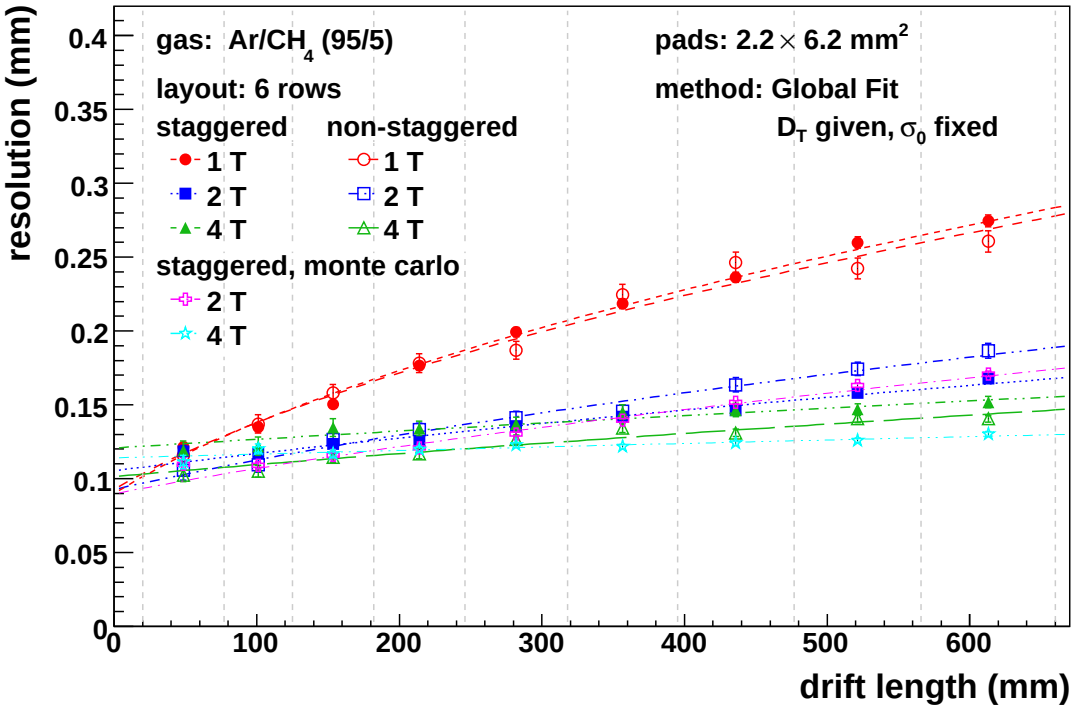

(b)

Figure 8.1: *Resolution for various magnetic fields using Ar/CH_4 (95/5): Results for staggered and non-staggered pad layouts are shown. Additionally the results of MC generated data using a staggered pad layout with six rows containing 3 damaged pads are presented. The curves display the result of a fit ($\sqrt{D_r^2 \cdot z + \sigma_{\text{zero}}^2}$) to the data points.*

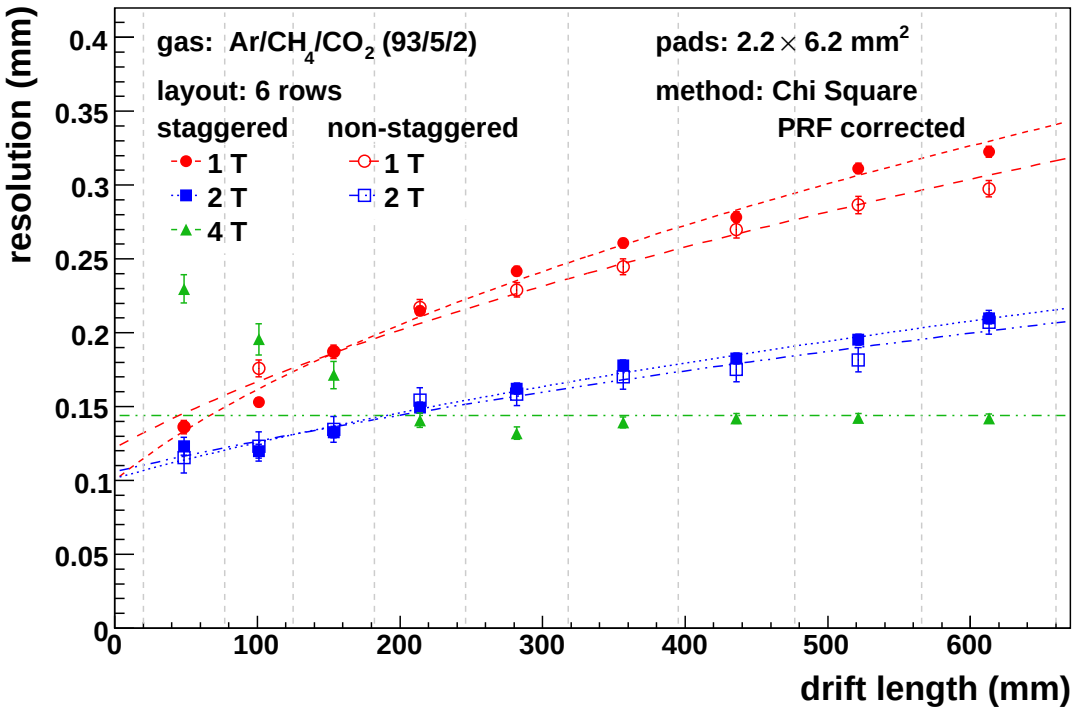

(a)

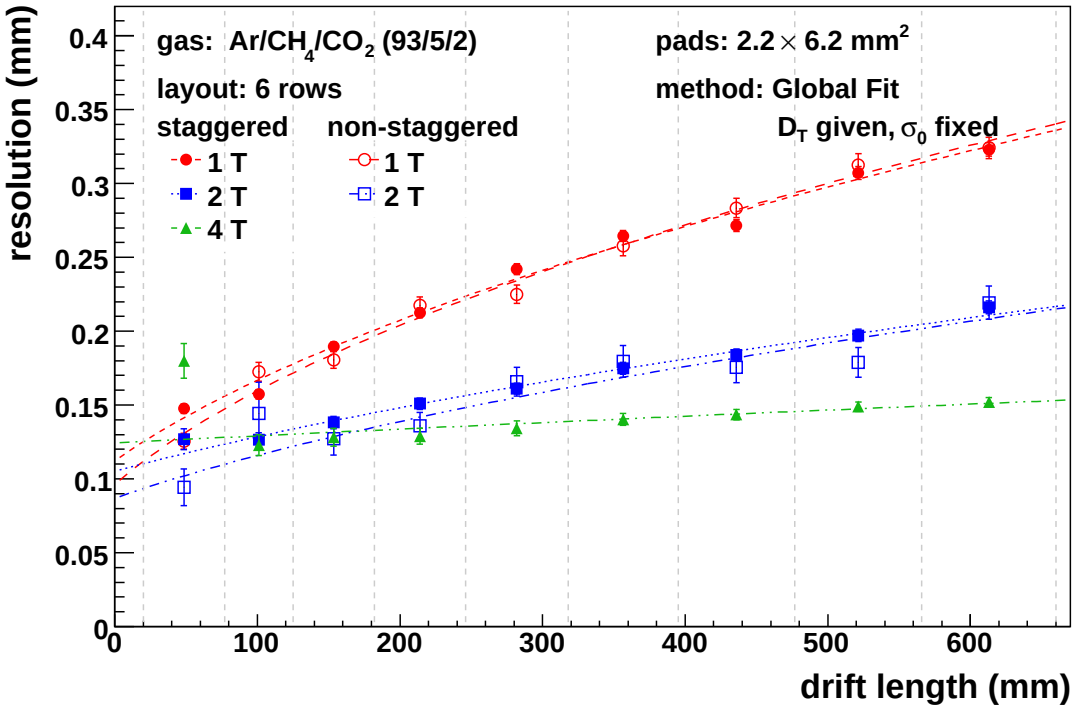

(b)

Figure 8.2: *Resolution for various magnetic fields using $Ar/CH_4/CO_2$ (93/5/2): Results for staggered and non-staggered pad layouts are shown. The curves display the result of a fit ($\sqrt{D_r^2 \cdot z + \sigma_{\text{zero}}^2}$) to the data points.*

using Ar/CH_4 (95/5). As presented in Section 7.4.1, the analysis shows similar results for the staggered and non-staggered pad layouts. In the case of the Chi Square Method, the agreement of the results determined for the two layouts is very good for a high magnetic field $B \geq 2\,\mathrm{T}$. As mentioned before, this suggests that the results are not limited by the influence of the Pad Response Function.

Figure 8.1 depicts also the results for simulated data. The two simulated data sets for which results are shown make use of a staggered layout with six rows. Three of the pads are marked as damaged. These pads are located at the same position as in the measured data. Details of the handling of the simulated data are presented in Section 7.1.1. The difference between the results for measured and simulated data is of the order of 5% for 2 T and 10% for 4 T. Possible reasons for this behaviour are discussed in Section 7.4.

Figure 8.2 shows results for data measured with $Ar/CH_4/CO_2$ (93/5/2). For this gas mixture no simulated data are available. The results for this gas mixture with 4 T magnetic field using the non-staggered pad layout are not shown. Due to a very small width of the signal, these results are strongly effected by systematic shifts caused by the Pad Response Function, which is discussed in Section 7.4.1. In case of a non-staggered arrangement of the pads, this effect leads to over optimistic values for the resolution (see Section 6.1.1). The results for data measured with the same gas and the same magnetic field but using a staggered pad layout, are also influenced by this PRF effect. But in contrast to the unshown results, these results are too pessimistic. This systematically pessimistic result is shown to emphasise, that the ratio of signal width to pad width is far from being optimal for this setting: $Ar/CH_4/CO_2$ (93/5/2), a magnetic field of 4 T measured with 2.2 mm wide pads. In the case of a lower magnetic field, the results for the two different layouts agree better.

Method	**Chi Square**				**Global Fit**			
Layout	**non-staggered**		**staggered**		**non-staggered**		**staggered**	
B	D_r	σ_{zero}	D_r	σ_{zero}	D_r	σ_{zero}	D_r	σ_{zero}
T	$10^2\sqrt{\mu m}$	µm	$10^2\sqrt{\mu m}$	µm	$10^2\sqrt{\mu m}$	µm	$10^2\sqrt{\mu m}$	µm
$Ar/CH_4/CO_2$ (93/5/2)								
1 T	113±2	122±5	127±1	100±3	127±2	96±6	123±1	112±3
2 T	69±4	106±8	74±2	101±5	76±4	87±11	74±2	105±5
4 T	—	—	0±5	143±1	—	—	34±3	124±4
Ar/CH_4 (95/5)								
1 T	96±2	87±5	103±1	87±6	101±2	93±6	105±1	90±3
2 T	57±2	91±3	54±1	96±5	64±2	93±5	51±1	106±2
4 T	30±2	110±2	33±1	107±3	41±2	102±3	38±3	120±4
Ar/CH_4 (95/5) (Monte Carlo)								
2 T	—	—	63±1	82±2	—	—	58±1	89±2
4 T	—	—	32±1	90±2	—	—	24±2	114±2

Table 8.1: *Fit values D_r and σ_{zero} for simulated and measured data are presented. For the last one the results for the two investigated gas mixtures Ar/CH_4 (95/5) and $Ar/CH_4/CO_2$ (93/5/2) are shown.*

Additionally Equation (7.1) is fitted to the results of all data sets shown:

$$\sigma = \sqrt{D_r^2 \cdot z + \sigma_{\text{zero}}^2}$$

The parameter σ_{zero} can be interpreted as the resolution at zero drift length. The dependency of the drift length is expressed with D_r. This parameter is closely related to the diffusion in the chamber, as discussed in Section 3.2.2.

The results of the fit are summarised in Table 8.1. As explained before, no results are presented for the case of the measurement with a non-staggered pad layout at a magnetic field of 4 T using $Ar/CH_4/CO_2$ (93/5/2). Additionally, it is clearly visible that the fit does not describe the data in the case of the staggered layout with the same gas mixture and the same magnetic field. Looking at the results for these settings determined with the Chi Square Method, the fit describes a constant function: $D_r = 0$. This underlines the conclusion that these results are highly limited by the systematic shifts caused by the PRF.

In the case of the gas mixture Ar/CH_4 (95/5), the fit can describe the data at all investigated magnetic fields. This includes the case of the simulated data. Therefore this gas mixture is discussed further.

To judge the resolution performance of a TPC, the parameter σ_{zero} can be used. Again, for the Global Fit Method the results for the staggered and the non-staggered pad layout show a difference which increases with the magnetic field.

The values determined by the fit to the results of the Chi Square Method show an agreement within the errors between the two investigated pad layouts. These values increase with the magnetic field. The errors are extracted from the fit. It should be mentioned, that the fit result for σ_{zero} is highly influenced by the data points at small drift length. The signal width is small for short drift lengths (see Table 7.4). Therefore, the correction of the systematic shifts caused by the PRF is limited. This effect becomes more important at higher magnetic fields.

The results for the measured data show a resolution around 100 µm for zero drift length. The results for magnetic fields of $B \leq 2\,\text{T}$ show that a spatial resolution of below 100 µm can be achieved. It must be pointed out, that these results are less influenced by systematic shifts, because the signal width is much broader. The results for the important case of a magnetic field of 4 T show values above 100 µm. This leads to the conclusion, that the PRF effect must be minimised for this case. The only possibility to achieve this is the optimisation of the ratio of the signal width to the pad width. Since the signal width can not be changed without choosing another gas mixture or modifying the amplification structure, the solution is to make the pads smaller. The aim for the ILC detector of a resolution under 100 µm over the whole drift length of 2 m, may be achievable with pads whose width is of the order of 1 mm. Studies are ongoing using the MediTPC with a new pad plane providing pads with a width of 1.27 mm.

Chapter 9

Summary, Conclusion and Outlook

9.1 Summary and Conclusion

9.1.1 Spatial Resolution

As the studies presented here show, the resolution measured with the setup described in Section 4.1 is mainly limited by a unoptimal ratio of the signal width to the pad width. The results for $Ar/CH_4/CO_2$ (93/5/2) show large systematic effects for the data sets which were measured at a magnetic field of 4 T. From the point of view of the resolution studies, Ar/CH_4 (95/5) is the better choice for the gas in a TPC with a GEM based readout. It provides a larger defocussing constant σ_0 than $Ar/CH_4/CO_2$ (93/5/2) and a smaller diffusion coefficient D_T, which leads to a smaller increase of the resolution value σ with the drift length.

From the results for a magnetic field $B \leq 2\,\mathrm{T}$, the conclusion can be drawn that a resolution σ_{zero} at zero drift of below 100 µm seems possible. But it must be pointed out, that in the presented analysis the value determined for the key setting for ILC of 4 T is above 100 µm. This is due to uncorrectable effects caused by the Pad Response Function. Because lower fields do not provide enough resolution for a larger drift length, this systematic effect must be minimised. This is possible by reducing the pad width.

With smaller pads it seems to be possible, that the resolution proposed for a TPC at the ILC can be achieved with a GEM based amplification system.

9.1.2 Test of the Fit Methods

The presented resolution has been calculated using two methods to determine the track parameters. These methods were tested using measured and simulated data. One method follows a traditional approach using a minimal least square technique to fit a curved track hypothesis to reconstruct three dimensional hits. This method is called the Chi Square Method. The second method which is called Global Fit Method makes use of a maximum likelihood technique. It fits a charge distribution which is given by the track parameters to the measured charge deposition. For this method three variations were tested, as it is explained in Section 7.4.

Both methods show similar results if they make use of information about the diffusion which is given by the diffusion coefficient D_T and the defocussing constant σ_0. In the case of the Chi Square Method using this information, it possible to minimise a systematic shift which is caused by the Pad Response Function. For the Global Fit Method, this means that

the width of the charge distribution in each row is fixed and not used as a free parameter in the fit.

Both methods suffer if a low number of rows is used in the fit. This leads to a bad ratio between the degrees of freedom and the number of data points. The setup used provided only six usable rows. Therefore, the methods were tested with simulated data sets that provided 19 rows. In all tests, the higher number of rows stabilises both fitting methods. For comparison with the measured data, all tests were performed with simulated data but using only six rows. The results for measured and simulated data exhibit similar behaviour.

The effect of damaged pads was studied by deactivating channels in the simulated data. It is small if the methods make use of the diffusion information. But some effects at small drift distances are not finally understood and need further studies.

The angular dependence of the PRF is not taken into account during the hit correction of the Chi Square Method. The tests show that this assumption is at least valid for inclination angles ϕ below 100 mrad. The results for larger angles are statistically Slimited.

9.2 Outlook

The studies presented show clearly that tests with a layout containing smaller pads and a larger number of rows are needed. Therefore, studies with the MediTPC using a modified pad layout with 14 rows and a pad size of $1.27 \times 7\,\mathrm{mm}^2$ have been started.

For further tests of the reconstruction method, the simulation program should be improved. A proper simulation of the electronics must be implemented. This includes possible cross talk between the pads and the effect of electronic noise.

Even though the effectivity of the Pad Response Function correction for the Chi Squared Method has been demonstrated, the influence of the threshold used during the determination of the PRFs should be investigated. During this study a threshold of 0.1‰ was used.

There are plans to build a larger prototype with a diameter of 80 cm. Its length in z will be 60 cm. It is designed to fit into the magnet test stand PCMag. This new magnet provides only a magnetic field of 1 T. But in contrast to the magnet for which the MediTPC was designed, the PCMag can be used at a test beam. The test stand is completed with silicon strip detectors which can be used as an external reference. This makes it possible to study the effect of inhomogeneities in the magnetic and the electric field. Also the tracking algorithms can be tested in a high density environment.

Part II

Search for Lepton Flavour Violating Leptoquarks in the HERA II Data of the H1 Experiment

Chapter 10

Overview

In the Standard Model, leptons and quarks balance each other out in the sense that a gauge theory with a different number of generation in the lepton and quarks sector is not renormalisable. A fundamental relationship between the lepton and the quark sector is not predicted by this theory. It is still an open question, if such a relationship exist, which would explain, that leptons and quarks are grouped into the same number of generations. As mentioned in Section 1.3, many theories exist which extend the Standard Model of particle physics by introducing this new relationship between the lepton and the quark sector. New particles are proposed which mediate this transition of quarks and leptons. These particles are named differently but the most suitable name may be *leptoquarks* (LQ).

The Buchmüller-Rückl-Wyler Model (BRW) [12] offers a description of 14 types of leptoquarks which are consistent with experimental observations. Details are presented in Section 12.3.

As the only *ep* collider in the world, HERA[1] is a unique facility to study the relationship between leptons and quarks including the search for leptoquarks. One of the experiments at HERA uses the multi-purpose detector H1, whose data is analysed in this thesis. The accelerator and the experiments are described in chapter 11.

The BRW model does not predict the flavour of the outgoing lepton in LQ mediated *ep* interactions. Therefore, an additional lepton flavour violation coupling (cf. Equation (12.8)) can be introduced. This thesis concentrates on final states with a muon as the outgoing lepton.

The production and decay of a lepton flavour violating leptoquark ($e^- q \to LQ \to \mu q$) would lead to an event topology with a high p_T muon and a jet back to back in the centre-of-mass system. This topology can be detected by a clear signal in many observables e. g. the muon momentum and an energy imbalance in the calorimeter. The SM background processes — as the production of lepton pairs, W-bosons and photons as well as neutral and charged current deep inelastic scattering — must be separated from a possible signal process. The signal selection is done by cuts on observables like the energy imbalance in the calorimeter (p_T^{calo}), the momentum imbalance ($V_{\text{ap}}/V_{\text{p}}$-ratio) and the difference of the azimuthal angle (ϕ) of the muon and the hadronic final state (HFS). The $e^- p$ data of the HERA II running period with a total integrated luminosity of $157.6\,\text{pb}^{-1}$ have been analysed. The performed search with a signal efficiency between 25% and 75% results in an observation of two data events. This is in good agreement with the SM expectation of 2.2 ± 0.6 events.

[1] **H**adron-**E**lektron-**R**ing-**A**nlage: German for Hadron-Electron-Ring-Accelerator.

Due to the low statistics of the signal selection, control selections with an increased number of selected events are investigated. A selection of charge current deep inelastic scattering (CC DIS) events prove the understanding of the HFS. In a second selection, the cuts on the muon quantities are relaxed to test the understanding of the muon description by the Monte Carlo simulation.

While no evidence for lepton flavour violation has been observed, limits for various combinations of the leptoquarks mass m_{LQ} and the coupling $\lambda_{\mu q} = \lambda_{eq}$ are deduced. Here, the modified frequentist approach is used to calculate the limit with a confidence level of 95%. The leptoquarks described in the BRW model are grouped by the Fermion number $F = |L + 3B|$, where L and B denote the lepton and baryon number, respectively. This number can be zero or two (see Table 12.1). While the leptoquarks with $F = 0$ couples mainly to e^+p, the limits are calculated only for the seven leptoquarks with $F = 2$. These are mainly produced in the e^-p collision.

Chapter 11

Experimental Setup: Accelerator and Detector

This chapter presents the DESY accelerator HERA and the H1 experiment which collected the data used for this analysis.

11.1 HERA

The HERA accelerator was operated from 1992 to mid 2007 as the only electron-proton collider in the world. It consisted of two separate storage rings which were located in a 6.3 km long tunnel. The protons p were accelerated to an energy of 820 GeV till 1998 and to 920 GeV afterwards. The electron energy amounted to 27.6 GeV which was much lower than the proton energy due to higher energy loses by synchrotron radiation. This led to a centre of mass energy of $\sqrt{s} = 319$ GeV for a proton energy of 920 GeV. The time interval between two bunches was

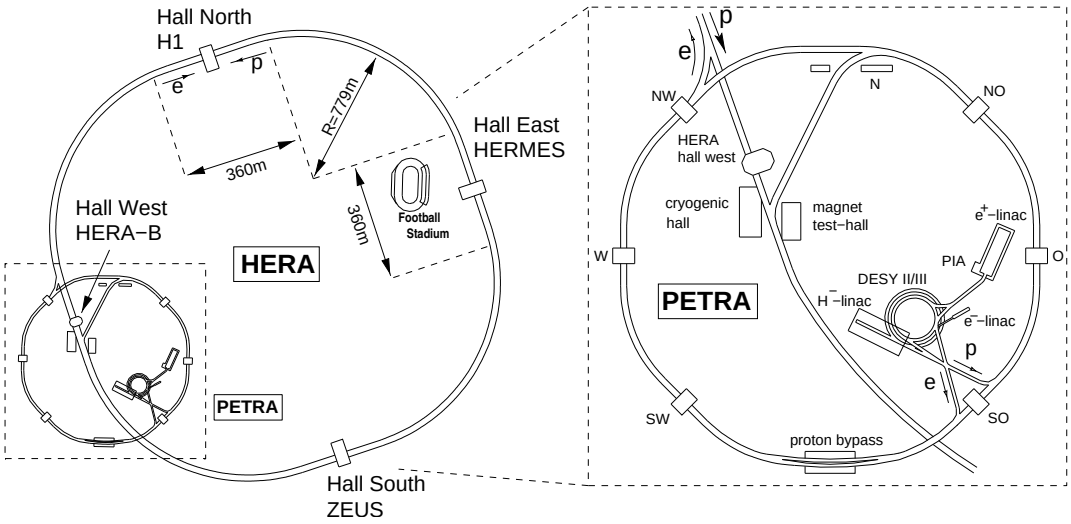

Figure 11.1: *Schematic top view of the HERA collider. The four experiments H1, ZEUS, HERMES and HERA-B are shown. On the right hand side, the pre-accelerator system is depicted enlarged.*

96 ns which led to a repetition rate of 10.4 MHz for the four experiments. As depicted in Figure 11.1, the two multi-purpose detectors H1 and ZEUS were located at the interaction regions where the two beams collided. After an upgrade in 2000 (HERA II phase) a luminosity in the order of $2 \times \cdot 10^{-31}\,\mathrm{cm}^2/\mathrm{s}$ was provided. The two other experiments HERA-B (till 2003) and HERMES used a fixed target and only one of the beams.

11.1.1 Polarisation at HERA

In the accelerator, the particles were held on their track by a homogeneous magnetic field perpendicular to the beams. Due to the acceleration by the magnetic field they emitted synchrotron radiation. Synchrotron radiation is linearly or elliptically polarised. This can change the orientation of the spin of the particle to be parallel or antiparallel to the magnetic field. The probabilities for the transition of spins along the field and against differ. Due to this difference a transversal polarisation builds up in storage rings after a large number of circulations.. This effect is known as the Sokolov-Ternov effect [55]. The rise time for an appreciable transverse polarisation was of the order of 40 min. For many analyses, the longitudinal polarised leptons are of interest, which will change the cross section for some SM processes: e. g. charge current deep inelastic scattering. During the HERA II upgrade, spin rotators were installed, which rotate the polarisation plane of the leptons. This is depicted in Figure 11.2.

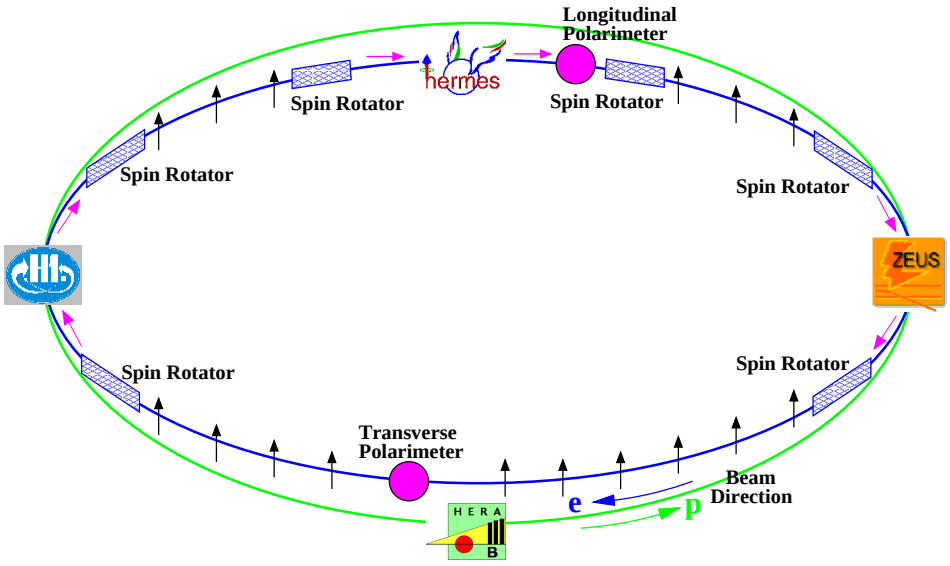

Figure 11.2: *Polarisation at HERA: The arrangement of the spin rotators and the position of the polarimeter are shown. The arrows indicate the spin direction of the lepton in the beam.*

The figure also shows the position of two polarimeters, which measured the polarisation using two different methods. Both methods were based on the Compton scattering of polarised photons on the leptons. The TPOL measured the transverse polarisation of the non rotated lepton spin [56]. After the spin rotation, the longitudinal polarisation was measured with the LPOL [57].

11.2 The H1 Detector

A schematic view of the H1 experiment is shown in Figure 11.3 on page 100. It was a typical multi-purpose detector with an asymmetric structure due to the large energy difference of the beams. This difference led to a boost in the direction of the incoming proton which defines the forward direction and the z-axis of the coordinate system. The right handed coordinate system is completed by the horizontal x- and the vertical y-axis. The angle ϕ is measured in the xy-plane to the x-axis and θ is the angle to the z-axis, whereas $\theta = 0$ means the forward direction.

The following description highlights the main components and starts from the innermost point of the detector. A full and more detailed description of the H1 detector can be found in [58].

11.2.1 Tracking System

As described in Part I the purpose of tracking systems is the measurement of the trajectory of charged particles. The H1 tracking system consisted of silicon trackers, drift chambers and multi wire proportional chambers (MWPC). It provided a full azimuthal acceptance and could measure particles in the polar angle region $5° < \theta < 178°$. Due to the asymmetric design of the detector, the tracking system is separated into a central and a forward part, which can be seen in Figure 11.4.

Central Tracking Detectors

The central part of the detector was surrounded by a superconducting solenoid providing a magnetic field of 1.15 T. From the curvature caused by a magnetic field the momentum of the particles could be determined. The Central Tracking Detectors (CTD) were subdivided into a vertex detector which was cylindrically aligned around the elliptic beam pipe followed by proportional and jet chambers.

Silicon Tracker The HERA II upgrade of the H1 detector included the installation of three silicon trackers: The Central (CST), the Forward (FST) and Backward Silicon Tracker (BST). The main task of the three silicon trackers was the determination of vertices. Thereby, the primary vertex is defined by the colliding particles, while the secondary vertices have their origins in decays of long-living particles which travel several hundreds of micrometers. The silicon trackers provided a very good measurement of tracks with an accuracy of $\sigma_{r\phi} = 12\,\mu\text{m}$ and $\sigma_z = 22\,\mu\text{m}$.

The CST covered the area of $30° < \theta < 150°$, while the FST had an angular acceptance of $8° < \theta < 16°$. The BST additionally assisted the identification of electrons at large angles of θ with a range of $162° < \theta < 176°$.

Proportional Chambers The following Central Inner Proportional chamber (CIP2000) was a MWPC (see Part I Section 3.2.2) as was the Central Outer Proportional chamber, which was located between the jet chambers. The CIP2000 replaced the former CIP and Central Inner Z chamber (CIZ) of the HERA I period. It provided a very fast signal with a timing resolution of 21 ns. Therefore, it was used as a trigger for ep collision events coming from the nominal vertex.

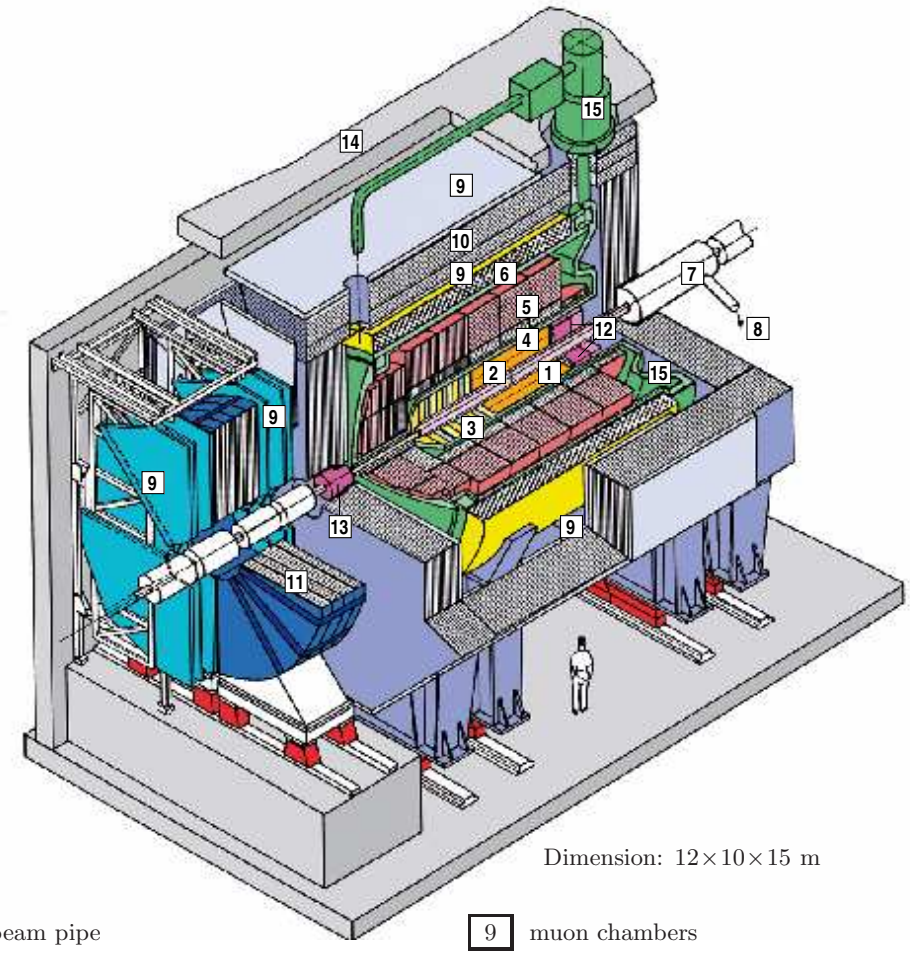

Dimension: 12×10×15 m

1	beam pipe	9	muon chambers
2	central tracking chambers	10	instrumented iron
3	forward tracking chambers	11	muon toroidal magnet
4	electromagnetic LAr calorimeter (lead)	12	warm calorimeter (SPACAL)
5	hadronic LAr calorimeter (stainless steel)	13	forward calorimeter
6	superconducting solenoid	14	concrete shielding
7	compensating magnet	15	cryostat
8	Helium cooling		

Figure 11.3: *A three-dimensional view of the the H1 detector with the main detector components.*

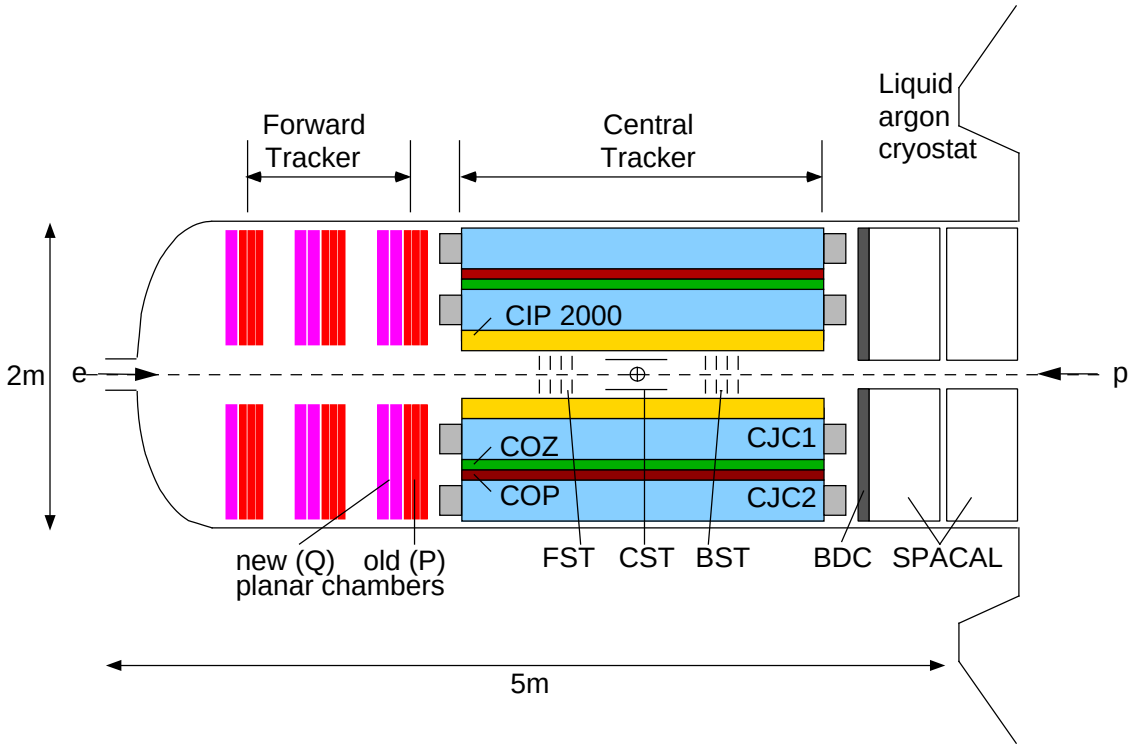

Figure 11.4: *The H1 tracking system: Schematic view of the Central and Forward Tracker in the rz-plane. Additionally the SpaCal is shown on the right side.*

Central Jet Chamber The Central Jet Chamber CJC1 (CJC2) consisted of 30 (60) cells with 24 (32) sense and 49 (66) cathode wires. The jet cell were rotated by 30° with respect to the radial direction so that the produced electrons drifted almost perpendicular to the track trajectory. They provided a good spatial resolution of $\sigma_{r\phi} = 170\,\mu\text{m}$ and $\sigma_z = 4\,\text{cm}$. The z information was determined by the measurement of the charge division at the end of the sense wires. This spatial resolution can be transferred in a momentum resolution of $\frac{\sigma_{p_T}}{p_T^2} = 0.01\,^{\text{c}}/_{\text{GeV}}$. Both were filled with a gas mixture of $\text{Ar}/\text{CH}_6/\text{CH}_6\text{O}$ with a proportion of 49.5/49.5/1. Their dimensions and placements are shown in Table 11.1.

As mentioned before, the two jet chambers were separated by the COP and the Central Outer Z chamber (COZ). The COZ provided a much better resolution in the z-direction of $\sigma_{rz} = 380\,\mu\text{m}$.

	radial r (mm)	**z (mm)**	**polar θ (°)**
CIP2000	150 — 200	-1100 — 1100	8 — 172
CJC1	203 — 451	-1125 — 1075	11 — 170
COZ	460 — 485	-1105 — 1055	25 — 156
COP	493 — 523	-1107 — 1165	25 — 156
CJC2	530 — 844	-1125 — 1075	26 — 154

Table 11.1: *Dimensions of the H1 Central Tracking System: Radial and z positions with respect to the nominal vertex and the corresponding polar angle acceptance are specified.*

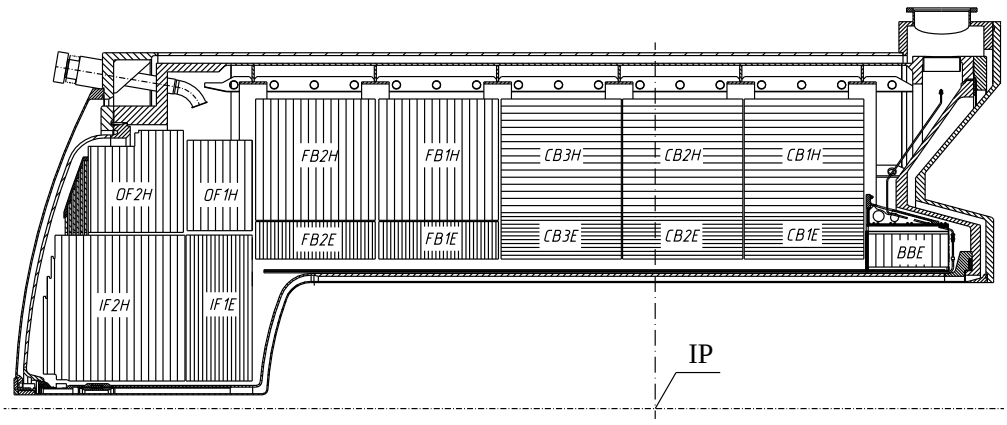

Figure 11.5: *Side view of one half of the LAr calorimeter: The cryostat, the segments and their orientation can be seen.*

Forward Tracking Detectors

The Forward Tracking System is shown on the left-hand side in Figure 11.4 and covered the angular range of $7° < \theta < 25°$. It was divided into three supermodules. Each of these modules consisted of three planar chambers (P), which were already installed during the HERA I phase. During the upgrade the MWPCs and the transition radiation detectors were removed and planar chambers (Q) were added. Seen from the direction of the CJC, the first two modules got two new chambers behind the old ones and the last module only one new chamber. The old chambers, in which each cell had four wires, were oriented with respect to the y-axis at $0°$, $+60°$ and $-60°$. The new chambers had eight wires and were oriented at $+30°$ and $+90°$.

11.2.2 Calorimeter

The tracking system was surrounded by the calorimeters. The central and forward direction was covered by the Liquid Argon calorimeter (LAr) and the backward direction was covered by the Spaghetti Calorimeter (SpaCal). The main task of the calorimetry is the energy measurement of charged and neutral particles.

Liquid Argon Calorimeter

The Liquid Argon calorimeter (LAr) was placed inside the magnetic coil to minimise the passive material in front of the measurement which ensured a better energy resolution. As shown in Figure 11.5 the LAr covered a large angular range of $4° < \theta < 154°$. Expressed in pseudorapidity

$$\eta = -\ln\left(\tan\frac{\theta}{2}\right), \tag{11.1}$$

a unit often used in boosted systems, the coverage is $-1.47 < \eta < 3.35$.

The LAr was a sampling calorimeter which used, as the name implies, liquid argon as the active material. The liquid argon had to be cooled down to $T = -183°\,\mathrm{C}$. It ensured a good stability and provided a simple calibration, a fine transverse granularity and homogeneity of signal response. The readout modules were mounted on the absorber plates.

The calorimeter was separated into an inner electromagnetic and an outer hadronic part. The electromagnetic part used a lead absorber with a thickness of 2.4 mm and a 2.35 mm gap in between. In total, its depth was 20 to 30 radiation lengths. The cell structure provided a high granularity. In contrast, the hadronic part was less granular. It covered five to eight nuclear interaction lengths generated by stainless steel absorber plates with 16 mm thickness with absorber gaps of 12 mm. These gaps conained 2×1.5 mm stainless steel and 2×2.4 mm liguid argon [59].

In the longitudinal direction, the LAr was segmented into eight wheels. All segments, which are named in Figure 11.5, were placed inside a cryostat. The layers were oriented concentrically in the central and backward parts and in the $r\phi$ plane in the forward direction. This ensured impact angles of more than 45°.

As a non-compensating calorimeter, the energy deposit by strongly interacting particles was smaller than that from electromagnetically interacting particles with the same input energy. This effect must be corrected during the reconstruction. The energy resolution of the calorimeter is for hadrons $\sigma_{\mathrm{had}}(E)/E = \frac{50\,\%}{\sqrt{E\,\mathrm{GeV}^{-1}}}$ [60] and for electrons $\sigma_{\mathrm{el}}(E)/E = \frac{12\,\%}{\sqrt{E\,\mathrm{GeV}^{-1}}}$ [61]. The systematic error of the energy scale for hadrons (electrons) is 2% (1%), which is presented in Section 13.1.3.

Additionally the PLUG in the very forward part of the H1 detector extended the θ acceptance below 4°. The instrumented iron served as tail catcher for particles penetrating the whole calorimeter and the coil.

Spaghetti Calorimeter (SpaCal)

As depicted in Figure 11.4 the Spaghetti Calorimeter (SpaCal) was plugged into the backward region which is not covered by the LAr. It provided an angular acceptance of $153° < \theta < 177.8°$. The main task was to detect the scattered electrons coming from ep interaction. Electrons which were scattered into the backward region have a p_T^2 below $150\,\mathrm{GeV}^2/\mathrm{c}^2$ and hence the SpaCal is of minor relevance for this analysis. Scintillating fibre bundles traversed the lead absorber. They gave the calorimeter its name as it looked like a package of spaghetti when viewed from the interaction point. The fibres were read out with photomultiplier. They provided an accurate position and fast timing information. With a timing accuracy of 1 ns this signal was used for the time of flight measurement and triggering.

11.2.3 Muon System

Muons are minimal ionising particles and lose only small amounts of their energy in calorimeters. Therefore, in contrast to other particles, which are most likely stopped inside the calorimeter, the muons escape the detector. To identify muons and measure their trajectory a muon system surrounded the detector. Analogous to the tracking system, it was split into a forward and a central part.

Central Muon Detector

The Central Muon Detector (CMD) formed an octagonal barrel which enclosed the inner part of the H1 detector. It was the outermost hermetic component and covered the full azimuthal angular range and the polar angle range of $5° < \theta < 175°$.

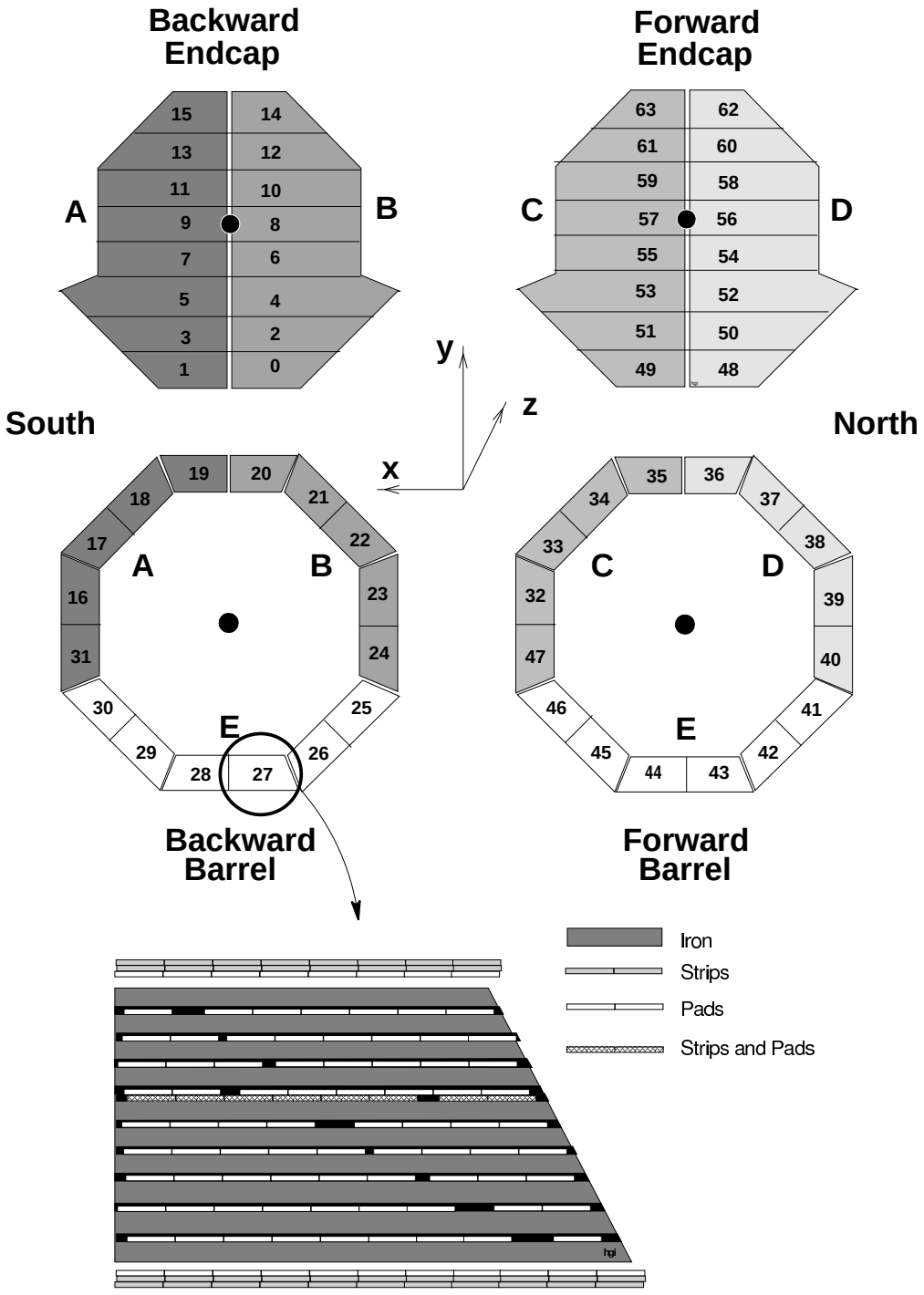

Figure 11.6: *Layout of the Central Muon Detector: The arrangement of the 64 modules is shown. One module is pictured in detail.*

As shown in Figure 11.6, it consisted of streamer tubes in the iron return yoke and inner and outer muon boxes on both sides of iron. These three additional active layers improved the muon tracking and linking and the coverage of the edges.

In the z-direction a forward and a backward end cap completed the CMD. Both caps were composed of 16 modules with different scape and orientation as shown in Figure 11.6.

Forward Muon System

The Forward Muon Detector (FMD) covered the angular range of $3° < \theta < 17°$. Its purpose was the precise measurement of muons with an energy larger then 5 GeV. A toroidal magnet was inserted between a module on each side at z =6.4 m and 9.4 m. Both modules consisted of two layers with circular wires measuring θ and one with radial wires, which measured ϕ. The whole system is shown in Figure 11.7.

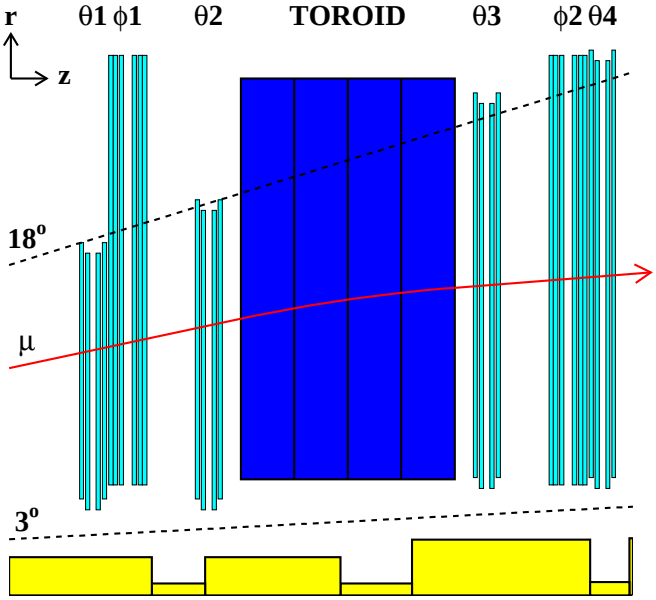

Figure 11.7: *Profile of the Forward Muon Detector: The six drift chambers are named after their position (θ_1-θ_4 and ϕ_1-ϕ_2).*

11.2.4 Time of Flight System

All events of physical interest originate from the *ep* collisions in the norminal interaction region. Therefore the HERA clock time of 96 ns was used to suppress processes out of the time. Such events are very likely to be background processes originating from interactions of the beam and the remaining gas (beam gas interaction) or of the beam halo and the beam pipe. To detect those events precise timing information is needed which was provided by plastic scintillators at various places. The main two scintillators of the Time of Flight System (ToF) were called veto-wall and placed at $z = -8.1$ m and -6.5 m.

11.3 Luminosity System

For most analyses in high energy physics, the integrated Luminosity

$$\mathscr{L} = \int L dt = \frac{\sigma}{n} \tag{11.2}$$

L : luminosity
$$\frac{dn}{dt} = \sigma \cdot L$$
σ : cross section of the process
n : number of events of the process

must be known. In the H1 experiment, the Bethe-Heiter process $ep \to ep\gamma$ is used to determine the luminosity $\mathscr{L}$. It provides a high cross section which can be precisely calculated using the theory of quantum-electro-dynamics (QED).

In most cases the electron was scattered under a small angle and escaped into the beam pipe where it was deflected by the various magnets of the beam system. The photons produced were not influenced by the magnetic fields and travelled in a straight line. Therefore the luminosity system was located down the beam pipe, as it is shown in Figure 11.8. It consisted of an Electron Tagger (ET) at $z = -33.9\,\mathrm{m}$ and Photon Tagger (PT) at $z = -102.9\,\mathrm{m}$. Both were placed close to the beam pipe.

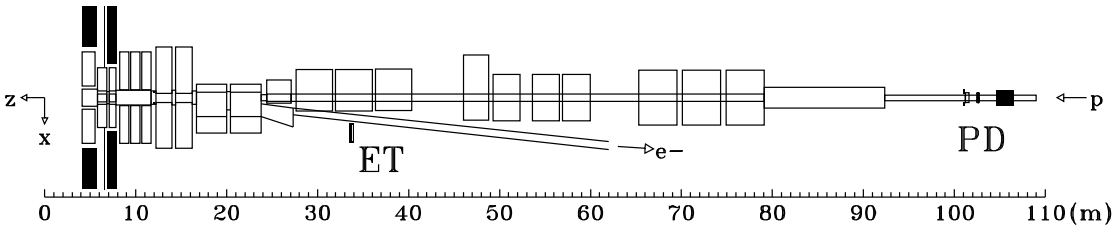

Figure 11.8: *The H1 Luminosity System: The Electron Tagger (ET) at $z = -33.9\,\mathrm{m}$ detects the electrons which are scattered at a very small angle. Photons are detected by the Photon Tagger (PT) at $z = -102.9\,\mathrm{m}$.*

For online control, the luminosity was measured by simultaneous hits in both taggers. Offline the luminosity can be verified by measuring the photon rate above a certain energy threshold. The main background processes are bremsstrahlung and beam gas interactions. Their rate could be measured with the pilot bunches, which were e bunches traversing the H1 detector without any matching p bunch. The precision of the luminosity measurements during the HERA II phase was $\Delta\mathscr{L} = 4\,\%$.

11.4 Data Acquisition and Trigger System

As mentioned before, collisions in HERA took place at a rate of 10.4 MHz. Events of physical interest were mixed with other unwanted events like cosmic particles, beam gas, beam pipe interaction (see Section 11.2.4) or noise of the detector's electronics. The data of the H1

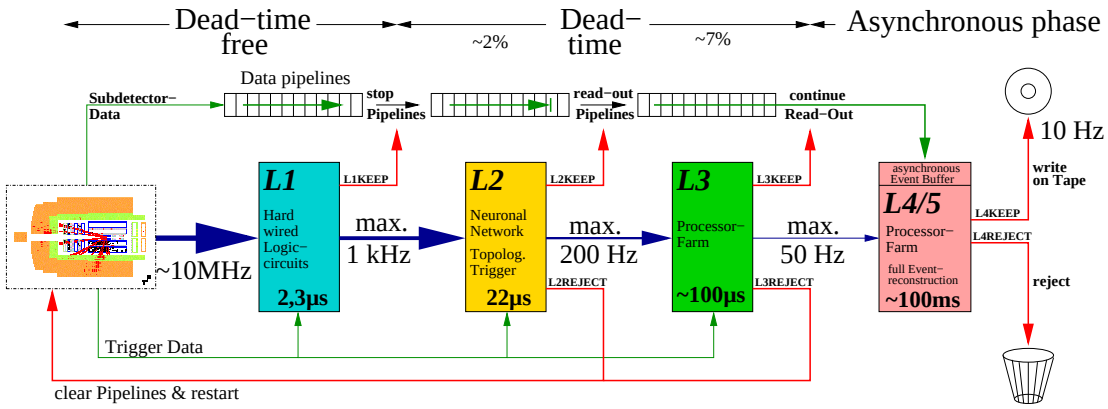

Figure 11.9: *The H1 Trigger System: The data flow through the four trigger levels is shown. The levels L1, L2 and L3 are working synchronised to the HERA clock. Only the first level is dead time free.*

detector could be written to disk with approximately 10 Hz. Hence a sophisticated trigger system was needed which took the decision of rejecting or keeping an event. Figure 11.9 shows the different levels of the system, which are described in the following paragraphs.

The raw data supplied by the detector parts were written in a circular pipeline, which means that the oldest data in the pipe was automaticly overwritten by the newest ones. The first level (L1) of the trigger was purely hardware based. It was composed of 256 trigger-elements, which were combined to 128 subtriggers. In an ideal case, every keep decision of every subtrigger would be passed to the next level, but to reduce the rate some subtriggers were prescaled. This means that only for each n-th event was the keep decision passed. L1 took only 2.3 µs for a decision and due to the pipeline caused no dead time of the detector.

The second level L2 needed 22 µs for a decision. It validated the L1 decision using a neural network and topology combinations. A keep decision of L2 had stopped the pipeline and triggered a readout of the full detector. This was the beginning of the dead time of the detector.

The next trigger level (L3) was not active until the beginning of 2006 [62]. Its input rate was around 200 Hz. It consisted of several Power PCs, which came to a decision in 100 µs.

Since the beginning of the HERA II phase in the year 2000 the last two levels were combined into one, called L4/L5. Its maximum input rate was 50 Hz. When the rate given by L3 was too high then prescales were used in L1. In this step a full event reconstruction was done by a Linux processor farm. Each event requires 100 to 150 kB and needed more than 500 ms for the reconstruction. Therefore this level ran asynchronous to the detector and the other levels.

11.5 Detector Simulation

In any high energy physics analysis a deep understanding of the detector response is needed to compare recorded data with the prediction made by several theory models. This includes studies of the geometrical acceptance, intrinsic relations of the different parts of the detector and the impact of the material on the response. Therefore the H1 detector is modelled in a detailed simulation using the framework GEANT3 [63]. It includes the instrumented part of

the detector as well as the passive material.

The simulation input are four-vectors of the particles of the final state which are obtained from a Monte Carlo generator. In the first step the following physical event features are produced: particle tracks and their behaviour in a magnetic field, generation of secondary particles, showering and fragmentation.

The outcome is processed during a second step which simulates the response of the active parts of the detector. This step generates the same output format as the measured raw data. Therefore, in the last step the same reconstruction process is used as for the real data.

Studies with data of cosmic rays and test beams demonstrated that simulated events can be compared with data. This makes offline modelling of the detector possible, which is essential for the comparison of nature with theoretical predictions.

Chapter 12

Introduction and Theory

This chapter will give an introduction to the physics of ep collisions. Besides the Standard Model processes like deep inelastic scattering, the production of Leptoquarks will be described. Here, the Buchmüller-Rückl-Wyler Model (BRW) will be presented as well as the topology of a lepton flavour violating leptoquark decay in the H1 experiment. Further possible background processes with a similar topology will be described and published limits on the mass of leptoquarks will be shown.

12.1 Standard Model Physics in *eq* Collisions

In experiments undertaken at HERA matter and its interactions are investigated. In two of these experiments, electrons or their anti-particles positrons[1] collided with protons. The electron interacted with a parton of the proton via the exchange of a gauge boson. The virtuality of this gauge boson is expressed by Q^2. Processes at high values of Q^2 are able to resolve the quark structure of protons and are therefore called deep inelastic scattering (DIS). Figure 12.1 shows the appropriate Feynman diagram.

DIS is divided into two sub-processes, which are discerned by the charge difference of the incoming and the outgoing lepton. In the neutral current process (NC), a γ or Z_0 are exchanged. Since both are neural and take no charge with them, the outgoing leptonic particle is the scattered electron. If a $W^{\pm}$ is transferred, the outgoing lepton is an electron-neutrino ν_e. While the charge difference is non zero, this process is called charged current (CC).

If $Q^2 \approx 0$, a real photon is exchanged and the process is referred to as photoproduction.

[1] In this section the term electrons will be used synonymous for both electrons or positrons, except where it is explicitly mentioned.

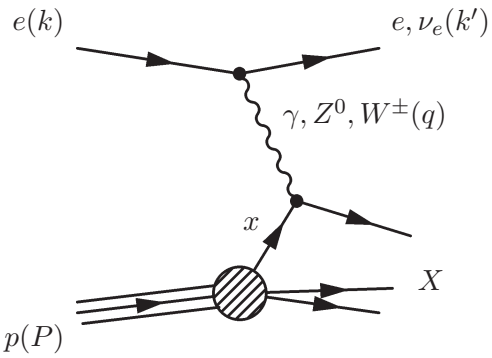

Figure 12.1: *Tree level Feynman diagram of NC/CC DIS in ep collisions: The four-momenta of the incoming (outgoing) lepton e or ν_e are labelled with k (k′). Resulting q is the four-momentum of the exchanged gauge boson. P denotes the four-momentum of the proton p and x is the momentum fraction carried by the struck quark. X represents the hadronic final state.*

12.1.1 Kinematics

The kinematics of the interaction is described by the following ensemble of Lorentz-invariants:

$$Q^2 = -q^2 = -(k - k')^2 \tag{12.1a}$$
$$W^2 = (P + q)^2 \tag{12.1b}$$
$$s = (P + k)^2 \tag{12.1c}$$
$$x = \frac{Q^2}{2Pq} \tag{12.1d}$$
$$y = \frac{Pq}{Pk} = \frac{1}{2}(1 + \cos\theta^*) \tag{12.1e}$$

As depicted in Figure 12.1, the proton four-momentum is given by P. The four-momentum of the exchanged gauge boson q is derived from the four-momenta of the incoming and outgoing leptons k and k'.

W^2 is the squared centre of mass energy of both the boson-proton subsystem and of the hadronic final state X. The centre of mass energy of the *ep* system is

$$\begin{aligned} \sqrt{s} &\approx \sqrt{4E_e E_p} \\ &= \sqrt{4 \cdot 27.6\,\text{GeV} \cdot 920\,\text{GeV}} \approx 319\,\text{GeV} \end{aligned} \tag{12.2}$$

and depends only on the energy of the initial particle, which is defined by the storage ring. The range of the Bjørken scaling variables x and y is limited to $0 < x, y < 1$. In the proton rest frame, y can be understood to be the relative energy transfer to the proton. The fraction of the proton momentum carried by the struck parton or quark is given by x [64].

In the interpretation of the proton in the infinite momentum frame, the three quarks act as free particles which is referred to as asymptotic freedom [65]. At lowest order, DIS can be understood as a two-body process between the probing electron and a quark. Due to energy conservation two kinematic variables are sufficient, if initial and final state radiation

(ISR/FSR) can be neglected. Usually x and Q^2 are the preferred choice. For centre of mass energies in the order of 100 GeV, the mass term can be neglected and the following relationships are valid:

$$Q^2 = xys \tag{12.3a}$$

$$W^2 = \frac{Q^2}{x} - Q^2 \ . \tag{12.3b}$$

12.2 Deep Inelastic Scattering

The double differential cross section for both DIS processes is given by [66]:

$$\frac{d^2\sigma^{e^\pm p}_{NC}}{dxdQ^2} = \frac{2\pi\alpha^2}{xQ^4} \left[Y_+ F_2^{NC\pm} \mp Y_- F_3^{NC\pm} - yF_L^{NC\pm}\right] \tag{12.4a}$$

$$\frac{d^2\sigma^{e^\pm p}_{CC}}{dxdQ^2} = \frac{G_F^2}{2\pi x}\left(\frac{m_W^2}{m_W^2+Q^2}\right)^2 \left[Y_+ F_2^{CC\pm} \mp Y_- F_3^{CC\pm} - yF_L^{CC\pm}\right](1 \pm P) \tag{12.4b}$$

$$\text{with} \qquad Y_\pm = 1 \pm (1-y)^2 \,,$$

where α defines the fine structure constant and $G_F^2 = 1.666 \cdot 10^{-5}\,\text{GeV}^{-2}$ the Fermi constant. The so called structure functions $F_i^{NC,CC\pm} = F_i^{NC,CC\pm}(x, Q^2)$ take into account that the proton enters the interaction as a composite object. They are related to the parton density functions (PDF) and differ for the neutral and charge current cross section. The PDF defines for the scale Q^2, the probability of finding a parton of type i with momentum fraction x. The CC DIS cross section depents on the polarisation of the incoming lepton (P).

In the interpretation of accelerator experiments as microscopes, the spatial resolution power is given by the squared momentum transfer. This leads to a resolution of 10^{-18} m for HERA providing a $Q^2 \approx 3 \cdot 10^4\,\text{GeV}^2$. So HERA, viewed as a top-performing microscope, can determine the structure functions and the PDFs with a high precision measurement of the NC/CC cross section for ep interactions. Figure 12.2 shows such a measurement. From the good agreement between the measured cross section and the prediction, it can be deduced that the quarks have no substructure down to 10^{-18} m [67].

12.3 Leptoquarks and Lepton Flavour Violation

As explained in Section 1.3, the Standard Model (SM) has its limitations. The symmetry between the quark and lepton sectors leads to suggestions for a more fundamental theory in which both should be closely related. In some extentions of the SM, new particles are introduced which mediate a transition of quarks and leptons. As mentioned before, a generic name for these particles may be *leptoquarks* (LQ).

As this name implies, leptoquarks describe the interaction of a lepton and a quark at the same vertex via a Yukawa coupling. This kind of process can violate the baryon and lepton numbers (see Section 1.2). If these quantum numbers are no longer conserved, a proton decay may be possible. This has not been observed. The lower limit for the proton lifetime is 10^{29} years [2].

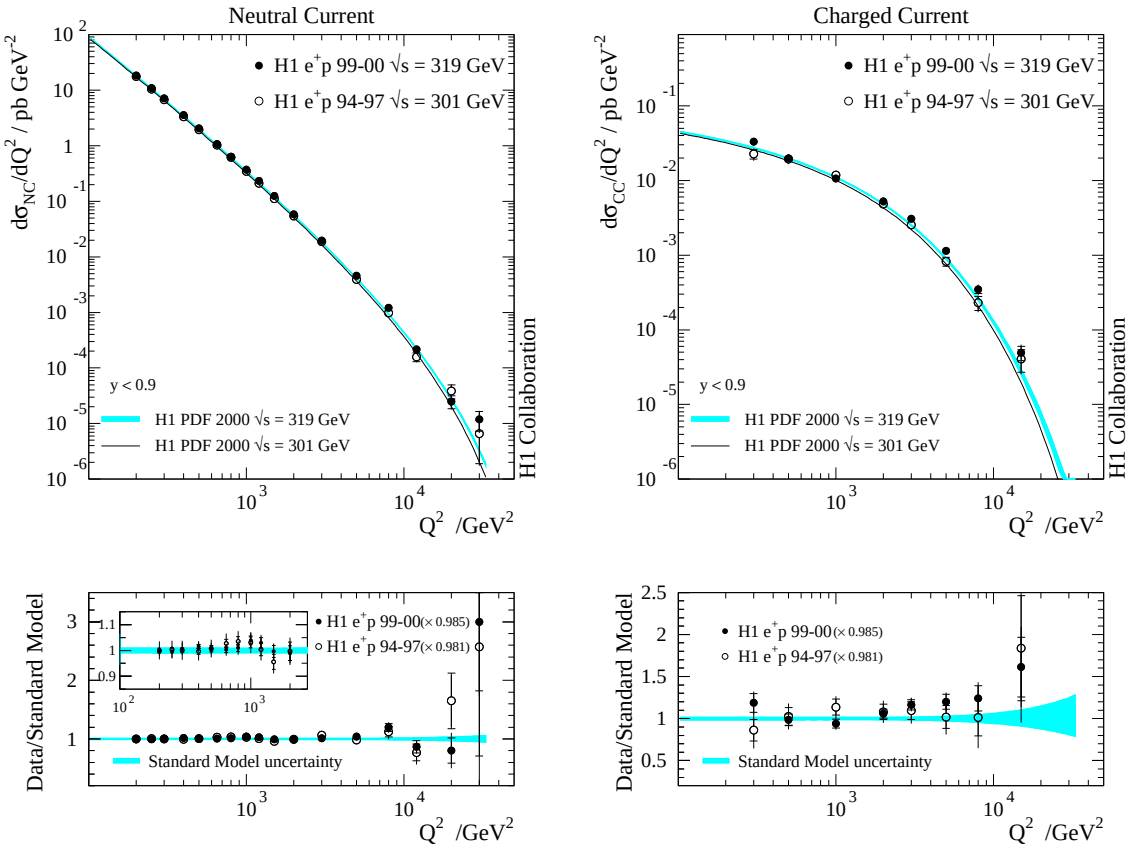

Figure 12.2: *H1 measurements of NC/CC DIS cross sections [66].*

Furthermore, LQs are coloured triplet bosons with a fractional charge carrying either spin 0 (scalar) or spin 1 (vector). The fermion number

$$\begin{aligned} F &\equiv |L + 3B| \qquad (12.5)\\ B &: \text{ baryon number}\\ L &: \text{ lepton number}\\ &\quad \text{(not to be mixed up with the lepton flavour number } L_i\text{)} \end{aligned}$$

is a useful definition for the description of this kind of particles. Leptoquarks with $F = 0$ couple to pairs of either lepton and quark or antilepton and antiquark. Contrarily the transition between lepton and antiquark or antilepton and quark are mediated by leptoquarks with $F = 2$. Thus the LQ signal possible at HERA is the interaction between an electron with a u- or d-type quark or their anti-particles.

It is possible to formulate a general dimensionless, $SU(3)_C \times SU(2)_L \times U(1)_Y$ invariant coupling which satisfies baryon and lepton number conservation [12]. In this formalism the following effective Lagrangian for scalar (S) and vector (V) leptoquarks can be written down:

$$\mathcal{L} = \mathcal{L}_{F=2} + \mathcal{L}_{F=0}\ , \quad \text{with} \tag{12.6a}$$

$$\begin{aligned}\mathcal{L}_{F=2} =& \Big[\Big(\lambda_L^{S_0}\bar{q}_L^c i\tau_2 l_L + \lambda_R^{S_0}\bar{u}_R^c e_R\Big)S_0^\dagger + \Big(\lambda_R^{\tilde{S}_0}\bar{d}_R^c e_R\Big)\tilde{S}_0^\dagger + \\ & \Big(\lambda_L^{\tilde{S}_1}\bar{q}_L^c i\tau_2\vec{\tau} l_L\Big)\vec{S}_1^\dagger + \\ & \Big(\lambda_L^{V_{1/2}}\bar{d}_R^c\gamma_\mu l_L + \lambda_R^{V_{1/2}}\bar{q}_L^c\gamma_\mu e_R\Big)V_{1/2}^\dagger + \Big(\lambda_L^{\tilde{V}_{1/2}}\bar{u}_R^c\gamma_\mu l_L\Big)\tilde{V}_{1/2}^\dagger\Big] + c.c.\ ,\end{aligned} \tag{12.6b}$$

$$\begin{aligned}\mathcal{L}_{F=0} =& \Big[\Big(\lambda_L^{V_0}\bar{q}_L\gamma_\mu l_L + \lambda_R^{V_0}\bar{d}_R\gamma_\mu e_R\Big)V_0^\dagger + \Big(\lambda_R^{\tilde{V}_0}\bar{u}_R\gamma_\mu e_R\Big)\tilde{V}_0^\dagger + \\ & \Big(\lambda_L^{\tilde{V}_1}\bar{q}_L\vec{\tau}\gamma_\mu l_L\Big)\vec{V}_1^\dagger + \\ & \Big(\lambda_L^{S_{1/2}}\bar{u}_R l_L + \lambda_R^{S_{1/2}}\bar{q}_L i\tau_2 e_R\Big)S_{1/2}^\dagger + \Big(\lambda_L^{\tilde{S}_{1/2}}\bar{d}_R l_L\Big)\tilde{S}_{1/2}^\dagger\Big] + c.c.\,.\end{aligned} \tag{12.6c}$$

To avoid a decay of the proton, this Buchmüller-Rückl-Wyler Model (BRW) is constructed in a way that no LQ type couples simultaneously to a u-type and a d-type quark.

In this thesis the Aachen notation is used, which differs from the notation used in [12]. In the following, $SU(2)$ singlet, doublet and triplet are labelled with subscript 0, 1/2 and 1 according to their weak isospin. It is assumed that the doublets and triplets degenerate in mass. L, R denote the lepton chirality: $\lambda_L^{S_0}$ signifies the Yukawa coupling of a scalar leptoquark with weak isospin of 0 to a left handed fermion which can be either a lepton or a quark. The left-handed quark and lepton doublets are labelled with q_L and l_L, while e_R, u_R, d_R represent the right-handed electron, u- and d-type quarks. The charge conjugate fermion field is denoted with *c.c.*.

Equations (12.6) imply the existence of ten different types of leptoquarks. Four of them couple to both chiralities. The Aachen notation distinguishes between leptoquarks coupling to left- and right handed leptons as different types. Therefore a superscript specifying the chirality is added.

The resulting 14 different types of leptoquarks being discerned are summarised in Table 12.1. Their quantum numbers, like spin J, fermion number F and charge Q, are given as well as the dominant process in ep scattering. It can be seen that leptoquarks with $F = 2$ are produced in collisions of e^-p, whereas for $F = 0$ leptoquarks e^+p is the main production channel. Due to the lower parton density of anti-quarks, which appear only as sea-quarks, the charge conjugate processes ($e_R^+\bar{u}_L \to l^+\bar{u}$) are suppressed, especially at high LQ masses resulting in high values of x.

Additionally, the coupling strength and the branching ratio

$$\beta_l = \frac{\Gamma_l}{\Gamma_l + \Gamma_{\nu_l}} \tag{12.7}$$

complete Table 12.1. To introduce lepton flavour violation an additional branching ratio is added:

$$\mathrm{BR} = \beta_l \times \beta_{LFV}\ , \quad \text{where}\ \ \beta_{LFV}^{\mu,\tau} = \frac{\Gamma_{\mu,\tau}}{\Gamma_\mu + \Gamma_\tau + \Gamma_e}\,. \tag{12.8}$$

12.3.1 Leptoquark production at HERA

Some of the leptoquarks in Table 12.1 ($S_1^L, V_{1/2}^R, V_1^L, \tilde{S}_{1/2}^L$) couple both to u- and d-type quarks. The decay width for both types is assumed to be equal.

type	J	F	Q	ep dom. process	β_l
S_0^L	0	2	$-1/3$	$e_L^- u_L \rightarrow \begin{cases} l^- u & 1/2 \\ \nu_l d & 1/2 \end{cases}$	
S_0^R	0	2	$-1/3$	$e_R^- u_R \rightarrow l^- u$	1
$\tilde{S}_0^R$	0	2	$-4/3$	$e_R^- d_R \rightarrow l^- d$	1
S_1^L	0	2	$-1/3$	$e_L^- u_L \rightarrow \begin{cases} l^- u & 1/2 \\ \nu_l d & 1/2 \end{cases}$	
			$-4/3$	$e_L^- d_L \rightarrow l^- d$	1
$V_{1/2}^L$	1	2	$-4/3$	$e_L^- d_R \rightarrow l^- d$	1
$V_{1/2}^R$	1	2	$-1/3$	$e_R^- u_L \rightarrow l^- u$	1
			$-4/3$	$e_R^- d_L \rightarrow l^- d$	1
$\tilde{V}_{1/2}^L$	1	2	$-1/3$	$e_L^- u_R \rightarrow l^- u$	1
V_0^L	1	0	$+2/3$	$e_R^+ d_L \rightarrow \begin{cases} l^+ d & 1/2 \\ \bar{\nu}_l u & 1/2 \end{cases}$	
V_0^R	1	0	$+2/3$	$e_L^+ d_R \rightarrow l^+ d$	1
$\tilde{V}_0^R$	1	0	$+5/3$	$e_L^+ u_R \rightarrow l^+ u$	1
V_1^L	1	0	$+2/3$	$e_R^+ d_L \rightarrow \begin{cases} l^+ d & 1/2 \\ \bar{\nu}_l u & 1/2 \end{cases}$	
			$+5/3$	$e_R^+ u_L \rightarrow l^+ u$	1
$S_{1/2}^L$	0	0	$+5/3$	$e_R^+ u_R \rightarrow l^+ u$	1
$S_{1/2}^R$	0	0	$+2/3$	$e_L^+ d_L \rightarrow l^+ d$	1
			$+5/3$	$e_L^+ u_L \rightarrow l^+ u$	1
$\tilde{S}_{1/2}^L$	0	0	$+2/3$	$e_R^+ d_R \rightarrow l^+ d$	1

Table 12.1: *The 14 leptoquark types of the Buchmüller-Rückl-Wyler classification [12] in the Aachen notation. Weak isospin and lepton chirality are given in the sub- and superscripts. In Columns 2-4 the spin J, the fermion number F and the electrical charge Q are denoted. The next column gives the dominant resonant production process in ep scattering (following Equations (12.6)). Leptoquarks coupling to a left-handed lepton doublet can decay into a neutrino-quark pair under charge conservation, therefore the charged lepton decay branching ratio is $\beta_l = \Gamma_l/(\Gamma_l + \Gamma_{\nu_l}) = 1/2$.*

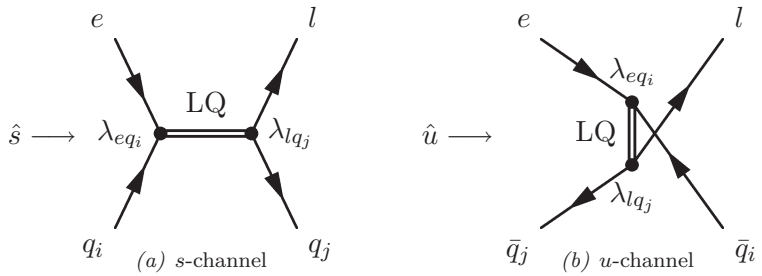

Figure 12.3: *Feynman graphs of s-channel – resonant leptoquark production and decay to a lepton-quark pair – and u-channel – exchange of a leptoquark. The quark generations are referred to by the indices i and j. It follows that the coupling of an electron to a quark of generation i is given by λ_{eq_i}. The other λ_{lq_j} denotes the coupling of the outgoing lepton l to a quark of generation j. The leptoquark mediates lepton flavour violation if the outgoing lepton l is a muon or tau lepton.*

In the effective s-channel production of leptoquarks in ep-scattering, the only relevant subprocess is the fusion of an electron and a quark of the generation i which carries the momentum fraction x. Figure 12.3(a) shows the Feynman-graph of this process which includes the possible decay in a lepton l and a quark of generation j.

The Feynman-graph of the corresponding u-channel exchange with the same initial and final state is depicted in Figure 12.3(b). Here a leptoquark, which can be virtual, mediates between the electron and a antiquark of the generation j.

If the outgoing lepton l is an electron e or the associated neutrino ν_e, the final state is equal to that of the NC/CC DIS as described in Section 12.1. The diagrams shown in Figure 12.3 must be added to matrix elements and lead to constructive or destructive interference terms.

However, this analysis investigates the case of the outgoing lepton as being a muon (l=μ). This entails that the transfered LQ has to mediate lepton flavour violation. Additionally it is assumed that

$$\lambda_{eq} = \lambda_{\mu q} \quad \text{and} \quad \lambda_{\tau q} = 0 \tag{12.9a}$$

$$\Leftrightarrow \quad \beta^{\mu}_{\text{LFV}} = 0.5 \quad \text{and} \quad \beta^{\tau}_{\text{LFV}} = 0\,. \tag{12.9b}$$

This is in contrast to the LQ production investigated in proton anti-proton collisions where LQ can be generated in pairs. A non zero value for λ_{eq} is not needed in this process. Further, the final state can contain a muon conserving the lepton flavour number. A more detailed discussion can be found in Section 12.3.4.

Since the final state is different from the SM processes, no interference has to be taken into account. The other lepton flavour violating case, where a tau is the outgoing lepton, is not covered by this analysis. While the neutrino flavour is not an observable at the HERA experiments, the cases where the outgoing lepton is a muon neutrino ν_μ or a tau neutrino μ_τ are covered by the search for leptoquarks decaying in electron neutrinos ν_e. Therefore, in the following the outgoing lepton should be understood as a muon. This means that only the neutral current decay channel of the leptoquarks S_0^L, S_1^L, V_0^L and V_1^L can be investigated.

For the study of processes in the s- and u-channel the following Mandelstam variables,

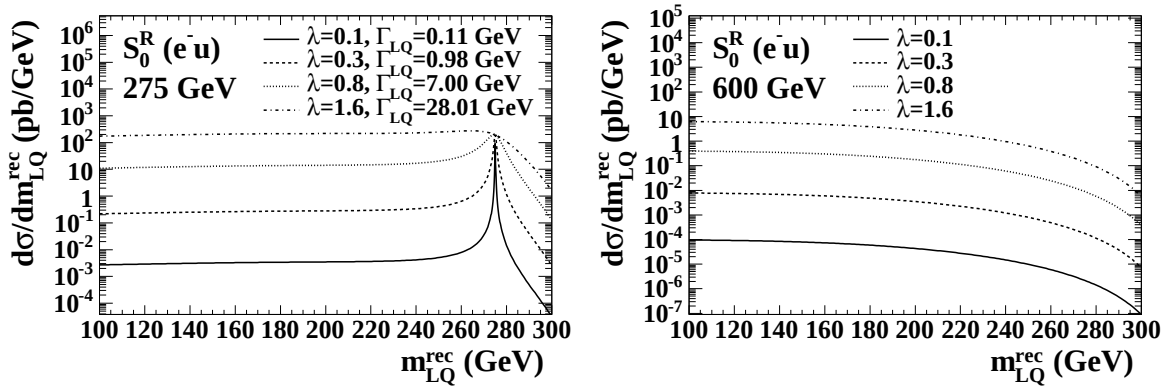

(a) 275 GeV *(b)* 600 GeV

Figure 12.4: *Examples for the cross section distribution for a scalar leptoquark versus the reconstructed leptoquark mass: (a) shows the resonant production for (a) 275 GeV S_0^R with different coupling strengths $\lambda = \lambda_{eq} = \lambda_{lq}$. A 600 GeV S_0^R will contribute via u-channel exchanges and off-shell s-channel effects to the cross section distribution, which is shown in (b). [68]*

which are Lorentz invariant, are useful:

$$\hat{s} = sx \tag{12.10a}$$

$$\hat{u} = Q^2 - s \ . \tag{12.10b}$$

The double differential cross section for the s-channel tree level process and u-channel exchange are as in the other following equations deduced in [12]:

$$\frac{d^2\sigma_s}{dxdy} = \underbrace{\frac{1}{32\pi\hat{s}}}_{\text{phase space}} \cdot \underbrace{\frac{\lambda_{eq_i}^2 \lambda_{lq_j}^2 \hat{s}^2}{(\hat{s}^2 - m_{\mathrm{LQ}}^2)^2 + m_{\mathrm{LQ}}^2 \Gamma_{\mathrm{LQ}}^2}}_{\text{Breit-Wigner LQ propagator}} \cdot \underbrace{q_i(x,\hat{s})}_{\text{parton density}} \times \begin{cases} \frac{1}{2} & \text{scalar} \\ 2(1-y)^2 & \text{vector} \end{cases} \tag{12.11a}$$

$$\frac{d^2\sigma_u}{dxdy} = \overbrace{\frac{1}{32\pi\hat{s}}} \cdot \frac{\lambda_{eq_i}^2 \lambda_{lq_j}^2 \hat{s}^2}{(\hat{u}^2 - m_{\mathrm{LQ}}^2)^2} \cdot \overbrace{\bar{q}_j(x,-\hat{u})} \times \begin{cases} \frac{1}{2}(1-y)^2 & \text{scalar} \\ 2 & \text{vector} \end{cases} , \tag{12.11b}$$

where the Yukawa couplings λ_{eq_i} and λ_{lq_j} refer to production and decay vertex (see Figure 12.3).

The total width Γ_{LQ} is derived from the sum over the partial decay widths of all possible final states. Taking the branching ratio into account for one final state with the leptoquark mass m_{LQ}, the following equation is valid:

$$\Gamma_{lq_j} = m_{\mathrm{LQ}} \lambda_{lq_j}^2 \times \begin{cases} \frac{1}{16\pi} & \text{scalar} \\ \frac{1}{24\pi} & \text{vector} \, . \end{cases} \tag{12.12}$$

As an example, Figure 12.4 shows the cross section of a S_0^R leptoquark of 275 GeV and 600 GeV. In the case of the resonant production of leptoquarks, Equation (12.11a) leads to a Breit-Wigner distribution with a peak in the x spectrum at $x_0 = m_{\mathrm{LQ}}/s$. As visible in

Figure 12.4(a), this is only the case for a small coupling ($\lambda < 1$). If a resonance is observable, the leptoquark mass can be reconstructed as expected at

$$m_{\mathrm{LQ}}^{\mathrm{rec}} = \sqrt{\hat{s}} = \sqrt{xs}\,. \tag{12.13}$$

Leptoquarks with masses above the centre of mass energy will contribute via u-channel exchanges and off-shell s-channel effects to the cross section distribution, which is shown in Figure 12.4(b).

In addition to a clear resonance for leptoquarks $m_{\mathrm{LQ}} < \sqrt{s}$, the existence of leptoquarks leads to a characteristic y-spectrum. This is distinguishable from the spectrum of NC/CC DIS which is given by $^{d\sigma}/_{dy} \propto y^{-2}$ (see Equations (12.3))

A scalar leptoquark in the s-channel decays isotopically in the rest frame, which leads to a flat y-spectrum. For vector leptoquarks the y-spectrum is described by $^{d\sigma}/_{dy} \propto (1-y)^2$. The distributions are vice versa for leptoquarks, which are mainly produced in the u-channel.

12.3.2 Topology of a Leptoquark decay in the H1 Experiment

The production and the decay of a lepton flavour violating leptoquark ($e^- q \to LQ \to \mu q$) would lead to an unique signature in the detector. Figure 12.5 shows a simulated event display of the signal process. Assuming a high mass of the LQ above 100 GeV, the muon as a decay product will have a high momentum resulting in a high p_T of this muon.

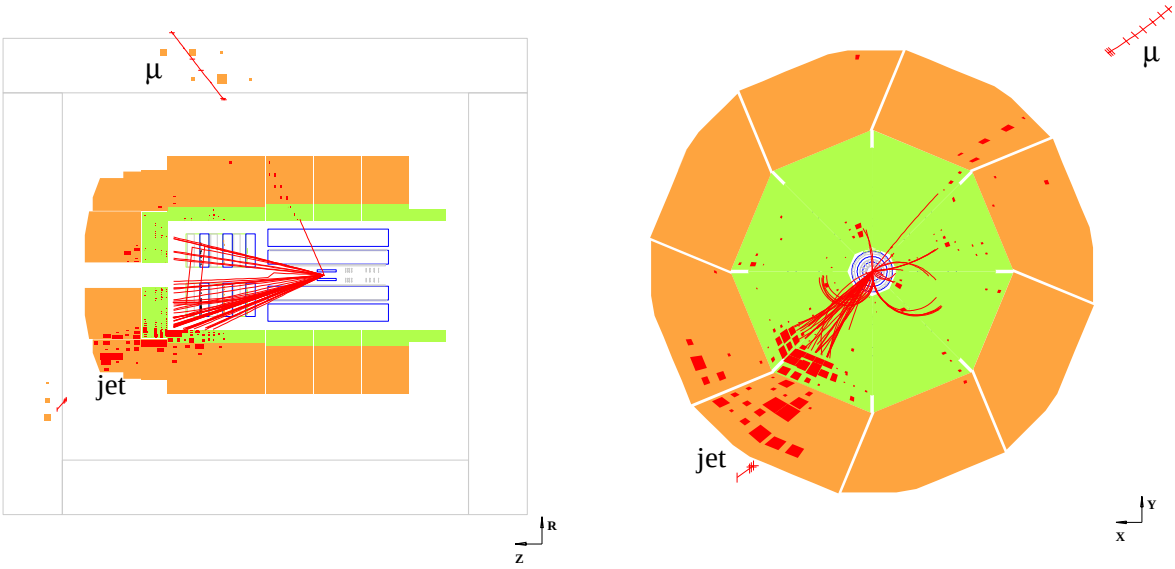

Figure 12.5: *MC simulated event display of the signal process $ep \to LQ \to \mu X$.*

Due to the confinement, the quark will hadronise. Because the secondary particles are produced with a low transverse momentum in comparison to the momentum of the quark, they will appear as a jet. The jet direction follows the direction of the quark which is back to back with the muon in the LQ rest frame. Since the LQ are produced at rest in the electron quark system, they will be produced with a low transverse momentum. Therefore, the jet and the muon are also arranged back to back in the $r\phi$ plane which is very rare in SM processes as presented in the following section.

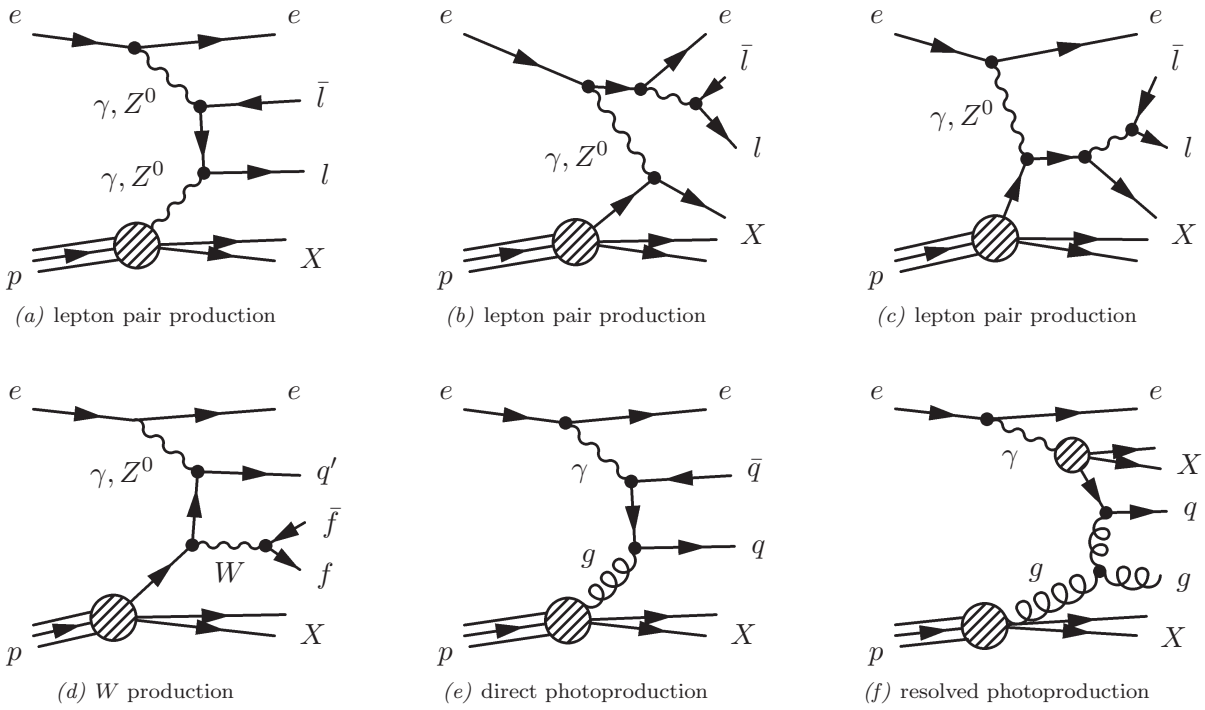

(a) lepton pair production *(b)* lepton pair production *(c)* lepton pair production

(d) W production *(e)* direct photoproduction *(f)* resolved photoproduction

Figure 12.6: *Dominant tree level Feynman diagrams of SM background processes in addition to NC/CC DIS in ep collisions.*

The muon with an energy of much higher than 200 MeV will appear as a minimal ionising particle (MIP), which means that it deposits only a small amount of its energy in the calorimeter (see also Section 13.1.1). Having the jet in the opposite sector of the detector leads to an imbalance in energy measured in the calorimeter ($p_T^{\text{calo}} \gg 0$).

12.3.3 SM background

Some Standard Model processes can lead to an event signature which is similar to a decay of a leptoquark into a muon-quark pair. These processes are described below. Their Feynman diagrams are depicted in Figure 12.6.

Lepton-Pair Production

The most prominent background source is the lepton-pair production which is shown in Figures 12.6(a) to 12.6(c). It can lead to a high momentum lepton in the final state. It is distinguished by the action of the proton into elastic, quasi-elastic and inelastic lepton-pair production:

elastic Only the two leptons are seen in the final state, the scattered electron and an intact proton leaving the detector through the beam pipe.

inelastic The electron is detected, which implies a large Q^2 of the event.

quasi-elastic The proton remnant is detected in the forward region. It can be misidentified as a jet.

A di-muon event, with one muon leaving the detector unidentified, can mimic an LFV signal: a high p_T muon and detection of hadronic energy.

W Production

The final state of the W production process is similar to the one of the lepton-pair production if the W decays into leptons. The main difference is that the second lepton is a neutrino. The Feynman diagram is shown in Figure 12.6(d). This process also leads to a high p_T lepton, which can be a muon, and a hadronic final state (HFS)

Photoproduction

Photoproduction (γP) is the scattering process with the highest cross section at HERA (150 µb). The incoming electron emits a quasi-real photon which couples to a parton of the proton. This process leads to low momentum transfer: $Q^2 \ll 1\,\text{GeV}$. The interaction of the photon and the parton can be *direct* as shown in Figure 12.6(e) or *resolved* if the photon fluctuates into hadrons and then interacts with a proton as depicted in Figure 12.6(f).

One of the hadrons may be wrongly identified as a muon. In this case the reconstructed final state looks very similar to a muon-quark pair, the signal of the investigated LFV process.

High-Q^2 NC/CC DIS

Also the NC/CC DIS can contribute as a background process. It is described in detail in Section 12.1. The neutrino in the CC DIS final state leads to an energy imbalance in the calorimeter like the LQ decay in μq. But to fake this signal process a particle must be misidentified as muon. The NC DIS can contribute if the electron is not detected and the HFS contains a muon. These muons are mainly in the jets and therefore not isolated as the muon in the signal process would be.

12.3.4 Experimental Searches for LFV and current limits

As mentioned before, a search for lepton flavour violating leptoquarks was performed on the HERA I data which had been collected from 1998 to 2000. The results are published in [69]. The obtained mass limits are summarised in Table 12.2.

$eq \rightarrow \text{LQ} \rightarrow \mu q$							
$F = 0$	$S_{1/2}^L$	$S_{1/2}^R$	$\tilde{S}_{1/2}^L$	V_0^L	V_0^R	$\tilde{V}_0^R$	V_1^L
$m_{\text{LQ}}(\text{GeV})$	302	309	288	299	298	333	459
$F = 2$	S_0^L	S_0^R	$\tilde{S}_0^R$	S_1^L	$V_{1/2}^L$	$V_{1/2}^R$	$\tilde{V}_{1/2}^L$
$m_{\text{LQ}}(\text{GeV})$	294	294	278	306	299	374	336

Table 12.2: *Lower limits on m_{LQ} with 95% CL assuming $\lambda_{\mu q} = \lambda_{eq} = 0.3$ obtained from the HERA I measurement [69].*

The same data was analysed to search for first generation leptoquarks. In this case the outgoing lepton l (see Figure 12.3) is an electron. No evidence for the existence of leptoquarks was found. Assuming a coupling of $\lambda_{eq} = 0.3$, masses above 275 to 325 GeV depending on

the LQ type were excluded at 95% CL [70]. Also, no evidence of first generation leptoquarks was found in the complete HERA II data ($449\,\mathrm{pb}^{-1}$). The mass limits were pushed to 295 to 310 GeV depending of the LQ type [71].

At the Tevatron, protons p and anti-protons $\bar{p}$ are brought to collision. The two experiments at the Tevatron D0 and CDF also searched for leptoquarks of the first and second generation. The Feynman diagrams of the main production processes are shown in Figure 12.7.

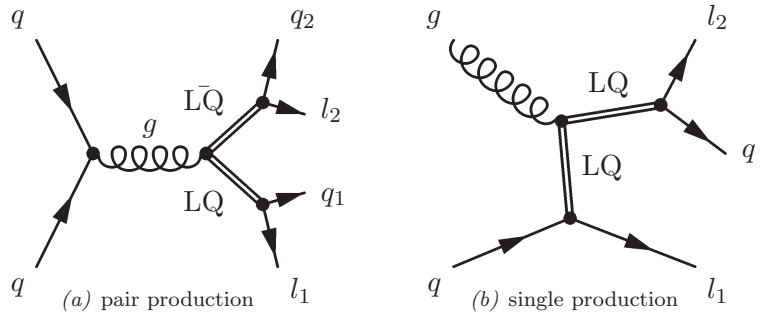

Figure 12.7: *LQ production in pp collision.*

Only the production of scalar leptoquarks is refered to here. In the case of a first generation leptoquark, the outgoing leptons $l_{1,2}$ can be an electron e or an electron-neutrino ν_e. The decay in a second of third generation lepton is not considered: $\lambda_{eq} \neq 0$ and $\lambda_{\mu q} = \lambda_{\tau q} = 0$. A similar assumption has been made for the search for second generation leptoquarks. Only the decay into a muon or the related neutrino is investigated. Hence, these searches are not sensitive to lepton flavour violation. D0 obtained a mass limit (95% CL) for first generation leptoquarks of 241 and 218 GeV for $\beta = 1$ and $1/2$, respectively [72]. The search for second generation LQ results in a limit of $m_{\mathrm{LQ}} > 274\,\mathrm{GeV}(226\,\mathrm{GeV})$ for $\beta = 1(1/2)$ [73]. CDF published the following limits (95% CL) for $\beta = 1(1/2)$: $m_{\mathrm{LQ}} > 236\,\mathrm{GeV}(205\,\mathrm{GeV})$ for the first generation [74] and $m_{\mathrm{LQ}} > 226\,\mathrm{GeV}(208\,\mathrm{GeV})$ for the second generation [75].

Since these searches performed at the Tevatron assume the absence of lepton flavour violation, they are not easy to compare with the one described in this thesis. To produce a LQ at HERA a non zero coupling λ_{eq} is mandatory. To observe a decay into a muon and a quark, a coupling $\lambda_{\mu q} > 0$ is needed. As mentioned before (cf. Equation (12.9)), it is assumed that $\lambda_{eq} = \lambda_{\mu q}$. If this assumption is transferred to the situation at the Tevatron, the possible decay channel can contain a electron and/or a muon and the related neutrinos. This leads to different branching ratios for the different decay channels: For example the branching ratio for a final state $\mu q \mu q$ changed from $1/4$ in the case without lepton flavour violation to $1/16$ assuming LFV. In the case of a $\nu q \mu q$ in the final state, the branching ratio is reduced from $1/2$ to $1/4$. Here it has been taken into account, that the neutrino flavour is not observable. Also final states (e. g.. $\nu q e q$), which were forbidden assuming a coupling of $\lambda_{eq} = 0$ and $\lambda_{\mu q} > 0$, become observable with a branching ratio of $1/4$. This is the same ratio as for the final state $\nu q \mu q$. Assuming this change of the branching ratios, a limit of $m_{\mathrm{LQ}} > 185\,\mathrm{GeV}$ can be deduced for a S_0^L type leptoquark ($\beta = 1/2$) from the D0 search in the $\nu q e q$ channel [72]. From the CDF results in the $\nu q \mu q$ cannel [75], a limit of $m_{\mathrm{LQ}} > 147\,\mathrm{GeV}$ can be calculated for the same LQ-type.

Chapter 13

Analysis

This analysis concentrates on the e^-p data of the HERA II period. As it can be seen in Table 12.1 on page 114, only the seven LQ types of the BRW model with $F = 2$ could be produced in e^-p collisions. As mentioned before, this analysis takes only the final state, with a muon as the outgoing lepton, into account.

First, the particle identification, reconstruction of the kinematic variables and energy calibration will be presented. After summarising the used measured data and their handling, the Monte Carlo data used for modelling the SM background as well as the signal process are described. This more general part is followed by the presentation of the signal selection including cuts, final results and signal efficiencies. Due to the low statistics in the signal selection, two control sections which are connected with the two parts of the final state of the signal process are presented. A CC selection demonstrates the understanding of the hadronic part and a muon selection tests the leptonic part.

This analysis is done using the framework H1OO-framework [76] and the Marana analysis package [77].

13.1 Reconstruction

To analyse the recorded events, particle identification, calculation of the kinematic variables and the calibration of the energy scale of the detector are needed.

13.1.1 Particle Identification

In the further analysis, the properties of electrons, muons and hadronic jets are taken into account.

Electron

Electrons and photons leave isolated and compact electromagnetic clusters in the calorimeter. The characteristic shower shape is used to separate their signal from those induced by hadronic particles. While photons are neutral, they are in contrast to the electrons not influenced by the magnetic field and produce no signal in the tracker. The angle of the electron θ^{e} is reconstructed from the primary vertex and the centre of gravity of the electromagnetic cluster. More details can be found in [78].

Muon

Muons are identified by their typical signature in the detector. Since the muon is a charged particle, a track can be measured in the inner tracking system. As mentioned before, the muon with an energy of above 200 MeV is a minimal ionising particle (MIP) which produces only a narrow trace in calorimeter. In contrast to all other particles, which are most probably stopped in the calorimeter, a muon can leave the detector and give a signal in the muon system (CMD and FMD), which is referred to as an outer track.

Depending on how well this signature is observed, the muons are sub-classified into five grades (decreasing with the order of quality):

Grade 1 Muons with the highest quality require an inner track linked to a well measured outer track in the instrumented iron.

Grade 2 Also here an inner and an outer track are required. But the linking criteria is relaxed to a maximal distance between the tracks of 0.5 in the $\eta\phi$-plane, where η denotes the pseudorapidity (cf. Equation (11.1).

Grade 3 These muons do not match with an outer track. A signal in the tail catcher is required within a distance of 0.5 in the $\eta\phi$-plane.

Grade 4 Estimators are used to characterise typical MIP pattern in the energy deposits in the LAr calorimeter.

Grade 5 A muon detected only by the FMD, without any associated inner track are classified with the lowest grade.

Hadronic Final State and Jets

The Hadronic Final State (HFS) is formed from all particles in the event excluding isolated leptons (muons or electrons). Therefore, the deposits in the LAr calorimeter are combined with tracking information and all clusters which are not associated to a track of an isolated lepton are combined to the HFS [79].

As mentioned in Section 12.3.2, quarks and gluons form jets due to the confinement and the low transverse momentum of the produced daughter particles. These jets are reconstructed using a k_T algorithm with a p_T weighted recombination scheme [80].

13.1.2 Kinematic Variables

There are several options available to reconstruct the kinematic variables of an event. These variables are introduced in Section 12.1.1. A more detailed description of the methods presented in the following can be found in [81].

Electron Method

The following method is used for events with a well measured scattered electron. Here the direction (the scattering angle θ^{e}) and the energy of the electron E_s^{e} are used.

$$Q^{2\,\mathrm{e}} = 2E_0^{\mathrm{e}} E_s^{\mathrm{e}} (1 + \cos\theta^{\mathrm{e}}) \tag{13.1a}$$

$$y^{\mathrm{e}} = 1 - \frac{E_s^{\mathrm{e}}}{E_0^{\mathrm{e}}} (1 - \cos\theta^{\mathrm{e}}) \,, \tag{13.1b}$$

where E_0^{e} denotes the energy of the initial electron of 27.6 GeV. The energy measurement is taken from the electron, because it is much more accurate than for hadrons, as it is presented in Section 11.2.2. In the case of LFV, this method can be used when replacing the electron by the scattered lepton.

Hadronic Method

For example in CC DIS, where no scattered lepton is available, the Jacquet-Blondel Method is used. The kinematic variables are determined exclusively by the hadronic final state (HFS). Here the *inclusive* HFS is used, this means that it is summed over all particles i in the event including isolated leptons but excluding the scattered electron.

$$Q^{2\,\mathrm{h}} = \frac{\left(\sum_i p_x^i\right)^2 + \left(\sum_i p_y^i\right)^2}{1 - y^{\mathrm{h}}} \equiv \frac{p_T^{\mathrm{h}}}{1 - y^{\mathrm{h}}} \tag{13.2a}$$

$$y^{\mathrm{h}} = \frac{\sum_i E^i - p_z^i}{2E_0^{\mathrm{e}}} \equiv \frac{(E - p_z)^{\mathrm{h}}}{2E_0^{\mathrm{e}}} \tag{13.2b}$$

This method is also used if a scattered electron is detected, e. g. during the calibration procedure. Including the scattered electron (as in NC DIS), the observable $E - p_z$ peaks at $2E_0^{\mathrm{e}} = 55.2\,\mathrm{GeV}$.

Double Angle Method

The Double Angle Method combines the information of the leptonic and the hadronic part of the event. It uses the scattering angle of the outgoing lepton and an effective angle of the hadronic system γ^{h} (exclusive HFS):

$$\tan\frac{\gamma^{\mathrm{h}}}{2} = \frac{(E - p_z)^{\mathrm{h}}}{p_T^{\mathrm{h}}} \tag{13.3}$$

Its main advantage is the insensitivity to the energy scale, which is influenced by the calibration or the energy loss of the measured particles before they reach the calorimeter. The kinematic variables are defined by:

$$Q^{2\,\mathrm{da}} = (2E_0^{\mathrm{e}})^2 \frac{\sin\gamma^{\mathrm{h}}(1 - \cos\theta^{\mathrm{e}})}{\sin\gamma^{\mathrm{h}} + \sin\theta^{\mathrm{e}} - \sin(\theta^{\mathrm{e}} + \gamma^{\mathrm{h}})} \tag{13.4a}$$

$$y^{\mathrm{da}} = \frac{\sin\theta^{\mathrm{e}}(1 - \cos\gamma^{\mathrm{h}})}{\sin\gamma^{\mathrm{h}} + \sin\theta^{\mathrm{e}} - \sin(\theta^{\mathrm{e}} + \gamma^{\mathrm{h}})} \tag{13.4b}$$

Mass Resolution

The Electron Method is not used in this analysis because the LFV leads to a scattered muon instead of an electron. The measurement of the muon energy is not good enough for a reliable reconstruction of the kinematic variables. In the case of the Double Angle Method only the angle of the muon, which is well measured, is used instead of θ^{e}. This method can produce unphysical values of M^{da} if it is used for the SM background processes. In these processes, the selected muon is not the scattered lepton and therefore has no relation to the kinematics of the process.

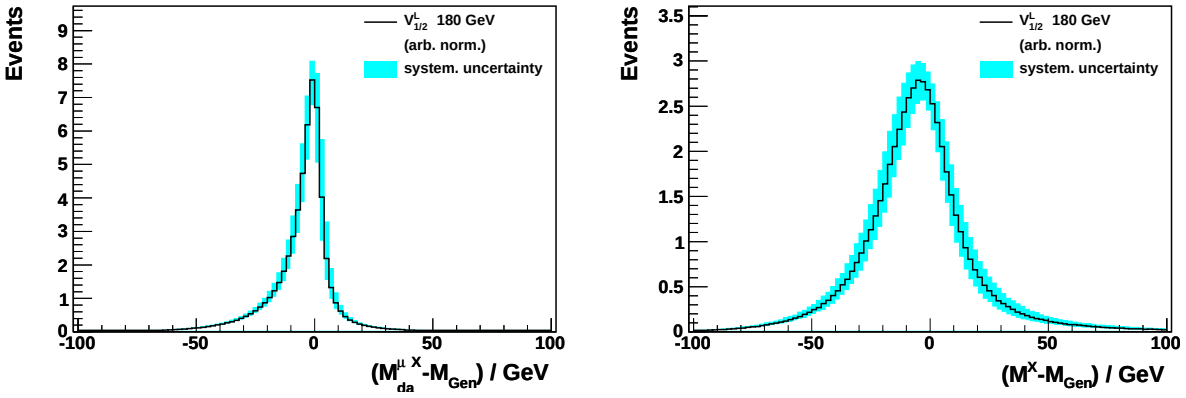

(a) double angle method *(b)* hadron method

Figure 13.1: *Mass resolution of different reconstruction methods for a leptoquark $V^L_{1/2}$ with a mass of 180 GeV: The Double Angle Method (left) shows a better resolution for the investigated channel ($eq \to \mu q$) than the Hadronic Method (right).*

Figure 13.1 shows a comparison of the Hadronic Method and Double Angle Method. The difference between the reconstructed mass $M^{\text{rec}} = \sqrt{sx^{\text{rec}}}$ and the generated mass M_{gen} is shown for a sample of a $V^L_{1/2}$ with a mass of 180 GeV decaying in a muon quark pair. It is clearly visible, that the resolution of Double Angle Method (4.5 GeV) is much better than the one of the Hadron Method (14 GeV). Therefore, the Double Angle Method will be used in this analysis.

13.1.3 Calibration

The calibration procedure makes use of the over constrained kinematics in NC DIS events.

Electromagnetic Energy

In this analysis, the standard calibration method is used [82]. As mentioned before, the Double Angle Method is nearly independent of the energy scale. The reconstructed kinematic information is compared to the electromagnetic energy reconstructed with the Electron Method. From this information, the mean values of $E^{\text{e}}/E^{\text{da}}$ are calculated in a fine binning of the impact position z and the angle ϕ. Figure 13.2 shows that after the calibration the electron energy scale is known with a precision of better than 1%.

Hadronic Energy

To calibrate the HFS, a high Q^2 NC DIS sample is used with $p^{\text{e}}_T > 10\,\text{GeV}$. Exactly one jet is required and a precise double angle determination is needed. The calibration is adjusted in bins of $(p^{\text{da}}_T)_e \approx (p^{\text{da}}_T)_{\text{jet}}$ and θ_{jet}. Details can be found in [79]. After the calibration procedure, the absolute energy scale of the jet is known to better that 2% as is demonstrated in Figure 13.3.

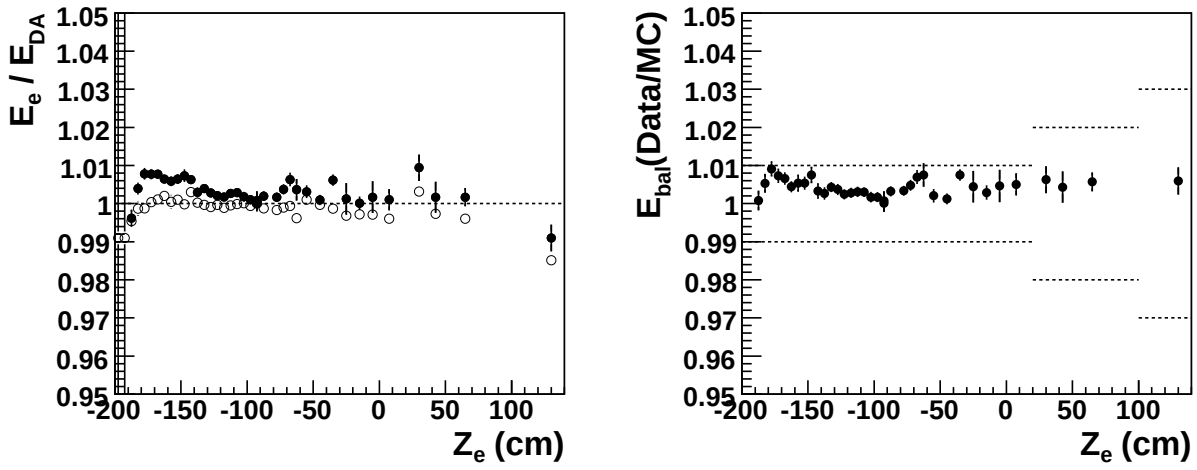

(a) *(b)*

Figure 13.2: *Test of the electron calibration using a NC sample for 2005 e^-p data: Figure (a) shows the ratio $E_{\mathrm{bal}} = {}^{E^{\mathrm{e}}}/_{E^{\mathrm{da}}}$ of the calibrated electron energy E^{e} and the energy E^{da} reconstructed with the double angle method. The ratio is shown as a function of the z-impact position z^{e} for data (black points) and Monte Carlo (open points). Figure (b) displays the ratio of ${}^{E^{\mathrm{data}}_{\mathrm{bal}}}/_{E^{\mathrm{MC}}_{\mathrm{bal}}}$. [83]*

13.2 Investigated Data and Used SM Monte Carlo

13.2.1 Data

This thesis concentrates on the analysis of the HERA II e^-p data which corresponds to an integrated luminosity of $158.9\,\mathrm{pb}^{-1}$. The maority of the data was collected in the years 2005 and 2006. The small ammount of the data which was taken in 2004 was added to the 2005 data set. As described in Section 11.1.1, since the HERA II upgrade, the accelerator provided the possibility to study longitudinally polarised electrons. The running of the accelerator HERA was divided into periods with right- and left-handed transverse polarisation of the lepton beam. Since LQs have a spin, their production is sensitive to the polarisation of the initial particles. Therefore, the analysed data was split into sets regarding the year and the polarisation. The

data set	run number range	luminosity	polarisation
05R	398286 - 402634 415620 - 427474	$31.8\,\mathrm{pb}^{-1}$	+36.8%
05L	402992 - 414712 427813 - 436893	$69.8\,\mathrm{pb}^{-1}$	-27.1%
06L	444094 - 458154	$35.6\,\mathrm{pb}^{-1}$	-23.5%
06R	458793 - 466997	$21.7\,\mathrm{pb}^{-1}$	+25.5%

Table 13.1: *Data sets used for the analysis.*

different sets are summarised in Table 13.1. In addition to the range of the run number (not all runs in this range are included in the data set), the integrated luminosity and the averaged

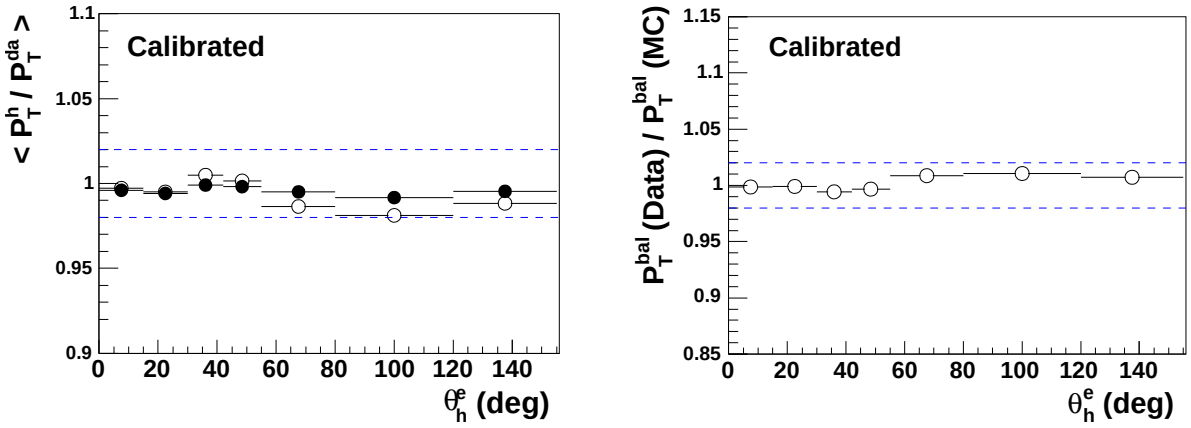

(a) *(b)*

Figure 13.3: *Test of hadronic jet calibration using NC sample of 2004 e^-p data: Figure (a) shows the ratio $p_T^{\mathrm{bal}} = p_T^{\mathrm{e}}/p_T^{\mathrm{h}}$ to test the absolute jet calibration for data (black points) and Monte Carlo (open points). The ratio is shown in dependence of the angle $\theta_{\mathrm{incl}}^{\mathrm{h}}$ of the inclusive HFS. Figure (b) shows the comparison of the calibration for data and Monte Carlo. [83]*

polarisation of the periods are displayed. The data-taking was further subdivided into runs of about one hour. Runs which were marked as *poor* was rejectedduring the selection for this analysis. Furthermore, only runs have been taken into account, in which the sub-detectors CJC1, CJC2, CIP, LAr, ToF and Luminosity system were switched on.

13.2.2 Monte Carlo

For the analysis, a set of simulated data describing the SM prediction (background) is needed as well as a set of signal event. Both were generated with Monte Carlo generators and passed through a detailed detector simulation (see Section 11.5).

Signal Simulation

To simulate a signal of LFV mediated by leptoquarks a modified version of the generator LEGO was used [84]. The generator includes initial QED radiation following the collinear approximation of Weizäcker-Williams. The DGLAP evolution equations [85] are used for the perturbative part in initial and final parton showers. For the non-perturbative hadronisation into parton showers, the JETSET package with Lund string fragmentation is used.

The signal expectation for a certain pair of parameters in the $m_{\mathrm{LQ}}/\lambda_{eq}$ phase space cannot easily be approximated by a basic function. To avoid the generation of samples with many events for each set of $m_{\mathrm{LQ}}/\lambda_{eq}$, a generic sample was produced with high statistics. This sample is then reweighted for each dedicated LQ-type and each set of parameters. Additionally, this procedure avoids challenging interpolations and fitting techniques to cover the complete phase space. In particular, the transition region from resonant production to the high-mass contact interaction region ($\approx 300\,\mathrm{GeV}$) is treated correctly by this approach.

A modified version of LEGO was used to ensure enough statistics over the full phase space $0 < x < 1$ before the folding with the proton PDF. The matrix element of the s-channel

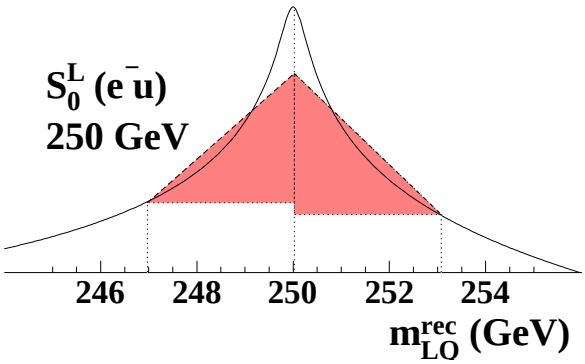

Figure 13.4: *The smoothing of the simulated leptoquark mass peak: To avoid large weights the Lorentz peak is replaced by a triangular shape with the same integral in an area of* $\pm 3\,\mathrm{GeV}$ *around the nominal leptoquark mass. [68]*

(Equation (12.11a)) was replaced by $\hat{s} \times 10^{-15}$ [68]. During generation and reweigting, the energy loss due to initial state radiation (ISR) is taken into account by $x_e = {}^{\tilde{E}_e}/_{E_e^0}$. The ISR reduces the centre of mass energy of the hard process to $\hat{s} = sxx_e$. Knowing the exact cross section from Equations (12.11) and the generated x, Q^2 and x_e, the events are reweighted for a certain LQ-type and a set of parameters m_{LQ}, λ_{eq} and $\beta_{\mathrm{LFV}}^{\mu,\tau}$. The weight is given by

$$w(LQ, m_{\mathrm{LQ}}, \lambda_{eq}, \beta_{\mathrm{LFV}}, Q^2, x, x_e) = \frac{\frac{d\sigma_{\mathrm{exact}}}{dxdQ^2}(LQ, m_{\mathrm{LQ}}, \lambda_{eq}, \beta_{\mathrm{LFV}}^{\mu,\tau}, Q^2, x, x_e)}{\frac{d\sigma_{\mathrm{generic}}}{dxdQ^2}(Q^2, x, x_e)}\,, \tag{13.5}$$

In the case of resonant leptoquark production, the event weight can be very large if the generated value of xx_e is near the Lorenz peak at ${}^{m_{\mathrm{LQ}}}/_{\hat{s}}$. This is especially so for small LQ widths (small couplings λ_{eq}), where the signal cross section can be dominated by a few events with a very large weight. To overcome this problem the mass peak is smoothed [68]. Therefore, the Lorenz peak is replaced by a triangular shape around the nominal LQ mass with same integral. This is depicted in Figure 13.4. Since a smoothing area of $\pm 3\,\mathrm{GeV}$ is chosen, which is smaller than the detector resolution (see Section 13.1.2), it does not influence the observable distributions.

SM Background

The main background processes of the SM, which have a similar topology as the signal process, have been summarised in Section 12.3.3. To simulate these processes, the following generators were used.

The largest background contribution inclzuding all three generations (e, μ, τ) of lepton-pair production, was generated with GRAPE 1.1 [86]. This generator is based on a full calculation of all electroweak diagrams, including Drell-Yang-processes and Z^0-bremsstrahlung. Intermediate photons and final state interference are taken into account. The samples of W production events were generated with EPVEC [87]. To simulated the photon background, the generator PYTHIA 6.1 [88] was used. The deep inelastic scattering was simulated using two generators. The neutral current process of the DIS was simulated with RAPGAP [89] and the the charged current was generated with DJANGO [90].

All used sets of MC are summarised in the Tables A.1 and A.2 which can be found in the appendix. The numbers of generated events and the corresponding integrated luminosity refer to the samples used for the 05 data sets. The samples for the 06 sets are very similar and differ only in some channels.

13.3 Selections

First, the general conditions like trigger and the rejection of non *ep* background are discussed. Afterwards, the selection of events with a topology of a LQ decay in a muon-quark pair is presented. The topology is described in detail in Section 12.3.2. This includes, besides the applied cuts, distributions of important observables and the signal efficiency. The very low statistics of the data in the signal selection does not allow a meaningful comparison of the observable distribution between data and the SM expectation. Therefore in addition, two control selections are presented which test that the data is described by the Monte Carlo simulation. Deviations between the data samples and the Monte Carlo simulations when selecting a SM process can indicate a deficiency in the understanding of the detector or the data. A selection of charged current deep inelastic scattering events tests the understanding of the hadronic part of the signal process. The weakening of the cuts of the muon observables leads to a muon selection. It demonstrates the description of the data by the simulation for the leptonic part of the signal process.

13.3.1 Trigger

For the calorimeter based triggers, the event topology of LQ decays into muon-quark pairs is similar to the CC DIS process. The muon deposits minimal energy in the calorimeter, which leads to an imbalance in the energy distribution in the calorimeter. This is also the case in a CC DIS event. Therefore, the triggers typically used by analyses of charged current deep inelastic scattering [82] are used by this analysis:

66: large missing energy with forward energy deposit.

67: large electromagnetic energy. A lower threshold of 6 GeV is applied.

77: large missing transverse energy E_T of above 2 GeV.

The use of triggers which tag muon signatures has been considered. The decision against these triggers is based on the large prescale factors (see Section 11.4) for these subtriggers and a malfunction of the muon trigger system in 2005 [91].

As it can be seen in Figure 13.5, the trigger efficiency is close to 100% for events with a $p_T^{\text{calo}} > 30\,\text{GeV}$, where p_T^{calo} denotes the transverse momentum reconstructed from the calorimeter alone. The trigger efficiency is deduced from a selection of pseudo CC DIS events. These are NC DIS events,where the scattered electron has been removed. Figure 13.6 clearly shows, that the main part of the signal can be found above $p_T^{\text{calo}} > 30\,\text{GeV}$ and will be triggered with a high efficiently near 100%.

13.3.2 Rejection of Non *ep* Background

The interactions of the beam with residual gas molecules or the beam pipe can produce events which do not originate from a nominal *ep* collision. Furthermore, cosmic muons or muons

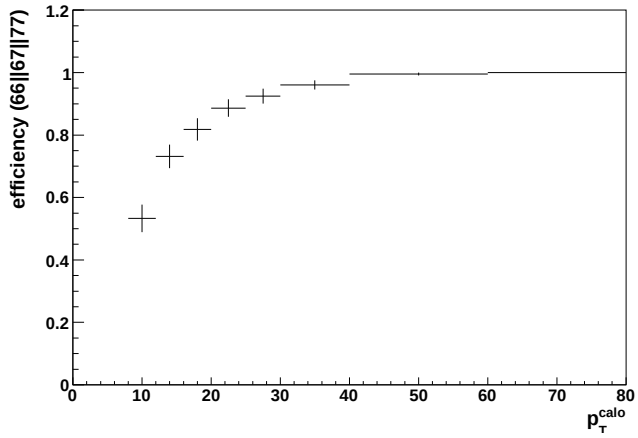

Figure 13.5: *Trigger efficiency for the trigger (66‖67‖77) as a function of* p_T^{calo}.

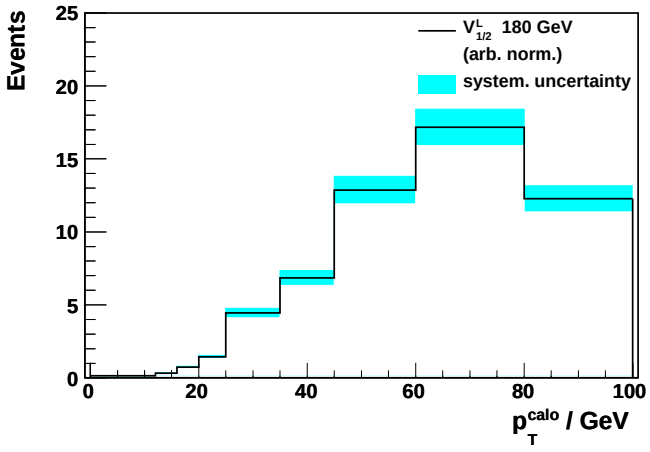

Figure 13.6: *Distribution of* p_T^{calo} *for the signal process.*

from the beam halo can lead to a recorded event. To suppress this non *ep* background, several actions have been taken.

Most of these background events do not come from the nominal vertex. Therefore, a cut is applied on the reconstructed vertex position: $|z_{\text{vtx}} < 35\,\text{cm}|$. This is equivalent to three standard deviations of the distribution of z_{vtx}. For the reconstruction of the vertex, at least one reconstructed vertex fitted track is required.

The *ep* interactions originate from the bunch crossings, whose nominal times are provided by the HERA clock. A certain time window is applied around this time T_0^{nom}. The measurement of the interaction time is based on the information from the CJC and the LAr calorimeter (see Section 11.2.1 and 11.2.2). The time T_0^{CJC} is deduced from the hits on the wires. Here, at least one selected track is needed in the event. If this is not the case, the CJC is not considered for the time measurement. The drift time of the CJC has to be taken into account. The acceptance timing window is ± 30 ticks around T_0^{nom}. The time between the bunch crossings measures 500 ticks $\equiv$ 96 ns. Events which are in a window around one or two bunch crossing earlier or later to nominal bunch crossing are accepted, too. The time T_0^{LAr} is determined by the energy deposit in LAr. This information is provided by the LAr trigger.

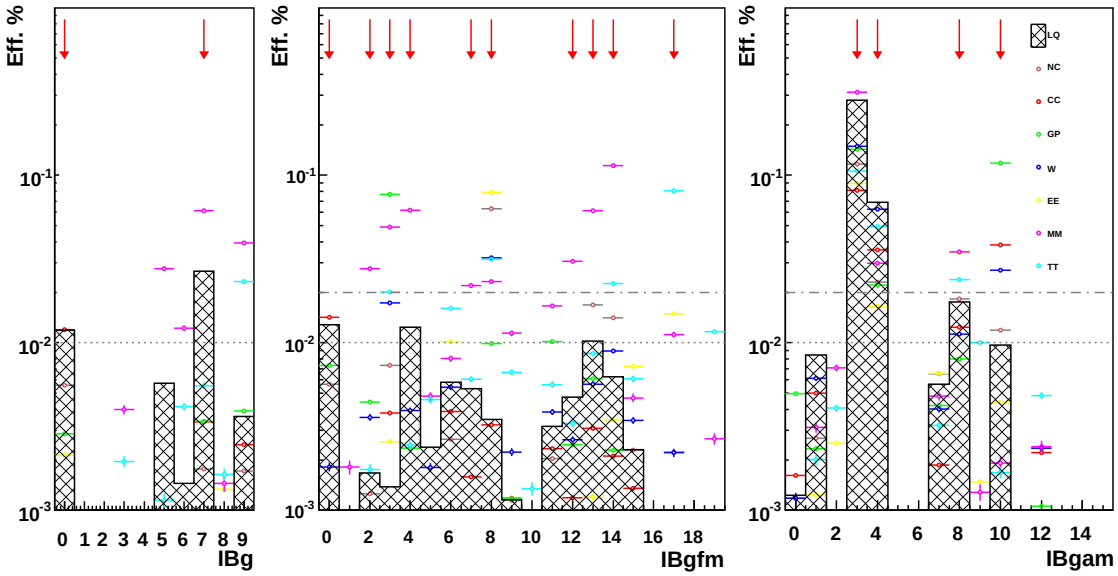

Figure 13.7: *Background finder efficiency: the safe (IBg) and two other sets (IBgfm and IBgam) of the BG finders are presented. The horizontal lines indicate the thresholds. Finders which tag more than 1% of the signal (corded) or 2% of the SM background processes (dots) are not used. This is indicated by the red arrows. The second threshold is only used for IBgfm and IBgam.*

The requirement to keep the event is $T_0^{\mathrm{LAr}} < 0.7$ bunch crossing time (96 ns).

Besides the cuts on the vertex position and the event timing, characteristic event topologies are rejected. These topologies are identified by *background finder* algorithms. Three different sets are available: A so called *safe* set (IBg) and two others from the Liverpool group (IBgfm) and the Marseille group (IBgam) [92]. From all sets only these algorithms are used which tag less than 1% of the signal process as non *ep* background. In addition, from the sets 'IBgfm' and 'Ibgam' all algorithms which tag 2% of the SM background processes are not used. The non used finders are indicated in Figure 13.7.

13.3.3 Signal Selection

The topology of the LFV process leads to a clear signal in many observables. As the decay of the LQ in a muon-quark pair indicates, the following particles must be found in the event:

- at least one reconstructed jet. As mentioned before, these jets are reconstructed using a k_T algorithm with a p_T weighted recombination scheme [80]. No further cuts on jet quantities are applied.
- at least one muon in the detector between $10 <^{\circ} \theta^{\mu_1} < 140^{\circ}$. The lower boundary is set due to large amount of hadronic background particles in the forward region. The coverage of the LAr defines the upper boundary. The muon deposits only a minimal energy in the calorimeter, which leads to large value of p_T^{calo} in case of a signal event. This observable is used as a discriminating variable (see below).

Cuts are also applied to the property of the particles. Here, μ_1 denotes the muon with the highest transverse momentum p_T:

- $p_T^{\mu_1} > 8\,\text{GeV}$: Originating from the LQ decay, the muon must have a high transverse momentum.
- $\Delta\phi^{\mu_1 - X} > 170°$: The muon and the jet are back to back in the $r\phi$ plane. In the rz plane the system is boosted due to the difference in the energy of the initial particles.
- $D_{\text{TrTr}}^{\mu_1} > 0.5$: Due to the back to back topology, the muon must be isolated. To be isolated, no other track should be found within a distance lower than 0.5 in the $\eta\phi$ plane to the track that is associated to the muon. The alternative isolation criteria, which is defined by not more than 5 GeV energy deposit in a cylinder with a radius of 25 cm around the muon direction, is not used in the signal selection. This is in contrast to the muon selection which will be presented in Section 13.3.5.
- Muons signatures in the forward direction are mainly produced by mis-identified hadrons from the proton remnant. They are badly described by the MC simulation. Therefore, muons with grade 4 are rejected (see Section 13.1.1).

The imbalance in the energy deposit in the calorimeter, which signify the signal process, justifies the following cuts:

- $p_T^{\text{calo}} > 25\,\text{GeV}$: The imbalance in the energy measurement leads to large values of p_T^{calo}, which denotes the momentum reconstructed from the calorimeter alone. This information is also used as trigger input, but in contrast to the observable used for the cut without energy calibration applied. The cut value is chosen due to low trigger efficiency below 25 GeV (see Figure 13.5).
- $V_{\text{ap}}/V_{\text{p}} < 0.2$: Here, the $r\phi$-plane is separated into two hemispheres by the direction of the HFS. This direction is given by the transverse momentum vector sum $\vec{p}_T^{\,X}$ of all energy deposits i in the calorimeter.

$$V_p = \sum_i \frac{\vec{p}_T^{\,X} \cdot \vec{p}_T^{\,i}}{|\vec{p}_T^{\,X}|} \quad \text{for} \quad \vec{p}_T^{\,X} \cdot \vec{p}_T^{\,i} > 0\,, \tag{13.6a}$$

$$V_{ap} = -\sum_i \frac{\vec{p}_T^{\,X} \cdot \vec{p}_T^{\,i}}{|\vec{p}_T^{\,X}|} \quad \text{for} \quad \vec{p}_T^{\,X} \cdot \vec{p}_T^{\,i} < 0\,. \tag{13.6b}$$

  In a signal-like event, the hemisphere with $\vec{p}_{T,X} \cdot \vec{p}_T^{\,i} < 0$ contains the muon. This leads to a small value of V_{ap}, while V_p is given by the sum of the quark/jet deposits and is therefore much larger. The ratio of $V_{\text{ap}}/V_{\text{p}}$ is expected to be close to zero for signal-like events, which can be seen in Figure 13.8(d). In contrast, the balanced topology of NC DIS and photoproduction events leads to values of about one.

Also the number of particles of a certain type can be employed to distinguish between signal and background like events.

- $N_{\text{iso}\,\mu} = 1$: While further muons in a signal-like event may appear in jets, the requirement of exactly one isolated muon reduces the lepton-pair production.
- $N_{\text{iso}\,e} = 0$: In events with LFV, the scattered lepton is a muon and no further isolated electrons should be detected.

SM Process	Event generator	Syst. error (%)
NC DIS	RAPGAP	10
CC DIS	DJANGO	10 / 25
γP	PYTHIA	50
ee,$\mu\mu$,$\tau\tau$-Prod.	GRAPE	30
W-Prod.	EPVEC	15

Table 13.2: *Theoretical cross section uncertainties for the dominant SM expectations applied in this analysis.*

Systematics Experimental uncertainties have been taken into account for the signal process and the SM background. For the last one additional theoretical uncertainties are considered.

The experimental uncertainties are determined by an up and down shift of the the following measured quantities:

- It is assumed that the muon identification efficiency has an uncertainty of 5% in the central and 15% in the forward region.
- The transverse momentum of the muon is measured with a precision of 5%.
- The spatial resolution of the muon trajectory is assumed to be 3 mrad for the θ measurement and 1 mrad for the measurement of ϕ.
- For the jets, a precision of the measurement of the azimuthal angle of 10 mrad in the central and 5 mrad in the forward region is taken in to account. In the transverse plane an accuracy for ϕ of 1 mrad is assumed.
- The determination of the integrated luminosity gives an overall uncertainty on the SM expectation of $\pm 4\%$.
- The polarisation is measured with a precision of 3%.

The contribution from each of these sources is added in quadrature. The uncertainties of the PDF are not taken into account for the systematic error given in the following. They do however enter into the limit calculation in correlation with the PDF uncertainty in the signal expectation (Section 14.2.1).

The theoretical uncertainties on calculated cross sections for the different MC generators are summarised in Table 13.2. The large errors (e.g. in the photoproduction) are due to higher order corrections. For the CC DIS an uncertainty of 10% is assumed, but it is inflated for the limit calculation to 25% due to deviations between data and MC in the γ^{h}-distribution. Details are described in Section 13.3.5.

Results After allcuts, two events are selected in the data. The contribution of each SM process to the signal selection is summarised in Table 13.3. The largest amount comes from the lepton-pair production, which contributes with 81%. The second largest contribution is the W-production with 10%. The expectation of all SM processes of 2.2 ± 0.6 agrees with the observation of two events. Event displays of these selected events are shown in appendix B.

Figure 13.8 shows the distribution of some of the observables without the dedicated cut on the observable, which is shown. All other cuts are applied. These figures demonstrate the efficiency of the cuts.

Set	0506 e^-p
$ee, \mu\mu, \tau\tau$-prod.	1.792±0.048(stat)±0.092(syst)±0.538(theo)
W-prod.	0.231±0.011(stat)±0.013(syst)±0.035(theo)
NC	0.140±0.030(stat)±0.007(syst)±0.014(theo)
CC	0.023±0.009(stat)±0.001(syst)±0.002(theo)
γ-prod.	0.015±0.005(stat)±0.001(syst)±0.008(theo)
SM total	2.201±0.566
DATA	2

Table 13.3: *Results for the signal selection for muon-quark pairs.*

There is no evidence for lepton flavour violation which allows the transition of a first generation lepton into one of the second generation. Hence, limits on the used model will be calculated. The technique and results are presented in the next chapter.

For leptoquark masses above $m_{\mathrm{LQ}} > 150\,\mathrm{GeV}$, most of the signal events measure a $p_T^{\mathrm{calo}} > 45\,\mathrm{GeV}$. This can be seen in Figure 13.8(a), which shows the distribution of p_T^{calo} for a leptoquark with a mass of $m_{\mathrm{LQ}} > 175\,\mathrm{GeV}$. Therefore, the signal selection is divided for the calculation of the limits into two bins: $25\,\mathrm{GeV} < p_T^{\mathrm{calo}} < 45\,\mathrm{GeV}$ and $p_T^{\mathrm{calo}} \geq 45\,\mathrm{GeV}$. In the second bin the background from standard model processes is reduced further, as seen in Table 13.4. This table presents the observation and the SM expectation for the different

Set	Total		$25\,\mathrm{GeV} < p_T^{\mathrm{calo}} < 45\,\mathrm{GeV}$		$p_T^{\mathrm{calo}} \geq 45\,\mathrm{GeV}$	
	SM	data	SM	data	SM	data
05 left handed	1.00±0.22	0	0.90±0.20	0	0.096±0.024	0
05 right handed	0.44±0.11	2	0.40±0.10	2	0.042±0.011	0
06 left handed	0.48±0.13	0	0.43±0.12	0	0.051±0.014	0
06 right handed	0.27±0.08	0	0.24±0.07	0	0.029±0.008	0

Table 13.4: *Results for the signal selection muon-quark pairs split into to bins of* p_T^{calo}

periods which are shown in detail in Table 13.1. The first bin is needed to achieve a good signal efficiency for low mass assumptions. This will be presented in the next section.

13.3.4 Signal Efficiency

The signal efficiency is calculated for various mass assumptions m_{LQ} by reweighting the general signal sample using Equation (13.5). Further details on the reweighting can be found in Section 13.2.2. For the calculation of the efficiency, it is assumed that $\lambda_{eq} = \lambda_{\mu q} = 0.3$. Figure 13.9 shows the signal efficiency for all seven LQ type with $F = 2$. The efficiencies are very similar. In addition to the efficency of the total selection ($p_T^{\mathrm{calo}} > 25\,\mathrm{GeV}$), the efficiency for the second bin $p_T^{\mathrm{calo}} > 45\,\mathrm{GeV}$ alone is presented. For the resonant production of LQ with masses $m_{\mathrm{LQ}} > 150\,\mathrm{GeV}$ the efficiency of the second bin is nearly as high as for the total selection. This demonstrates, that in this case most of the signal contributes to the second bin. Furthermore, it can clearly be seen, that for LQ masses $m_{\mathrm{LQ}} < 150\,\mathrm{GeV}$ the efficiency of the bin $p_T^{\mathrm{calo}} > 45\,\mathrm{GeV}$ is very low in comparison to the total selection. The difference at

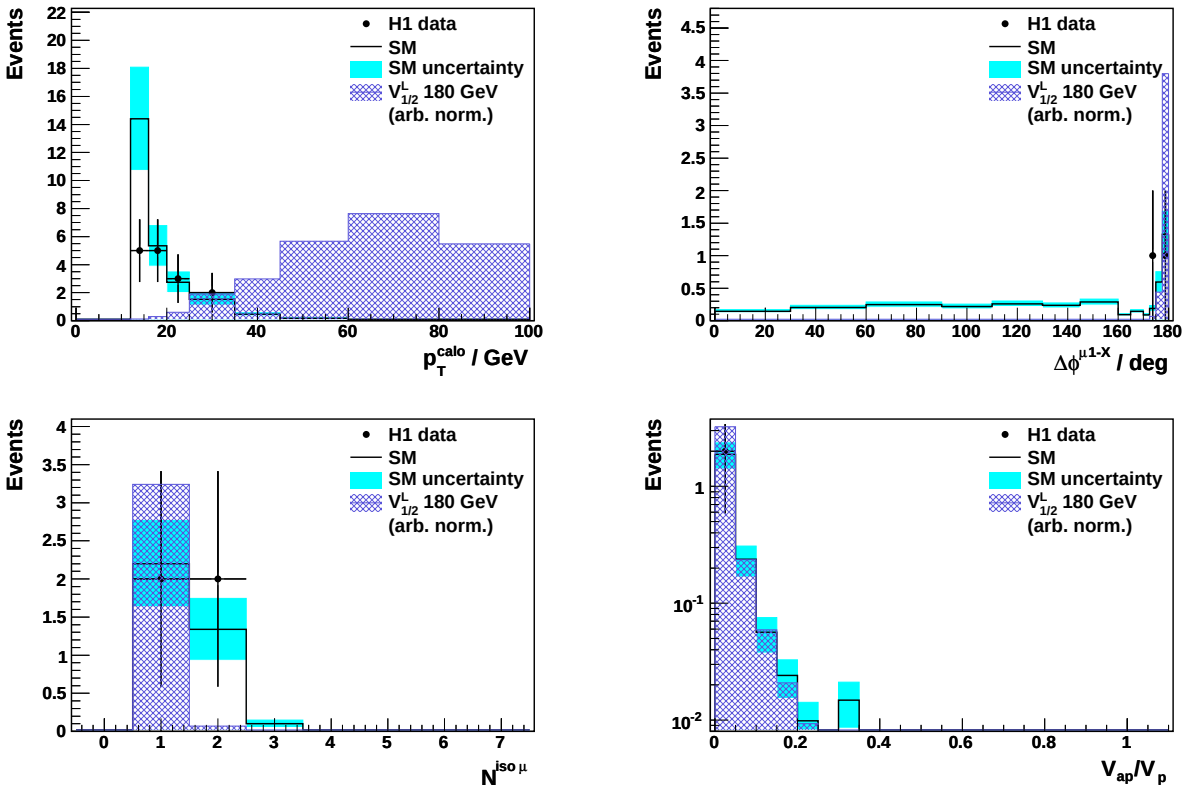

Figure 13.8: *Signal selection: Distributions of p_T^{calo}, $\Delta\phi^{\mu_1-X}$, $N_{\text{iso}\,\mu}$ and $V_{\text{ap}}/V_{\text{p}}$-ratio are shown. They are presented without the cut on the observable which is shown. In the case of p_T^{calo} the cut is reduced to 12 GeV.*

masses $m_{\text{LQ}} > 300\,\text{GeV}$ is due to the change from the resonant production to the contact interaction with a larger u-channel contribution.

13.3.5 Control Selections

The low statistics of the signal selection does not allow a comparison of the distributions of data and simulation. Therefore two control selections are investigated. Events from charged current deep inelastic scattering are selected to test the understanding of the jets and the HFS, which build one part of the signal process. In a second selection, the cuts on the muon observables are weakened to get a muon sample with higher statistics. This sample demonstrate the understanding of the leptonic part of the signal. The cuts used for the control selections are summarised in Table 13.5. In addition, the cuts used for the signal selection are shown. The modification of the cuts will be motivated in the following sections.

CC Control Selection

Because this selection should demonstrate only the understanding of the hadronic part of the signal process, no cuts on any muon observables are used. The jet requirement is kept. The CC DIS process has a neutrino as the scattered lepton in the final state (see Section 12.2), which leads to an energy imbalance as in the signal process. This allows the test of the trigger

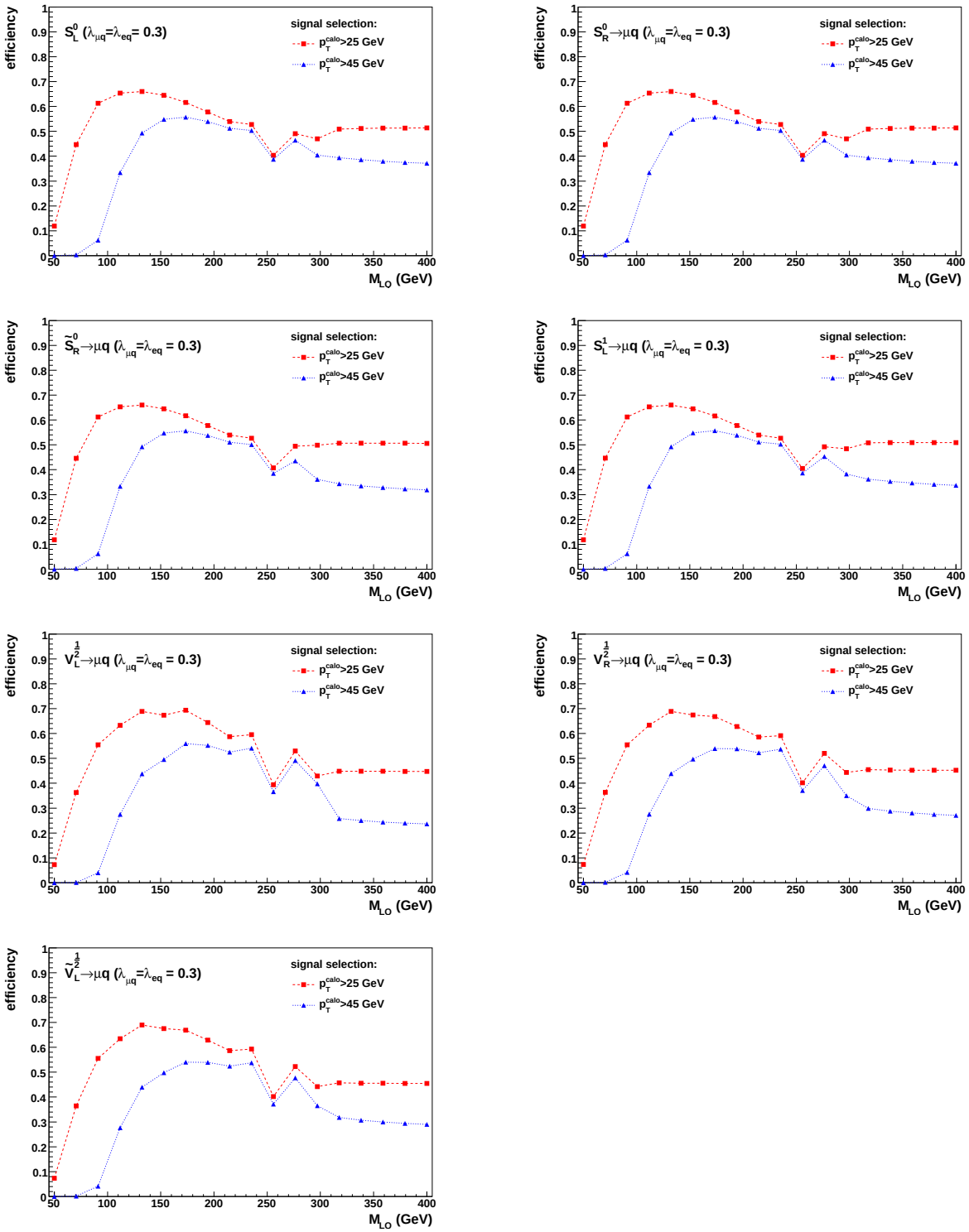

Figure 13.9: *Signal selection efficiency for the seven types of leptoquarks which are investigated. It is presented for two different cuts on* p_T^{calo}.

Observable	Selection		
	Signal	**CC**	**Muon**
p_T^{calo}	$> 25\,\text{GeV}$	$> 12\,\text{GeV}$	
$V_{\text{ap}}/V_{\text{p}}$	$< 0.2\,\text{GeV}$		—
N_{jet}	> 0		
$N_{\text{iso}\,e}$	$= 0$		—
$N_{\text{iso}\,\mu}$	$= 1$	—	> 0
iso_μ	$D^{\mu_1}_{\text{TrTr}} > 0.5$	—	$(D^{\mu_1}_{\text{TrTr}} > 0.5) \parallel (E^{25\,\text{cm}}_{\text{dep}} < 5\,\text{GeV})$
θ^{μ_1}	$> 10°$ $< 140°$	— —	$> 10°$ $< 140°$
$p_T^{\mu_1}$	$> 8\,\text{GeV}$	—	$> 8\,\text{GeV}$
$\Delta\phi^{\mu_1 - X}$	$> 170°$	—	—
y^{h}	—	> 0.1 < 0.9	—
Q^2_{h}	—	$> 500\,\text{GeV}^2$	—

Table 13.5: *Summary of cuts used for the selection of the signal selection and the two control selections (CC and muon).*

conditions. Due to this imbalance, the cut on the $V_{\text{ap}}/V_{\text{p}}$-ratio is also used. The cut on the value of p_T^{calo} is reduced to 12 GeV to increase the statistics. The choice is motivated by the trigger acceptance, as it is shown in Figure 13.5. Because both the signal process and the CC DIS process do not have an electron in the final state, the veto on isolated electron is kept. Additionally, the kinematic phase space has been reduced to $0.1 < y^{\text{h}} < 0.9$ and $Q^2_{\text{h}} > 500\,\text{GeV}^2$ to be consistent with dedicated CC DIS analyses.

set	**0506 e^-p**
CC	$5979 \quad \pm 4 \quad (\text{stat})^{+73}_{-82}\,(\text{syst}) \pm 598\,(\text{theo})$
γ-prod.	$41.9 \pm 2.2(\text{stat})^{+5.3}_{-3.9}(\text{syst}) \pm 20.4(\text{theo})$
$ee, \mu\mu, \tau\tau$-prod.	$11.8 \pm 0.1(\text{stat})^{+1.1}_{-1.2}(\text{syst}) \pm 3.5\,(\text{theo})$
NC	$11.4 \pm 1.0(\text{stat})^{+1.0}_{-0.7}(\text{syst}) \pm 1.1\,(\text{theo})$
W-prod.	$9.8 \pm 0.1(\text{stat})^{+0.3}_{-0.4}(\text{syst}) \pm 1.5\,(\text{theo})$
SM total	$6052 \pm ^{+681}_{-682}$
DATA	5698

Table 13.6: *Results for the CC control selection.*

Table 13.6 shows the number of selected events for the data and the SM prediction, which is divided into the contributing processes. CC DIS events are selected with a purity of 99%. The table also demonstrates the agreement between data and MC total event numbers within the errors.

Distributions of p_T^{miss}, p_T^{calo}, γ^{h}, Q^2_{h}, y^{h}, $V_{\text{ap}}/V_{\text{p}}$-ratio and $E - p_z$ are presented in Figure 13.10. Here an acceptable agreement between data and simulation can also be seen for most of the variables. The deviations between data and MC in the γ^{h}-distribution will be discussed later. In the same context the disagreement in the p_T^{calo}-distribution will be addressed.

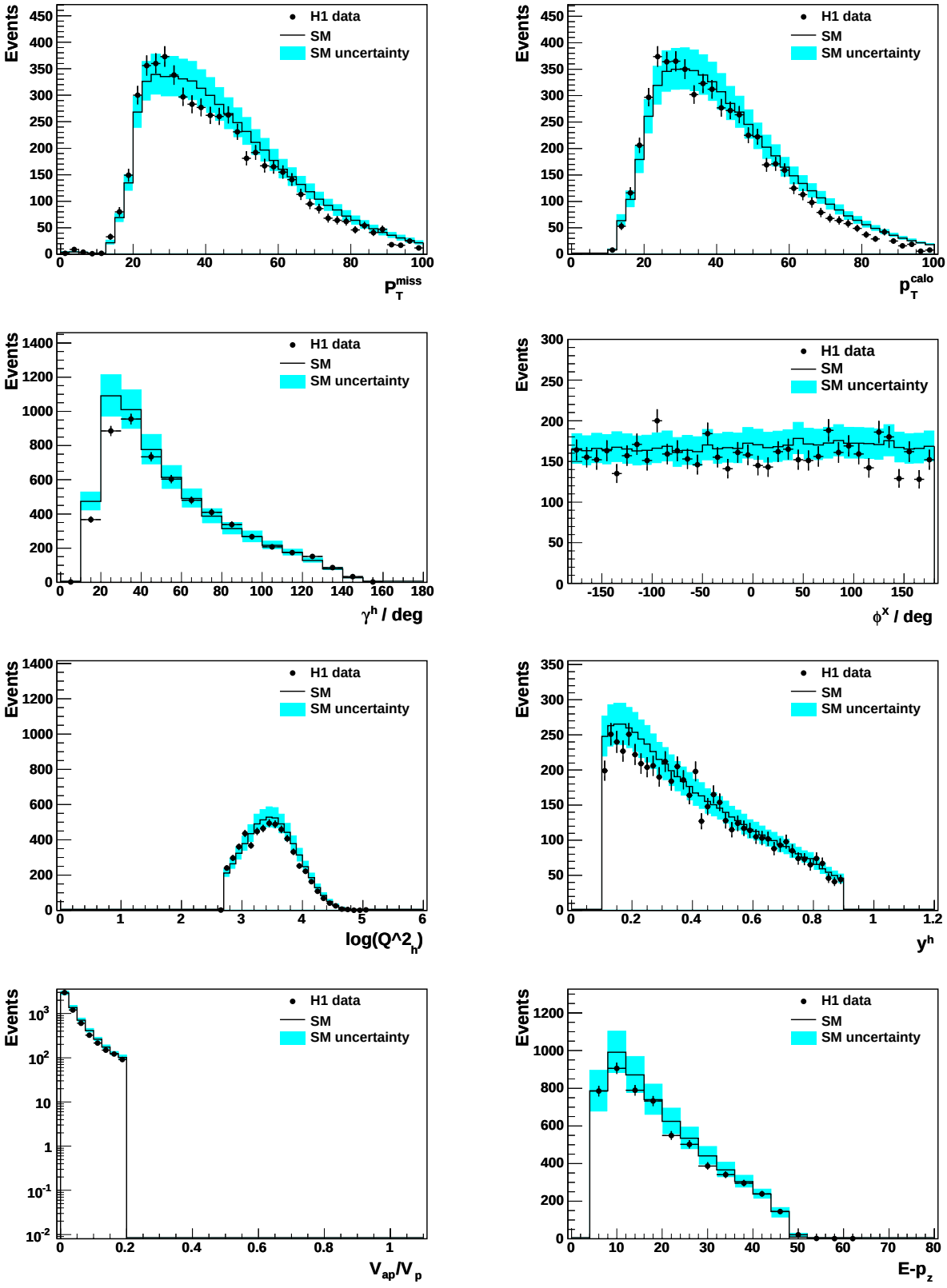

Figure 13.10: *CC control selection: Distributions of p_T^{miss}, p_T^{calo}, γ^{h}, Q^2_{h}, y^{h}, $V_{\mathrm{ap}}/V_{\mathrm{p}}$-ratio and $E - p_{\mathrm{z}}$ for the 0506 ($e^- p$) data sample.*

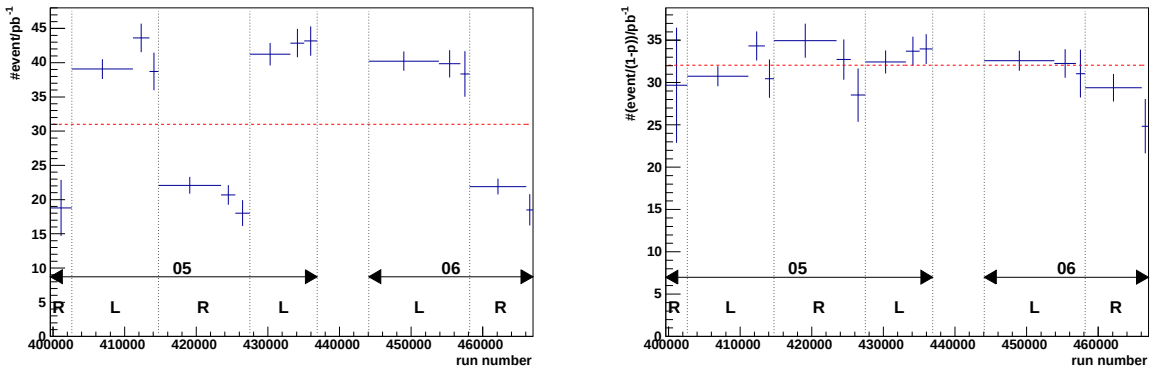

(a) *(b)*

Figure 13.11: *Yield for the CC control selection: The vertical lines indicate the different running periods. The horizontal dashed line shows the result of a fit of a constant function to the yield. The variation in the event yield for the different periods that is seen in Figure (a) is due to the change of the CC cross section as a result of the polarisation of the incoming lepton beam. Figure(b) shows the same yield with a polarisation correction. The yield is divided by $1 - P$, where P denotes the average polarisation of the running period (see Table 13.1).*

Figure 13.11 shows the yield for the selection of CC DIS events. This process is very sensitive to the polarisation P, which can be seen in the yield. The cross section of CC DIS process in $e^- p$ interaction is changed by a factor of $(1 - P)$. Figure 13.11(b) depicts the corrected yield, which is divided by $1 - P$. It shows a constant behaviour within statistical fluctuation ($\chi^2/\text{ndf} = 17/14$).

The γ^{h}-distribution The distribution of γ^{h} shown in Figure 13.10(c) exhibits a deficit of data in comparison with MC simulation at low values of γ^{h}. Figure 13.12 shows the same distribution with the cut on p_T^{calo} increased to 25 GeV and 45 GeV. It can clearly be seen that the deficit becomes more prominent at high value of p_T^{calo}. There is a strong correlation

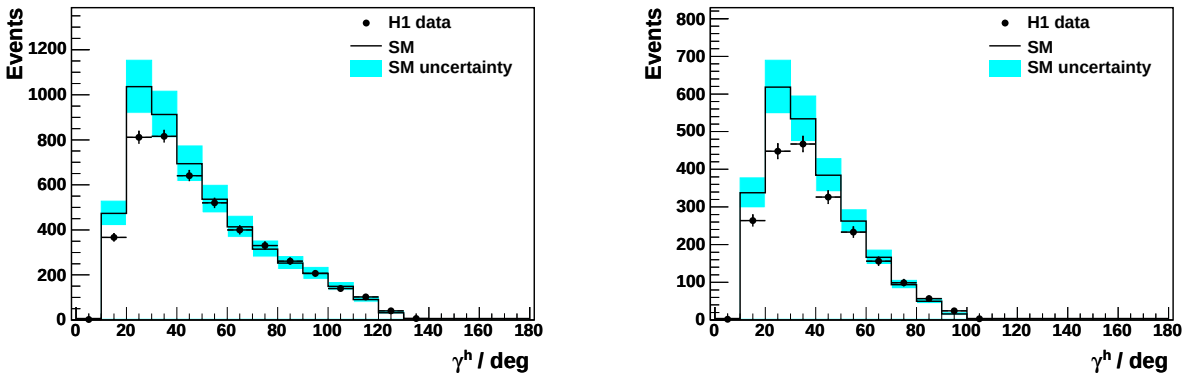

(a) $p_T^{\text{calo}} > 25\,\text{GeV}$ *(b)* $p_T^{\text{calo}} > 45\,\text{GeV}$

Figure 13.12: *Distribution of γ^{h} for $p_T^{\text{calo}} > 25\,\text{GeV}$ (left) and $p_T^{\text{calo}} > 45\,\text{GeV}$ (right).*

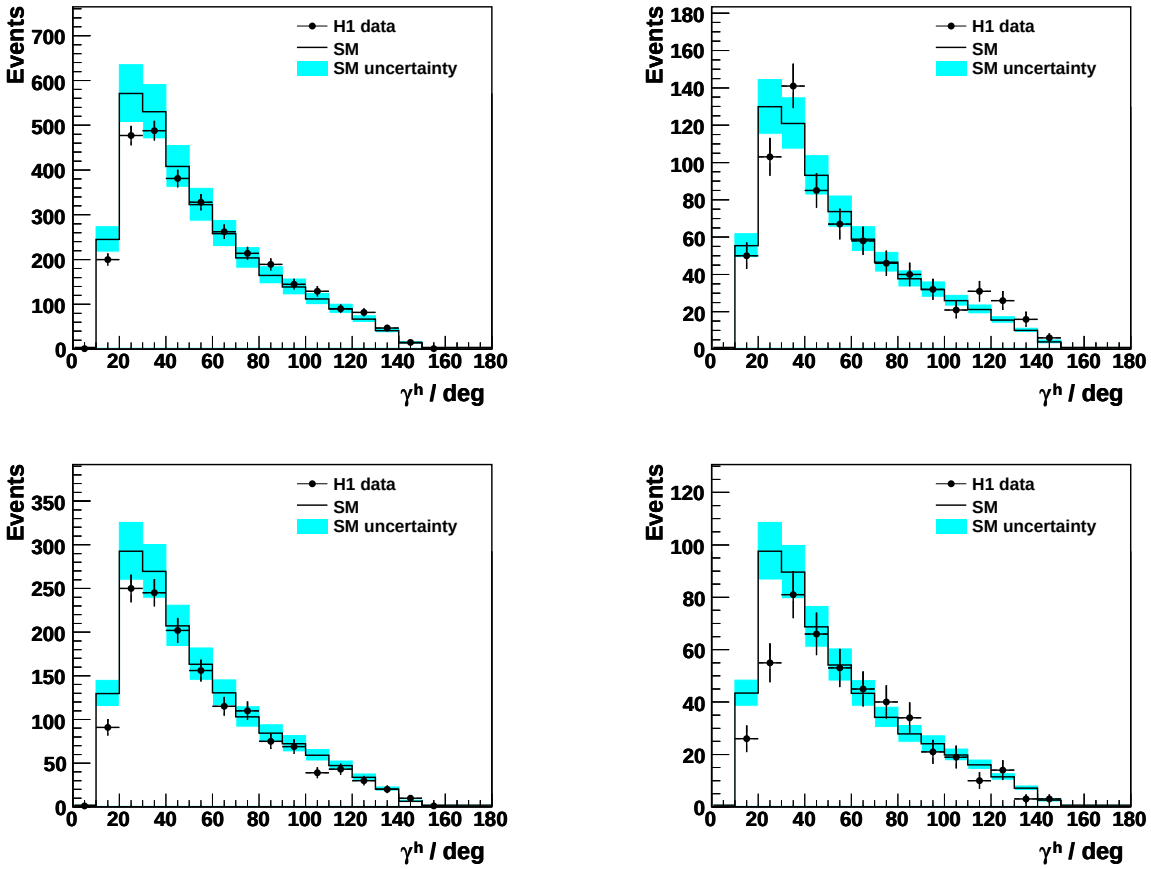

Figure 13.13: *Distribution of γ^{h} for the four analysed periods (05 left handed, 05 right handed, 06 left handed and 06 right handed).*

between this increase and the deviations which can be seen in the p_T^{calo} distribution (see Figure 13.10(b)). The deficit is less pronounced in the distribution of p_T^{miss}, which is shown in Figure 13.10(a). This observable produces similar values as p_T^{calo} for CC DIS events, but it makes use of particle candidates instead of calorimeter clusters.

The γ^{h}-distribution for the four periods which are analysed (see Table 13.1) are presented in Figure 13.13. No large variations can be seen between the different periods. Also the larger deviations in the 06 right handed data are in statistical agreement with the other periods.

This problem in describing the data with the simulation of the SM processes has also been seen in another analysis, which is dedicated to the investigation of the CC DIS process [93]. In this analysis, the trigger and other sources have been checked and are excluded as an explanation of the deficit. It should be pointed out that this deviation in the γ^{h}-distribution mainly affects the selection of CC DIS events and is not seen in the other analysis e. g. of NC DIS [93].

Since no reason for the deficit has been found, the following treatment will be used: Regarding the two distributions which correspond to the binning border used for the limit calculation ($p_T^{\mathrm{calo}} > 25\,\mathrm{GeV}$ and $45\,\mathrm{GeV}$), the largest deviation is 25%. Therefore the error on the CC DIS sample is inflated from 10% to 25%. The CC DIS process contributes in the order of 1% to the signal selection. This can be seen in Table 13.3. Hence, the effect on the total error

of the signal selection, which is used for the limit calculation and presented in Table 13.4, is negligible.

In addition the unknown source of the deficit could influence the detection of the signal process, too. The decay of a LQ into a muon-quark pair also leads to small values of γ^{h}, which can be seen in Figure 13.14(h). To take this into account, the signal efficiency presented in Section 13.3.4 is downgraded by 25% before it is put into the limit calculation.

This treatment overestimates the actual defect caused by the deficit seen in the γ^{h}-distribution. But this assumption will lead to a most conservative limit. The shown deficit should be investigated further. A reweighting of the signal and the CC DIS process should also be considered. This would lead to a stricter limit than the global downscaling.

Muon Control Selection

To investigate the leptonic part of the signal process with higher statistics, the selection criteria are weakened. The cuts on the following observables are removed: $V_{\mathrm{ap}}/V_{\mathrm{p}}$, $\Delta\phi^{\mu_1-X}$ and $N_{\mathrm{iso}\,\mu}$. Some of the other cuts are relaxed:

- The cut on p_T^{calo} is reduced to 12 GeV. This is the same value which is used in the CC DIS control selection.
- Both criteria defining the muon isolation are used in this selection. This means that in addition to the criteria used in the signal selection muons are considered as isolated if less than 5 GeV energy deposit is detected in a cylinder with radius 25 cm around muon direction.

The cuts on the muon properties like transverse momentum ($p_T^{\mu_1}$) and direction (θ^{μ_1}) are kept unchanged.

Set	**0506 e^-p**
$ee, \mu\mu, \tau\tau$-prod.	52.8±0.3(stat)±2.8(syst)±15.8(theo)
γ-prod.	15.6±0.9(stat)$^{+1.2}_{-2.0}$ (syst)±7.8 (theo)
W-prod	4.9±0.1(stat)±0.3(syst)±0.7 (theo)
NC	4.4±0.5(stat)±0.3(syst)±0.4 (theo)
CC	0.4±0.1(stat)±0.1(syst)±0.1 (theo)
SM total	78.2±18.8
DATA	82

Table 13.7: *Results for the Muon control selection.*

Table 13.7 shows the number of selected events. It demonstrates a good agreement between data and MC. Lepton-pair production is still the main contribution. The number of photoproduction events has been increased. This can be explained by the lower cuts on p_T^{calo}. The contribution from CC DIS is below 1%. This means that the deviations seen in the CC DIS selection do not influence this selection. Figure 13.14(h) shows the distribution of γ^{h} for the muon selection. The comparison of distribution suffers from the statistics which is still low. The deviations between the data and the SM prediction at low γ^{h} are visible, but they are covered by the statistical and systematical error. The systematical error is mainly caused by the theoretical error on the photoproduction, which is dominating in this region.

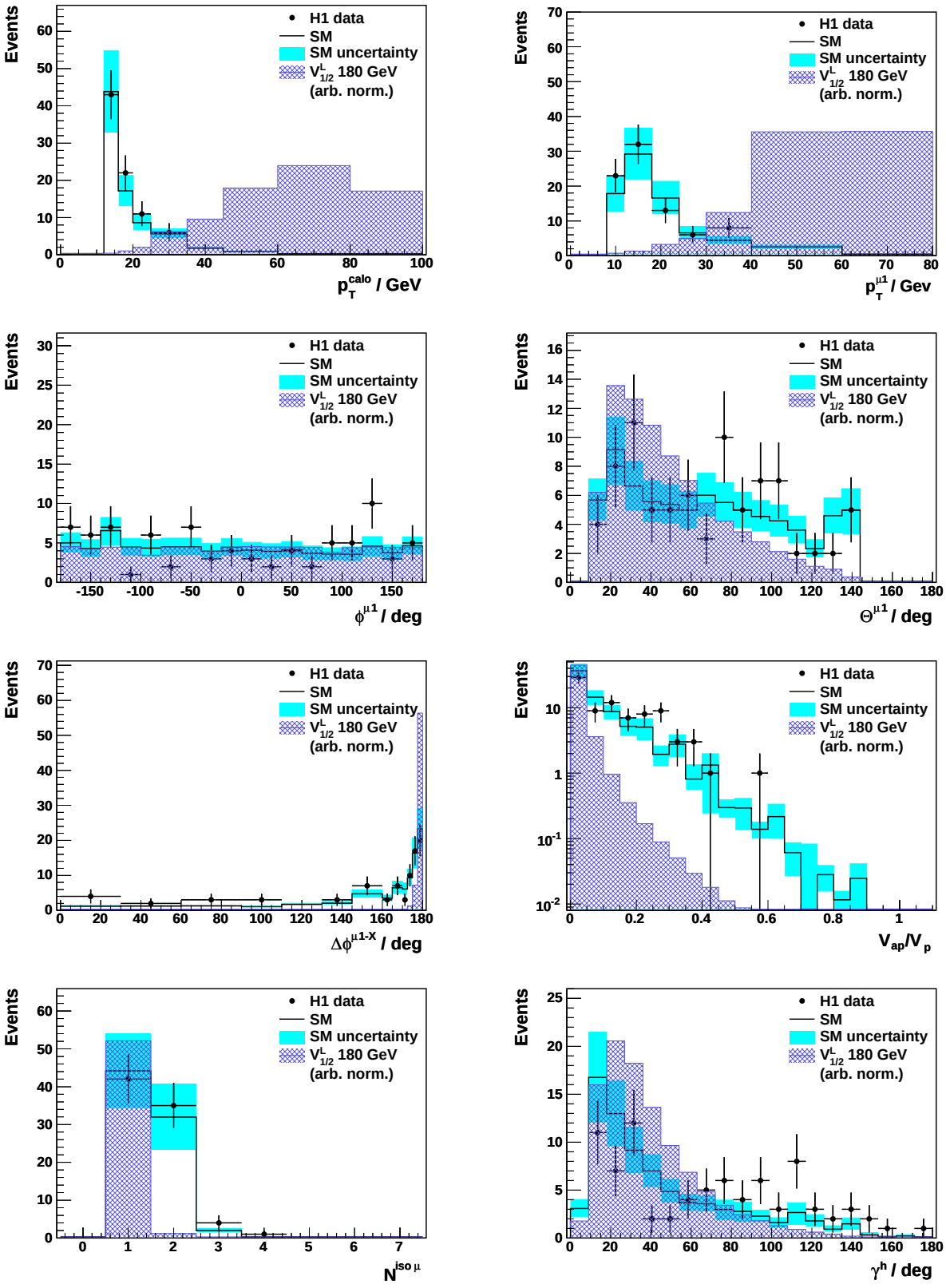

Figure 13.14: *Muon control selection: Distribution of p_T^{calo}, $p_T^{\mu_1}$, ϕ^{μ_1}, θ^{μ_1}, $\Delta\phi^{\mu_1-X}$, the $V_{\text{ap}}/V_{\text{p}}$-ratio, the number of isolated muons $N_{\text{iso}\,\mu}$ and γ^{h} for the 0506 (e^-p) data sample.*

Additionally, Figure 13.14 depicts the distribution of some important observables. For the muons, these are the momentum $p_T^{\mu 1}$, the direction ϕ^{μ_1} and θ^{μ_1} as well as the number of isolated muons $N_{\mathrm{iso}\mu}$. The distributions of p_T^{calo}, $\Delta\phi^{\mu_1 - X}$ and the $V_{\mathrm{ap}}/V_{\mathrm{p}}$-ratio are shown to validate the cuts which have been made in the signal selection. All distributions show an agreement of the data with the simulation. Unfortunately, the statistics is still low in some histogram bins.

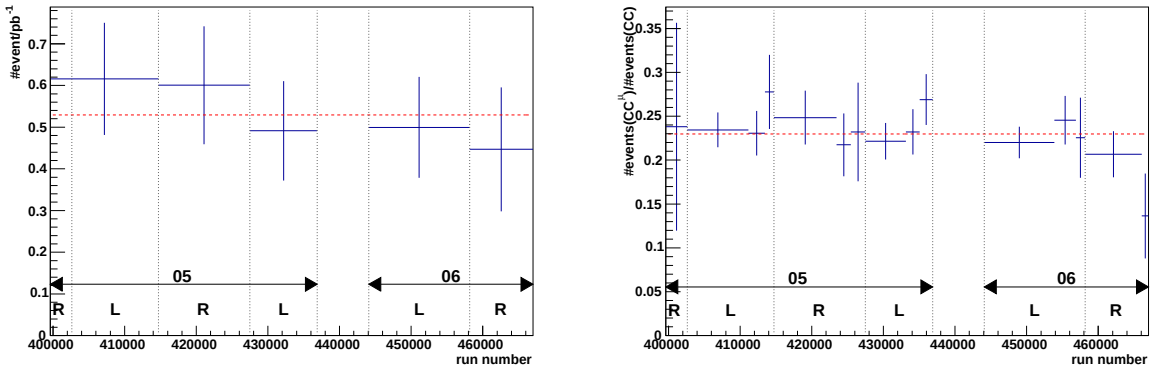

(a) *(b)*

Figure 13.15: *Yield for the Muon control selection: The vertical line indicate the different running periods. The horizontal dashed line shows the result of a fit of a constant function to the yield. Figure (a) shows the yield of the muon control selection. Figure (b) shows the ratio of the number of the events of the CC Control selection with an additional muon requirement ($N_\mu > 0$) to the total number of events in this selection as a function of the run number.*

The yield of the muon selection is presented in Figure 13.15. It is constant over all data periods and amounts to $0.52\,^{\mathrm{event}}/_{\mathrm{pb}^{-1}}$. Additionally, the yield of the CC DIS selection is shown. It presents the ratio of the number CC DIS events, which are selected with an additional requirement of at least one identified muon, to the number of selected CC DIS events without this requirement. Due to this normalisation, the dependency of the CC DIS cross section on the polarity of the incoming lepton is cancelled out. The yields demonstrate a constant working of the muon identification in all periods. The failure of the muon trigger system does not have any effect on the event selections made in this analysis.

Chapter 14

Statistical Interpretation and Limits

As presented in the previous chapter, the signal selection provides an efficiency between 18% and 56% to detect the lepton flavour violating process: $ep \rightarrow LQ \rightarrow \mu q$. In addition to the efficiencies presented in Section 13.3.4, the reduction of the signal efficiency of 25% is taken into account, which is described in Section 13.3.5. In the analysed data, two events are observed. This is in perfect agreement with the Standard Model expectation of 2.2±0.6 events. This can be seen in Figure 14.1, which shows the spectra of the reconstructed mass using the

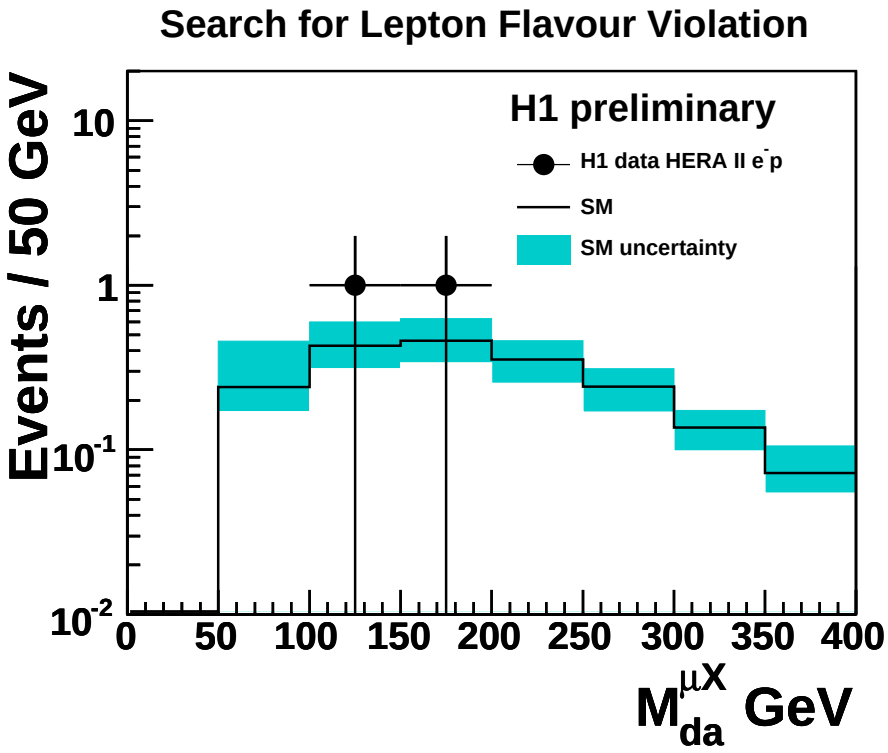

Figure 14.1: *Mass spectrum for the process $ep \rightarrow LQ \rightarrow \mu q$. The Mass is reconstructed using the double angle method and the muon as the scattered lepton.*

Double Angle Method with the muon as the scattered lepton. This method is described in Section 13.1.2. There, it is also presented, that SM processes can produce unphysical values

$M_{\mathrm{da}}^{\mu X} > \sqrt{s} = 320\,\mathrm{GeV}$, because in these processes the muon is not related to the scattered lepton and to the kinematic process. Therefore the expected mass distribution extents beyond the centre of mass energy $\sqrt{s}$. However, the two events have reasonable masses.

While no evidence for lepton flavour violation has been found, limits on the Buchmüller Rückl Wyler model will be presented. First, the modified frequentist method is introduced which is used for the limit calculation. Afterwards, the calculation of the limits for any point in the $m_{\mathrm{LQ}}/\lambda_{eq}$ phase space is described. Results will be presented for the coupling in dependency of the mass and for the mass at a fixed coupling of $\lambda_{eq} = \lambda_{\mu q} = 0.3$.

The chapter ends with a discussion of the results including a comparison between observation of the H1 collaboration and other experiments. An outlook on the further analysis of lepton flavour violating processes will be given.

14.1 Statistical Analysis

Different approaches exist for the statistical analyses which compare experimental data to the theory prediction. The advantages and the disadvantages of the different methods have been debated for a long time. An overview can be found in [94].

One of the methods often used in high energy physics make use of the Bayesian theorems. Its purpose is to test a prior probability of a theory against others, which is given by the theoretical signal assumption. It will provide as an outcome, a probability of this theory for the experimental observation which has been put in.

The other method is the frequentist method. It does not bet on a certain theory among others, but tests the compatibility of the experiment's observation with a given theory which is not under debate.

14.1.1 Modified Frequentist Method

This analysis follows the H1 tradition of frequentist limits. The analysed data are separated into several channels depending upon the year, the polarisation and the binning in p_T^{calo}.

It is non trivial to combine these multiple channels and deduce a decision if the experimental outcome is signal-like or background-like. A test statistic X needs to be defined which merges the different channels into one discriminating variable. It is defined such that it increases monotonically from background-like to signal-like. The likelihood ratio fulfils these requirements.

A large number of toy experiments is performed to get a well defined probability distribution over the test statistics. First, the signal-plus-background hypothesis is investigated: The probability of observing $s_i + b_i$ events in a toy experiment with s_i signal and b_i background events in each channel i after the observation of d_i data events follows a Poissonian distribution:

$$P(s_i + b_i) = \frac{e^{-(s_i+b_i)}(s_i + b_i)^{d_i}}{d_i!}\,. \tag{14.1}$$

For the background only hypothesis, the probability is given by

$$P(b_i) = \frac{e^{-(b_i)}(b_i)^{d_i}}{d_i!}\,. \tag{14.2}$$

To define a weight for each channel, which corresponds to its signal sensitivity, the following likelihood ratio for each channel i is chosen:

$$X_i = \frac{P(s_i + b_i)}{P(b_i)} \tag{14.3}$$

To combine n channels, the product of X_i is used, which gives the overall likelihood ratio:

$$X = \prod_{i=1}^{n} X_i \tag{14.4}$$

After the toy experiments have been performed, the confidence level can be extracted from the probability distribution: From the fraction of the experiments were X is compatible with the test statistics of the observation X_{obs}, the confidence level for the signal-plus-background hypothesis can be defined:

$$CL_{s+b} = P_{s+b}(X \leq X_{\text{obs}}) = \int_0^{X_{\text{obs}}} \frac{dP_{s+b}}{dX} dX \,, \tag{14.5}$$

where dP_{s+b}/dX is the probability density function (pdf) of the test statistics for signal and background events. By defining a limit of $1 - CL_{s+b} = 95\%$ for observing more than $s + b$ events, predictions can be excluded which are to maximally 5% compatible with the observed data. Those prediction include the expected background as well as the expectation from the theory which is tested.

The data can fluctuate below the background expectation or the theory prediction. The limit becomes unnaturally restrictive if the downwards fluctuations are large because this is considered as very unlikely. Using a low statistics sample however, this is not the case. The consideration becomes wrong, if no events are observed. In this case, a better interpretation gives a worse experimental performance than a strong exclusion limit.

To overcome this problem, the frequentist method is modified [95]. The sensitivity of the experiment is stated along with the limit. This sensitivity can be defined by the average upper limit that would be obtained by an experiment observing the expected background and no true signal: The CL of the background-only hypothesis is given by:

$$CL_b = P_b(X \leq X_{\text{obs}}) = \int_0^{X_{\text{obs}}} \frac{dP_b}{dX} dX \tag{14.6}$$

The modified frequentist method was used in [6, 68]. It strongly reduces the dependence on the expected background. The approach is also followed here to get the more conservative limit CL_s on the number of signal events, which is defined by

$$CL_s = \frac{CL_{s+b}}{CL_b} \tag{14.7}$$

It should be mentioned that the range of the confidence level for the background-only hypothesis is limited: $0 \leq CL_b \leq 1$. The upper limits on the signal events N_{lim} is set to $CL_s \leq 5\%$ for $N \geq N_{\text{lim}}$.

Systematic uncertainties enter the calculation as an offset of the predicted number b_i and s_i. Here, a Gaussian distribution around the average value is assumed. A lower physical bound at zero is taken into account.

14.2 Limits on the process $ep \to \mu q$

The four different data periods, which are separated into two bins depending on p_T^{calo}, enter the calculation as different channels. The results for these channels are summarised in Table 13.4. Additionally, the inputs from the published results from the HERA I phase [69] are used for the limit calculation. Here, data including e^-p ($\mathscr{L} = 13.7\,\text{pb}^{-1}$) and e^+p ($\mathscr{L} = 66.5\,\text{pb}^{-1}$) interactions have been taken into account. These inputs are not separated into two p_T^{calo}-bins. Therefore, in total ten channels are used for the calculation.

14.2.1 Limit Calculation

To get the confidence level, the number of selected signal events (N) is needed for a certain combination of model parameter such as LQ-type, the LQ-mass (m_{LQ}), the coupings for the production (λ_{eq}) and the decay ($\lambda_{\mu q}$). It is calculated by reweighting the general signal sample as it is described in detail in Section 13.2.2. Every selected event is weighted using the weighting factor $w(LQ, m_{\text{LQ}}, \lambda_{eq}, \beta_{\text{LFV}}, Q^2, x, x_e)$ which is given by Equation (13.5). As mentioned in Section 12.3.1, it is assumed that the coupling to the first and second generation is equal: $\lambda_{eq} = \lambda_{\mu q} \Leftrightarrow \beta^{\mu}_{\text{LFV}} = 0.5$ (cf. Equation (12.9)).

The limit calculation is performed in such a way, that it is searched for the set of parameters for which $N(LQ, m_{\text{LQ}}, \lambda_{eq}, \beta_{\text{LFV}})$ is equal to N_{lim} with $CL_s \leq 5\%$ for $N \geq N_{\text{lim}}$. It is convenient to find the highest coupling $\lambda_{eq} = \lambda_{\mu q}$ for each LQ-type with a mass m_{LQ} which is still compatible with 5% CL. A larger coupling is excluded with 95% CL. Constraints on the coupling λ_{eq} from the search for first generation leptoquarks are not taken into account in this thesis. The influence of these constraints is discussed below within the context of the assumptions made for β_{LFV}. Analogously, it is searched for the mass m_{LQ} assuming a fixed coupling $\lambda_{eq} = \lambda_{\mu q} = 0.3$. Here, lower masses can be excluded.

In contrast to the search for first generation LQ which has to handle a large NC/CC DIS background, no binning in the mass m_{LQ} and the kinematic variable y is used. Instead a separation into two bins $25\,\text{GeV} < p_T^{\text{calo}} < 45\,\text{GeV}$ and $p_T^{\text{calo}} \geq 45\,\text{GeV}$ is used, which is introduced in Section 13.3.3.

14.2.2 Results

Since the interaction of e^-p is the main production channel for all LQ-types with a fermion number $F = 2$ (see Table 12.1 on page 114), only results for these seven types are presented. The analysed data provides a factor of ten more integrated luminosity as the e^-p data taken during the HERA I phase. A huge increase of sensitivity is expected.

Figure 14.2 shows the upper limit (95% CL) of the coupling $\lambda_{\mu q}$ for LQ decaying into muon-quark pair as a function of the LQ-mass m_{LQ} . The investigated process mediates lepton flavour violation. The limits are most stringent at small masses $m_{\text{LQ}} \approx 100\,\text{GeV}$. The exclusion limits are less stringent for higher LQ-masses because the LQ production cross section decreases rapidly for higher values of x corresponding to a falling parton density function. Near the kinematical limit $m_{\text{LQ}} = \sqrt{\hat{s}}$, the limit on the resonant production turns into a limit on virtual effects of the u-channel exchange and the off-shell s-channel process. At this transition region, a steep rise in the limits can be observed. Due to the initial state radiation and very low parton density functions, the transition region is shifted to smaller

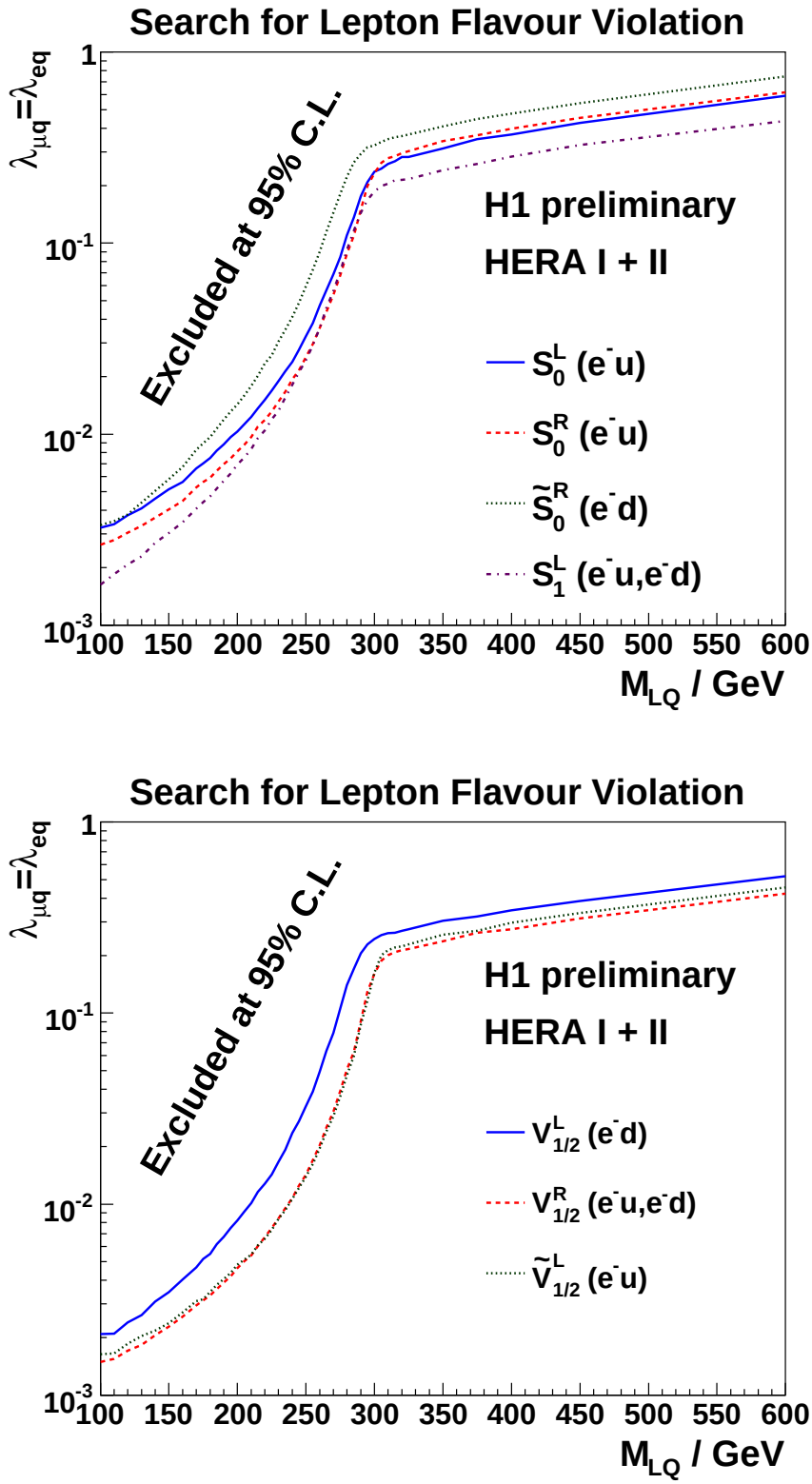

Figure 14.2: *Limits as a function of the leptoquark mass on the coupling constant $\lambda_{eq} = \lambda_{\mu q}$ at 95% CL. The limits are shown for the four scalar LQ (a) and three vector LQ (b) with $F = 2$. The brackets contain the dominant production process (cf. Table 12.1)*

masses $m_{\mathrm{LQ}} \approx 300\,\mathrm{GeV}$.

The bin $p_T^{\mathrm{calo}} \geq 45\,\mathrm{GeV}$ contains most of the signal for $m_{\mathrm{LQ}} > 150\,\mathrm{GeV}$, as it is presented in Figure 13.9 on page 135. While no candidate has been observed in this bin, the limits mainly depend on the signal cross section.

Leptoquarks with couplings to both valence quarks exhibit the best limits. As it can be seen in Table 13.1, slightly more data with left-handed polarisation are analysed. This results in better limits for the left-handed type. This is not true for the resonant production ($m_{\mathrm{LQ}} < 300\,\mathrm{GeV}$) of the two types S_0^L and S_0^R. These types differ only in their decay channel. The left-handed type additionally decays into a neutrino quark pair. This final state is not covered by this search. Therefore, the left-handed type S_0^L is not as strongly excluded as the right-handed type S_0^R. This argument is only true for the resonant production. The missing sensitivity for the neutrino-quark decay is not compensated for by the amount of data measured with left-handed polarisation. For masses $m_{\mathrm{LQ}} > 300\,\mathrm{GeV}$, the additional decay mode does not influence the cross section. Due to the polarisation, in this mass region, the limits for the left-handed S_0^L is stronger than the one for the right handed S_0^R.

$F = 2$	S_0^L	S_0^R	$\tilde{S}_0^R$	S_1^L	$V_{1/2}^L$	$V_{1/2}^R$	$\tilde{V}_{1/2}^L$
m_{LQ}(GeV)	336	323	290	420	374	434	406

Table 14.1: *Lower limits on m_{LQ} for the LQ-types with $F = 2$ assuming $\lambda_{\mu q} = \lambda_{eq} =$ 0.3.*

Table 14.1 summerises the limits on the mass m_{LQ} . The assumption $\lambda_{\mu q} = \lambda_{eq} = 0.3$ has been made. Depending on the LQ-types, masses below 290 to 453 GeV are excluded. This is an improvment of 12 to 114 GeV in comparison to the limits determined by the HERA I analysis, which are shown in Table 12.2 on page 119.

Figure 14.3 shows the comparison of the results of this analysis and the results of the analysis of HERA I data for the LQ-type S_0^L. The improvement in the excluded phase space is clearly visible. The new limits on the coupling $\lambda_{\mu q}$ are up to three times stricter. This improvement is mainly due to the increase of the integrated luminosity. Ten times more $e^- p$ was accumulated during the HERA II phase than during the HERA I phase. This increase more than compensates for the loss of signal efficiency due to the down weighting to take the deficit in the γ^{h}-distribution into account (Section 13.3.5). The separation of data according to the polarisation of the incoming lepton also improves the sensitivity. Due to the low background, this effect is small in comparison with the increase of the data analysed.

Figure 14.3 also shows the results from the search for first generation LQ [71]. This analysis is sensitive to the coupling λ_{eq} assuming that no lepton flavour violation takes place ($\beta_{\mathrm{LFV}}^{\mu,\tau} = 0$). The full amount of data (HERA I+II $e^{\pm}p$) are analysed. Only limits up to a LQ-mass of 400 GeV are deduced.

A future combination of both searches would allow to determine also the branching ratio of lepton flavour violation $\beta_{\mathrm{LFV}}^{\mu}$. In a first approach, it could be assumed that no transition into a tau is mediated by the leptoquark. In this case, the limits that are derived in this thesis (assuming $\beta_{\mathrm{LFV}}^{\mu} = 0.5$) can be interpreted as limits on the product of the couplings

$$\lambda_{\mu q}^{\beta_{\mathrm{LFV}}^{\mu}=0.5} \equiv \sqrt{\lambda_{eq}^{\mathrm{free}} \cdot \lambda_{\mu q}^{\mathrm{free}}}\,, \tag{14.8}$$

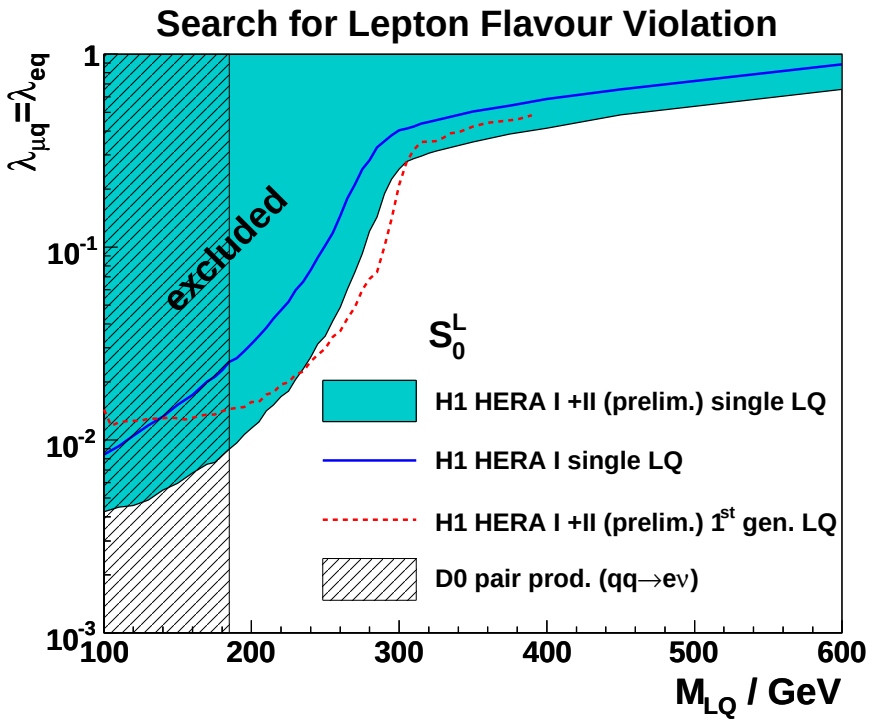

Figure 14.3: *Comparison with other results: Additionally to the results of this analysis for a LQ S_0^L the results of the HERA I (black, solid line) and the HERA I+II analysis of the first generation LQ (red dashed line) are shown. The phase space excluded from D0 searches is presented by the corded area.*

where λ^{free} denotes the coupling without any assumption on the branching ratio of lepton flavour violation. If $\lambda_{eq}^{\text{free}}$ is constrained by first generation searches, the limits on $\lambda_{\mu q}^{\beta_{\text{LFV}}^{\mu}=0.5}$ can be reinterpreted to a limit on the coupling $\lambda_{\mu q}^{\text{free}}$. If the possible decay of LFV LQ with a tau in final state is also investigated, it is possible to determine $\beta_{\text{LFV}}^{\tau}$.

The limit deduced from the D0 experiment is also depicted in Figure 14.3. Due to the production mechanism, this limit is independent on the coupling λ. The value of 185 GeV is deduced taking the difference in the branching ratios between $p\bar{p}$ interactions and ep collisions into account. Details about this difference and the derived limit can be found in Section 12.3.4. For not too small couplings (λ) or high masses (m_{LQ}), HERA is more sensetive and is probing unexplored phase space.

Chapter 15

Summary, Conclusion and Outlook

15.1 Summary and Conclusion

The complete $e^- p$ data taken during the HERA II phase has been anaysed in search of lepton flavour violation mediated by leptoquarks. The final state containing a muon quark pair was investigated. In the data corresponding to an integrated luminosity of $158.9\,\mathrm{pb}^{-1}$, two candidates have been selected. The observation fits perfectly with the SM expectation of 2.2 ± 0.6, which comes mainly from lepton-pair production.

The agreement between data and the simulation has been studied with two control selections. A selection of CC DIS events and a muon selection, based on the signal selection using relaxed cuts, were investigated. A deviation between data and the simulation has been observed at low values of γ^{h}. While no reason for this deficiency has been found, the systematical error for the CC DIS process has been inflated from 10% to 25%. To take possible effects on the signal efficiency into account, the efficiency has been reduced by 25%.

While no evidence for lepton flavour violation has been found, limits with 95% CL on the model parameter of the BRW model are deduced. The limits on the Yukawa coupling $\lambda_{\mu q}$ vary between $1.8671 \cdot 10^{-3}$ and 0.82 depending on the leptoquark mass and the type. In comparison with the analysis of HERA I data, the limits on the coupling $\lambda_{\mu q}$ are up to three times stricter.

Additionally, limits on the leptoquark mass m_{LQ} are calculated assuming $\lambda_{\mu q} = \lambda_{eq} = 0.3$. Masses between 290 and 406 GeV are deduced depending on the type of the leptoquark. The limits on the masses have been improved by between 12 and 114 GeV in comparison to the results obtained by the HERA I analysis.

15.2 Outlook

The presented analysis should be continued. The difference between the data and the simulation which has been observed in the selection of CC DIS must be understood. Since it is most pronounced at low values of γ^{h} and high values of p_T^{calo}, its influence on the signal selection efficency must be investigated further. This would allow to remove the artificial reduction of the signal efficiency by 25%, or to replace it by an event based weight depending on γ^{h} and/or p_T^{calo}.

Furthermore, all HERA II data should be analysed including the data of $e^+ p$ interactions. This data provides an integrated luminosity of $177\,\mathrm{pb}^{-1}$, which is in the order of three times

more than that recorded during the HERA I phase. This will allow an investigation of the seven LQ-types with $F = 0$, which have not been studied in this thesis.

Additionally, the HERA I data should be re-analysed, using a binning in p_T^{calo} and the same set of cuts as presented here.

A search for the other lepton flavour violating decay mode into a tau quark pair should also be performed. If the results of this search also gives no evidence for LFV, limits can be calculated making no assumption for the branching ratio between the lepton generations.

The LHC will provide an environment to study leptoquarks. The high luminosity and the high centre-of-mass energy will ensure that leptoquarks may be discovered or the limits will improve further. As in the case of the experiments at the Tevatron, due to the similar initial state, the analyses does not include the mediation of lepton flavour violation.

Part I & II

Summary, Conclusions and Outlook

This chapter summarise the results of the two parts of this thesis. A more detailed summary of Part I and Part II can be found in Chapter 9 and Chapter 15, respectively.

16.1 Part I: A TPC at the ILC

Data taken with the TPC prototype MediTPC which uses a GEM based amplification system has been analysed to study the spatial resolution of such a device. This study is part of a design phase for a detector at the International Collider.

It is very important to consider the Pad Response Function to achieve a resolution of $\sigma_{r\phi} \approx 100\,\mu\text{m}$ at zero drift length. To reach the requirement of a spatial resolution of below 100 µm for the complete drift length, the ratio of the signal given by the charge spread to the pad width must be optimised. It has been shown that from the two investigated gases Ar/CH_4 (95/5) is the best choice for this purpose. Nevertheless, the results show that a pad width of 2.2 mm is not sufficient if a magnetic field of 4 T is applied. The pad size should be reduced to of the order of 1 mm.

Two reconstruction methods to determine the track parameters have been tested. A new approach has been compared to a traditional approach which is based of a row based reconstruction of the centre-of-gravity of the localised charge information and a Chi-Square-Fitting method. The new approach uses a maximum likelihood technique to fit a charge expectation determined by the track parameters to the measured charge of all pad in all rows at once. In both cases, it is best to use the information about the diffusion as an input parameter. This provides the most reliable reconstruction and performs best in the presence of damaged pads or in the cases of a small number of pad rows.

Further studies using a smaller pad size as well as a larger read-out area have been started.

16.2 Part II: Search for Lepton Flavour Violation at HERA II

The complete HERA II e^-p data of the H1 experiment ($158.9\,\text{pb}^{-1}$) have been searched for lepton flavour violation mediated by leptoquarks. These particles are described by an extension Buchmüller-Rückl-Wyler Model (BRW) [12]. Final states with a muon have been taken into account. The search selected two events in the data, which is good agreement with the expectation of the Standard Model of 2.2 ± 0.6 events.

While no evidence for the signal process have been found, limits with a 95% CL in the $m_{\text{LQ}}/\lambda_{eq}$ -phase space have been calculated. In comparison with the results of the HERA I analysis, the results presented here exclude significantly more phase space. Assuming a coupling of 0.3, leptoquark masses between 290 and 406 GeV can be excluded with 95% confidence level depending on leptoquark type.

Bibliography

[1] S. Weinberg, A Modell of Leptons, Phys. Rev. Lett. **19**, 1264–1266 (1967).

A. Salam, *Elementary Particle Theorie*, page 367ff, Almquist und Wiksells, Stockholm, 1968.

S. L. Glashow, Partial Symmetries of Weak Interactions, Nucl. Phys. **22**, 579–588 (1961).

[2] C. Amsler et al., Review of Particle Physics, Journal of Physics G **33** (2006), `http://pdg.lbl.gov`.

[3] O. Schäfer, Ein Monitorsystem für gasbasierte Detectoren am Internationalen Linear Collider, Diplomarbeit, Universität Rostock, Germany, December 2005, DESY-THESIS-2006-040.

[4] P. W. Higgs, Broken Symmetries, Massless Particles and Gauge Fields, Phys. Lett. **12**, 132–133 (1964).

P. W. Higgs, Broken Symmetries and the Masses of Gauge Bosons, Phys. Rev. Lett. **13**, 508–509 (1964).

P. W. Higgs, Spontneous Symmetry Breakdown without Massless Bosons, Phys. Rev. **145**, 1156–1163 (1966).

F. Englert and R. Brout, Broken Symmetry and the Mass of Gauge Vector Mesons, Phys. Rev. Lett **13**, 321–322 (1964).

G. S. Guralnik, C. R. Hagen, and T. W. B. Kibble, Global Conservation Laws and Massless Particles, Phys. Rev. Lett. **13**, 585–587 (1964).

[5] *The LEP Electoweak Working Group*, `http://lepewwg.web.cern.ch/LEPEWWG`.

[6] R. Barate et al. (LEP Working Group for Higgs boson searches Collaboration), Search for the standard model Higgs boson at LEP, Phys. Lett. **B565**, 61–75 (2003), hep-ex/0306033.

[7] Y. Ashie et al. (Super-Kamiokande Collaboration), Evidence for an oscillatory signature in atmospheric neutrino oscillation, (2004), hep-ex/0404034.

M. H. Ahn et al. (K2K Collaboration), Indications of neutrino oscillation in a 250-km long-baseline experiment, Phys. Rev. Lett. **90**, 041801 (2003), hep-ex/0212007.

S. N. Ahmed et al. (SNO Collaboration), Measurement of the total active B-8 solar neutrino flux at the Sudbury Neutrino Observatory with enhanced neutral current sensitivity, Phys. Rev. Lett. **92**, 181301 (2004), nucl-ex/0309004.

K. Eguchi et al. (KamLAND Collaboration), First results from KamLAND: Evidence for reactor anti- neutrino disappearance, Phys. Rev. Lett. **90**, 021802 (2003), hep-ex/0212021.

[8] Z. Maki, M. Nakagawa, and S. Sakata, Remarks on the Unified Model of Elementary Particles, Prog. Theor. Phys. **28**, 870ff (1962).

[9] J. C. Pati and A. Salam, Lepton Number as the Fourth Color, Phys. Rev. **D10**, 275–289 (1974).

[10] G. G. Ross, *Grand Unified Theories*, Benjamin/Cummings, 1984, ISBN 0-8053-6967-8.

H. Georgi and S. L. Glashow, Unity of All Elementary Particle Forces, Phys. Rev. Lett. **32**, 438–441 (1974).

P. Langacker, Grand Unified Theories and Proton Decay, Phys. Rept. **72**, 185 (1981).

[11] S. Dimopoulos and L. Susskind, Mass without Scalars, Nucl. Phys. **B155**, 237–252 (1979).

S. Dimopoulos, Technicolored Signatures, Nucl. Phys. **B168**, 69–92 (1980).

E. Farhi and L. Susskind, Technicolor, Phys. Rept. **74**, 277 (1981).

[12] W. Buchmüller, R. Rückl, and D. Wyler, Leptoquarks in Lepton Quark Collisions, Phys. Lett. **B191**, 442–448 (1987).

[13] J. Brau et al., Interational Linear Collider Refernece Design Report, Vol 1: Executive Summary, 2007, ILC-REPORT-2007-001.

[14] J. Brau et al., Interational Linear Collider Refernece Design Report, Vol 4: Detector, 2007, to be published.

[15] T. Krämer, Track Parameters in LCIO, LCNote (2006), LC-DET-2006-004.

[16] R. L. Glückstern, Uncertainties in track momentum and direction, due to multiple scattering and measurement errors, Nucl. Instrum. Meth. **24**, 381–389 (1963).

[17] TESLA Technical Design Report, Technical Report DESY 2001-011, DESY, Notkestraße 85, 22607 Hamburg, Germany, March 2001.

[18] LCTPC Collaboration, TPC R&D for an ILC Detector, LCNote (2007), LC-DET-2007-005.

[19] D. R. Nygren, The Time Projection Chamber: A new 4 Pi Detector for Charged Particles, PEP-0144.

[20] *Magboltz*, `http://cyclo.mit.edu/drift/www/aboutMagboltz.html`.

[21] R. Veenhof, *Garfield – Simulation of gaseous detectors*, `http://garfield.web.cern.ch/garfield/`.

[22] I. Smirnov, *HEED Simulation Programme for Energy Loss.*

[23] W. R. Leo, *Techniques for Nuclear und Particle Physics Experiments*, Springer-Verlag, Berlin, Germany, 2nd edition, 1994.

[24] D. Buskulic et al. (ALEPH Collaboration), Performance of the ALEPH detector at LEP, Nucl. Instrum. Meth. **A360**, 481–506 (1995).

[25] L. Landau, On the energy loss of fast particles by ionization, J. Phys. USSR 8 (1944).

[26] P. Vavilov, Ionization losses of high-energy particles, Sov. Phys.-JETP 5 (1957).

[27] S. Seltzer and M. Berger, Energy Loss Straggling and of Protons and Mesons: Tabulations of the Vavilov Distribution, National Academy of Sciences Publication, Nuclear Science Series Report No. 39 (1964).

[28] W. Blum and L. Rolandi, *Particle Detection with Drift Chambers*, Springer, 1993.

[29] U. Fano, On the theory of ionization yield of radiations in different substances, Phys. Rev. 70 (1 & 2) **70** (1946).

U. Fano, Ionization yield of radiations ii. the fluctuation of the number of ions, Phys. Rev. 72 (1) **72** (1947).

[30] T. Lohse and W. Witzeling, *Instrumentation in High Energy Physics*, chapter 2, World Scientific, Singapure, 1992.

[31] T. Lux, *Studies for a Time Projection Chamber for the International Linear Collider and Measurement of Beauty Cross Sections in Deep Inelastic Scattering at HERA*, Doktorarbeit, DESY-THESIS-2005-019.

[32] G. Charpak and B. Southworth, New Particles Detectors: The Multiwire Proprotinal Chamber and The Drift Chamber, CERN-SIS-PU-77-08.

[33] A. Breskin et al., High flux operation of the gated multistep avalanche chamber, Nucl. Instr. Meth. **178**, 11 (1980).

[34] F. Sauli, GEM: A New Concept for Electron Amplification in Gas Detectors, Nucl. Instrum. Meth. **A386**, 531–534 (1997).

[35] Y. Giomataris, P. Rebourgeard, J. P. Robert, and G. Charpak, MICROMEGAS: A high-granularity position-sensitive gaseous detector for high particle-flux environments, Nucl. Instrum. Meth. **A376**, 29–35 (1996).

[36] B. Ketzer, Q. Weitzel, S. Paul, F. Sauli, and L. Ropelewski, Performance of triple GEM tracking detectors in the COMPASS experiment, Nucl. Instrum. Meth. **A535**, 314–318 (2004).

[37] S. Bachmann et al., Charge amplification and transfer processes in the gas electron multiplier, Nucl. Instrum. Meth. **A438**, 376–408 (1999).

S. Bachmann et al., Development and applications of the Gas Electron Multiplier, Nucl. Instrum. Meth. **A471**, 115–119 (2000).

[38] *Gas Detectors Development - CERN*, `http://gdd.web.cern.ch/GDD`.

[39] M. E. Janssen, Auflösungsstudien an einer Zeit-Projektions-Kammer (TPC) mit GEM-Gasverstärkungssystem, Diplomarbeit, Universität Dortmund, Germany, September 2004, DESY-THESIS-2004-049.

[40] P. Schade, private communication.

[41] C. K. Bowdery, editor, *ALEPH Handbook*, volume 1, CERN, 2 edition, 1995.

[42] F. Gaede, T. Behnke, N. Graf, and T. Johnson, LCIO: A Persistency Framework for Linear Collider Simulation Studies, ECONF **C0303241**, TUKT001 (2003), physics/0306114.

[43] M. Ball, N. Ghodbane, M. E. Janssen, and P. Wienemann, A DAQ System for Linear Collider TPC Prototypes Based on the ALEPH TPC Eelectronics, LCNote (2004), physics/0407120.

[44] A. Imhof, private communication.

[45] R. Brun and F. Rademakers, ROOT: An object oriented data analysis framework, Nucl. Instrum. Meth. **A389**, 81–86 (1997).

[46] A. Krivoshey, *DOTCONF++:library for parsing configuration files*, 0.0.3a edition, `http://www.foss.kharkov.ua/~voodoo/`.

[47] R. Diener, Study of Reconstruction Methods for a Time Projection Chamber with GEM Gas Amplification System, Diplomarbeit, Universität Hamburg, Germany, May 2006, DESY-THESIS-2006-040.

[48] M. Ball, *Methods and Results for Calibration and Track Separation of a GEM based TPC using a UV-Laser*, Doktorarbeit, Universität Hamburg, Germany, to be published.

[49] M. Hauschild, *Kalibration der zentralen Jetkammer des OPAL-Detektors mit UV-Laserstrahlen: Methoden und Ergebisse am Jetkammer-Prototypen (FSP)*, Doktorarbeit, Physikalisches Institut der Universität Bonn, 1988, BONN-IR-88-57.

[50] R. K. Carnegie et al., Resolution Studies of Cosmic-Ray Tracks in a TPC with GEM Readout, Nucl. Instrum. Meth. **A538**, 372–383 (2005), physics/0402054.

[51] R. Mankel, Pattern recognition and event reconstruction in particle physics experiments, Rept. Prog. Phys. **67**, 553 (2004), physics/0402039.

[52] D. Karlen, P. Poffenberger, and G. Rosenbaum, TPC Performance in Magnetic Fields with GEM and Pad Readout, Nucl. Instrum. Meth. **A555**, 80–92 (2005), physics/0509051.

[53] LCG Project, Miniut Home Page,
`http://seal.web.cern.ch/seal/snapshot/work-packages/mathlibs/minuit/`.

[54] D. Karlen et al., JPTC,
`http://wwwlinearcollider.ca/groups/uvic/tpc/resources/files`.

[55] A. A. Sokolov and I. M. Ternov, On Polarization and spin effects in the theory of synchrotron radiation, Sov. Phys. Dokl. **8**, 1203–1205 (1964).

[56] D. P. Barber et al., The HERA polarimeter and the first observation of electron spin polarization at HERA, Nucl. Instrum. Meth. **A329**, 79–111 (1993).

[57] M. Beckmann et al., The longitudinal polarimeter at HERA, Nucl. Instrum. Meth. **A479**, 334–348 (2002), physics/0009047.

[58] I. Abt et al. (H1 Collaboration), The H1 detector at HERA, Nucl. Instrum. Meth. **A386**, 310–347 (1997).

[59] B. Andrieu et al. (H1 Calorimeter Group Collaboration), The H1 liquid argon calorimeter system, Nucl. Instrum. Meth. **A336**, 460–498 (1993).

[60] B. Andrieu et al. (H1 Calorimeter Group Collaboration), Results from pion calibration runs for the H1 liquid argon calorimeter and comparisons with simulations, Nucl. Instrum. Meth. **A336**, 499–509 (1993).

[61] B. Andrieu et al. (H1 Calorimeter Group Collaboration), Beam tests and calibration of the H1 liquid argon calorimeter with electrons, Nucl. Instrum. Meth. **A350**, 57–72 (1994).

[62] A. W. Jung et al., First Resuts from the Third Level of the H1 Fast Track Trigger, Proc. of the 15$^{\text{th}}$ IEEE NPSS RealTime Conference (May 2007).

[63] R. Brun and F. Carminati, *GEANT Detector Description and Simulation Tool*, 1993, `http://consult.cern.ch/writeup/geant/`.

[64] R. P. Feynman, Very High-Energy Collisions of Hadrons, Phys. Rev. Lett. **23**, 1415–1417 (1969).

[65] D. J. Gross, The Discovery of Asymptotic Freedom and the Emergence of QCD, Proc. Nat. Acad. Sci. **102**, 9099–9108 (2005).

[66] C. Adloff et al. (H1 Collaboration), Measurement and QCD analysis of neutral and charged current cross sections at HERA, Eur. Phys. J. **C30**, 1–32 (2003), hep-ex/0304003.

[67] C. Adloff et al. (H1 Collaboration), Search for new physics in e+- q contact interactions at HERA, Phys. Lett. **B568**, 35–47 (2003), hep-ex/0305015.

[68] L. Linus, *Search for Lepton Flavour Violation with the H1 Experiment at HERA*, Doktorarbeit, University of Zürich, Swizerland, 2006.

[69] A. Aktas et al. (H1 Collaboration), Search for lepton flavour violation in e p collisions at HERA, Eur. Phys. J. **C52**, 833–847 (2007), hep-ex/0703004.

[70] A. Aktas et al. (H1 Collaboration), Search for leptoquark bosons in e p collisions at HERA, Phys. Lett. **B629**, 9–19 (2005), hep-ex/0506044.

[71] C. Diaconu, I. Panagoulias, and C. Helebran (H1 Collaboration), A Search for Leptoquarks in ep collitions at HERA, **H1-prelim-07-164** (2007).

[72] V. M. Abazov et al. (D0 Collaboration), Search for first-generation scalar leptoquarks in p anti-p collisions at s**(1/2) = 1.96-TeV, Phys. Rev. **D71**, 071104 (2005), hep-ex/0412029.

[73] V. M. Abazov et al. (D0 Collaboration), Search for single production of scalar leptoquarks in p anti-p collisions decaying into muons and quarks with the D0 detector, Phys. Lett. **B647**, 74–81 (2007), hep-ex/0612012.

[74] D. E. Acosta et al. (CDF Collaboration), Search for first-generation scalar leptoquarks in $p\bar{p}$ collisions at $\sqrt{s} = 1.96$ TeV, Phys. Rev. **D72**, 051107 (2005), hep-ex/0506074.

[75] A. Abulencia et al. (CDF Collaboration), Search for second-generation scalar leptoquarks in $p\bar{p}$ collisions at $\sqrt{s}$ = 1.96-TeV, Phys. Rev. **D73**, 051102 (2006), hep-ex/0512055.

[76] T. H. O. Group, *The H1 OO Physics Analysis Project*, 3.1 edition, Dezenber 2007, `https://www-h1.desy.de/icas/oop/3.1/oo.ps`(H1 internal).

[77] E. Sauvan, F. CassolBrunner, and M. Peez, *Marana: A Library for the analysis of the H1 events*, August 2005, internal H1 note.

[78] P. Bruel, *Recherche d'interactions au-deladu Modele Satdars a HERA*, PhD thesis, Univaerty of Paris XI, Orsay, May 1998.

[79] M. Peez et al. (CPPM Marseille Collaboration), An energy flow algorithm for Hadronic Reconstruction in OO: Hadroo2, H1 note H1-01/05-616.

[80] S. D. Ellis and D. E. Soper, Successive combination jet algorithm for hadron collisions, Phys. Rev. **D48**, 3160–3166 (1993), hep-ph/9305266.

[81] S. Bentvelsen, J. Engelen, and P. Kooijman, Reconstruction of (x, Q**2) and extraction of structure functions in neutral current scattering at HERA, NIKHEF-H-92-02.

[82] C. Adloff et al. (H1 Collaboration), Measurement of neutral and charged current cross sections in electron proton collisions at high Q**2, Eur. Phys. J. **C19**, 269–288 (2001), hep-ex/0012052.

[83] G. Brandt, *Analysis of Events with Isolated Leptons and Missing Transverse Momentum in ep Collitions at HERA*, PhD thesis, Ruperto-Carola Universität, Heidelberg, Germany, 2007.

[84] K. Rosenbauer, *Suche nach Leptoquarks und Leptogluonen im H1-Experiment bei HERA*, Dissertation, RWTH Aachen, Germany, 1995.

[85] G. Altarelli and G. Parisi, Asymptotic Freedom in Parton Language, Nucl. Phys. **B126**, 298 (1977).

V. N. Gribov and L. N. Lipatov, Deep inelastic e p scattering in perturbation theory, Sov. J. Nucl. Phys. **15**, 438–450 (1972).

Y. L. Dokshitzer, Calculation of the Structure Functions for Deep Inelastic Scattering and e+ e- Annihilation by Perturbation Theory in Quantum Chromodynamics. (In Russian), Sov. Phys. JETP **46**, 641–653 (1977).

[86] T. Abe, GRAPE-Dilepton (Version 1.1): A generator for dilepton production in e p collisions, Comput. Phys. Commun. **136**, 126–147 (2001), hep-ph/0012029.

[87] U. Baur, J. A. M. Vermaseren, and D. Zeppenfeld, Electroweak vector boson production in high-energy e p collisions, Nucl. Phys. **B375**, 3–44 (1992).

[88] T. Sjostrand et al., High-energy-physics event generation with PYTHIA 6.1, Comput. Phys. Commun. **135**, 238–259 (2001), hep-ph/0010017.

[89] H. Jung, Hard diffractive scattering in high-energy e p collisions and the Monte Carlo generation RAPGAP, Comp. Phys. Commun. **86**, 147–161 (1995).

The RAPGAP Monte Carlo for Deep Inelastic Scattering, `http://www.desy.de/~jung/rapgap`.

[90] G. A. Schüler and H. Spiesberger, DJANGO: The Interface for the event generators HERACLES and LEPTO, In *Hamburg 1991, Proceedings, Physics at HERA, vol. 3* 1419-1432. (see HIGH ENERGY PHYSICS INDEX 30 (1992) No. 12988).

[91] M. Steder, 2007.

[92] E. Chabert et al., QBGFMAR: An updated PHAN Package for Cosmic and Halo Muon Topological Rejection in High P_T Physics Analysis, H1 internal notes (1998).

C. Veelken, H1NonepBgFinder - Rejection of Cosmic Muon and Beam-Halo Events in the H1OO Framework, H1 internal notes (2002).

[93] R. Placakyte, private communication, 2007.

[94] G. Zech, Frequentist and Bayesian confidence limits, Eur. Phys. J. direct **C4**, 12 (2002), hep-ex/0106023.

[95] G. J. Feldman and R. D. Cousins, A Unified approach to the classical statistical analysis of small signals, Phys. Rev. **D57**, 3873–3889 (1998), physics/9711021.

List of Figures

List of Tables

Appendix A

MC samples

Generator	SM process	phase space	events	$\int \mathcal{L}dt(\mathrm{pb}^{-1})$
RAPGAP	NC DIS	$Q^2 > 4\,\mathrm{GeV}^2,\ y > 0.08$	987671	259.70
		$Q^2 > 100\,\mathrm{GeV}^2,\ y > 0.08$	399490	876.14
		$Q^2 > 400\,\mathrm{GeV}^2,\ y > 0.08$	4799950	5141.40
		$Q^2 > 1000\,\mathrm{GeV}^2,\ y > 0.08$	399996	1512.71
		$Q^2 > 2500\,\mathrm{GeV}^2,\ y > 0.08$	199998	2890.05
		$Q^2 > 5000\,\mathrm{GeV}^2,\ y > 0.08$	199998	9483.60
		$Q^2 > 10000\,\mathrm{GeV}^2,\ y > 0.08$	199998	38004.21
		$Q^2 > 20000\,\mathrm{GeV}^2,\ y > 0.08$	199998	238971.53
RAPGAP	NC DIS	$Q^2 > 4\,\mathrm{GeV}^2,\ y \leq 0.08$	127509	20.48
		$Q^2 > 100\,\mathrm{GeV}^2,\ y \leq 0.08$	59994	95.19
		$Q^2 > 1000\,\mathrm{GeV}^2,\ y \leq 0.08$	399996	1368.15
DJANGO	CC DIS	$Q^2 > 100\,\mathrm{GeV}^2$	1200000	17040.40
		$Q^2 > 10000\,\mathrm{GeV}^2$	500000	88596.87
GRAPE	ee-Prod.	$p_{T,l} > 8\,\mathrm{GeV}$	379200	300000.00
		$p_{T,l} > 20\,\mathrm{GeV}$	151649	30000.00
	$\mu\mu$-Prod.	$p_{T,l} > 8\,\mathrm{GeV}$	119169	50000.19
	$\tau\tau$-Prod.	$p_{T,l} > 8\,\mathrm{GeV}$	111596	100000.00
EPVEC	W-Prod. (lep.)	$Q^2 > 4\,\mathrm{GeV}^2$	54201	100068.72
	W-Prod. (had.)	$Q^2 > 4\,\mathrm{GeV}^2$	101495	100009.78

Table A.1: *Part A of the summary of the SM background samples employed in the analysis. the number of events and integrated luminosity refer to the samples used for 05 periods.*

Generator	SM process	phase space	events	$\int \mathcal{L}dt$ (pb^{-1})
PYTHIA	dir. γP (uds)	$\hat{p}_T > 5\,\mathrm{GeV}$	1273327	150.12
		$\hat{p}_T > 10\,\mathrm{GeV}$	999990	402.04
		$\hat{p}_T > 15\,\mathrm{GeV}$	1059989	1991.27
		$\hat{p}_T > 25\,\mathrm{GeV}$	1299987	20239.16
		$\hat{p}_T > 40\,\mathrm{GeV}$	139998	20038.93
		$\hat{p}_T > 75\,\mathrm{GeV}$	9999	79024.73
		$\hat{p}_T > 95\,\mathrm{GeV}$	9999	86217.80
PYTHIA	dir. γP (c)	$\hat{p}_T > 5\,\mathrm{GeV}$	411839	90.07
		$\hat{p}_T > 10\,\mathrm{GeV}$	345235	433.72
		$\hat{p}_T > 15\,\mathrm{GeV}$	299997	2079.32
		$\hat{p}_T > 25\,\mathrm{GeV}$	239997	19837.57
		$\hat{p}_T > 40\,\mathrm{GeV}$	9999	13052.33
PYTHIA	dir. γP (b)	$\hat{p}_T > 5\,\mathrm{GeV}$	44505	89.96
		$\hat{p}_T > 10\,\mathrm{GeV}$	59999	388.74
		$\hat{p}_T > 15\,\mathrm{GeV}$	59999	1893.63
		$\hat{p}_T > 25\,\mathrm{GeV}$	59999	20949.66
PYTHIA	res. γP (uds)	$\hat{p}_T > 5\,\mathrm{GeV}$	7892059	149.94
		$\hat{p}_T > 10\,\mathrm{GeV}$	3299967	404.33
		$\hat{p}_T > 15\,\mathrm{GeV}$	2340006	1998.67
		$\hat{p}_T > 25\,\mathrm{GeV}$	1559984	20229.54
		$\hat{p}_T > 40\,\mathrm{GeV}$	99999	22568.55
		$\hat{p}_T > 75\,\mathrm{GeV}$	9999	425489.36
		$\hat{p}_T > 95\,\mathrm{GeV}$	9999	8927678.57
PYTHIA	res. γP (c)	$\hat{p}_T > 5\,\mathrm{GeV}$	13232	89.73
		$\hat{p}_T > 10\,\mathrm{GeV}$	9999	475.97
		$\hat{p}_T > 15\,\mathrm{GeV}$	9999	3047.02
		$\hat{p}_T > 25\,\mathrm{GeV}$	9999	34861.58
PYTHIA	res. γP (b)	$\hat{p}_T > 5\,\mathrm{GeV}$	13225	89.97
		$\hat{p}_T > 10\,\mathrm{GeV}$	9999	653.70
		$\hat{p}_T > 15\,\mathrm{GeV}$	9999	3569.55
		$\hat{p}_T > 25\,\mathrm{GeV}$	9999	37151.66
PYTHIA	prompt γP	$\hat{p}_T > 10\,\mathrm{GeV}$	49999	8316.36
		$\hat{p}_T > 20\,\mathrm{GeV}$	19999	65094.55
		$\hat{p}_T > 40\,\mathrm{GeV}$	19999	2604036.45

Table A.2: *Part B of the summary of the SM background samples employed in the analysis. the number of events and integrated luminosity refer to the samples used for 05 periods.*

Appendix B

Event displays

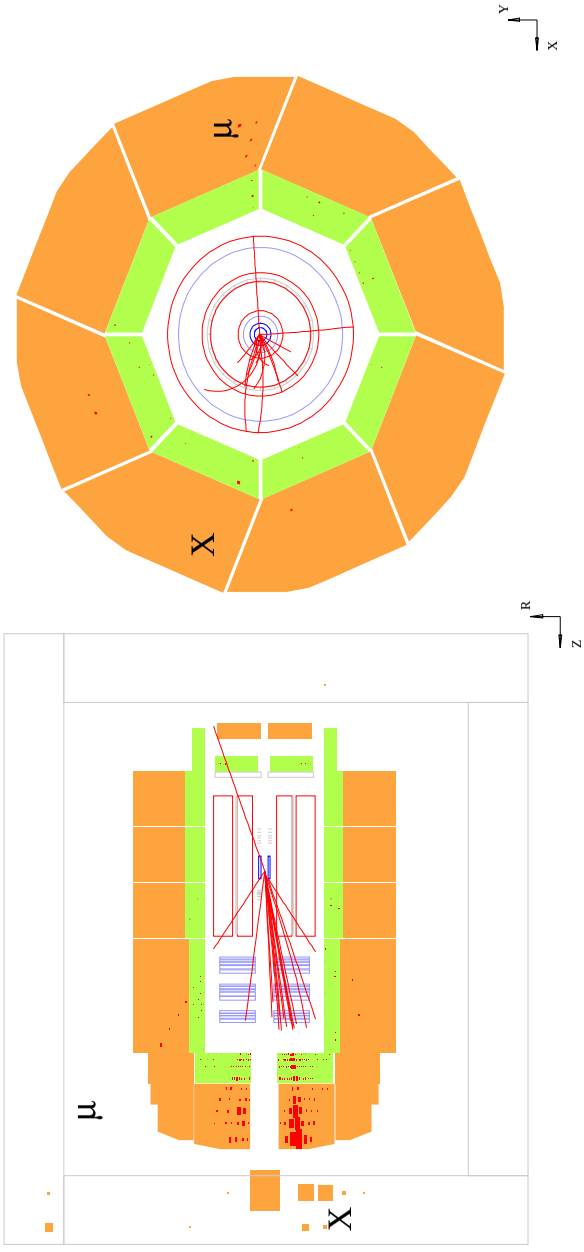

Figure B.1: *Event display (run 421547, event 99635): This event contains one identified muon, which is isolated. The second isolated track which goes into the SpaCal is not referred to an identified particle. It could be the scattered electron as well as a muon (small signal in the CMS). The proton remnant gives the HFS in the forward region. Due to the failure of the identification of the particle in the backward region, it is unclear if this event is a lepton-pair production or W-production.*

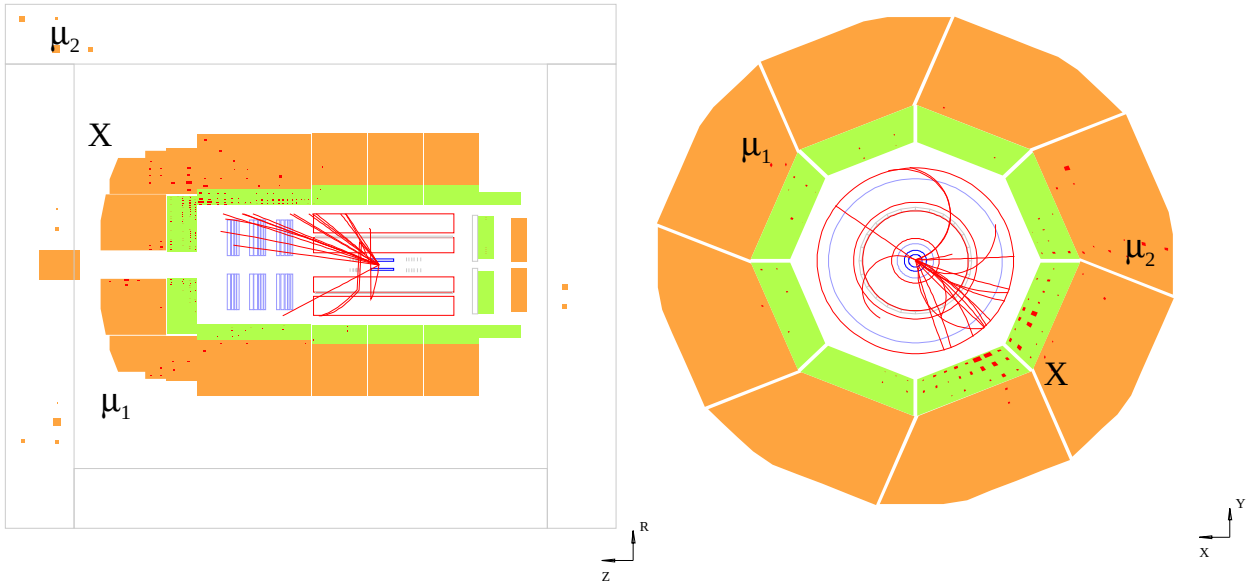

Figure B.2: *Event display (run 425829, event 45637): Two muons are clearly visible. Both are identified as muons. One is isolated while the other is near the HFS. This event is most likely lepton-pair production.*

Acknowledgement

On this last, yet certainly not least page, I would like to to thank these people who took part in this project.

I say thank you to:

- my Professor Dr. Rolf-Dieter Heuer for giving me the opportunity to make my PhD thesis in the interesting research field of particle physics.
- Ties Behnke, Felix Sefkow and Jenny List for their supervision, care and advice.
- Ralf Diener, who's interesting and pointing questions, who's observation and answers pushed the analysis of the MediTPC data forward.
- Markus Ball and all the other members of the FLC TPC group for all the useful discussions, their help and support.
- The same is true for Emmanuel Savan, David South, Martin Wessels, Gerhard Brandt and the whole REx-Group.
- the referees of my H1 analysis: Andre Schöning and Ringaile Placakyte.
- the referees of my Dissertation and Disputation Prof. Rolf-Dieter Heuer, JProf. Johannes Haller and Prof. Peter Schleper.
- the questioners of my Disputation.
- the HERA machine group and the H1 experiment, without their efforts this analysis would not have been possible.
- Prof. Dean Karlen for his detailed explanation of Global Fit Method and his framework JTPC as well as the nice stay in his working group in Victoria, Canada.
- again Jenny List, Ralf Diener, Ties Behnke and Felix Sefkow as well as Klaus Dehmelt for the careful reading of the whole or some parts of the manuscript of this thesis and their very useful comments.
- Jane Hofmann and Steve Aplin for checking the spelling and correcting my German-like Grammar.
- my parents Marga and Edo Janssen as well as my sister Dorit and her boyfriend Sven for there support.
- and my boyfriend Manfred for all his love, all the support, the soothing words and his patience especially during the writing phase of my thesis.